Characterisation of highly active nuclear waste simulants

Neepa Paul

Submitted in accordance with the requirements for the degree of
Doctor of Philosophy

The University of Leeds
Institute of Particle Science and Engineering
School of Chemical and Process Engineering

September 2014

The candidate confirms that the work submitted is his/her own, except where work which has formed part of jointly authored publications has been included. The contribution of the candidate and the other authors to this work has been explicitly indicated below. The candidate confirms that appropriate credit has been given within the thesis where reference has been made to the work of others. The title of the publications:

Characterising highly active nuclear waste simulants. Paul, N., Biggs, S., Edmondson, M., Hunter, T. N. & Hammond, R. B.

Synthesis of nuclear waste simulants by reaction precipitation: Formation of caesium phosphomolybdate, zirconium molybdate and morphology modification with citratomolybdate complex. Paul, N., Biggs, S., Edmondson, M., Hunter, T. N. & Hammond, R. B., Maxwel, L.

The candidate confirms contribution to all publications included carrying out relevant experimental studies, obtaining data, analysis of data and writing of the paper. Contribution of co-authors included discussion of results, proof reading and making relevant amendments.

Dedicated to my parents

Ananta Sindu and Nomita Paul

Acknowledgements

I would like to express gratitude to my supervisors, Simon R. Biggs, Robert B. Hammond, Timothy N. Hunter and Michael J. Edmondson (NNL). for giving me the opportunity to carry out this PhD research in the Institute of Particle Science and Engineering (IPSE) at the University of Leeds and in the National Nuclear Laboratory (NNL) at Sellafield, and their constant support and assistance throughout this project. I would also like to thank the nuclear and crystallisation group in IPSE.

I am very grateful to the EPSRC, NNL and Sellafield Ltd. for the support of an Industrial CASE award scholarship and the opportunity to work on an industrially motivating project and widening my knowledge on nuclear waste processing. In particular I would like to thank the HALES team at NNL/Sellafield Ltd for their support.

I would like to especially thank my wonderful parents, sisters, Anamika and Jessica, my brother in law, Nikhil, and my amazing nephew, Hari for their endless support throughout my Ph.D. Last but not least I would like to thank my lovely Fiancé, Avi for the continuous encouragement and for being my rock!

Thank you to all my family and friends!

Abstract

Nuclear power is a non-carbon emitting energy resource generating 18% of electricity to the UK. As with any type of industrial process the waste management strategy is an important step to define considering the environmental, economic and political factors. However, the nuclear industry faces ongoing challenges to underpin a well-defined waste treatment strategy due to the high heat load and the radioactive nature of the products produced. Reprocessing of spent nuclear fuel produces a highly active liquor (HAL) waste stream. HAL is currently stored in a number of highly active storage tanks (HASTs). Within the HASTs, solid materials are known to have precipitated from the HAL over time. Particle simulants provide a route for understanding the physical behaviour, it is the synthesis of the particle simulants and the characterisation of these solid-liquid systems that are the interest of this study.

An understanding of the HAL waste properties is required for its safe transport, storage and eventual disposal of the HASTs are to be safely emptied and decommissioned. Collaboration with the National Nuclear Laboratory (NNL), at Sellafield UK, provided the opportunity to manufacture the HAL simulants, caesium phosphomolybdate (CPM) and zirconium molybdate (ZM), on larger scale. Manipulation of the aspect ratio of ZM particles is also investigated. The initial step of the synthesis produces spherical CPM which leads to the production of cubic ZM, the final step requires the addition of an organic additive, citric acid, where cuboidal zirconium citratomolybdate (ZMCA) is formed. Molecular modelling analysis revealed growth inhibition of the {2 0 0}, {-2 0 0}, {0 2 0} and {0 -2 0} faces, due to greater number of Zr sites for citratomolybdate complex affiliation. Distinct particle properties are established for CPM, ZM and ZMCA and compared to a common oxide particle material titanium dioxide (TiO_2).

The results of this study highlight the influence of key aspects of the HAL particulates, such as size and shape, on relevant solid-liquid properties such as sedimentation and rheology. The influence of bulk liquid properties such as electrolyte concentration and pH were also investigated. Sedimentation behaviour was characterised by fitting the experimental data to the Richardson-Zaki model, yielding a fitting parameter *n* (cognate to particle size and shape) and thus demonstrated a settling relationship with particle shape, sphere > cubic > cuboidal.

The rheological behaviour explored was categorised into four groups: (i) flow behaviour data was fitted to a simplified Cross model yielding two parameters *K* (related to viscosity) and *n* (extent of shear-thinning); (ii) dependency of viscosity on particle volume fraction was characterised using the Krieger-Dougherty model yielding fitting parameter [μ] (particle's contribution to suspension viscosity) and maximum packing fraction ϕ_m, this demonstrated the relationship, cuboidal > sphere > cube; (iii) yield stress was characterised using an empirical model derived by Heymann et al (2002) yielding a fitting parameter σ^* (cognate to particle shape and size) and demonstrating a relationship, sphere > cuboidal > cubic; (iv) characterisation of compressive yield stress demonstrated the relationship, cuboidal > cubic > sphere.

The results indicate various possible behaviours within the tanks which may impact the storage, remobilisation and pipeline transport of this class of nuclear waste. Ultimately, it is of importance to establish the effect of solid-liquid properties on the behaviour of HAL for current processing, post operational clean out (POCO) and life-time assessment.

Table of Contents

List of Figures

List of Tables

List of Acronyms

Acronym	Definition
ABS	Acoustic Backscatter System
AC	Ammonium Carbamate
AFM	Atomic Force Microscopy
AGR	Advanced Gas Reactors
API	American Petroleum Institute
APT	Associated Particle Technique
ASME	American Society Of Mechanical Engineers
BFDH	Bravais, Friedel, Donnay and Haker
CN	Caesium Nitrate
CPM	Caesium Phosphomolybdate
CPM-H2O	Ceasium Phosphomolybdate in Water
CVF	Constant Volume Feeder
CYS	Compressive Yield Stress
DECC	Department of Energy & Climate Change
DI	Deionised
DLCA	Diffusion Limited Cluster Aggregation
DLVO	Derjaguin Landau Verwey And Overbeek Theory
EdF	Électricité de France
EDL	Electric Double Layer
EDX	Energy dispersive X-ray
EPR	Electron Paramagnetic Resonance
EPSRC	Engineering And Physical Sciences Research Council
GDF	Geological Disposal Facility
GDIS	Graphical Display Interface Structure
GULP	General Utility Lattice Program
HA	Highly Active
HAL	Highly Active Liquor
HALES	Highly Active Liquor Evaporation and Storage
HAS	Highly Active Storage
HAST	Highly Active Storage Tanks
HLW	High-Level Waste
IChemE	Institution of Chemical Engineers
ICSD	Inorganic Crystal Structure Database
IPSE	Institute of Particle Science of Engineering
KD	Krieger and Dougherty
LHS	Left Hand Side
LLWR	Low Level Waste Repository

Acronym	Definition
MNL	Magnesium Lathanide
MRI	Magnetic Resonance Imaging
MS	MATERIALS STUDIO
NDA	Nuclear Decommissioning Authority
NII	Nuclear Installations Inspectorate
NNL	National Nuclear Laboratory
ONR	Office of Nuclear Regulations
PMA	Phosphomolybdic Acid
POCO	Post Operational Clean Out
PSD	Particle Size Distribution
PWR	Pressurized Water Reactor
PXRD	Powder X-Ray Diffraction
QCM	Quartz Crystal Microbalance
R&D	Research And Development
RHS	Right Hand Side
R-Z	Richardson & Zaki
SEM	Scanning Electron Microscopy
s-HLLW	Simulated High Level Liquor Waste
TiO2	Titanium Dioxide
WAR	Water Acid Reduction
WEC	World Energy Council
XRD	X-Ray Diffraction Analysis
YS	Yield Stress
ZM	Zirconium molybdate
ZMCA	Zirconium Citratomolybdate
ZMH	Zirconium Molybdate Hydrate

1 Introduction

Summary

This chapter considers the nuclear industry background and highlights the section of the process where this PhD thesis contributes to. Clear aims and objectives are stated. A management strategy is provided to highlight the milestones of the project, this is to meet the demands of aims and objectives.

1.1 Sustaining nuclear power

The UK Government is committed to the production of electricity through nuclear power, the strategy includes build new power stations (“new-build”), decommissioning and maintenance of new and current nuclear power plants. Nuclear and coal-fired power stations that are due to close in the next 20 years provide a combined electricity supply of approximately 50% to the UK (DECC, 2013). The energy gap which is being created must be filled as there is increasing demand for electricity due to advances in technology and change in consumer conduct.

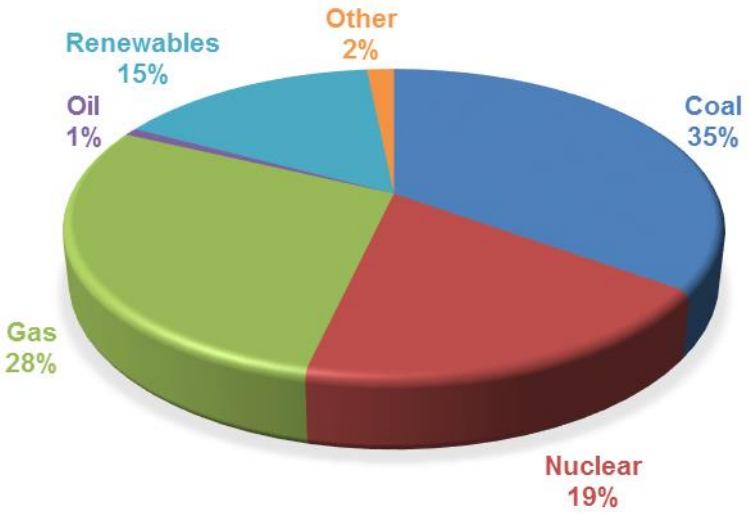

Figure 1.1-1 The average electricity generation sources of 2013 within the UK. Renewables include statistics of solar, wind, hydro and bio energy sources (DECC, 2013).

Figure 1.1-1 illustrates the electricity sources in the UK. Nuclear power is a non-carbon emitting energy resource with an actual global electricity generation of 2,346 TWh of in 2011, compared to wind generating 377 TWh and solar generating 52 TWh (WEC, 2013). Nuclear power has the potential to close this energy gap, to tackle challenges associated with climate change, and to provide energy security on a national and global basis.

Nuclear power has the potential to contribute to the reduction in greenhouse gas emissions and meet governmental targets of 80% reduction by 2050 (DECC, 2014). Figure 1.1-2 illustrates the potential of nuclear power to help meet global technical challenges. The New Nuclear Build Generation Company have started the build of two EPR (Gen III+PWR) reactors at Hinckley point C.

Figure 1.1-2 An illustration portraying nuclear power aims to tackle the key issues the UK face involving the energy gap. With an increase in domestic energy bills and fuel poverty, nuclear power has the ability to overcome these issues.

Support from the UK government is addressed through the recently published industrial strategy. This outlines the case for the UK to re-invigorate its nuclear power industry, including opportunities for economic growth and energy security. A consortium of sectors involving the UK government, industrial partners and academia are required to work together on a long-term partnership if this strategy is to be realised. The strategy describes opportunities in the new build programme (operations and maintenance), waste management and decommissioning.

Issues regarding the nuclear industry have been discussed at length by many authors and include political issues, environmental impacts, economic evaluation and public opinion (Van der Zwaan, 2008, Comission, 2008). High levels of safety and efficiency, increase sustainability and reduced waste production are some of the key issues which need to be resolved. Therefore, it is of interest to further improve nuclear waste treatment strategies which ultimately contributes to an improvement in nuclear and environmental safety aspects.

As with any type of industrial process, the waste management strategy is an important step to define the environmental, economic and political factors. Due to the radioactive nature of the products produced the nuclear industry faces a hazardous challenge in the development to underpin a well-defined waste treatment strategy. This is particularly important as process plants near the end of routine operation require clean out and in addition a legacy of old facilities requiring remediation. It is of interest to optimise and improve nuclear waste treatment strategies that will ultimately contribute to

improvements in nuclear and environmental safety and have the potential to significantly reduce costs.

1.2 Organisation of the UK nuclear industry

The operation of existing nuclear power stations in the UK is currently overseen by EdF Energy (Oxide based reactors) and Magnox (Magnox based reactors). Spent fuel from these reactors is sent to the Sellafield nuclear licensed site in Cumbria for reprocessing – see Chapter 2. The Sellafield site also houses a number of legacy facilities dating from the 1950's and associated with the weapons programme, early processing of nuclear material and commercial power production. These legacy facilities are in a deteriorating condition and their clean-up is considered a priority.

The Sellafield site is operated by Sellafield Limited, a contractor operated company managing the assets and liabilities of the Sellafield site on behalf of the Nuclear Decommissioning Authority (NDA). The NDA is government owned organisation tasked with delivering efficient operation and clean-up of the UK nuclear industry.

A key aspect of delivering a strategy for a nuclear future in the UK is research and development (R&D) and associated innovations. A recent review of R&D in the nuclear industry established two new bodies; the Nuclear Innovation Research Office (NIRO) and Nuclear Innovation Research Advisory Body (NIRAB). The latter being tasked with advising Government on developments in, and strategy for the nuclear industry; NIRO collates information in order to inform NIRAB. Concurrently, the National Nuclear Laboratory (NNL) was taken into direct government ownership. The responsibility of NNL has been expanded to advise on important aspects of the nuclear industry such as, providing and maintaining a UK capability and acting as a technology translator to introduce innovation into the industry, in addition to its commercial activities.

1.3 Research aims and objectives

Approximately 3% of spent nuclear fuel is considered waste (ONR, 2000). This is separated out during reprocessing (see Chapter 2). The waste is consolidated at Sellafield in the Highly Active Liquor Evaporation and Storage (HALES) Plant. The waste, representing a wide range of exotic isotopes is concentrated in this plant to produce Highly Active Liquor (HAL), this is stored in a number of highly active storage tanks (HASTs) in controlled storage conditions, incorporating temperature maintenance and agitation systems. Within the HASTs, solid materials are known to have

precipitated from the HAL over time. Particle simulants provide a route for understanding the physical behaviour of these solids.

The inventory of HAL with its significant active content (radiation and heat) represents one of the greatest potential hazards to the Sellafield site (ONR, 2000). In order to reduce this hazard the Office of Nuclear Regulations (ONR) have regulated HALES to significantly reduce the quantity of stored HAL (ONR, 2000). The HAL contains solids that must be kept in dispersion to avoid the formation of a particle bed at the base of the HASTs. Particle bed formation can lead to a number of issues including blockages (during pipeline transport) and localised corrosion due to 'hot spots' where the radioactive, heat generating solids have settled leading to elevated temperatures. Elevation of temperature promotes corrosion and reduces the integrity of vessel life. It is therefore necessary to develop a good understanding of the solids behaviour and to look for opportunities to optimise the suspension and re-suspension process.

The radioactive nature of the HAL makes direct measurement of the solids behaviour impossible. Therefore realistic simulants, based on a good understanding of the chemistry, have been produced to represent the solid particles contained in HASTs.

This PhD research project is focused on understanding the particle characteristics of the solids contained in HAL. There are 5 main types of HAL solids: zirconium phosphates, barium/strontium nitrate, caesium phosphomolybdate (CPM), zirconium molybdate (ZM) and magnesium lanthanide nitrates (MLN). Of these, CPM and ZM are of particular interest due to the inability to dissolve them in existing plant liquors, i.e. nitric acid. The aim of this research is to identify and understand the physico-chemical properties of ZM and CPM. Further investigation aims to look for opportunities to alter the morphology of these particles to promote improved settling behaviours. This research also aims to apply molecular modelling techniques to characterise the crystallographic morphology of the fission products. Ultimately, leading to the characterisation of HAL solid properties and subsequent behaviours. The main objectives which are required to be attained are as follows:

- Particle synthesis and characterisation. Initial stages will require particle synthesis of nuclear waste simulants. Followed by the development of morphological specific particles via incorporation of an organic additive. Application of numerous particle characterisation

techniques will help understand the physical and chemical properties of each particulate system.

- Morphological prediction of ZM. Various computational models will be applied based on Bravais-Friedel-Donnay-Haker (BFDH), surface and attachment energies to predict the particle morphology. Surface chemistry analysis will give an insight on the atomic interactions and how they affect the change of the crystal morphology in the presence of an additive.
- Particle sedimentation behaviour. Understand the influence of particle properties (particularly size, shape and density) on sedimentation behaviour. A combination of particle characteristics and sedimentation behaviour can establish the stability of each particle dispersion that can be applied to rheological measurements. Sedimentation behaviour can be characterised using gravitational force or centrifugal force techniques, both of which will be explored in this research.
- Suspension rheology behaviour. The key aim for this section of the research is to develop a reliable rheological technique for complex dispersions (i.e. suspensions containing non-spherical, size polydisperse particles). A reliable protocol will enable analysis and determine the influence of particle properties on rheological behaviour. Particle morphology manipulation during synthesis of ZM particles enabled this research to assess the direct effect of shape on rheological behaviour.

The overall aim of this research is to identify, synthesise and characterise relevant solid-liquid properties for HAL particle simulants. Particle morphology manipulation enables research to be carried out on a novel material, zirconium citratomolybdate (ZMCA). Experimental techniques help characterise the simulants in terms of particle shape, shape, density, sedimentation rate, rheological properties and colloidal stability. The ultimate aim is to broaden the understanding of the impact of particle size, shape and particle surface chemistry on the process plant operations.

1.4 Research application

The design and build of new nuclear facilities is a significant undertaking and attracts an associated price-tag, the build of evaporator D, for example, is estimated to be ~£600 m. Therefore there is significant advantage in maximising the asset lifetime by minimising corrosion. One such example, the HALES HASTs that are constructed of stainless steel and corrode over a

period of operation. The corrosion is due to the acidic nature of HAL and the temperature at which they are maintained. It is recognised that for every 10°C rise in temperature the rate of corrosion doubles (Davis, 2000). In the case of the storage tanks it has been identified that when HAL is transferred to the tanks under certain conditions the solids may settle out. This causes a hot spot as the solids form ‘blanketing’ layers and due to the heat generating nature of the solids its results in a localised increase in temperature.

Localised heat sources of HAL solids is due to the decay of caesium (Cs) and strontium (Sr) isotopes, they originate from CPM and barium/strontium nitrates. This behaviour is known as radiogenic heating. Zirconium (Zr) isotopes are short-lived which have mainly decayed during the fuel cooling periods prior to the reprocessing and thus ZM becomes inactive. Similarly, molybdenum (Mo) isotopes are short-lived and therefore the decay heat from Mo is not considered an issue for HAL processing.

The hotspots are mainly due to the sedimentation of the HAL solids contained in the liquor. The HASTs have in-built agitation systems (Jet ballasts and airlifts) to prevent deposition however inefficient operation or operational failure may lead to the formation of ‘hotspots’. Other possible causes are crystallisation due to lower operating temperatures and pipe line blockages. Post Operational Clean Out (POCO) of the process vessel prior to decommissioning is also expected to be challenging due to the potential for a change in liquor viscosity and a variation of solids concentration.

Improvement of the process operations for safe and efficient removal and storage of HAL requires the understanding of solid properties and behaviour of HAL. This knowledge is essential for optimisation of current processing, POCO and life-time integrity of the tanks. The rationale behind this research is to broaden the understanding of the influence of particle properties on process plant operations. The integration of laboratory experiments to industrial applications is important to define. Figure 1.4-1 illustrates an overview of the integration.

The rheological parameters which are being investigated should directly link to the overall engineering design of the waste treatment equipment. By investigating a key rheological parameter, the yield stress, the energy required to re-suspend a settled bed can be obtained. The sedimentation rate is an important parameter when transporting the suspension out of the tank, during the flow of the suspension through pipes and then when in the buffer stock, the sedimentation rate of the solids should be known. This is

due to the fact that sedimentation could occur within in the pipes which in effect can cause blockages, this could be avoided. Figure 1.4-1 outlines the relevance of the laboratory measurements to industrial application.

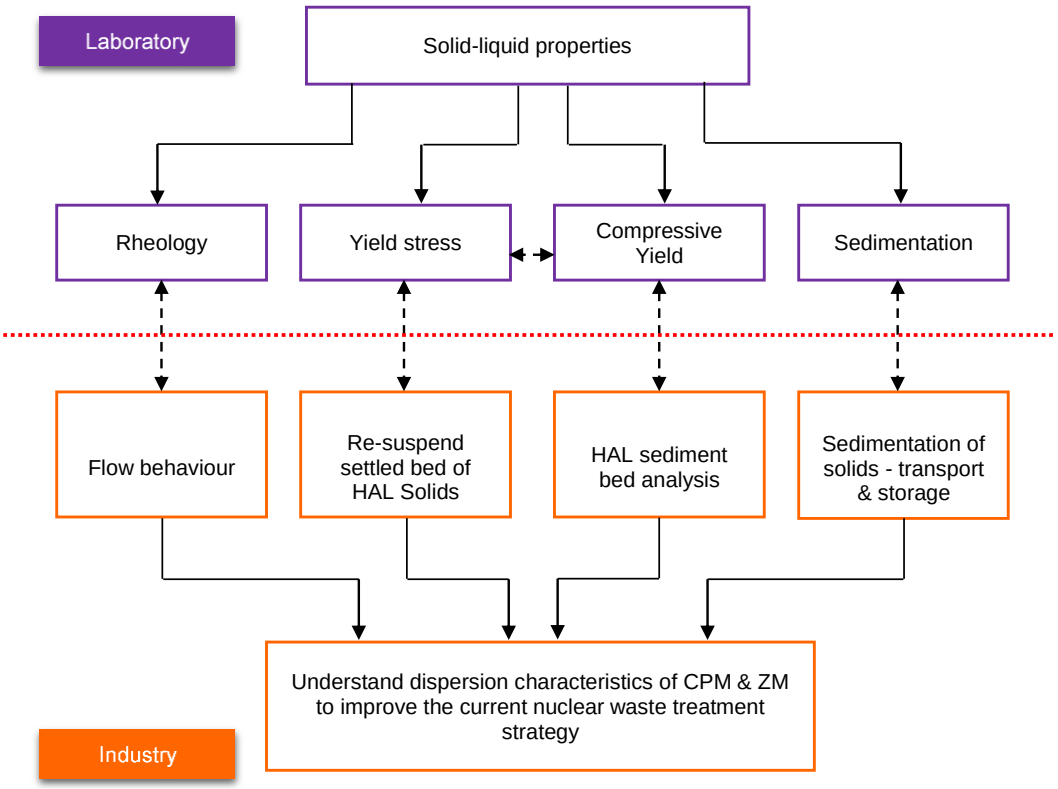

Figure 1.4-1 Flow diagram representing the experimental techniques in relation to the industrial application

Relevant information for the life-time assessment of the storage tanks may be developed through the consideration of the surface chemistry of the HAL solids. The manner in which the molecules interact with the surface of the HASTs/cooling pipes could be modelled, the energy to overcome the interaction between them could be predicted. This prediction of behaviour allows the effect of poor heat transfer and corrosion to be assessed.

The nuclear industry provides challenging environments for research to be carried out due to the fact the material is radioactive. Nuclear waste simulants provides the gateway for understanding the behaviour of the solids contained in the HASTs (HAL solids). The ultimate aim for this research is to contribute an understanding of the transportation, hydrodynamic, chemical & physical properties for CPM and ZM solids to improve upon the current nuclear waste treatment strategy.

1.5 Thesis delivery

The overall layout of the thesis is illustrated in Figure 1.5-1. Chapter 1 introduces the fundamental concepts of nuclear power generation. The aim for this chapter is to discuss the future of nuclear power and the contribution of this energy source to the national and international markets. The nuclear industry faces many challenges and this chapter describes the application of the key findings and how they can contribute to developing solutions. Chapter 2 describes the components of the nuclear fuel cycle, mainly focusing on reprocessing of spent nuclear fuel. Origins of the precipitated HAL solids and their effects on processing will also be discussed in this chapter.

Particle synthesis (e.g. CPM, ZM and ZMCA) and characterisation techniques are discussed in Chapter 3. Synthesis control and optimisation are essential topics included in this chapter to obtain a high yield, morphological specific particle (ZMCA). The results show particle characterisation using various techniques to define the key particle properties. Crystallography fundamentals are discussed in Chapter 4 where optimisation and energy calculations predict the morphology of ZM crystals. The calculations include morphological predictions using the inter-planar spacing distance and the application of interatomic potentials.

Chapters 5 and 6 are behavioural chapters, where the influence of particle properties on sedimentation and rheology, respectively, will be discussed. Chapter 6 in particular focuses on the development of a rheological technique appropriate for complex dispersions. Rheological parameters, yield stress and compressive yield stress, will be discussed to establish the influence of particle shape. Chapter 7 summaries the key conclusions made from this research and suggests future development of the research. The outline of the thesis is illustrated in Figure 1.5-1.

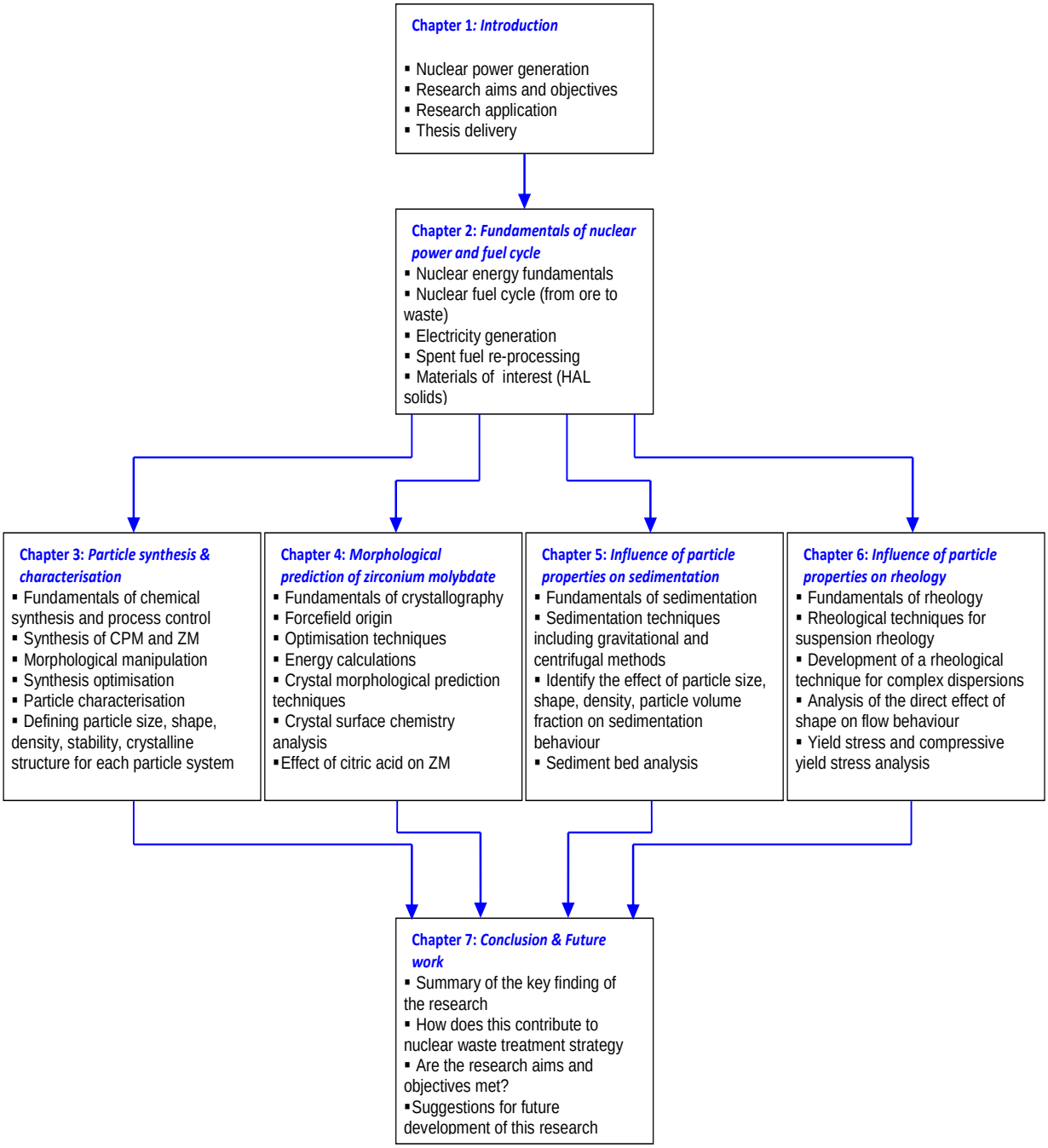

Figure 1.5-1 A schematic illustration of the thesis route-map highlighting the key components related to this thesis. The individual chapters describe the main aims and objectives to be achieved.

2 Fundamentals of nuclear power and The Nuclear Fuel Cycle

Summary

This chapter considers the nuclear industry background and highlights the section of the process where this PhD thesis contributes. Clear aims and objectives are stated. A management strategy is provided to highlight the milestones of the project, this is to meet the demands of aims and objectives.

2.1 Nuclear Physics

The discovery, during 1930's, of initiating and controlling nuclear reactions played an important role in nuclear power generation (Smyth, 1945). Nuclear fission reactions produce a large amount of energy and the mass of the atoms and subatomic particles differ from the start of the reaction to the end. During the reaction matter disappears i.e. mass is displaced, this is known as mass defect. The mass defect is converted into energy from the Einstein's theory $E=mc^2$, which considers the energy (E) in Joules, uniformity of mass (m) in kg and the speed of light (c), 3×10^8 ms^{-1}. According to this theory the source of nuclear energy is the change in mass of the species produced from the fission reaction.

Atoms are complex structures, for any given element they consist of protons (*Z*), neutrons (*N*) and electrons (*e*). The atomic nucleus contains a number of protons and neutrons bound together by nuclear forces. Each proton carries a unit charge and neutrons are uncharged, therefore the unit charge of the atom is equivalent to the number of protons. With the nuclei comprising of practically all of the mass of the atom, the remaining volume is occupied by orbiting electrons, which determine the chemical behaviour of the element.

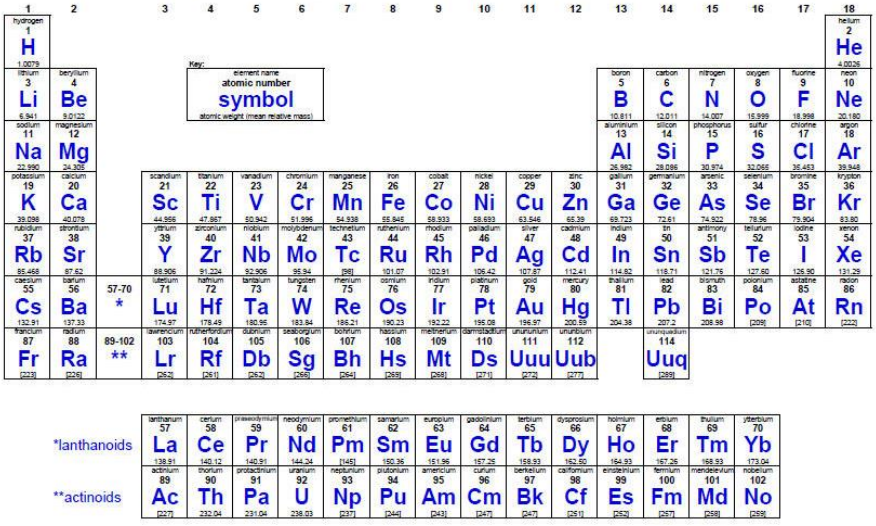

Figure 2.1-1 The periodic table of elements based on their atomic mass and weight (Winter, 1993)

As illustrated by the periodic table, Figure 2.1-1, elements differ by with respect to the number of protons, matching the atomic number, this identifies the position of the element on the periodic table. The atomic weight is the sum of the number of protons and neutrons. Differing amount of neutrons, where the atomic number is the same but the atomic weight is different, produces different isotopes of the atoms. Thus, they are distinguished by the

mass number and are often expressed prefixed to the name or the symbol of the element. An example of this relevant to the production of nuclear power is uranium. Uranium (U) naturally occurs in rocks and soils and mainly consists of 99.3% ^{238}U (92*Z*+146*N*) and 0.7% ^{235}U (92*Z*+143*N*).

Nuclear power is generated in nuclear fission reactors, which is the central component in the nuclear fuel cycle. Two common isotopes U^{235} and Pu^{239} are used as nuclear fuel due to their ability to undergo nuclear fission. Uranium provides the bulk of the nuclear fuel in most current reactors. During nuclear fission a neutron is captured by an unstable atomic nucleus of a high atomic number, causing the nucleus to split into two radioactive daughter nuclei (the mass of each fragment is lower than the parent) and the release of some neutrons. The equation below describes the fission of ^{235}U.

$$^{235}_{92}U + {}^{1}_{0}n \rightarrow {}^{141}_{56}Ba + {}^{92}_{36}Kr + 3{}^{1}_{0}n \qquad 2.1\text{-}1$$

In the case of uranium, fission produces neutrons that can initiate further fissions if they encounter other ^{235}U atoms, producing yet more neutrons, this is known as a chain reaction. Since three neutrons are released the reaction, if not controlled, will accelerate. Nuclear fission reactors are designed to control the rate of the chain reaction.

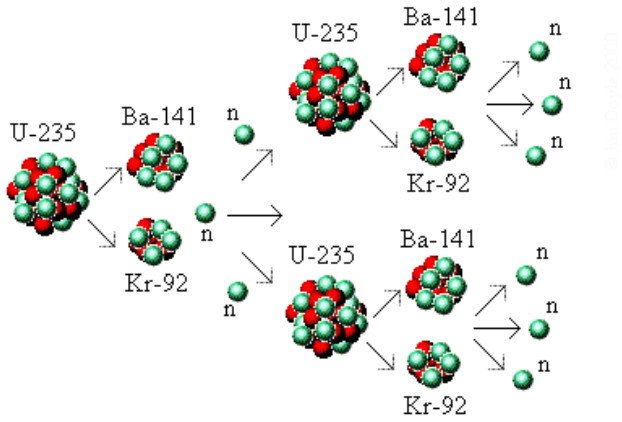

Figure 2.1-2 The fission reaction of uranium-235 and the production of three neutrons and two fission by-products

The chain reaction, illustrated in Figure 2.1-2, is dependent on the number of neutrons captured by a U nucleus. In principle each neutron released could go on and produce three more neutrons, however this is not usually the case. A proportion of neutrons are unable to escape from the reaction zone or can be absorbed by non-fissile material. The chain reaction depends on the average number of neutrons produced from each fission reaction that are effective in propagating (k_{eff}) the chain reaction further (Wilson, 1996).

- If k_{eff} >1, the reaction rate increases exponentially, where there is a high concentration of fissile atoms. A combination of k_{eff} being greater

than 1 and a short time period between each reaction, causes the potentially explosive release of the fissile atoms.

- If k_{eff} <1, the sample is small, the reaction may need to be started by an external neutron and the reaction may approach completion. This type of reaction is under investigation on thorium and accelerator driven systems.
- If k_{eff} =1, the minimum amount of fissionable material required for chain reaction initiation and maintenance. This is known as the criticality condition, where the reaction continues at steady state.

As the fission fragments fly apart at high speed, a considerable amount of thermal energy is released, approximately 200 million eV for each fission event (Hodgson, 1999). The heat can be used to boil water and drive a turbine to produce electricity, similar to that of oil and coal power stations.

Alongside heat, the fission reaction produces radioactive by-products. There are fission product elements, about half the atomic mass of the fissile materials. Most of the radioactive isotopes produced have half-lives ranging from fractions of a second to a few decades although a few have half-lives of millions of years. A second mechanism for the formation of by-products including ^{239}Pu is through the neutron capture of ^{238}U. Even though ^{238}U is not fissioned by thermal neutrons, it can readily absorb them to form the unstable ^{239}U. This is followed by the beta decay to form neptunium, ^{239}Np, then beta decay to produce ^{239}Pu which is itself capable of self-sustained fission. The reaction is expressed in the equation 2.1-2.

$$^{238}_{92}U + ^{1}_{0}n \rightarrow ^{239}_{92}U \xrightarrow{\beta-} ^{239}_{93}Np \xrightarrow{\beta-} ^{239}_{94}Pu \qquad 2.1\text{-}2$$

Once these by-products are produced, they are unstable and undergo any one of the three decay mechanisms. The radioactive emissions are alpha-particle, beta-particle or gamma-rays. Alpha particles are the emission of a helium nuclei from a nucleus, these are slow and heavy particles with low penetrating power. Beta particles are emitted from the nucleus at high speeds with a charge of -1 and 1/2000th mass of a proton, therefore equivalent to an electron. These are fast and light particles with medium penetrating power. High energy electromagnetic waves, known as gamma rays, are produced when the nucleus changes from a higher energy level to a lower energy level. The gamma rays have no mass or charge and have a high penetration power.

Radioactive emissions can cause damage at a cellular level leading to cancerous growths and physical abnormality. Although radioactivity is

naturally occurring in the environment it is important to prevent large accumulations. It is therefore essential to carefully manage the storage and disposal of spent fuel and the associated fission products.

2.2 Nuclear power generation

The nuclear fuel cycle consists of a number of distinct stages, illustrated in Figure 2.2-1.

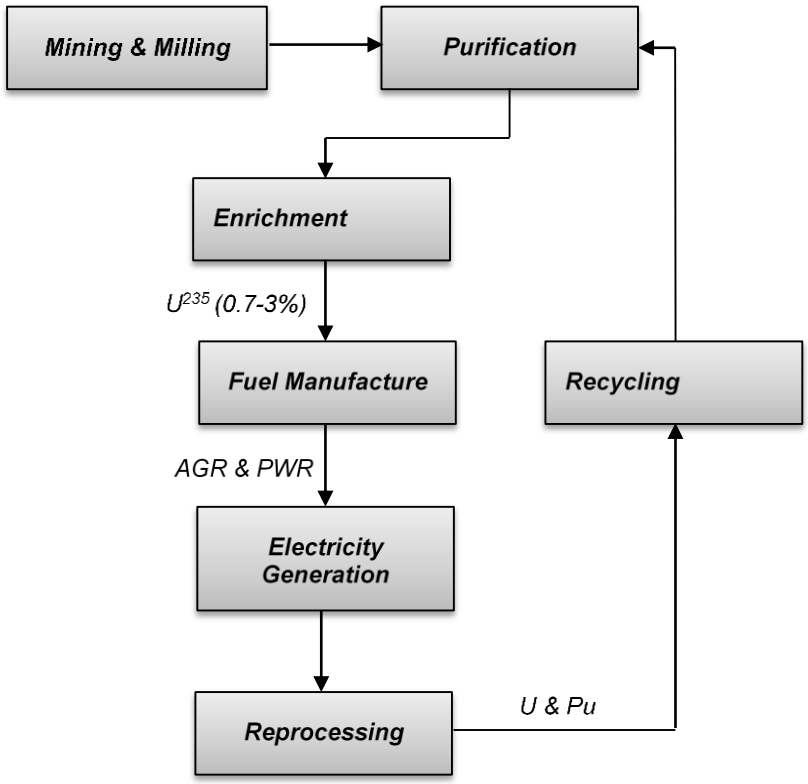

Figure 2.2-1 A flow diagram representing the front-end of the nuclear fuel cycle. The flow diagram describes the transition from uranium ore to electricity generation by nuclear power.

2.2.1 Mining and milling of uranium ore

The process starts by obtaining uranium ore from mines where it is available, the most common sites are in Australia, Asia, Canada, Europe, Russia and USA.

The uranium is excavated in rock form and it is then extracted by a number of methods, dependant on the type of ore. The process options for low grade ores include conventional sulphuric acid leaching, whereas high grade ore includes high pressure acid leaching. The leaching is followed by solid-liquid separation, solvent extraction, precipitation and drying of the product. This process is known as milling and produces uranium diuranate (yellowcake), through precipitation.

2.2.2 Purification of uranium oxide

The yellowcake concentrate which is produced is not directly usable as a fuel for the nuclear reactor and therefore it must be processed prior to use in nuclear reactors. When the uranium exits the mining site it leaves as a stable form of oxide, however it still contains impurities and thus has to be refined before the conversion to uranium hexafluoride takes place. The main components to be removed during refining are elements such as boron and cadmium (high neutron capture of thermal neutrons), elements prone to produce volatile fluorides (e.g. molybdenum and chromium) and other elements which have similar properties to uranium, for example thorium. Traditionally in the yellowcake is refined by a wet process, where a solvent extraction method is used.

In refineries in the UK the yellowcake is directly dissolved in nitric acid. Where by the yellowcake is fed in a co-current flow to nitric acid. The uranium extraction is governed by the ionic concentrations of uranium and nitrite in the aqueous phase. Once the uranium is purified, the conversion to uranium hexafluoride can take place.

The production of uranium hexafluoride involves the reaction of tetrafluoride with fluorine. Uranium tetrafluoride is fed into an inert bed of calcium fluoride, at a controlled rate into a reactor. This is then fluidised with nitrogen and fluorine at reduced pressure. The reaction produces gaseous uranium hexafluoride, this followed by filtration to remove solids and then further condensed. The gases containing nitrogen and unconverted fluorine are recycled. The solid uranium hexafluoride is extracted from the condenser and melted. The uranium hexafluoride is used in the next stage of the fuel cycle to enrich the quantity of uranium (Wilson, 1996).

Refining takes place in the UK at the Springfield's fuel manufacturing plant near Preston.

2.2.3 Enrichment of uranium (U^{235})

Natural uranium consists of two main isotopes known as ^{235}U (0.7%) and ^{238}U (99.3%). The ^{235}U is the fissionable isotope. Modern nuclear reactors are required to have a higher concentration of ^{235}U, somewhere between 3 – 5% to ensure a sustainable chain reaction; this can be created through a process known as enrichment. There are two enrichment processes used in the UK: gas centrifuge and gas diffusion. The advantages of using uranium hexafluoride is that it is gaseous at 60^{o}C and fluorine has only one isotope.

The concentration of ^{235}U is increased to between 2-5% (Wilson, 1996). The enriched uranium hexafluoride is then converted to enriched uranium or uranium oxide; this is then used for fuel production.

2.2.4 Fuel manufacturing

There are two principle types of fuel, uranium metal (old technology) and uranium oxide. Metal fuel is manufactured into large rods, due to its lower conductivity, and the oxide fuel is produced as small pellets stacked in narrow pins, the pins are arranged in bundles called assemblies.

Metal fuel, is clad in a magnesium alloy called Magnox which lends its name to the fuel, reactor type and cycle. There are two key factors to consider when manufacturing Magnox fuel, the cladding must be kept below 662^{o}C as phase change from alpha to beta of uranium metal can take place and below 450^{o}C to avoid oxidation. The fuel elements typically contain 12 kg of uranium as a rod, where the diameter of the rod is 28 mm and the length can vary between 965-1070 mm. The design of the fuel rod and cladding is dependent on the reactor design, therefore a number of different designs of Magnox fuel rod exist.

The oxide fuel is manufactured as uranium dioxide pellets. These pellets are then loaded into tubes made of zirconium alloy or stainless steel; the tubes are constructed for geometric purpose whereby the Advanced Gas Reactors contain a collection of 36 tubes and for Water Reactors 157 to 241 are used (Wilson 1996).

2.2.5 Nuclear fuel reactors

The aim of a typical nuclear reactor is to supply energy in a secure and controlled manor to an electric generator. It is the fission heat which is used to drive the turbo-alternators in a controlled manor. There are many parameters considered in the design of the thermal reactors; from the fissile material type through to prevention of radioactive waste escaping. Key parameters include the properties of the fissile material, prevention of corrosion by creating a metal shell around the fissile material (cladding), insertion of light elements (moderator) to reduce the speed of high speed neutrons, a coolant to carry the heat generated to the steam generator and shielding to protect the public against radiation. All reactors are contained within a steel-lined concrete structure to act as an environmental shield.

2.2.5.1 Gas reactors

Gas cooled reactors are graphite moderated reactors cooled by pressurised carbon dioxide. First generation reactors, Magnox (Figure 2.2-2 (a), use natural uranium fuel encased in a magnesium alloy. The origin of the name Magnox, is the magnesium alloy and no oxidation, and is being phased out. Second generation reactors, Advanced Gas Reactors (AGR), Figure 2.2-2 (b), use enriched uranium oxide as fuel, typically between 2.5-3%. The fuel is encased in stainless steel cans. The basic operation of these reactors involve the fuel to be placed in the individual channels through the moderator. Carbon dioxide coolant is supplied via large blowers. The coolant is passed through the core of the reactor, bottom to top, into the heat exchanger. This in turn heats the water in an isolated steam circuits which is used to drive the steam turbines.

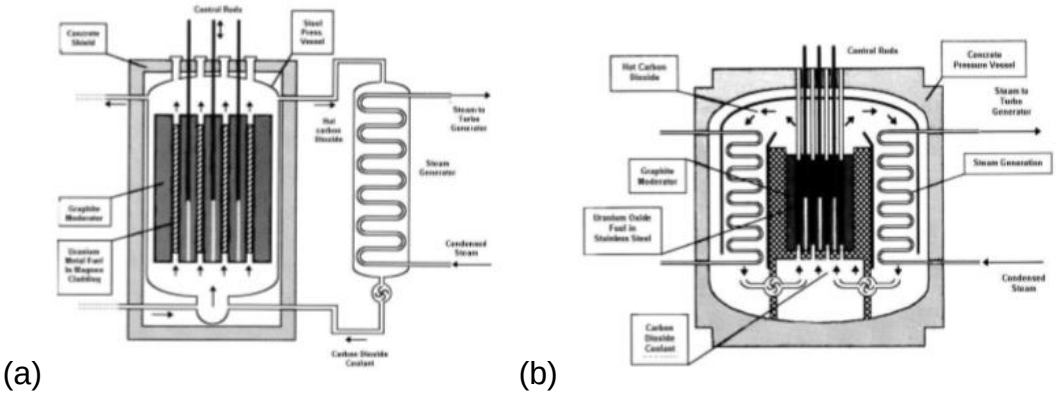

(a) (b)

Figure 2.2-2 Schematic diagram illustrating the main components of (a) Magnox reactor and (b) an AGR (Wilson, 1996).

The use of uranium oxide fuel in AGR has desirable processing advantages, they can work at a higher melting point than metal, higher operating temperatures and improved thermal efficiency. An AGR fuel assembly involves 36 stainless steel clad pins, they encapsulated in graphite casings to provide structural strength and a channel for the carbon dioxide coolant gas to flow between.

2.2.5.2 Pressurised water reactors (PWR)

The PWR, as illustrated in figure 2.2-3, provides 60% of the world's nuclear power generation. The reactor contains a compact core pressure vessel. This vessel is able to operate using ordinary water at high enough pressure to prevent boiling yet achieve desired temperatures. The properties of water enable it to act both as a moderator and a heat-transfer medium. The pressure vessel is connected to a steam generator which forms the first

coolant circuit. Steam generators consist of many narrow pipes through which the water from the nuclear reactor core travels to the turbine. During this process the heat is transferred to a secondary coolant circuit where the water at low pressure boils and drives the steam turbine.

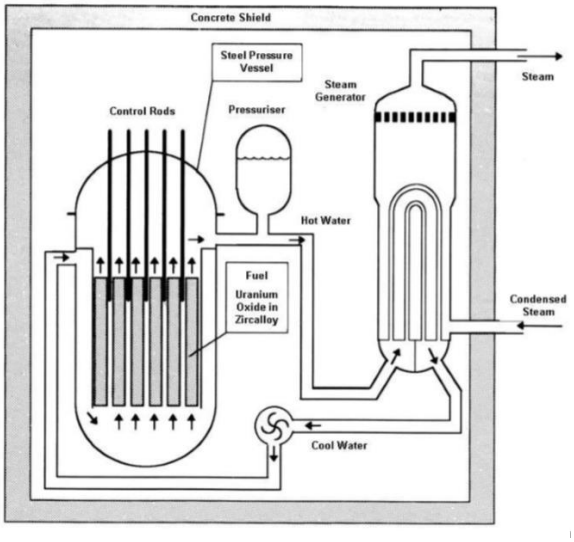

Figure 2.2-3 Schematic diagram illustrating the main components of a PWR (Wilson, 1996).

The PWR core can contain 157-241 fuel assemblies. The fuel input is usually enriched uranium dioxide fuel pellets clad with Zircaloy, the slightly alloyed zirconium is used to reduce corrosion effects and for low neutron absorption. The open space between the fuel rods allow cooling water to flow between them to maintain operating temperatures.

2.3 Reprocessing of spent fuel

The main aim of fuel reprocessing is to separate the waste from the remaining usable uranium and plutonium which can be recycled into new fuel, as illustrated in figure 2.3-1. The spent fuel which is obtained from the nuclear reactor contains approximately 96% uranium, 1% plutonium and 3% radioactive waste (unusable fission products). Following the 4-6 year cooling period (dependant on the fuel type) at the reactor sites, to allow short lived isotopes to decay, the spent fuel is transported to storage ponds at Magnox and (Thermal Oxide Reprocessing Plant) THORP, located at Sellafield in the UK. Magnox reprocesses uranium metal fuel and THORP reprocesses oxide fuels. The timeline which storage takes place at the plants differ considerably, for instance at the Magnox plant storage is limited to approximately 180 days; whereas at THORP storage can be approximately 4-5 years.

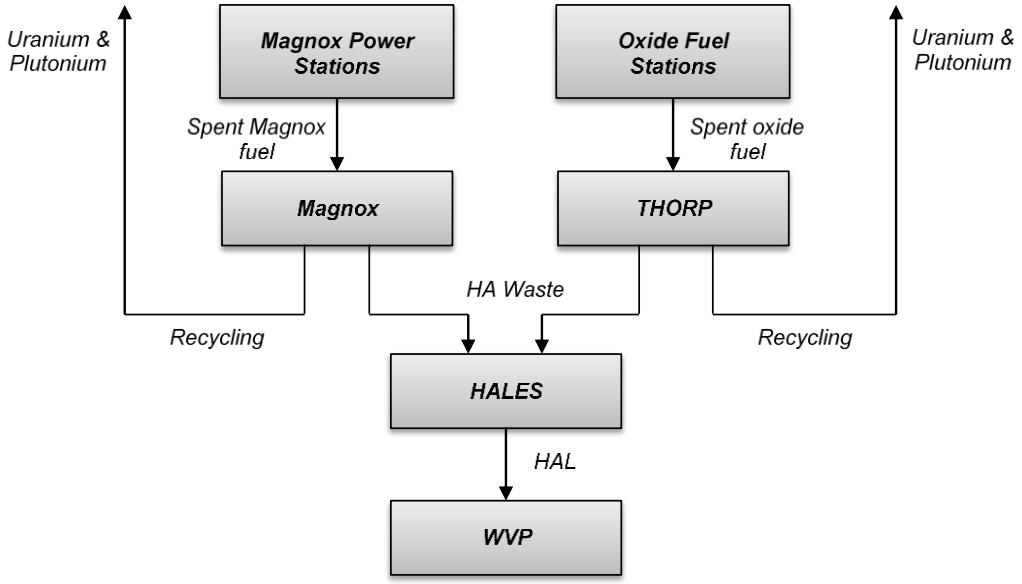

Figure 2.3-1 A flow diagram representing the reprocessing-end of the nuclear fuel cycle. This part of the fuel describes the separation of U and Pu and the storage of HAL.

Reprocessing takes place and the separated uranium and plutonium are recycled back into the nuclear fuel cycle. Both reprocessing routes produce raffinate (fission products dissolved in nitric acid). The raffinate from both processes are combined at the highly active liquor evaporation and storage (HALES) plant. In HALES the raffinate is concentrated through evaporation to form HAL which is stored in HASTs.

2.3.1 Evaporator operation and design

There are currently three evaporators operating in HALES. Evaporators A and B treat Magnox highly active raffinates and evaporator C, Figure 2.3-2, concentrates oxide raffinates. Construction of evaporator D is currently underway to support reprocessing operations as the previous evaporators are close to their end of expected operational life.

Figure 2.3-2 Image representing evaporator C prior to installation. The top of the vessel is in the foreground (NNL, 2008c).

A typical evaporator process is illustrated below in Figure 2.3-3. The feed is continuously added to the vessel through a Constant Volume Feeder (CVF). The continuous addition of the HA raffinite is to replace the volume removed as condensate. The vessel is operated under reduced pressure, approximately 1/12th of the atmospheric pressure, to maintain the boiling point of the aqueous solution between 50-60^{o}C (NNL, 2008b). Low operating pressure reduces the rate of vessel corrosion by the acidic nature of the solution and thus extending the evaporators operating life.

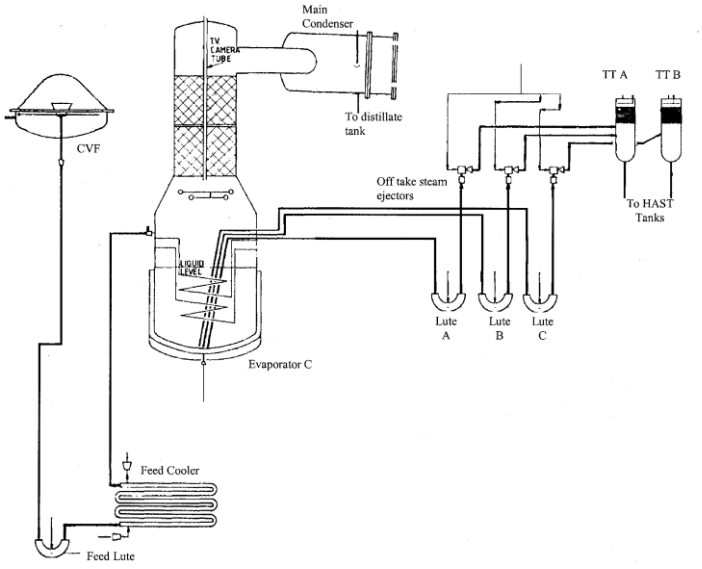

Figure 2.3-3 A schematic diagram illustrating the main components of an evaporation process (NNL, 2008a)

The feed is passed through a feed lute, where the pressure difference between the feed and evaporator vessels can be maintained. To prevent flash boiling in the evaporator vessel the feed is then passed through the feed cooler. Once the liquor enters the vessel partial pressure steam heating boils the liquor.

Figure 2.3-4 illustrates the internal features of the evaporator. Each evaporator is approximately 3 meters in diameter, the lower section, and 10 meters tall. This unit operation is made of speciality grade stainless steel. HA raffinites have a working capacity of 2-2.6 m of the lower section of the vessel. The typical kettle-type structure contains a lower section where the evaporation occurs and an upper section distrainment section.

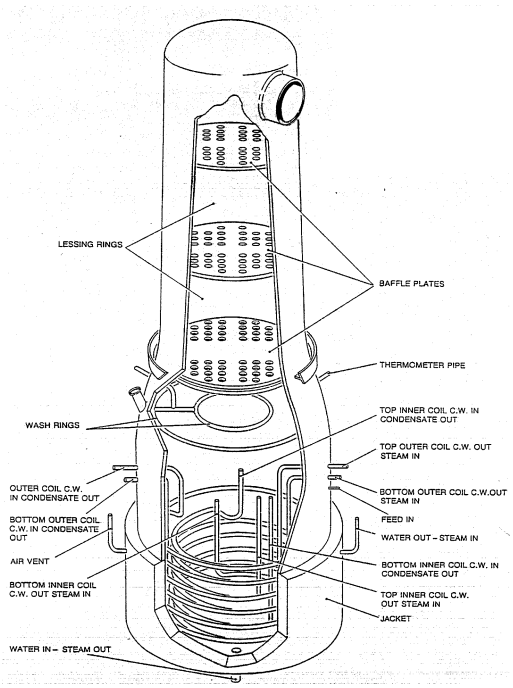

Figure 2.3-4 Schematic diagram illustrating the evaporator used for concentration of the HAL. This diagram highlights the main components used for volume reduction (NNL, 2008c).

The key features at the base of the vessel contain 6 cooling coils, the liquor is heated by the low pressure water system fed into the jacket around the base. The upper section contains a packed bed of stainless steel rings, this is to reduce the spray of liquid droplets created from the boiling liquors. The elimination of the liquid droplets contributes to the efficiency of the evaporation process as reaction between the liquid droplet and the rising vapour would increase the activity of the condensate and contaminate the batch. The vapour exits at the top of the vessel and passes into a water cooled condenser. The evaporate acid is recycled into the beginning of the reprocessing cycle.

The end of the evaporation batch depends on the origin of the fuel and is determined by their chemical concentration and liquor density. Magnox HA batches contain raffinites from 140-180 tonnes of uranium fuel (teU), compared to Oxide HA batches which contain 40-80 teU. The density and the radioactive heat for oxide HA batches are of concern as they can limit the operation of some batches. Occasionally some batches contain a mixture of Magnox and Oxides raffinites, these are known as 'blended batches' and adhere to similar limits of the Oxide limits. The HALES evaporators currently have a throughput of approximately 100 m^3 per day and the liquor can be evaporated to 20-100 times its initial volume within the evaporator. On average, batch evaporator liquor containing 40-180 teU can take approximately 5 weeks for the full evaporation process.

The process end-point can be defined depending on the density of the HA rafinates (usually for evaporator C) and the concentration of the evaporator solution (usually evaporators A and B). The initial stages of the end-point involve the addition of water as a feed to the evaporation process, this is known as Water Acid Reduction (WAR). At the end of the evaporation process the nitric acid molarity can reach to 10-11 M, WAR reduces the molarity to 2-3 M where the liquor can be sent to the highly active storage tanks (HASTs) for storage without further treatment. The evaporator is then cleaned out using nitric acid and/or water, ready for the next cycle.

2.3.2 Storage of highly active liquor

Reprocessing of irradiated nuclear fuel produces High Level Waste (HLW) in liquid form. This is stored as Highly Active Liquor (HAL) in a number of Highly Active Storage Tanks (HASTs). HAL is a concentrated solution of fission products in nitric acid. There are two types of HASTs,

- "Old-Side" where there is no agitation, horizontal, 1-3 cooling coils, no jacket, contains liquors from 1950's.
- "New-Side" which contains Jet Ballasts and Airlift (in-tank agitation systems), and significant redundancy in cooling coils.

There are currently 21 HA storage tanks located at the HALES plant, 13 of which are the new-side tanks. Construction of the recent HAST design began in the 1960's. Figure 2.3-5 illustrates the exterior and interior design of the New-side HASTs, respectively.

(a)  (b) 

Figure 2.3-5 Images representing the highly active storage tanks (a) the exterior of the tank where the stainless steel tank is encased in concrete and (b) the image highlights the cooling coils and agitation systems .

The capacity of the tank is 150 m^3 with a working volume of 140 m^3. Radioactive decay of the fission products is able to heat the liquor to boiling point. The HAL is therefore cooled by water pumped through a number of cooling coils within the tanks. The HAL currently generates heat of approximately 20-460 kW per tank and is maintained between 50-60^{o}C. It is important to maintain the temperature within this range. If the bulk temperature falls below 45^{o}C then crystallisation of solids in HAL may occur, this can inhibit the heat transfer mechanism and causing localised hot spots.

A key engineering feature of the HASTs is the agitation system implemented. HAL contains a number of high density precipitated solids which can deposit at the bottom of the tank. There are two main agitation systems in place:

- Air-lifts to maintain the HAL solids in suspension.
- Jet ballasts to re-suspend the settled bed of HAL solids from the bottom of the HAST.

Air lifts inject compressed air into the liquor which creates a circular flow around the airlift within the HAST, as shown in Figure 2.3-6

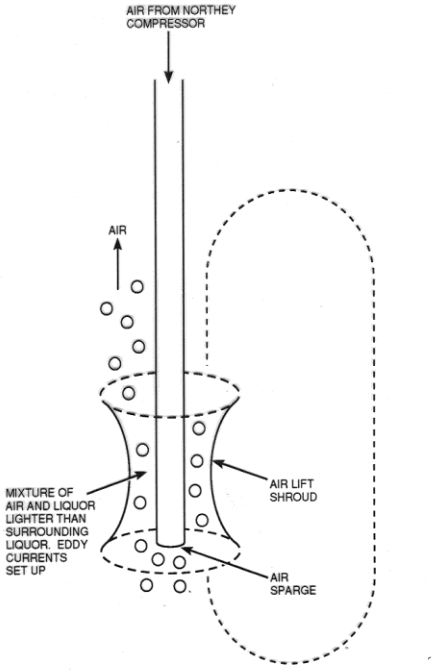

Figure 2.3-6 Schematic illustrating the mechanism of the airlift and how the solids are kept in suspension (NNL, 2008c)

There are four airlift circulators within each New-side HAST, located near the base of the tank. These are used to homogenise the contents of the tank, this is vital for representative sampling. Figure 2.3-7 illustrates the mechanism of the jet ballasts.

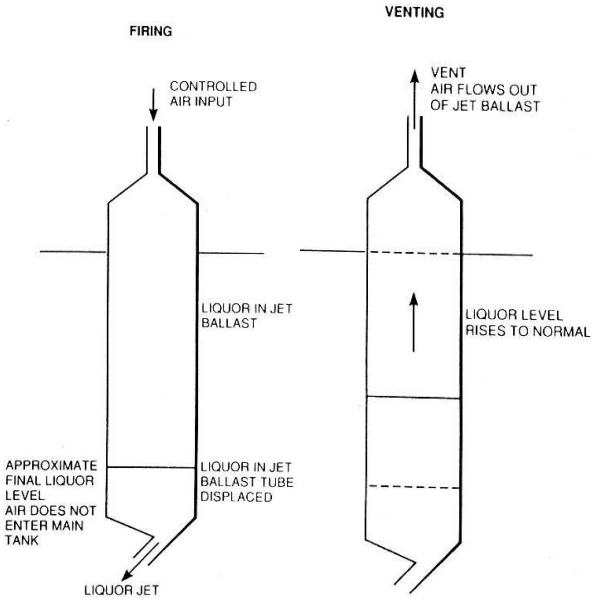

Figure 2.3-7 A schematic diagram illustrating the mechanism of the jet ballast (a) the jet ballast is empty (b) the jet ballast is occupied up with the HAL (NNL, 2008c)

From Figure 2.3-7, the jet ballasts agitation system consists of a cylinder fitted with a nozzle at the bottom. This type of agitation mechanism uses compressed air to drive the HA liquor in and out of the ballasts via the lower

nozzle. Compressed air is applied to the jet ballast above the liquor, from the air reservoir, this enable the liquor to be driven out of the ballasts to agitate the settled bed of HAL solids at the bottom of the tank. The air is allowed to vent and once equilibrium is achieved the cylinder re-fills with liquor. Within the HASTs there are 6 peripheral jet ballasts (Figure 2.3-7) and 1 central.

The peripheral jet ballasts are 0.6 m by 5.0 m, they have a conical shaped cylinders with a lower outwardly facing nozzle. The central jet ballast is 0.9 m by 5.0 m, similar cylindrical shape to the peripherals with a single lower nozzle facing down toward the centre of the base of the tank. Jet ballasts are operated in sequence, a full cycle of 15-30 minutes for all 7 jets to fire where each jet firing lasts between 40-80 seconds (NNL, 2008c). The extent of re-suspension and agitation is dependent on the volume of HA liquor extracted.

HASTs provide agitation and in-tank evaporation of the HAL. Evaporation is achieved by a temperature difference within the tank, where the cooling system is reduced at the top of the tank, creating a heated layer approximately 20^{o}C above the bulk temperature. The evaporation is enhanced by blowing warm air across the surface of the liquor. An alternative method is to implement the airlifts re-circulators, where air is blown through the bulk of the liquor.

2.3.3 Vitrification of high level waste

HAL is sent to the vitrification plant for treatment. Prior to vitrifcation HAL is essentially a solution of metal nitrates, it is converted to a blend of mixed oxides during calcination. A blend, usually 75:25 Magnox to Oxide by equivalent total waste oxides, is then dosed with 2% wt/wt of lithium nitrate to improve glass uniformity and inhibit the formation of unwanted phases.

Calcination process takes place at reduced pressure to eliminate corrosion effects. During this process the solution is progressively evaporated and de-nitrated to produce a fine powder, known as the calcine. The calcine is mixed with borosilicate at 1100^{o}C to produce a final encapsulated glass block. Once the desired volume is achieved the glass product is stored in specially designed stainless steel containers. The containers can store approximately 400 kg of glass. The glass product is allowed to cool in these containers and sealed.

2.3.4 Waste Disposal

Radioactive waste is produced from the nuclear fuel cycle. This varies from the vitrification of fission products, described above, to the disposal of secondary materials (e.g. gloves, analytical instruments – contaminated with radioactive material). There are three levels of radioactive waste:

i. **Low level waste**, this includes protective clothing of workers, and other substances with low levels of radioactive contamination. These re disposed of in a near-surface facility at the Low Level Waste Repository (LLWR);

ii. **Intermediate waste**, such as operational vessels, reactor walls etc. These are often immobilised in inert material such as cementitious grout and currently disposed of in over ground stores at the Sellafield site.

iii. **High level waste**, resulting from the concentration of fission products during reprocessing. This is stored currently at Sellafield.

The intermediate and high level waste are stored pending a decision on the building of a Geological Disposal Facility (GDF), this is the Governments preferred option for long-term disposal.

2.4 Conclusions

This chapter has described the basic elements of the nuclear fuel cycle including the fuel manufacture, power generation, reprocessing and waste management. Special emphasis has been placed on those areas with particular relevance to this thesis.

3 Synthesis and particle characterisation of nuclear waste simulants

Summary

This chapter describes the synthesis of zirconium molybdate and caesium phosphomolybdate. Manipulation of the change in morphology by incorporating an organic additive will be discussed. Appropriate particle characterisation techniques will be employed to establish solid properties.

3.1 Introduction

Caesium phosphomolybdate (CPM) and zirconium molybdate (ZM) precipitate out from highly active liquor (HAL) during reprocessing of spent nuclear fuel. This research aims to contribute to the improvement of the nuclear waste treatment strategy. Fundamental understanding of how the HAL solids are formed, characterisation of the solid-liquid properties and ultimately the behaviour of HAL is required for current processing, POCO and life-time assessment of the infrastructure.

A key focus of this chapter is to highlight optimisation of reaction conditions, product handling post-synthesis and determination of the physico-chemical properties to create a controlled environment to form a morphological specific product. The overall process implemented to produce nuclear waste simulants is presented below:

Ultimately, it is of importance to determine the mechanism of how the HAL solids are formed to then understand chemical modification to obtain solids with desirable processing properties. Elemental and structural characterisation during and post-synthesis enable the determination of particle properties in terms of particle size, shape and density and physicochemical properties such as the effect of surface charge on the stability of HAL dispersions.

3.2 Literature review

3.2.1 Particle synthesis of nuclear waste simulants

During reprocessing of spent nuclear fuel, the useful uranium and plutonium are removed and recycled from the fission products and actinides. The fission products and actinides are dissolved in nitric acid and concentrated, as previously mentioned in chapter 2. It is at this stage where the precipitation of CPM and ZM occur, due to the high concentration of zirconium, caesium and molybdenum ions. Therefore, it is important to replicate the conditions (acidity and temperature) in which the HAL solids are formed for comparative studies.

Many studies have been carried out to understand the formation of ZM (Clearfield and Blessing, 1972, Xuegang et al., 2012, Prinetto et al., 1995, Monroy-Guzmán et al., 2003, Doucet et al., 2002), compared to CPM where

publically available literature is limited. Various techniques for ZM synthesis have been developed, this thesis is based on the sol-gel precipitation method by (Clearfield and Blessing, 1972). This research describes the production of $ZrMo_2O_7(OH)_2(H_2O)_2$, this is formally known has zirconium molybdenum dihydroxide dihydrate, ZMH. Initial stages of the synthesis required treatment of the reagent, zirconium oxide dichloride octahydrate, $ZrOCl_2(H_2O)_8$. This was re-crystallised repeatedly for purification, from 6 to 8M hydrochloric acid. This is was followed by preparation of aqueous reactant solutions of 200 mL 0.5 M $ZrOCl_2(H_2O)_8$ and 200 mL of 1M sodium molybdate, $Na_2MoO_4(H_2O)_2$. White, amorphous ZM gel precipitated out and then acidified by using hydrochloric acid, the overall acidity of the solution was 3-4 M. The mixture was heated under reflux for several days, high temperatures enabled re-precipitation of partial ZM dissolution. The high temperatures and acidic concentration of this synthesis are comparable to real-time conditions. Crystallographic properties were determined using XRD, these will be discussed in the following chapter, Chapter 4.

Another precipitation study involved composing a simulated high level liquor waste (s-HLLW) (Xuegang et al., 2012). This composed of 15 elements at different concentrations, where by the highest concentration levels were of zirconium and molybdenum, 0.708 g/L and 0.680 g/L, respectively. Zirconium ions were produced from zirconium nitrate ($Zr(NO_3)_4(H_2O)$) and molybdenum ions were produced from ammonium molybdate ($(NH_4)Mo_7O_{24}(H_2O)$). The s-HLLW was poured into a reaction vessel, where it was heated to 95^{o}C under reflux. Precipitation of ZM was produced and the production was dependent on the concentration of the Zr/Mo ratio. The elemental composition was based on the assumption of the burn up of fuel from PWR. This assumed that the fuel burn up is 50 000 MWd/tU and it has been left to cool for 10 years and reprocessed by the Plutonium Uranium Redox Extraction (PUREX). This replicates conditions that occur with the current processing of spent fuel.

Other methods of ZM synthesis involve oxidation catalytic methods (Prinetto et al., 1995). This involved the preparation of MoO_x/ZrO_2 catalysts in one of three ways (i) equilibrium adsorption method (ii) dry impregnation or (iii) mechanical mixing of ZrO_2 with MoO_3. An example is the equilibrium adsorption method where the oxide support, ZrO_2, was mixed with ammonium heptamolybdate. There the adsorbed Mo species can be controlled by the pH of ammonium heptamolybdate solution. This produced, according to the XRD analysis, the anhydrous ZM, $ZrMo_2O_8$.

Kumar et al. studied the potential of separation of long-lived radionuclide such as ^{137}Cs and ^{90}Sr (Kumar et al., 2003). The potential use of these isotopes for various industrial sectors, ranging from medicine to irradiation facilities for food processing, has required an understanding of their properties. They synthesised ZM using zirconium ions added to ammonium hepamolybdate, and observed the sorption behaviour the radionuclides in nitric acid.

Monray-Guzman has discussed the production of gel ZM and its effect on Mo/Tc generators (Monroy-Guzmán et al., 2003, Monroy-Guzman et al., 2008, Monroy-Guzman et al., 2012). This is of great importance for research in nuclear medicine, where technetium, ^{99}Tc, is used a diagnostic agent. This research describes the production of titanium molybdate gels for these generators, these can be irradiated after synthesis. They have considered that as zirconium and titanium have similar chemical properties, both have been produced by alkaline hydrolysis of the zirconium/titanium solutions in the presence of molybdates.

Reprocessing of spent nuclear fuel contains the precipitated solids along with various types of elements therefore Doucet et al. observed the mechanism of ZM formation through simulated solutions (Doucet et al., 2002, Rao et al., 1990). These aqueous solutions closely resemble those to be present in nuclear fuel reprocessing plants. This particular study created a simulated solution composed of 8 elements with varying concentrations, representative elemental concentrations. The highest element concentration included zirconium and molybdenum, at 0.98 g/L and 0.96 g/L, respectively. The zirconium ions were liberated from zirconyl nitrate solution ($ZrO(NO_3)_2$) and the molybdenum ions were liberated from molybdenum oxide (MoO_2). The reagents were made up as stock solutions where they were under reflux at 80^oC, once they were produced other elements were added to the mixture. This mixture was heated to 100^oC where the formation of ZM was studied. This study has assumed that ZM formation is a result of a series of surface reactions rather than colloidal precipitations. Other applications include the use of thermal expansion materials (Lind et al., 2001, Evans, 1999).

A study conducted by (Magnaldo et al., 2007) discussed the nucleation and kinetic properties of ZM to predict a possible mechanism for fouling. Fouling within the nuclear waste tanks are known to occur. By understanding the kinetics, this could be avoided and therefore the integrity of the infrastructure will not be compromised. Synthesis involved preparing molybdenum in nitric

acid solution, from molybdenum oxide powder. Zirconium in nitric acid was formed from zirconium carbonate hydrate. SEM images illustrate near cubic aggregated ZM particles. A possible nucleation scenario assumed is that deposited ZM particles are liable to surface nucleation and growth which is initiated by localised nucleation events in the bulk. This has the ability to create a fouling layer including other debris.

3.2.1.1 Influence of citric acid on molybdenum ions

As previously mentioned in the Chapter 2, POCO is a crucial stage for decommissioning. This is where all the radioactive and harmful materials will be removed prior to the dismantling of the infrastructure. POCO requires the clean out of any remaining solids inside the vessels and pipeline. A possibility is through dissolution. Once the solids have been dissolved, the solids will be able to re-precipitate in a controlled environment, this is the point where additives may be added to the solution where morphological manipulation can take place of ZM particles. This could be advantageous for processing.

This research aims to provide reliable data to improve the processing of the HAL waste, where suitable waste streams can be created for future vitrification and storage. Therefore an organic additive, citric acid has been chosen for morphological manipulation. A concern is the breakdown citric acid, or any other organic compounds, due to irradiation of the material. With this in mind, addition of citric acid may not be a viable option for recent, new-side HASTs where radioactive nuclides are undergoing decay. Instead, there could be a possible application of this morphological manipulation process to take place for the HAL waste stream stored in the old-side HAST. It is assumed that the material is non-active due to the time-period of HAL storage.

The interaction of molybdenum and citric acid has been studied. A key feature of this interaction is the production of a citratomolybdate complex. Complexes of molybdenum and citric acid are mainly used for analytical applications and in corrosion resistant alloys (Vukasovich and Farr, 1986). The citratomolybdate complex has been identified in numerous studies (Samotus et al., 1991, Alcock et al., 1990, Zhou et al., 1997, Cruywagen et al., 1995). Alcock et al. synthesised $K_4[Mo_4O_{11}(cit)_2]6H_2O$, where the complex anion was determined using XRD(Alcock et al., 1990). The structure of the complex contains a central oxygen atom bound to two molybdenum atoms. Each of the molybdenum atoms are octahedral coordinated, the tridentate citric acid ligands are bound to the molybdenum

atoms. The citric acid OH and O atoms of the carboxylate groups form covalent bonds with the molybdenum atoms. The central oxygen atom essentially creates an oxygen bridge, Mo-O-Mo, where the citratomolybdate complex is cis-bound with two citrate ligands.

Currently there have been no studies on the citratomolybdate complex formation in a highly acidic environment, especially in ZM synthesis. This thesis aims to characterise the interaction of this complex with ZM to produce zirconium citratomolybdate (ZMCA).

3.2.2 Solid chemistry of HAL

There are five main solids which are known to precipitate over time in Highly Active Liquor (HAL). Irradiated fuel is dissolved in nitric acid where inorganic materials form, known as, barium/strontium nitrate, zirconium phosphates, magnesium (lanthanide) nitrates, caesium phosphomolybdate and zirconium molybdate. The formation of these solids are known to create processing issues, therefore the HALES operations are designed to control precipitation of the solids. However, the precipitation of some species is inevitable. The primary species requiring consideration are discussed below.

3.2.2.1 Barium/strontium nitrate

Barium nitrate ($Ba(NO_3)_2$) is the least soluble of the phases and crystallises in an high acidic environment. Crystallisation occurs at the initial stages of the evaporation process where the acidity is high. The solids are readily soluble in weak acid or water, such that during WAR ($Ba(NO_3)_2$) is partial re-dissolving. The solid crystallises with a relatively high density of 3.2 kg/L, consequently making them rapid settling solids. Co-precipitation of $Ba(NO_3)_2$ with strontium (Sr^{90}) results in the barium-strontium complex, $Ba_{2-x}Sr_x(NO_3)_2$. Sr^{90} is of particular interest, due to the radioactive decay which significantly contributes to heat output and therefore may contribute to accelerated corrosion.

Previous research highlights the slow cooling crystallisation process of $Ba(NO_3)_2$ and the effect of dopants such as Sr^{2+} and Ca^{2+} (Orley, 2009). The doping of these ions indicated possible influences on morphological behaviour rather than solubility. $Ba(NO_3)_2$ crystallise with ease dependant on the acid concentration, in the case at 3M nitric acid. Molecular modelling allowed the calculation of bulk, defect and surface properties of $Ba(NO_3)_2$ and the effect of dopants on morphology.

3.2.2.2 Magnesium lanthanide

This phase specifically precipitates in Magnox and Magnox-rich Blend HAL. Crystallisation occurs at high concentrations, this is a potential issue in the HAST. High temperatures and weak acidic environments cause the solubility of magnesium lanthanide to increase. The crystal structure can change during formation, complex structures such as large hexagonal crystal can be formed. The presence of radioactive lanthanide isotopes contributes to the processing issues. These solids tend to form on the cold surfaces of the HAST cooling coils, this affects the heat transfer and results in localised heating. Radioactive decay of lanthanide isotopes results in heat generation.

3.2.2.3 Zirconium phosphates

Zirconium phosphates can occur in organic (e.g. zirconium dibutyl phosphate) or inorganic (e.g. zirconium hydrogen phosphate) forms, however the dibutyl phosphate species rapidly decays in the HAST environment. The solids form from any residual phosphate left over after formation of CPM. These crystalline solids are formed in the initial stages of the evaporation process and are fine, white flakes usually forming a mobile gel. If that particles are in abundance the viscosity may increase. High phosphate concentration can in turn increase the overall viscosity of the HAL suspension. Slow settling and easy mobilisation of the solids post-settling are desired processing characteristic of this phase.

3.2.2.4 Caesium phosphomolybdate

CPM precipitates during evaporation and is dependent on molybdenum ion concentration. It is formed by the co-precipitation of $[PMo_{12}O_{40}]^{3-}$ solution complex with caesium ions. The availability of molybdenum limits the formation of CPM. CPM solids are insoluble in acidic solution and are high density solids, therefore a rapid settling phase. The radioactive decay of Cs^{134} and Cs^{137} contribute to radiogenic heat output of this solid.

Molecular modelling techniques have been implemented to derive the interatomic potential of CPM (Khan, 2011). The potential development enabled calculating bulk and surface properties using numerous molecular modelling packages. Key highlights included the morphological prediction of CPM when surrounding by water molecules. This indicated the dominating (1 1 0) face to be most stabilised with increased interactions of water molecules due to the increased number of oxygen present on that surface.

3.2.2.5 Zirconium molybdate

ZM phases form by the conversion of CPM during reprocessing of spent nuclear fuel, in nitric media. The conversion is assisted by low acidic concentrations and high temperatures. ZM is insoluble in acidic solution with a high density.

Crystal growth and morphological studies of ZM highlights included understanding the kinetics and mechanisms for CPM to ZM conversion (Masheder, 2011). The change in morphology using various organic and inorganic dopants were investigated to gain an understanding of chemistry interactions of ZM particles.

The ability to tune the morphology through doping during formation presents the opportunity produce a material which is favourable mobilised, particularly where the solids may be dissolved and re-precipitated during POCO and decommissioning operations.

3.2.3 Fundamentals of particle science

It is known that colloids are found in everyday life, they are present in porous rocks, clays and smoke. The study of the interparticle interactions between colloids has led to the greater understanding of the colloidal behaviour. Colloids have one dimension in the range of 1 nm to 1 μm suspended in a fluid, demonstrating a large surface to volume ratio. Therefore in colloidal systems there are many molecules which are close to the interface between one phase and the other (Hamley, 2000).

The behaviour of fine particles is greatly determined by the surface forces rather than body forces, where by the surface area to mass is much larger for the finer particles. The surface area to volume ratio can be determined from the particle diameter. The expression describes the decrease in particle diameter as the surface forces tend to dominate the behaviour of the overall suspension, relative to the body forces which are dependent on the mass of the particles. The magnitude of the surface forces acting between the particles is much higher for particles with a small diameter, compared to the reduced magnitude of their body forces. Surface forces occur as a result of physic-chemical interactions such as the van der Waals, electrical double layer, bridging and steric forces. For the purpose of this research van der Waals and the electrical double layer forces will be considered.

3.2.3.1 Brownian motion

The fluid molecules of the dispersed medium are subject to thermal and kinetic motion. The motions are transferred to the suspended particles. The thermal energy from the environment results in the vibration of the liquid molecules. The vibrating liquid molecules and particles undergo collisions. The random nature of the collisions results in the undirected motion of the particles. The random path of a Brownian particle was discovered by Robert Brown by detecting this behaviour in the motion of pollen grains in water in 1827 (Perrin, 1914, Franks, 2008).

The distance travelled by the Brownian particle cannot be determined from the initial and final position as the motion does not occur in a straight line. Factors affecting the Brownian motion are temperature and particle size. Further analysis of the Brownian motion indicated diffusion of particles from a high concentrated to a lower concentrated region. Einstein derived the average distance (*L*) of a Brownian particle over a period of time (*t*) (Einstein, 1905, Einstein, 1956), given by equation 3.2-1

$$L = \sqrt{\frac{2kT}{3\pi x\mu}t} \qquad 3.2\text{-}1$$

The relationship considers the Boltzmann's constant ($1.381 \times 10^{-23} J/K$), temperature (*T*), particle diameter (*x*) and the viscosity of the fluid (μ). The increase in temperature increases the distance travelled by the particle and a decrease in particle size and fluid viscosity reduces the distance travelled.

3.2.3.2 Contributing Forces of Interaction

3.2.3.2.1 Van der Waals forces

Attractive van der Waals forces occur between atoms located in two different particles. Dispersion forces arise from Columbic interactions between instantaneous dipole movements within the atoms of the two particles.

Each atom consists of a positively charged nucleus with orbiting negatively charged electrons separated by a short distance. At any given time a fluctuating dipole exists between the nucleus and the centre of the electron density. Figure 3.2-1 illustrates the effect of the effect of fluctuating dipole.

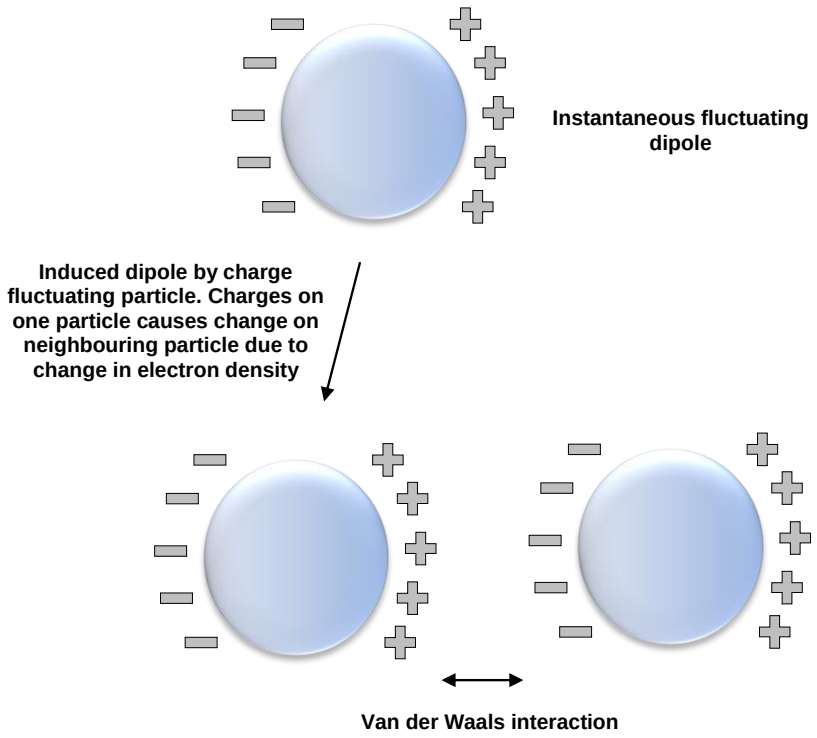

Figure 3.2-1 illustration of instantaneous induced dipole. Partial charges of induced dipoles results in the rise of attractive forces, Van der Waals, where particles come into contact.

The fluctuating dipole movement is induced to all other atoms contained within both particles. The arrangement of the fluctuating dipole within the atom of both particles determines the overall energy of the system. Illustrated in figure 3.2-1 is the lowest energy configuration of the dipoles, in relation to both particles. Dipoles contained within the atoms of the same material of both particles are aligned such that the centres of electron density of both particles do not coincide with each other, resulting in an overall net attraction of the particles. Typically, van der Waals interactions can be attractive or negative depending on the dielectric properties of the medium.

The summation of the interactions of all the atoms in both particles can be determined by the van der Waals interaction energy (V_{vdW}). This expression (Equation 3.2-2) considers two spherical particles separated by a distance (*x)* and the particle diameter (*d*)

$$V_{vdW} = -\frac{A_H d}{24x} \quad \text{3.2-2}$$

The van der Waals force (F_{vdW}) can be determined by the following expression

$$F_{vdW} = -\frac{A_H d}{24x^2} \quad \text{3.2-3}$$

The interaction of two particles in a given suspending fluid is expressed by the Hamaker constant (A_H). Negative values of A_H results in a repulsive

interaction and positive values result in attractive interactions. The value is determined from the dielectric constants of the interacting particles and the intervening suspending fluid. Table 1 represents values for a number of oxide minerals dispersed in water.

Table 1 Hamaker constant values of various oxide minerals dispersed in water (Franks (2008)).

Particle 1	Suspending fluid	Particle 2	A_H(J)
Alumina	Water	Alumina	5.0×10^{-20}
Zirconia	Water	Zirconia	8.0×10^{-20}
Silica	Water	Silica	0.7×10^{-20}
Titania	Water	Titania	5.5×10^{-20}

The values in Table 1 indicates all the mineral oxide particles dispersed in water to be dominated by attractive forces. Zirconia particles in water indicate a strongly attractive network compared to the respective oxide particles.

3.2.3.2.2 Electric double layer forces

Attractive forces have been considered previously, however repulsive forces are also present within the suspension. The repulsive forces can be described in terms of the electric double layer theory. Considering metal oxide particles (for example TiO_2, SiO_2 and Al_2O_3) in vacuum the positively charged metal ions and negatively charged oxygen ions are balanced. Once the metal oxide particles are immersed in an aqueous solution, i.e. water the particle surface reacts with the water molecules to produce hydroxyl groups. The case of TiO_2, this interaction can be defined as Ti-OH. The extent of surface ionisation reactions is determined by the pH of the suspending medium (Hunter et al., 2001). Low pH conditions result in a positively charged surface ($Ti\text{-}OH_2^+$) and high pH conditions result in a negatively charged surface ($Ti\text{-}O^-$). Thus, surface ionisation is dependent on the affiliation of (H^+) and (OH^-) ions on the metal oxide particle surface.

Particles with surface charge and an ionic environment tend to segregate into a number of distinct regions. Overall, the separation charge between the surface and the bulk solution forms a potential difference known as the surface potential (ψ_0). Particle surface have readily available sites for oppositely charged counterions from the bulk solution. Each particle is surrounded by a diffusive cloud filled with counterions, this maintains the electrical stability of the system. Overlapping of counterion clouds surrounding the charged particles increases the concentration of the

counterions in the gap between the particles. Particles with the same charge results in a repulsive potential due to the osmotic pressure gradient, this is known as electrical double layer (EDL) repulsion.

The thickness of the EDL can be determined by the Debye length (κ^{-1}), the Debye screening parameter (κ) for monovalent salts can be determined by the following expression (Israelachvili, 1992)

$$\kappa = 3.29\sqrt{[c]} \qquad 3.2\text{-}4$$

Where [c] is the molar concentration of the monovalent electrolyte. The thickness of the EDL surrounding the particle can be affected by the background electrolyte concentration. Large Debye lengths suggest a repulsive particle network at a large separation distance. Compression of the Debye length occurs with the addition of salt into the bulk solution, this increases the concentration of counter-ions around the particle. Thus the EDL decreases giving rise to the van der Waals interactions with in the system. The EDL is illustrated in Figure 3.2-2.

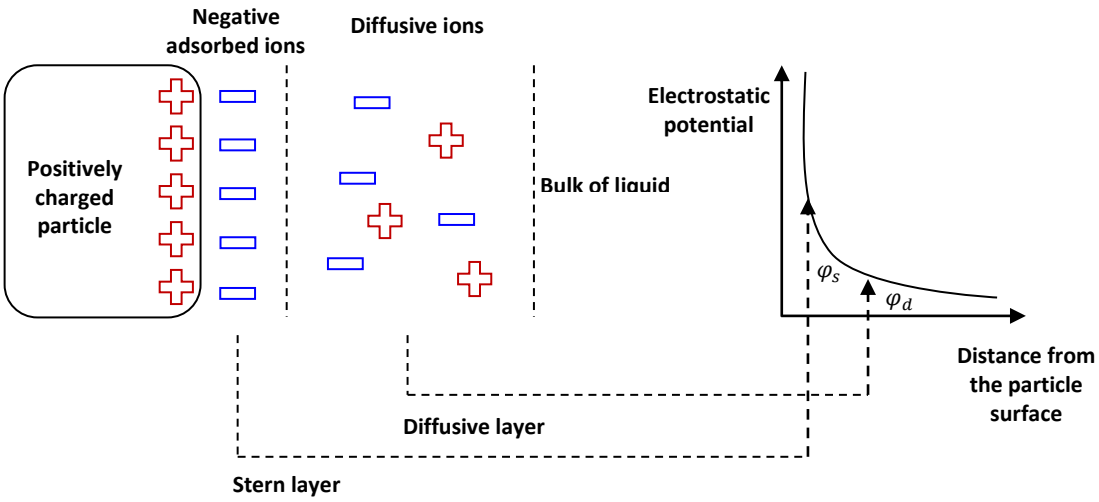

Figure 3.2-2 A diagram representing the electric double layer, models such as the diffusive double layer and the stern plane are also highlighted.

The diffuse double layer shows two regions where the ionic atmosphere is able to segregate. Firstly, the diffuse double layer is formed when the counter-ions are in proximity of the colloidal surface. The counter-ions in the solution will become dominant when close to the surface due to the electrostatic interactions. They collectively diffuse through the solution due to the balance of the electrostatic forces and those forces which are the result of thermal motion. Secondly, the outer diffusion region is where the concentration of the counter-ions decreases and therefore moves away from the particle surface. The alignment of the counter-ions on the surface of the colloid is known as the stern plane. This portrays the relationship between

the interface of the colloid with a positive charge and the outer diffusive layer where there is a plane of negatively charged counter-ions.

The EDL potential energy (V_{EDL}) can be expressed by (Israelachvili, 1992)

$$V_{EDL} = \pi\varepsilon\varepsilon_0 d\Psi_0^2 e^{-\kappa x} \quad 3.2\text{-}5$$

The expression considers the relative permittivity of water (ε), the permittivity of free space (ε_0) which is approximated to be $8.854 \times 10^{-12} C^2/J/m$, the surface potential (Ψ_0) the particle surface to surface separation distance (x) and the diameter of a spherical particle (d).

Challenges to directly measure the surface potential, due the surface surrounded by immobile ions, of the particles have led to alternative measures. The measurement of the zeta potential is located within a few Angstroms from the surface (Franks, 2008).

3.2.4 DVLO Theory

The stability of colloidal particles in an aqueous solution can be explained by the Derjaguin-Landau-Verwey-Overbeek (DVLO) theory (Derjaguin and Landau, 1941, Verwey et al., 1948, Derjaguin et al., 1987). Stabilisation of a colloidal dispersion can be altered by manipulating the electrostatic interactions. Methods include changing the bulk salt concentration, ion valence and pH.

The DVLO theory is classical explanation of dispersion stability which considers the balance between two forces which are of opposing nature. Attractive short-range forces, known as the van der Waals forces and repulsive electrostatic forces (Ducker et al., 1991). Also known as the total potential energy and is expressed by

$$V = V_R + V_A \quad 3.2\text{-}6$$

Where V_R is the repulsive potential due to the overlap of the electric double layers on the colloidal particles, and V_A is the attractive van der Waals energy. The force is the negative of the gradient of potential energy with respect to the separation of the colloidal particles, which can be expressed as:

$$\boldsymbol{F} = -\frac{\boldsymbol{dV}}{\boldsymbol{dh}} \quad 3.2\text{-}7$$

A typical variation of the potential energy as a function of particle-particle separation distance is illustrated below. The attractive van der Waals term

describes an inverse-square dependence and the repulsive electrostatic term indicates an exponential decay dependence.

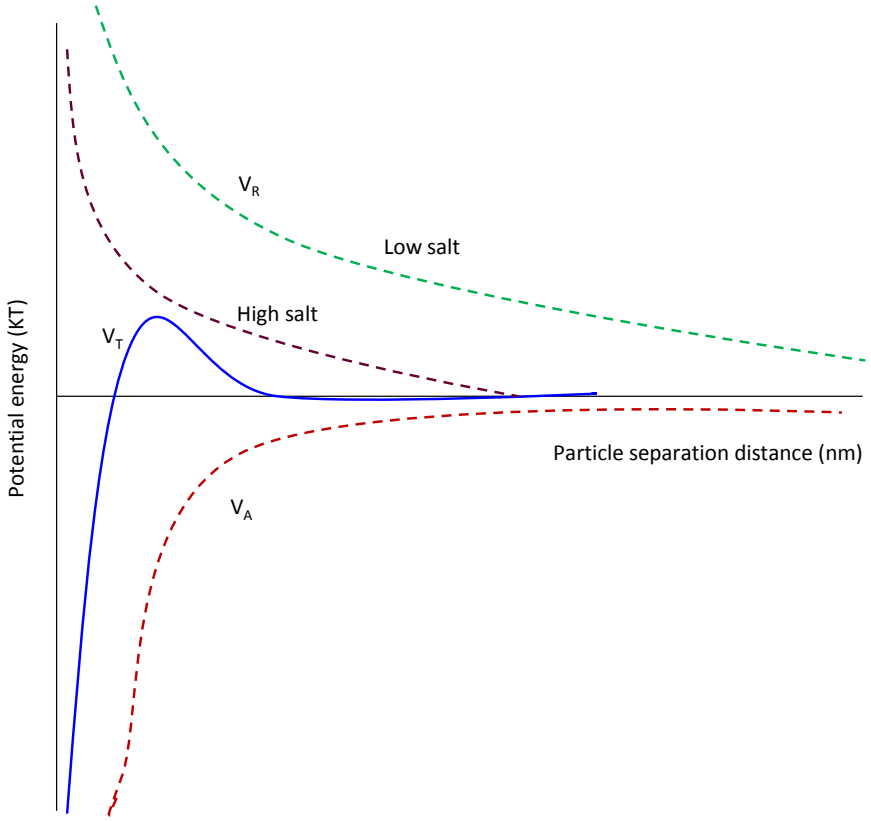

Figure 3.2-3 This graph corresponds to the potential energy as a function of separation distance between particle surfaces

Figure 3.2-3 illustrates the typical energy barrier for colloidal particles with high and low salt concentration. The presence of varying salt concentration indicates the dependence on the electrostatic repulsive potential. The increase in bulk salt concentration results in the reduction of the electrostatic potential barrier and thus gives rise to the increase in attractive potential contributing to the total interaction energy. Thus, decreasing the stability of the dispersion.

This research aims to determine the difference in sedimentation and rheological behaviours as a function of electrolyte concentration. The interest lays in how the HAL solids behave when dispersed in water and varying concentration of nitric acid. It is therefore important to define the change in surface charge of the HAL solids and electrolyte concentration of the HAL dispersions to relate to current plant operations and POCO of nuclear waste.

3.2.5 Fundamentals of particle characterisation techniques

3.2.5.1 Scanning electron microscopy (SEM)

This technique is based on firing a high energy electron beam onto a sample, known as the scanning electron microscopy (SEM) technique (LEO ElectronMicroscope GmbH, Germany). The sample is bombarded with electrons causing emission of secondary electrons and x-rays (Dunlap, 1997).

Figure 3.2-4 illustrates key components of the SEM technique, electron beam generation, electron beam manipulation and the beam specimen interaction. An electron beam gun is located at the top of the microscope where is generates primary electron beam. Electron beam manipulation controls the size, shape and position of electron beam on the sample. Beam interaction involves the contact of the electron beam with the sample which results in various types of signals to be released. The figure below illustrates the main components of an SEM technique.

The electron gun is composed of three sections. A filament, grid gap (controls the flow of electrons) and a positively charged anode to attract and accelerate electrons down the microscope.

Electromagnetic lenses and coils are located in the microscope coil. As the beam passes down the column it tends to diverge, however it is converged by the electromagnetic lens and directed onto the sample. The electrons in motion are affected by electric and magnetic fields. The electric gun is controlled by electrostatic fields, whereas the converging lenses are controlled by magnetic fields. Magnetic fields are generated by passing an electric current through a copper wire, these are known as electromagnetic lenses. Key elements of the SEM technique are illustrated in Figure 3.2-4.

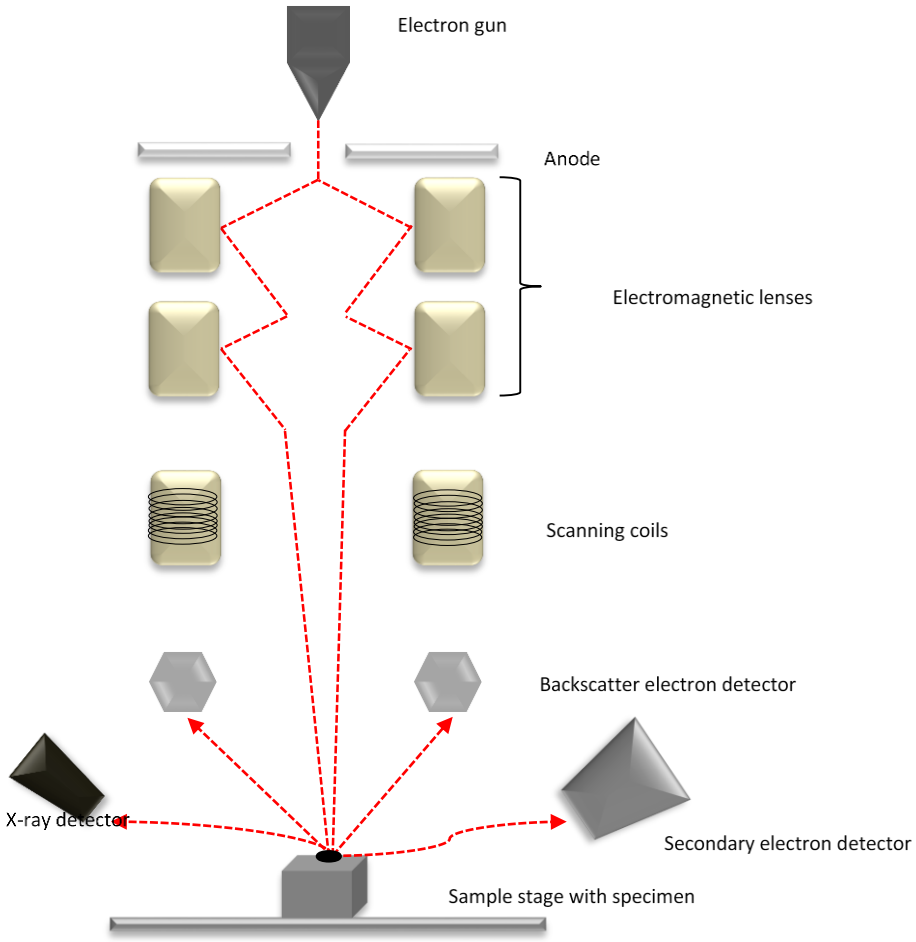

Figure 3.2-4 A schematic illustrating the main components of the SEM technique. The red dotted line represents the electron beam and the scattered beams after the beam has hit the sample.

Signal detection is initiated by a primary electron entering the sample. Electrons from the focused beam interacts with the sample and form a new trajectory, this is known as scattering. Electrons can be detected as backscattered or secondary. Backscattered electrons occurs when an incoming electron rebound back out, this is a form of elastic scattering. Secondary electrons are detected when a new electron is ejected out from an atomic orbital, energy of an electron from the focus beam is lost to an atom. This is known as inelastic scattering. The secondary electrons are detected and plotted (detected intensity vs detector position), this is viewed at the typical SEM image. The image generated is based on the surface of the particles.

3.2.5.2 Energy dispersive X-ray (EDX)

When electrons are ejected from specific orbits of an atom in the sample, there is a release of radiation, in the form of x-rays (T. Yurugi, 2001). This is

the third type of detection unit which the SEM also contains. Elemental information can obtained from the x-rays generated.

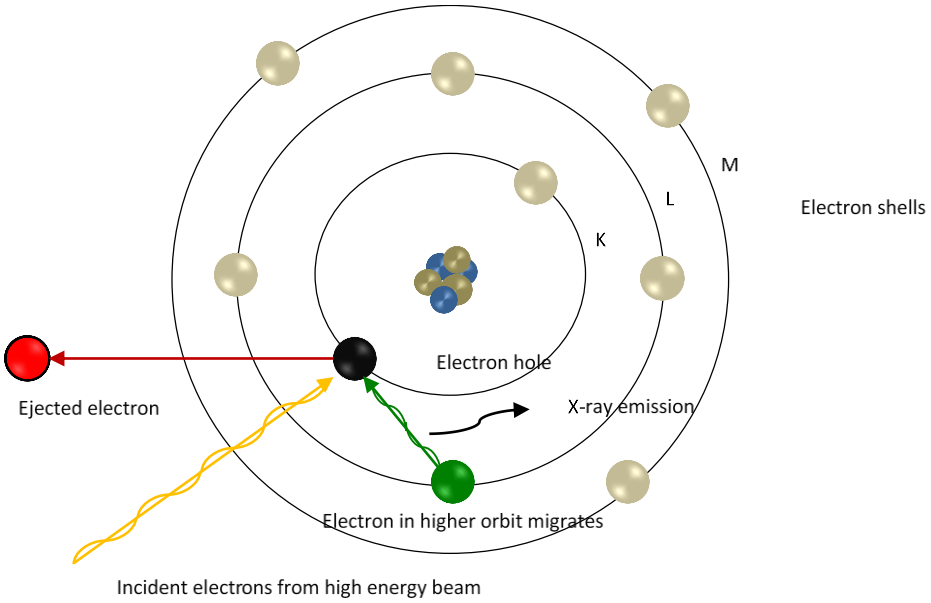

Figure 3.2-5 An illustration representing the change in electrons within an atom to produce x-rays. The x-rays produced are characteristic of the element and therefore used in elemental analysis such as EDX.

Figure 3.2-5 illustrates the production of x-rays. To stimulate the emission of x-rays the high energy beam of electrons is focused on the sample. When the atom within the targeted sample is at rest it contains ground state electron. This is located in the discrete energy orbital bound to the nucleus. The incident beam is able to excite and eject an electron in the discrete orbital. Secondary electrons and an electron hole are now created. An electron from a higher energy orbital then replaces ejected electron. The energy difference between the higher energy orbital to the lower energy orbital is released in the form of x-ray. As the number of hits increase, the x-rays will not have sufficient energy to be classified as being omitted from the originating element. This is known as background x-rays. It is the number and energy of x-rays emitted from a sample that is measured by EDX.

3.2.5.3 Laser diffraction techniques for particle size distribution

Laser diffraction is used to measure particle size. A laser beam is passed through a dispersed particulate system, the intensity of light diffracted is measured. Particle size is calculated using the diffraction pattern.

Figure 3.2-6 illustrates the main components of the technique. A light source is provided by He-Ne laser with a wavelength of 0.633 nm. Sample

dispersion flow cell unit is key to quality size measurements. The flow cell has the ability to provide a well dispersed homogenous sample to the laser beam at a desired particle concentrate. Light scattered by the sample is then focused onto a photosensitive silicon detector.

The basic principles of this technique is to measure the angular variation in intensity of scattered light as the laser beam passes through a dispersed particulate system. Large particles scatter light at a smaller forward-angle and smaller particles at a larger forward-angle. Laser diffraction uses the Mie theory to calculate the particle size distribution, assuming a volume equivalent sphere model. The relationship between the size and angle can be defined by approximation though Fraunhofer diffraction theory. This is followed by, for smaller particles, the application of the Mie scattering theory. The main components of the laser diffraction technique are illustrated in Figure 3.2-6.

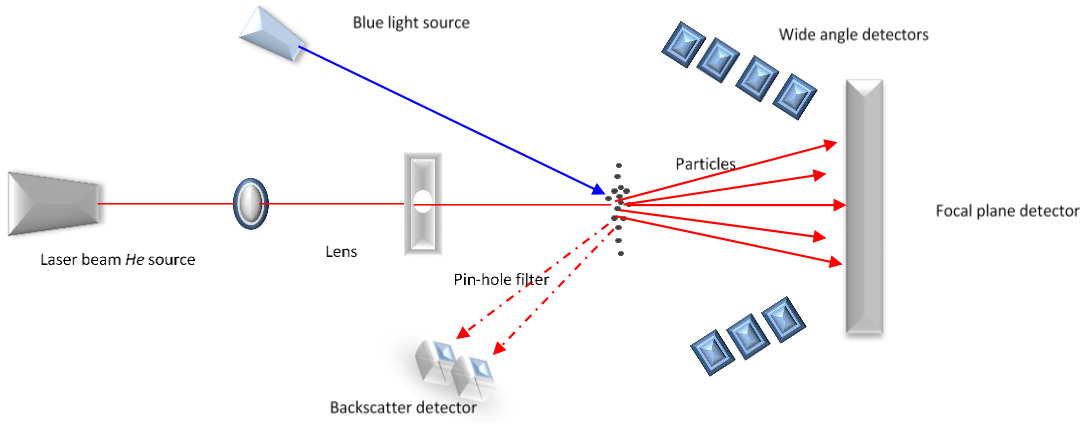

Figure 3.2-6 An illustration of the main components required in a laser diffraction technique, where the red line represents the laser beam passing through the system.

Fraunhofer is known to be one approximate expression of the Mie scattering theory. This theory is can only be applied when the particle size is large (ten times the size of the laser wavelength) and the scattering angle must be small (< 30^{o}). The approximation is limited to the decrease of particle size, within the sub-micron region. The Fraunhofer approximation can no longer be implemented. In this case the Mie scattering theory can be used.

Mie theory, developed by Gustav Mie in 1908, is a complex theory which is derived from the Maxwell's equation to obtain the incident, scattered and internal fields (Mie, 1908). This theory requires the knowledge of optical properties such the refractive index and the imaginary component of both the dispersant and the fluid. Inaccurate calculations can occur when implementing the Mie theory to large particles, this can be resolved by using

the Fraunhofer theory. Therefore, both theories are used in conjunction for calculating the light intensity pattern to ensure a wider measurement range is covered.

There are fundamental concepts to consider when using this technique (1) results are volume based and (2) results are equivalent spheres (Malvern, 1997). Particle size distribution is derived to produce volume based results. For example, 10% of the distribution is in the particle size category 6-7 µm. This is representative of 10% of the total volume of particles in this distribution. The particle size is based on the assumption that the particles are perfect spheres. Consider the particle illustrated in figure 3.2-7

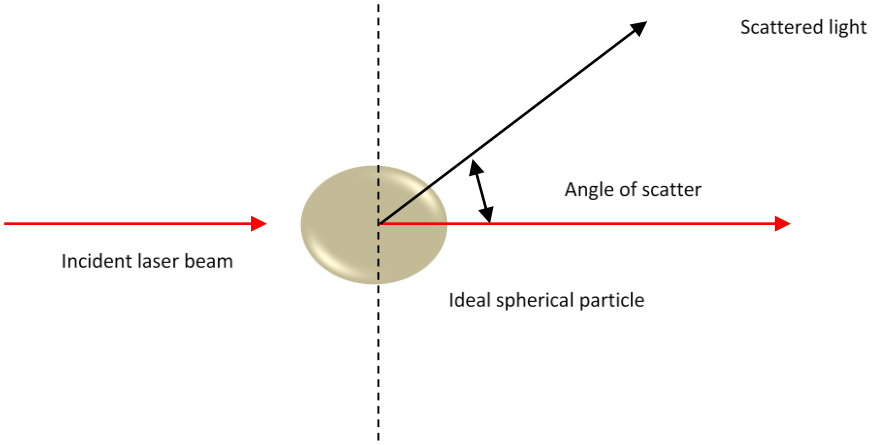

Figure 3.2-7 An illustration of an ideal spherical particle and how the laser diffraction techniques and the parameters required to generate a scatter pattern to produce the PSD.

A unique dimension cannot describe this three-dimensional particle. This is only applicable for a sphere. When considering a cubic particle, 20 µm could potentially describe the edge length or diagonal.

A single unique number to describe the size of non-spherical particles should be defined. A comparison of a feature of the non-spherical particle to an imaginary spherical particle is required. Typical methods include

- Equivalent surface area. Calculation of a theoretical sphere which has the same surface area of the original particle.
- Equivalent length. Diameter of a theoretical sphere that has the same maximum or minimum length of the original particle.

Mastersizer calculates the diameter using the volume. The volume of the particle in figure x is 50 x 25 x 10 = 13750 μm^3. This volume will be taken and a diameter of an imaginary particle that is equivalent in volume will create a sphere diameter of 30 µm.

3.2.5.4 X-ray diffraction technique (XRD)

X-rays are scattered from the lattice planes of a crystal. The scattered x-rays are from adjacent lattice planes, this is where the beams interfere with one another. The resultant x-rays are only observed when the interference is constructive. The condition of constructive interference is expressed as Braggs Law (Bragg, 1934) in equation 3.2-8 and Figure 3.2-8.

$$2d_{hkl}\, sin\theta = n\lambda \qquad 3.2\text{-}8$$

Where λ is the wavelength of x-rays, θ is the scattering angle and d_{hkl} is the inter-planar spacing between family of reciprocal lattice plane.

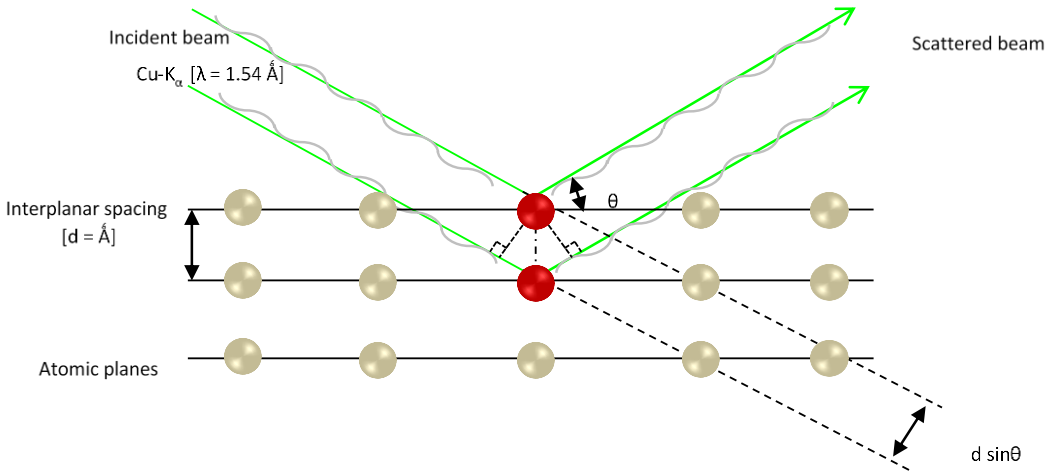

Figure 3.2-8 An illustration of constructive interference of an incident beam, according to the Bragg's law.

Location of the ions and molecules within the crystal is readily available from this information. Angular position of the peak relates to the size of the crystal cell. Peak intensity correlates to the type of atom located on the plane.

3.2.5.5 Zeta potential measurements

Zeta potential is the measure of the magnitude of the electrostatic repulsion or attraction between particles (Hamley, 2000). It determines the stability of colloidal suspensions, defined by potential at the surface of a moving charged particle in a stationary solution. This is essentially the potential which distinguishes the continuous phase from the stationary layer of the fluid attached to the colloid.

The zeta potential is influenced by the surrounding environment, as mentioned previously. The ionic charge distribution is greater within the EDL region when compared to the bulk. The EDL provides an adjacent layer of the counter anions, thus increasing the concentration of anions, which in turn

reduces the overall particle's surface potential. Figure 3.2-9 illustrates the zeta potential of a charged particle

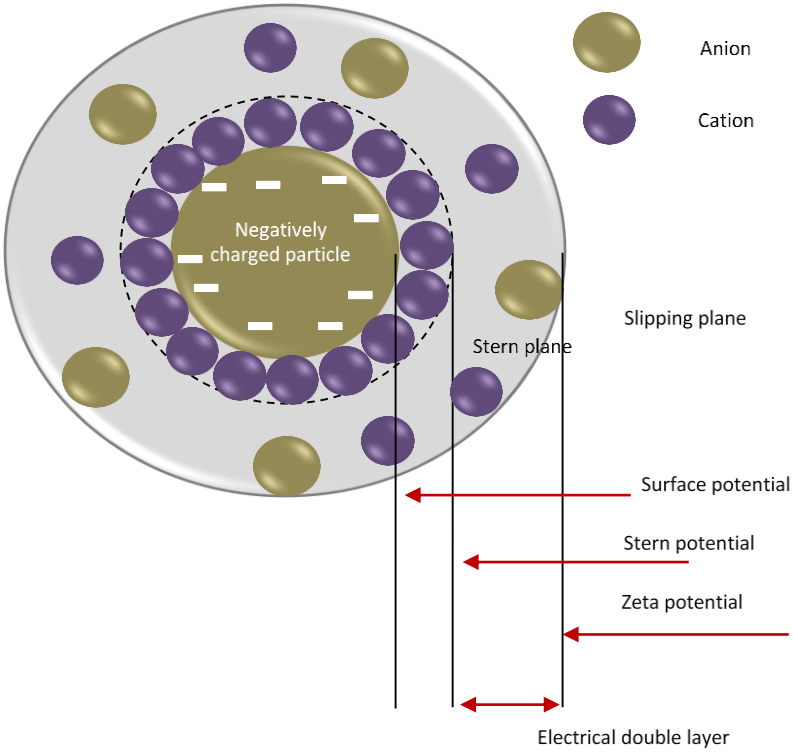

Figure 3.2-9 A schematic representation of the zeta potential with respect to the surface and Stern potential layers.

These are fundamental parameters which contribute to the stability of a dispersion. The Zetasizer Nano uses electrophoretic light scattering to measure the electrophoretic mobility and subsequently derive the zeta potential (Malvern, 2004). An electric field is applied to the solution containing dispersed particles.

Electrophoresis is a process where the charged particles migrate towards the electrode of the opposite charge. Viscous forces of the medium will create resistance of the moving particles. It is when the electric and viscous forces are maintained at equilibrium that the particles move at a constant velocity, known as the electrophoretic mobility of the particles. The velocity is dependent on a number of factors:

- Viscosity of the medium
- Zeta potential of the particle
- Strength of the applied force
- Dielectric constant of the medium

By directly measuring the electrophoretic mobility (U_E) of a particle the zeta potential can be determined by applying the Henry equation, expressed in equation 3.2-9

$$U_E = \frac{2\varepsilon z f(Ka)}{3\mu} \quad \text{3.2-9}$$

Where ε is the dielectric constant, z is the zeta potential, *f(Ka)* is the Henry's function and μ is the viscosity of the medium. Henry's constant can take a value of either 1.5 or 1.0. For aqueous solutions of moderate electrolyte concentrations the Smoluchowski approximation is used, where *f(Ka*) is set to 1.5. For non-polar solvents the Huckel approximation is used, where *f(Ka*) is set to 1.0.

3.2.6 Particle Characterisation Techniques of Nuclear Waste

The US has dominated the nuclear field with their contribution to nuclear research. Studies have been carried out on their nuclear site in Hanford including organic characterisation, separation of actinides, immobilisation of Cs in Hanford sediments, microstructural and rheological characterisation (Campbell et al., 1994, Horwitz et al., 1995, Flury et al., 2002, Smith et al., 2000, Chang and Smith, 1996a). The key difference between their waste streams and the UK waste streams is that they are alkaline. Taking these into account, this section discusses the particle characterisation techniques which have been implemented to analysis waste streams of the nuclear fuel cycle.

Nuclear research in the in UK is limited, characterisation of waste streams in particular. This research aims to contribute to the nuclear fuel literature in terms of particle synthesis, morphological modification and behavioural studies. In the production of precipitated HAL solids, it is important to understand the kinetics of the crystallisation system.

The effect of radiation on the nuclear spent fuel solids are of great interest. One study conducted by (Fourdrin et al., 2012) looked at the irradiation effects in ZM. They managed to synthesis ZM particles using zirconyl nitrate and sodium molybdate dehydrate as reagents. The reactor vessel was heated to 85^{o}C and left for 4 hours. The radiation stability was tested by irradiating the ZM particles with gamma and electron sources at a dose range of 10-100 kGy. XRD data illustrated after irradiation with gamma no change in peak position or width was exhibited. SEM images prior and post irradiation showed no change in particle morphology. This therefore suggests that the crystalline structure of ZM is unaffected by radiation

effects. Colour change of the yellow appearance of the initial ZM sample to a blue colour post irradiation was observed. A proposed mechanism of the colour change suggested it was due to the creation of electron holes. Electrons are trapped within the structure, where the possible sites are known to be molybdenum (VI) and zirconium (IV) cationic sites. Under irradiation these cations are known to reduce (Cozar et al., 2008). This observation was supported by electron paramagnetic resonance (EPR) spectroscopy, where the relative intensity of the peaks were strongly enhanced after irradiation. This therefore suggests that the increase of electron centre presence is responsible for the colour modification after irradiation.

Material characterisation of radioactive waste has been carried out by (Carasco et al., 2010) in Croatia. Elemental characterisation was carried out with associated particle technique (APT) and Monte Carlo calculations. The aim was to identify materials within the waste by mixing cement with the waste and then employing an external cement cylinder around the drum (~1m^3) containing the mixture. The Monte Carlo simulation has revealed that materials can be identified through thick slabs of cement and concrete, this is only if the excited nuclei produce gamma rays with enough energy. This particular research shows the quality control of the waste by characterising the elements present in the drum.

Other researchers have found that gamma/x-ray imaging is a promising technique where the physical and chemical properties of waste slurries can be identified (Pettier et al., 2003). Gonzani has carried out research by identifying nuclear materials, this is by the production of gamma rays by nuclear reactions (Gozani et al., 2004). This particular paper focuses on the detection of other dense materials as well as nuclear materials, these include chemical agents and explosives (Gonzalez-Romero, 2011). Nevertheless this coincides with other researchers that gamma/x-ray imaging provides accurate information about nuclear waste. Furthermore, the size, shape and density of nuclear waste materials can be characterised by this method (Kettler et al., 2007).

Nuclear waste characterisation at the Hanford sites, Washington include studies on particles properties and rheological behaviour (Chang and Smith, 1996a). Chang et.al have characterised nuclear waste simulants using different additives were induced such as glycolic acid and nitric acid. Smith et al. identified the particulate suspensions and found (sodium hydroxide

(NaOH) rods and FeO(OH) agglomerates; rheological and microstructural parameters were also explored. Additionally, the study explored the increase in electrolyte strength from 0.1M to 1M $NaNO_3$ and found the number-averaged particle size doubled, thus leading to an aggregated system.

3.2.7 Literature review conclusion

Previous research indicates a lack of robust methods to produce large quantities of particles for extensive physical characterisation on nuclear waste simulants. Optimisation of ZM synthesis procedure to obtain a morphological specific product is an area of interest which has not been considered to a great extent. Overall, publically available literature on characterisation of nuclear waste suspension is dominated by the US.

Currently there have been no in depth studies on the citratomolybdate complex formation in a highly acidic environment, especially in ZM synthesis. POCO is a crucial stage for decommissioning. This is where all the radioactive and harmful materials will be removed prior to the dismantling of the infrastructure. POCO requires the clean out of any remaining solids inside the vessels and pipeline. A possibility is through dissolution. Once the solids have been dissolved, the solids will be able to re-precipitate in a controlled environment, this is the point where additives may be added to the solution where morphological manipulation can take place of ZM particles. This study aims is to understand the formation of the nuclear waste simulants, CPM and ZM and produce a morphological specific ZMCA particles which could be advantageous for nuclear waste processing.

3.3 Materials and Methods

3.3.1 Pre synthesised materials

Nuclear relevant analogues for radioactive slurry materials can be costly to manufacture and difficult to handle. As a result, initial research in this project has concentrated on slurries prepared from a simple mineral oxide particle, titanium dioxide (TiO_2).

The data collected using this TiO_2 sample provides baseline data for comparison with nuclear waste analogue slurry materials that will be studied in detail later in this project. Throughout the study, there are references to a ZM (sol-gel) particulate system. Initial stages of this research also characterised this material. This was provided by NNL from a previous study (Masheder, 2010).

TiO_2 has three naturally occurring forms known as rutile, anatase and brookite Research reported here is for anatase particles obtained from Degussa (Germany). The average particle size is 1.78µm, it has a density of 3.78 gcm^{-3}, anatase is a fine white powder and is a common standard for preliminary experiments.

The results discussed in this study are of particles which have been synthesised. Synthesised material include caesium phosphomolybdate (CPM), zirconium molybdate (ZM) and zirconium citratomolybdate (ZMCA). There is currently only limited information available on these particles. The aim of this research is to characterise these particulate materials to obtain a greater knowledge of their hydrodynamic properties. Table 2 represents all the materials used in the study.

Table 2 Materials used for analytical measurements and raw materials required for synthesis

Compound	Chemical Name	Formula	Purity/ Concentration	Supplier
Titanium dioxide	Titania	TiO_2	99.8%	Degussa
Dodecamolybdophosphoric acid	Phosphomolybdic acid	$H_3PMo_{12}O_{40}$	80%	ACROS Organics
Caesium nitrate		$CsNO_3$	99.8%	Alfer Aesar
Zirconium(IV) oxynitrate	Zirconyl nitrate	$ZrO(NO_3)_2$	212 g/L	Johnson and Matthey
3-carboxy-3-hydroxypentanedioic acid	Citric acid	$C_6H_8O_7$	99.8%	Fisher Scientific
Nitric acid		HNO_3	70% (16M)	Fisher Scientific

3.3.2 Particle synthesis

Particle synthesis of nuclear waste simulants was investigated to produce the required amount material for particle characterisation and behavioural studies. Synthesis of the nuclear waste simulants were carried out in a batch reactor vessel, with a set-up illustrated in Figure 3.3-1.

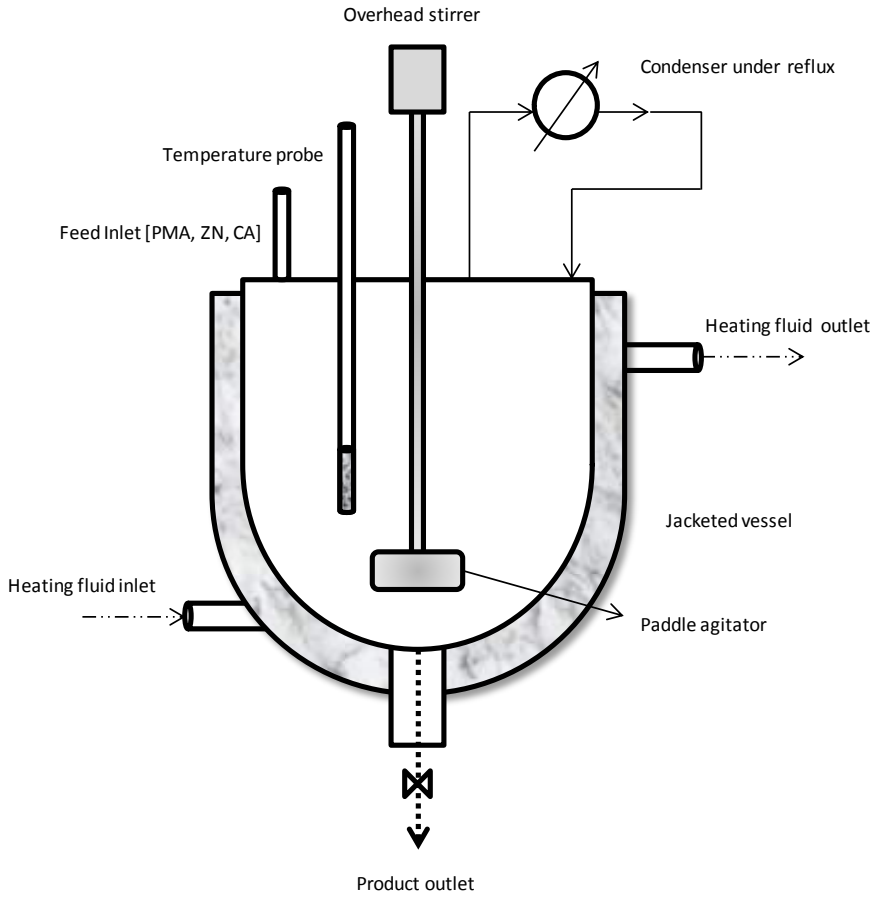

Figure 3.3-1 4L batch reactor vessel set-up for CPM, ZM and ZMCA synthesis. The reactor vessel is a jacketed vessel contained silicon oil for heating purposes, an overhead paddle agitator, a condenser with circulating water at 5ºC, a temperature probe to monitor the reaction temperature.

3.3.2.1 Synthesis of caesium phosphomolybdate (CPM)

Synthesis of CPM involved preparing phosphomolybdic acid (PMA) and caesium nitrate (CN) solutions. The CPM method was based on an internally circulated document within NNL. PMA and CN solutions were individually prepared by dissolving the solids, at a ratio of 3:1 PMA (242 g) to CN (82 g), in 2 M nitric acid under continuous stirring. Preparation of the PMA and CN solutions were carried out separately in two individual 2 L beakers, where the solids were stirred until they were fully dissolved, at room temperature. The CN was then dispensed into the empty 4 L reactor vessel, illustrated in figure 3.3-1, and heated to 50ºC. PMA was added at a rate of 16.67 mL/min, using a 20 mL syringe, to the CN over a 1 hr period. Following the complete addition of the PMA, the solution was maintained at 50ºC with continuous stirring (approximately 200 rpm).

Yellow CPM solids precipitated out during the 48 hrs reaction period. Separation of the CPM solids from the mother liquor was achieved by decanting. The final dispersion was left to stand for 1 hr during which time phase separation of the CPM solids was achieved and a clear supernatant

produced. The removal of the supernatant required a hand pump. The remaining solids were collected and oven dried at 50˚C for 48 hrs, the solids did not require a cleaning step.

The overall synthesis method of CPM is illustrated in figure 3.3-2.

3.3.2.2 Synthesis of zirconium molybdate (ZM)

The ZM synthesis was also based on an internal report from NNL, this method originated from the Clearfield and Blessing sol-gel method (Clearfield and Blessing, 1972). The method implemented in this research provides an alternative to the sodium molybdate compound used in the earlier research, and instead uses CPM as a reagent. Synthesis of ZM required the initial conditioning of 397 mL zirconyl nitrate (ZN) dissolved in 6M nitric acid at 100˚C. This was carried out in a 1 L round bottomed flask, under reflux. Initially the zirconyl nitrate solution gives a milky-white appearance when added to nitric acid. Conditioning of zirconyl nitrate at 100ºC allows breakdown of the $ZrO(NO_3)_2$ compound to produce $[Zr]^{4+}$ ions, to give a clear solution. The solution was left to cool down to room temperature prior to the ZM synthesis.

A 2 L CPM suspension using 121 g of PMA and 41 g of CN (from a batch directly synthesised in Section 3.3.2.1) was synthesised in the 4 L reactor vessel (as above). After 48 hrs (optimum time for CPM production), the suspension was heated up to 90ºC. The zirconyl nitrate solution was then added at a rate of 16.67 mL/min using a 20 mL syringe over a 1 hr period with continuous stirring (~200 rpm) whilst the reaction medium was maintained at 90ºC under reflux. The experimental set-up is as shown in Figure 3.3-1.

Conversion of CPM to ZM can be a lengthy process, sometimes taking up to 14 days. The conversion is visually monitored by the associated colour change from yellow to white, which is characteristic of the change from CPM to ZM.

Once again, at the conclusion of the reaction, the precipitated ZM solids were left to naturally settle and the liquor was decanted. The solids were washed once with 2M nitric acid to remove excess zirconium. The extracted and washed solids require oven drying at 50˚C.

The overall synthesis method of ZM is illustrated in Figure 3.3-2.

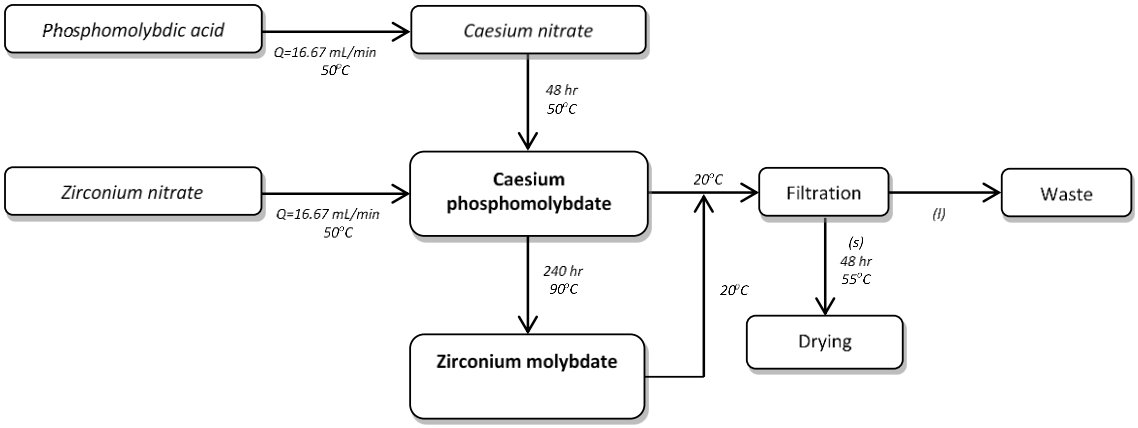

Figure 3.3-2 **A schematic illustrating the synthesis steps for CPM and ZM particle formation.**

3.3.2.3 Synthesis of zirconium citratomolybdate (ZMCA) – Method 1

This research explored two types of ZM particles to understand the changes to particle characteristics associated with morphological elongation. Elongation of the particles required the ZM synthesis to be modified with an organic additive, citric acid. As mentioned in Section 3.2.1.1, the citric acid is known to form a citratomolybdate complex (Samotus et al., 1991, Alcock et al., 1990, Zhou et al., 1997, Cruywagen et al., 1995), this initiated the interest in the influence of the complex interaction with ZM.

Initially, a simple ZMCA synthesis method was investigated, which required only the addition of citric acid to be added simultaneously with the zirconyl nitrate over a period of 1 hr to the CPM conversion (as described in Section 3.3.2.2). 20 mol% of the citric acid is added to the synthesis and reaction conditions are similar to the ZM method. The reaction was kept at 90°C, for 336 hrs under reflux with continuous stirring at 200 rpm. The same cleaning procedure with nitric acid was undertaken also as per the ZM synthesis.

The overall synthesis ZMCA, Method 1, is illustrated in Figure 3.3-3.

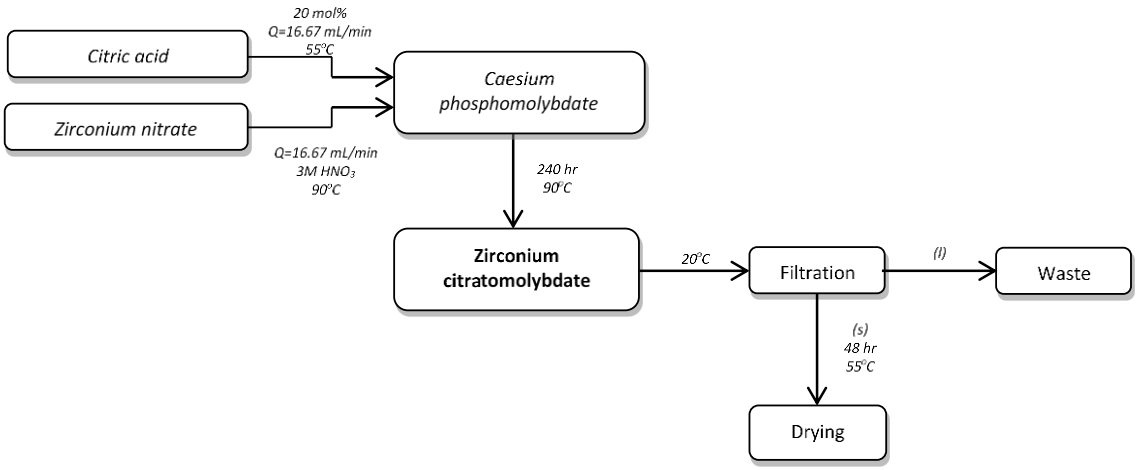

Figure 3.3-3 A schematic illustrating the synthesis steps required for morphological modification of ZM to produce ZMCA particles with incorporation of citric acid.

3.3.2.4 Synthesis of zirconium citratomolybdate (ZMCA) – Method 2

Initial experiments with Method 1 gave an overall poor conversion of the CPM to ZMCA (see Section 3.4.1.3 discussion) and thus a modified method, illustrated in Figure 3.3-4, was implemented to improve the conversion. The optimised ZMCA synthesis method, in contrast to the initial Method 1, required the change in the citric additive induction time to *t=30 mins*, change in additive flow rate to 3.34 mL/min and the addition of a washing step. The intent to optimise the key parameters was to improve the overall yield conversion achieved in Method 1, the reasoning will be further discussed in Section 3.4.1.3 and 3.4.1.4. The reaction was kept at 90ºC, under reflux with continuous stirring at 200 rpm. Post filtration, it was necessary to wash the ZMCA product with ammonium carbonate (AC), this is to dissolve any excess CPM and to generate a high yield of uniform ZMCA particles.

The overall synthesis method 2 of ZMCA is illustrated in Figure 3.3-4.

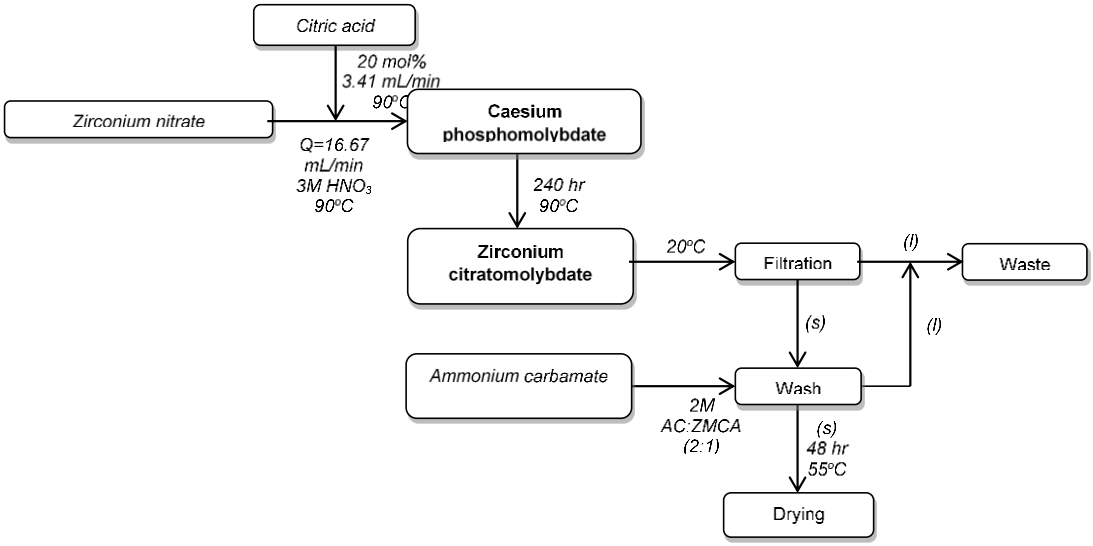

Figure 3.3-4 **Schematic illustrating the optimised method of ZMCA synthesis.**

3.3.3 Particle characterisation

3.3.3.1 Sample Preparation

The results reported here are for TiO_2 particles dispersed in water. Typical sample preparation for the dispersion involved adding the TiO_2 particles to water under mechanical agitation at pH 6. Smaller quantities of material are required and in these cases, samples are prepared in 36 mL vials and agitated using a rotary mixer. After agitation, all samples were then sonicated for approximately 20 minutes prior to a measurement. This is a

necessary part of the protocol to ensure a homogeneous suspension is obtained.

The aim for this chapter is to obtain reliable and reproducible results for each characterisation technique, to create a standard protocol for later research, and to explore the effect of sample preparation prior to an experiment. The bonding network within the sample is an important factor, as this will affect the outcome of the results, especially when considering rheology data. It is necessary for the sample to be prepared in such a way as to ensure consistent material properties.

3.3.3.2 Particle shape

The particle shape and size was characterised by using the Scanning Electron Microscopy (SEM) technique. The sample was dried and coated with platinum with a coating thickness of 5 nm. This is to increase the conductivity of the electrons passing through the device and onto the sample. There is an electron gun at the top of the microscope where electrons are released, emitting a beam of high energy electrons. The beam then passes through magnetic lenses and reaches a coil at the bottom where scanning of the sample takes place. The magnetic lenses assist in the focusing of the electrons. The working distance of the sample to chamber was maintained at 3 mm with an electron intensity of 5 keV.

3.3.3.3 Particle Size

A Malvern Mastersizer 2000 (Malvern Instruments Ltd., UK) was used to obtain the particle size distribution information for liquid dispersions of the TiO_2 and the relevant nuclear waste simulants. For each sample tested, the particulate solids were suspended in water and a few drops of the stock solution were added to a water-filled, stirred measuring cell until the correct obscuration value needed for accurate data was obtained. Each sample was analysed over 10 s and averaged over 10 repeat measurements. The optical properties were derived by varying the input parameters and to compare variation with the different properties. The refractive indices were taken to be 2.49, 1.29 and 1.19 for TiO_2, CPM and ZM respectively, with an imaginary refractive index of 0.01. The refractive index of the dispersant was taken to be 1.33.

3.3.3.4 Particle density

The density of each articulate system was measured using a Micromeritics AccuPyc 1330 (Micrometrics Instrument Corporation, US). This Pycnometer determines the density and volume by measuring the pressure change of

Helium in a calibrated volume. Once the calibration was completed a known weight of the solids were loaded into the cell. The density was determined using the helium displacement theory.

3.3.3.5 Particle stability

Zeta potential measurements were taken by using the Malvern Zetasizer Nano series. Dispersion (of 0.5 wt%) were subjected to electrophoresis, where the velocity was measured using the Laser Doppler Velocimetry and Malvern's patented M3-PALS© system. The Henry equation is then applied to obtain the electrophoretic mobility of the particles. The Smoluchowski approximation (1.5) was used to determine the Henry's function. A stock solution was prepared where the pH of the dilute suspension was varied with 0.1 M potassium hydroxide (KOH). The sample was transferred to a cell (manufacturer's recommended cell) where an incident laser beam is scattered by the particles at an angle of 17º, this is then combined with a reference beam. This produces fluctuating intensity signals, the fluctuations are directly proportional to the speed of the particles.

3.3.3.6 Crystalline structure

Analysis of the crystalline structure was characterised using the x-ray diffraction (XRD) technique (Bruker D8, UK). Approximately 1g of material is required to be tightly packed, with a flat surface into a sample mount. This sample arrangement provides good signal to noise ratio, and therefore avoid fluctuations in the intensities. The main parameters required for the technique is the radiation source, in this case it is a copper source (Cu K_α) with an electron beam of 40 keV hitting the sample. The wavelength is known to be 1.54 Å and 1.6 kW of energy in the radiation source.

3.3.3.7 Elemental analysis

Elemental analysis of the particles were carried out using energy dispersive x-ray spectroscopy (EDX) on the SEM. The electron beam of the SEM provides the high energy beam of charged electrons to be focused onto the sample and therefore allow excitation of the electron. The electron intensity was altered to 20 keV and the working distance was changed to 8 mm. Two approaches were used to for elemental characterisation; (i) point and ID which allows you to specify localised points and analyse the elements present and (ii) mapping where you can locate the position of the atoms within the sample.

3.4 Results and discussion

3.4.1 Particle synthesis

3.4.1.1 Synthesis of Caesium phosphomolybdate

CPM formation is a double replacement reaction, where both the reactants phosphomolybdic acid, $H_3PMo_{12}O_{40}$, and caesium nitrate, $CsNO_3$, dissociate into $[PMo_{12}O_{40}]^{3-}$ and $[H]^+$ ions from PMA and $[Cs]^+$ and $[NO_3]^{3-}$ ions from caesium nitrate. The proposed formation of CPM, based on the molecular formula, chemical structure and the initial quantities of raw materials, is expressed by the following stoichiometric equation, 3.4-1

$$H_3PMo_{12}O_{40} \cdot 14H_2O_{(aq)} + 3CsNO_{3(aq)} \rightarrow Cs_3PMo_{12}O_{40} \cdot 14H_2O_{(s)} + 3HNO_{3\,(aq)} \quad \text{3.4-1}$$

With a net ionic precipitate reaction:

$$[PMo_{12}O_{40} \cdot 14H_2O]^{3-}{}_{(aq)} + 3[Cs]^+_{(aq)} \rightarrow Cs_3PMo_{12}O_{40} \cdot 14H_2O_{(s)} \quad \text{3.4-2}$$

This reaction produced a conversion of 94% after 48 hrs, with constant temperature and agitation speed. The precipitated solids, when separated from the liquor and dried, produced a crystalline product with a bright yellow appearance. Figure 3.4-1 illustrates SEM images of CPM post-synthesis.

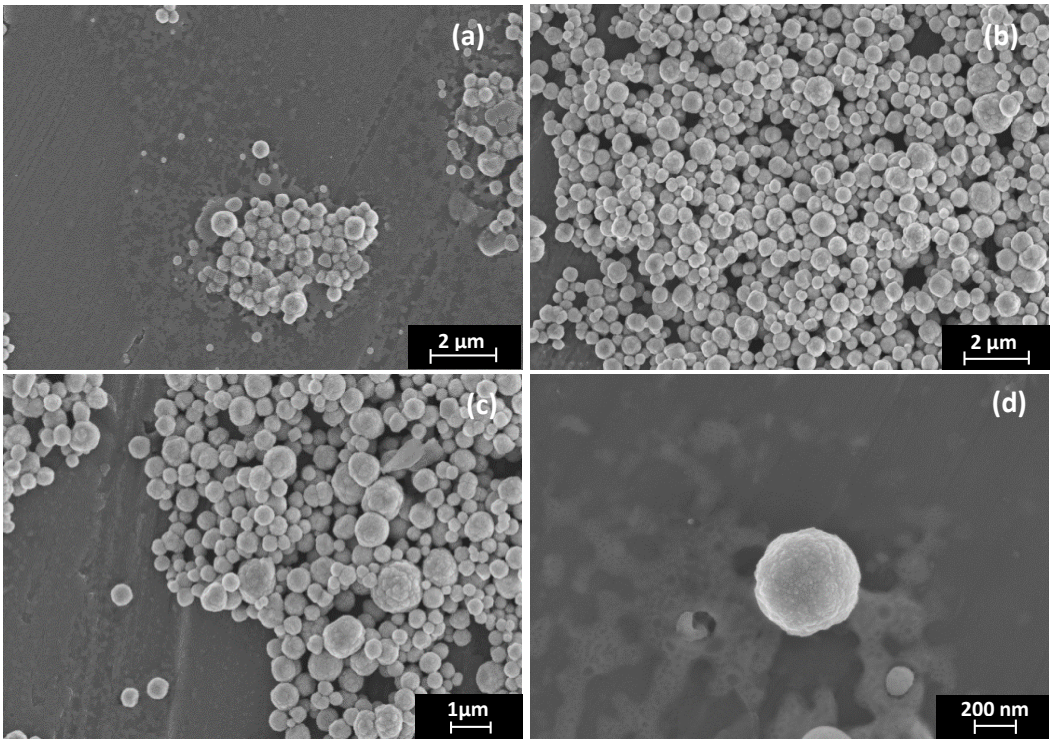

Figure 3.4-1 Scanning electron microscope images of synthesised caesium phosphomolybdate particles. Images are taken at different magnifications: (a) 23.01 K; (b) 23.25 K; (c) 29.32 K; (d) 151.09 K.

The SEM images in Figure 3.4-1 show the synthesised CPM sample to be submicron, near size monodisperse, spherical particles. The primary particle size is ~200 nm with a range of larger aggregates having sizes of ~1 µm. With an increase in magnification to 151.09 K it appears that the 200 nm particles are polycrystalline and themselves consist of smaller spherical particles, identified by the roughened surfaces of the primary CPM aggregate. Figure 3.4-2 illustrates a proposed mechanism of CPM aggregate formation.

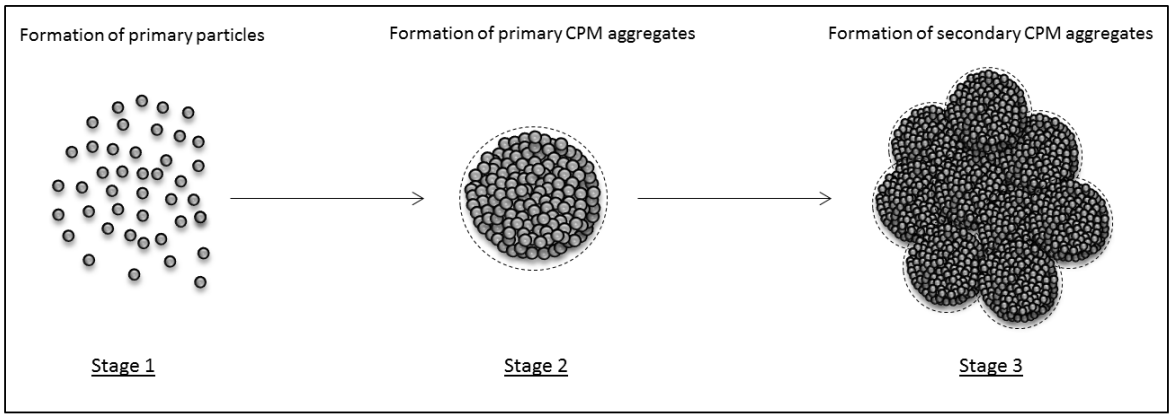

Figure 3.4-2 Proposed aggregation mechanism for caesium phosphomolybdate particles. Stage 1: formation of the nanocrystallites; Stage 2: formation of the primary aggregates, consisting of cemented nanocrystallites; Stage 3: formation of the secondary aggregate, consisting of the submicron aggregates.

The proposed mechanism in Figure 3.4-2 suggests there are three distinct stages in the formation of the overall CPM particles. In Stage 1, nano-crystallites are formed (the size of which has not been defined); in Stage 2 the attractive van dan der Waals forces in the system causes the aggregation of these nanocrystallites and the formation of a primary spherical CPM aggregate with a size of ~200 nm (illustrated in figure 3.4-1 (d)); and, in Stage 3 the primary aggregates themselves form larger secondary aggregates, with an overall size of a few microns.

3.4.1.2 Synthesis of zirconium molybdate

It may be assumed the initial step of ZM formation is the breakdown of CPM at high temperatures, which leads to the formation of the oxomolybdate complex, $[Mo_2O_5]^{2+}$. The assumption is based on research conducted by (Zhou et al., 1997 and Cruywagen et al., 1995). The liberation of the complex reacts with the $[Zr]^{+}$ released from the conditioned $ZrO(NO_3)_2$. It is the reaction between CPM and zirconyl nitrate which produces ZM particles. The proposed formation of ZM, based on the molecular formula, chemical structure and the initial quantities of raw materials, is expressed by the following stoichiometric equation

$$Cs_3PMo_{12}O_{40} \cdot 14H_2O_{(aq)} + 6ZrO(NO_3)_{2(aq)} + 3HNO_{3(aq)} + 10H_2O_{(aq)} \rightarrow$$
$$6[ZrMo_2O_7(OH)_2] \cdot 2H_2O_{(s)} + H_3PO_{4(aq)} + 3CsNO_{3(aq)} + 9H_2O_{(aq)} \quad \text{3.4-3}$$

With a net ionic precipitate reaction:

$$[PMo_{12}O_{40}]^{3-}_{(aq)} + [Zr]^{+}_{(aq)} \rightarrow [ZrMo_2O_7(OH)_2] \cdot 2H_2O_{(s)} \quad \text{3.4-4}$$

This reaction produced a conversion of 84% after 48 hrs, at constant temperature and agitation speed. The precipitated solids separated from the liquor and dried produced a crystalline product with a cream/white appearance. SEM images of ZM particles are illustrated in Figure 3.4-3.

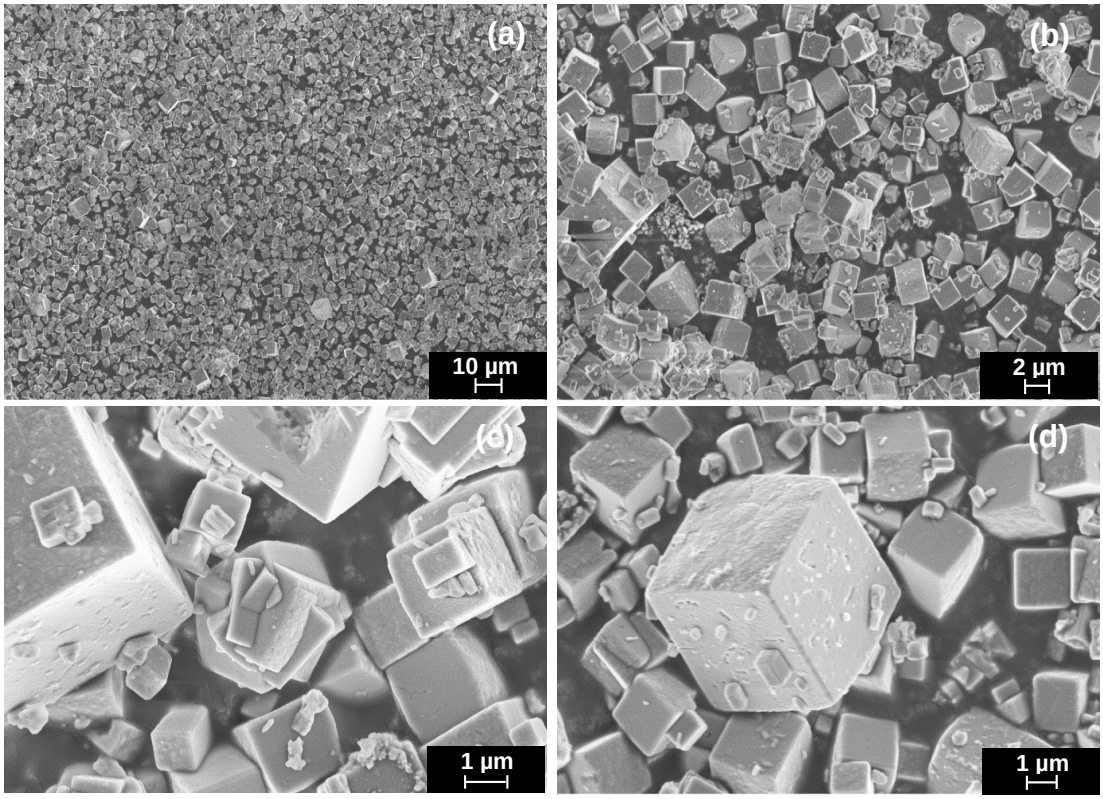

Figure 3.4-3 Scanning electron microscope images of synthesised zirconium molybdate particles. Images are taken at different magnifications: (a) 1.74 K; (b) 7.79 K; (c) 19.66 K; (d) 27.99 K.

The SEM images, in Figure 3.4-3, illustrate that basic particle shape of ZM to be cubic. Individual particle sizes range from approximately 500 nm to 3µm. Figure 3.4-3 (c) and (d) show the presence of finer cubic ZM particles in addition to the larger 3 µm ZM particles, this is indicative of some moderate size polydispersity; however the majority of particles were of a size order between 3 µm.

Figure 3.4-3 (c) shows evidence of multiple penetration twinning, where crystals are formed by growth and pass through each other. There are various mechanisms associated with the incorporation of growth units to form penetration twins, where the crystal units seem to grow simultaneously but independent of each other (Cahn, 1954). A proposed mechanism for

multiple twinning ZM morphologies is a change in the lattice during formation, which can be due to a substituting growth unit. In this case both $[Mo_2O_5]^{2-}$ and $[Zr]^{+}$ are the crystal nuclei which exist in solution. Substitution of a large ion takes place along the c-axis and the incorporation of the growth units on growth interfaces (0 0 4) or (0 0 $\bar{4}$). The incorporation of growth units results in the formation of a twinned crystals (Wang et al., 1998). Multiple penetration twinning occurs when two or more structures contain interpenetrating lattice and therefore occur in pairs. As the planes of symmetry are identical, the crystals units pass through each other during growth (Jaswon and Dove, 1956).

For both CPM and ZM production, considering the initial quantity of the molybdate compound, it can be concluded that the concentration of $[Mo_2O_5]^{2-}$ ions released in solution controls the rate of reaction and ultimately the yield of solid produced. It is therefore of importance to control the release of the $[Mo_2O_5]^{2-}$ complex to obtain the desired solid product.

3.4.1.3 Staged synthesis of zirconium citratomolybdate with Method 1

The conversion of CPM to ZMCA proved to be a challenge, therefore further characterisation was required to fully understand the mechanism. Throughout the ZMCA synthesis 2 mL aliquots were extracted at 24 hr, 192 hr and 330 hr intervals. The samples were analysed by SEM imaging to observe the morphological changes at varying stages of the reaction, Figures 3.4-4 to 3.4-6.

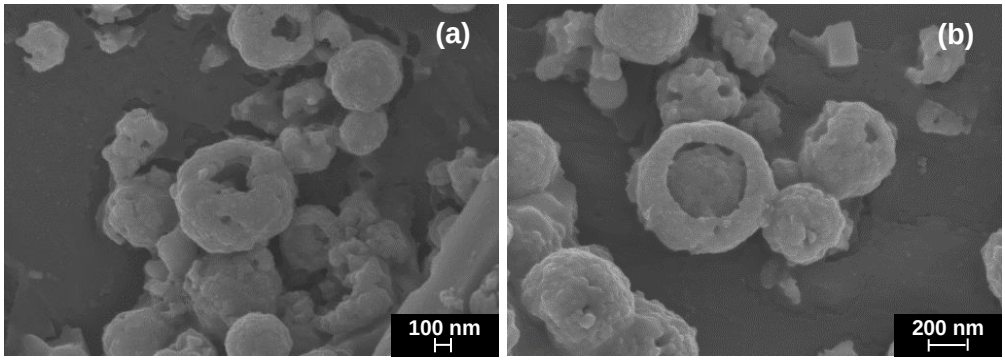

Figure 3.4-4 Scanning electron images illustrating the breakdown of caesium phosphomolybdate, 24hours into the synthesis. The images were taken at different magnifications: (a) hollow centre crystal at 130.56 K; (b) filled centre crystal at 152.60 K.

Initial SEM images in Figure 3.4-4 of CPM shows smooth surfaces of the polycrystalline crystals. After approximately 24 hrs it can be seen from the SEM images that the CPM breaks down, due to the increase of temperature from 50 to 90^{o}C (Eiden and Maret, 2002). The aggregates are shown to dissolve and form a hollow centre Figure 3.4-4 (a), and in some cases as

shown in Figure 3.4-4 (b), a filled centre. Hollow spheres are produced by Ostwald ripening or differential diffusion within the solid spheres (Cölfen, 2001, Yang and Zeng, 2004, Hu et al., 2011). In the latter case, the breakdown of the CPM releases reagents causing the solution concentration to increase past their supersaturation point. This is an ideal environment for spontaneous nucleation to occur and causes a layer of crystalline CPM on the outside of the CPM surface. Contingent to the production of a diffusion pathway through the outer crystalline layer of CPM, the inner core dissolves. At this stage, the supersaturation rate increases in solution again, above the solubility of CPM, leading to secondary nucleation on the external surface. Secondary nucleation increases the thickness of the outer CPM layer as the inner core is depleted, thus producing hollow sub-micron CPM spheres as illustrated in Figure 3.4-4 (a). Similar behaviours have been observed for calcium carbonate by Yu et al., (Yu et al., 2006). In some cases low supersaturation rates and insufficient diffusion pathway produces filled sub-micron CPM spheres, as illustrated in Figure 3.4-4 (b).

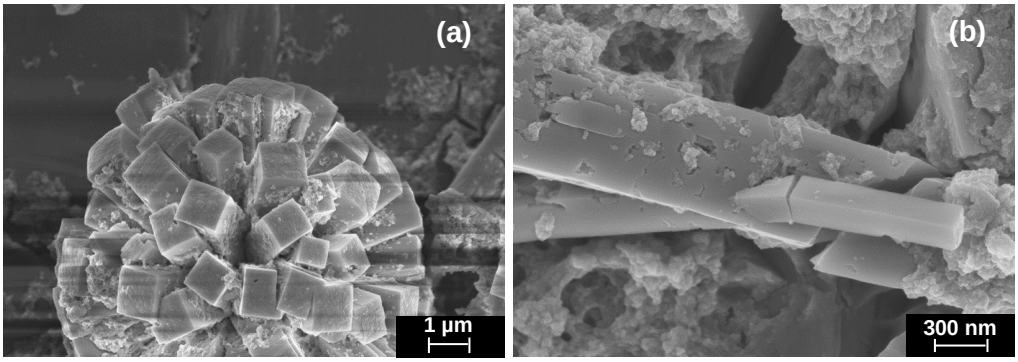

Figure 3.4-5 Scanning electron images illustrating the formation of zirconium citratomolybdate, 192 hrs into the synthesis. The images were taken at different magnifications: (a) contact twinning at 29.63 K; (b) penetration twinning at 125.70 K.

Figure 3.4-5 indicates 192 hrs into the synthesis where the formation of elongated ZMCA particles are observed. Figure 3.4-5 (a) indicates a growth penetration twin at an angle. This occurs at a rotation axis, where its forms a new symmetry which results in a plane where the atoms are shared of the two crystals.

Figure 3.4-5 (b) indicate ZM growth initiated by multiple cyclical twinning. This is a type of contact twin where the compositional surfaces are not parallel during growth. A spherical ball is formed when the ZMCA particles have twinned along the dominating plane resulting in the branching behaviour. The branching occurs along the dominating axis and new nucleation events will result in the formation of complex structures with radiating growth mode from a central nucleus. There are many factors

influencing the growth and the nucleation of the particles which involve the solubility and acidity of the additive used.

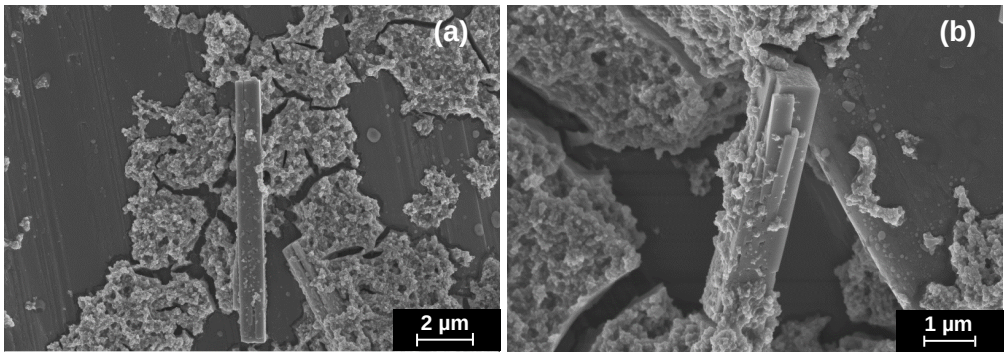

Figure 3.4-6 Scanning electron images illustrating the formation of zirconium citratomolybdate, 336 hours into the synthesis. The images were taken at different magnifications: (a) fully developed zirconium citratomolybate at 21.02 K; (b) step growth of crystals at 37.63 K.

Figure 3.4-6 illustrates 336 hrs into the synthesis, it is evident from the SEM images the formation of the elongated ZM particles has occurred. Figure 3.4-6 (b) indicates crystal step growth. It is suggested for ZMCA synthesis 336 hrs of reaction time is not a sufficient amount of time for 100% conversion of CPM to ZMCA. Further studies on crystal growth and the mechanisms are required to better understand this type of behaviour.

One of the assumptions, given two weeks of reaction time, there is still a significant amount of unconverted CPM in the final product. The SEM image, illustrated in figure 3.4-7, taken after full reaction time is indicative of this. There is a large amount of debris surrounding the cuboidal ZM particles. This assumption can be supported by an elemental analysis, energy dispersive x-ray on the SEM.

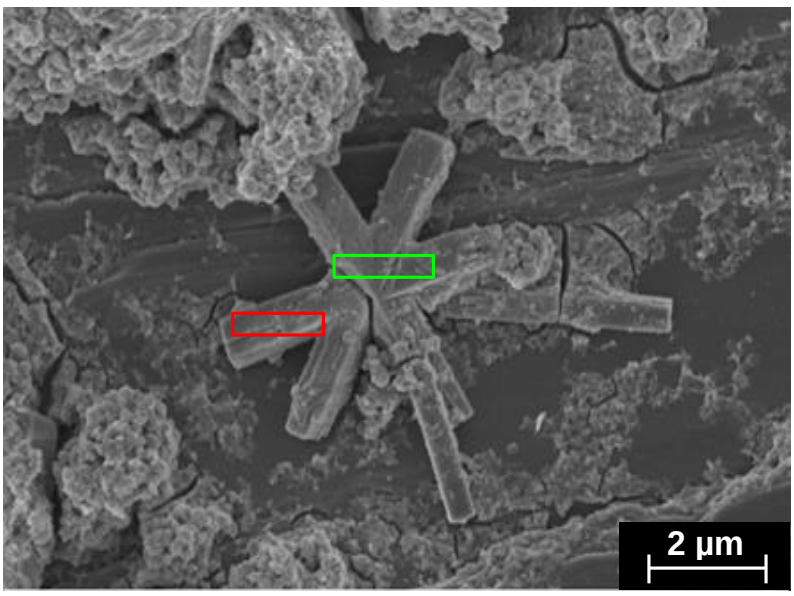

Figure 3.4-7 Scanning electron microscope image used during electron dispersive spectroscopy analysis. The image illustrates zirconium citratomolybdate at 336 hrs into the synthesis. The EDX main parameters: working distance at 8 mm; electron intensity at 20 keV.

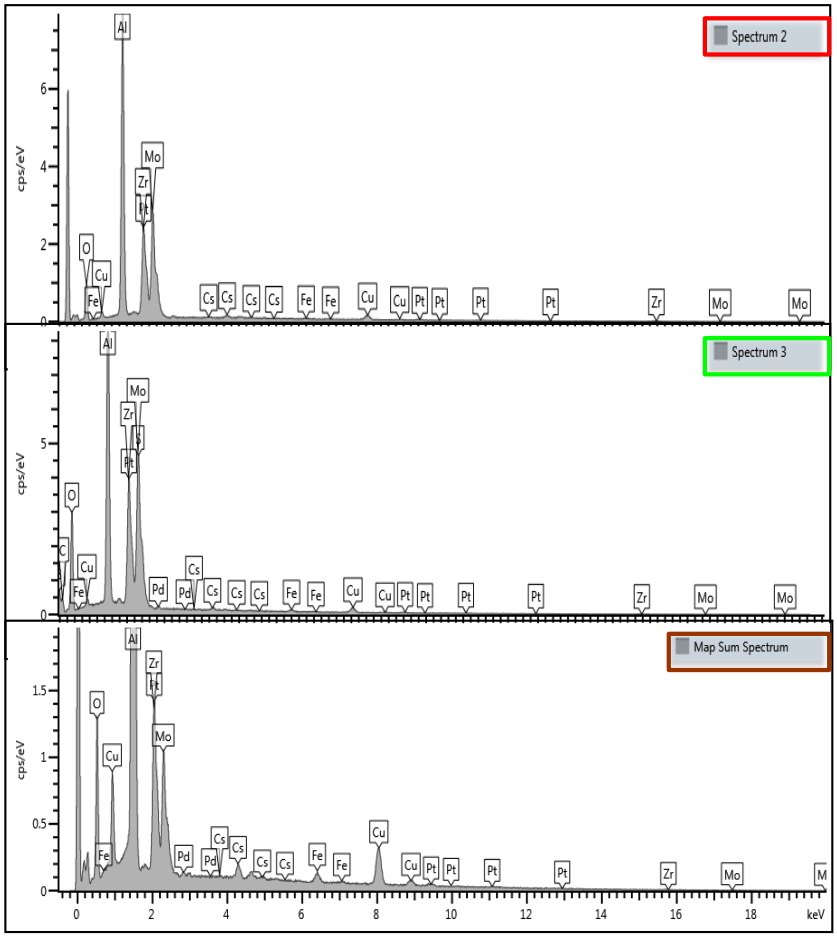

Figure 3.4-8 Electron dispersive spectroscopy point and identification method. The image illustrates the spectrum of specific locations of the sample (spectrum 2 and 3) and a mass spectrum of both locations.

From Figure 3.4-8 the EDX pattern demonstrates the number of x-rays and energy emitted from the sample (y-axis) and the energy levels with respect to the atoms (x-axis). The SEM images shows the location of the point where the analysis took place, the surface of the elongated ZM particle. The atoms present are to be expected, showing Zr, Mo and O atoms. The presence of C atoms, indicates the presence of citric acid. From the EDX pattern there is evidence of Cs atoms present, which indicates the unconverted CPM. This can be further analysed by applying the EDX mapping technique as illustrated in Figure 3.4-9. The sample is scanned and relies on the detection of the x-ray. The importance of this is to locate the position of the atoms in the sample.

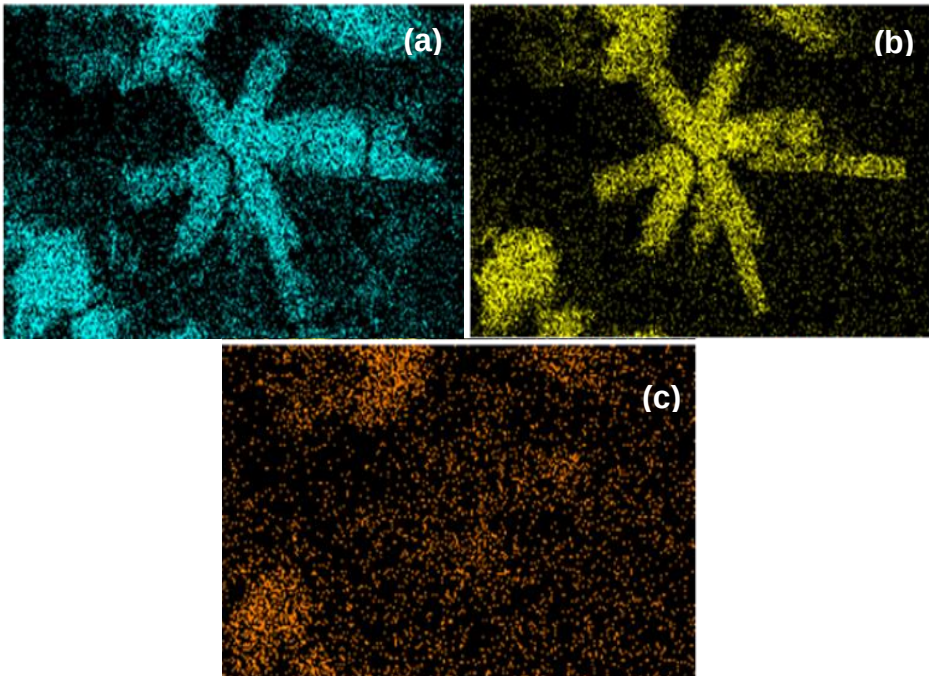

Figure 3.4-9 Electron-dispersive x-ray images displaying elemental mapping of zirconium citratomolybdate at 336 hrs. Images taken for several elements: (a) Zr Lα1; (b) Mo Lα1; (c) Cs Lα1.

As expected there are large amounts of Zr and Mo atoms within the sample, most of which are in region of the ZMCA particles. Analysis of the location of Cs atoms, with support from the SEM and EDX pattern, the debris around the ZMCA is that of the unconverted CPM. Therefore it can be established that in the final product of the ZMCA particles the yield is relatively low, which justifies the hypothesis.

From this finding, it is of great interest to optimise the synthesis to increase the yield of ZMCA. This has been carried out by controlling a number of factors of the reaction. It is acknowledged that by controlling certain parameters, you can tailor the synthesis to produce particles of the same shape, narrow size distribution and an unaggregated system (Rahman and Padavettan, 2012).

The initial approaches involved the understanding of the chemistry within the system. The final approach looked at controlling the feed rate of the reagents and induction time of the additive.

3.4.1.4 Synthesis of ZMCA – Method 2

An intermediate step (formation of citratomolybdate complex) in the ZMCA synthesis is expressed in equation 3.4-5.

$$Cs_3PMo_{12}O_{40} \cdot 14H_2O + 3HNO_3 \xrightarrow[90^oC]{} 6{Mo_2O_5}^{2+} + H_3PO_4 + 6H_2O \xrightarrow[Zr^+]{} 2\left[{MoO_4}^{2+}\right] + 2H_3cit^- \rightarrow [(MoO_2)_2O(cit)_2]^{6-} + 3H_2O \quad \textbf{3.4-5}$$

As mentioned previously it is the liberation of the molybdenum ions which drive the formation of ZM. From the above equation, it is the interaction between the molybdenum ions and the citric acid which drive the change in morphology to form ZMCA.

Citric acid forms a complex with the molybdenum ion known as citratomolybdate (Alcock et al., 1990, Cruywagen et al., 1995, Samotus et al., 1991, Zhou et al., 1997). It is this complex which then adsorbs onto a surface of the ZM particle, which then inhibits the growth on that particular surface, where the other surfaces continue to grow, which in turn results on the elongated, cuboidal shape. The bent angle of the Mo-O-Mo at 137^{o} (Zhou et al., 1997) and the steric hindrance of the citric acid groups only allow the citratomolybdate complex to bind to specific ZM faces. It is assumed the behaviour is due to the cis-arrangement of the two citric acid ligands, this prevents any binding to the concave side of the central Mo-O-Mo bond.

According to the results from the SEM images and EDX, they are in accordance to the assumption that there is a significant amount CPM excess in the final product. This has led to the optimisation of the ZMCA synthesis. There are two main objectives for the synthesis optimisation, this involves creating a batch of uniform cuboidal shaped particles and a high yield. The optimised method involved a change in the following parameters

- Flow-rate of the additive
- Initial time of additive incorporation
- Washing of final batch

Taking the above into consideration and the chemical influence of the additive, this research has explored the options of synthesis optimisation. Method 2 included, an increase of additive flow rate to 3.34 mL/min from 1.67 mL/min, altering the additive induction time to t=30 mins from t=0 and addition of an AC washing step for CPM dissolution. Implementing method 2, Figure 3.3-4, produced uniform batches of elongated, cuboidal ZMCA particles. The appearance of the particle is presented by the SEM images in figure 3.4-10.

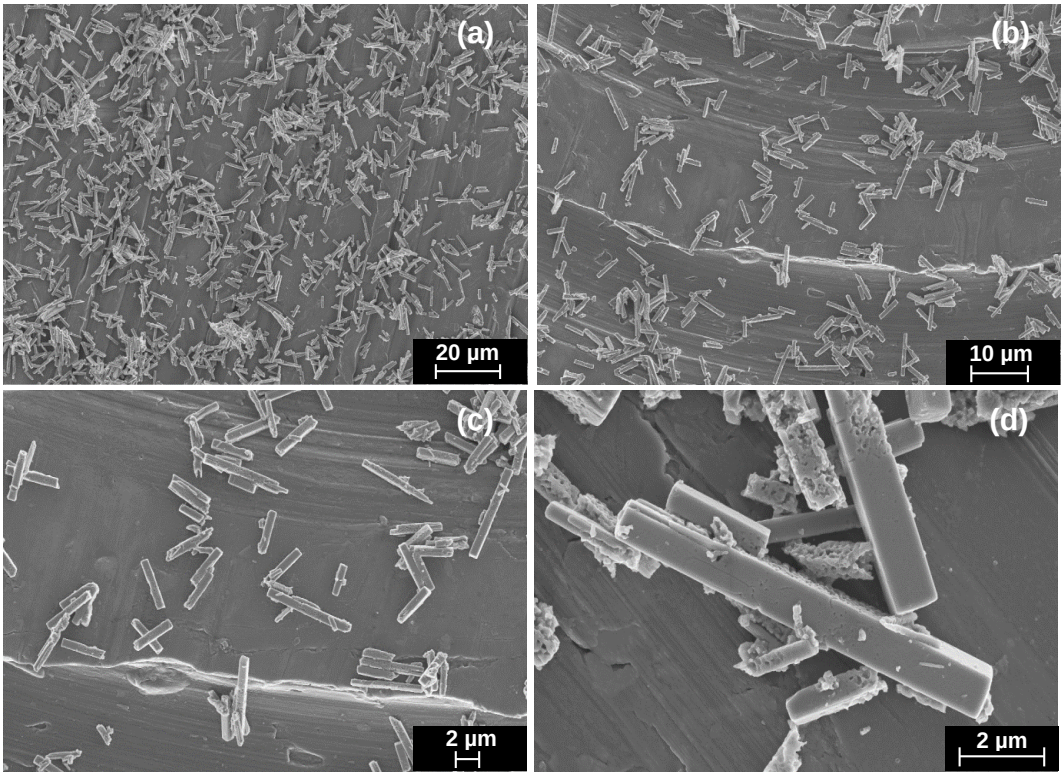

Figure 3.4-10 Scanning electron microscope images of synthesised zirconium citratomolybdate particles. Images are taken at different magnifications: (a) 1.90 K; (b) 3.16 K; (c) 6.74 K; (d) 25.05 K.

The SEM images in Figure 3.4-10 indicate a uniform batch of cuboidal ZMCA has been produced with no surrounding unconverted CPM. A variation in magnification intensity enables an overview of the batch and an enlarged image of an individual particle. This is allows identification of any areas within the sample where debris could be present. From Figure 3.4-10, it is evident there is no unconverted CPM present in the final batch. The application of the optimised method proved to be successful.

A change of the additive feed, from 1.67 mL/min to 3.34 mL/min was implemented. The increased feed rate results in the accumulation of the growth units, citrate ions, above the critical supersaturation concentration. Above this point growth of the crystal can occur. By increasing the feed rate, it enhances the interaction of the growth units. In this case the molybdenum and citrate ions. The initial method had a shorter nucleation period because the additive was insufficiently supplied. This kept the solute concentration below the critical superaturation concentration, where crystal growth was limited.

The initial time of addition of the additive was changed from adding with the zirconyl nitrate ($t = 0\,\mathrm{min}$) to adding the additive at $t = 30\,min$. The initial time period enables the interaction of the two growth units, $[Mo_2O_5]^{2+}$ and [Zr]

$^{+}$, to form ZM particles. The delay of citric acid incorporation, enables the interaction of citraite ions and $[Mo_2O_5]^{2+}$ to form the citratomolybdate complex which acts as an inhibitor on selective ZM surfaces.

The aim of increasing the feed rate and time delay of the additive is to increase the rate of reaction of the ZMCA particles with a high yield. Previous batches of ZMCA with the initial method produced poor yield ranging from 20% to 40% (the main difference for these are dependant the total reaction time). However, implementing the new method enabled the production of 70% for a reaction time of 5 days. Due to equipment failure, the reaction did not have the full two weeks of conversion, however, from the results obtained it is most certain 90-100% could have been achieved for the new method.

The washing regime was prepared by separating the precipitated solids from the supernatant, via filtration, and dispersed in 2M AC. The solids were washed with 2M ammonium carbonate, at a 2:1 ratio of AC washing agent to ZMCA solids. This was left until the CPM was fully dissolved (identified by the disappearance of the yellow colour), this procedure requires 10 mins. The ZMCA particles and the AC washing agent dispersion underwent a centrifugal separation, where the dispersion was subjected to a centrifugal field of 3500 rpm for 10 mins. The supernatant was removed as waste and the solids were re-dispersed in 2M nitric for neutralisation, for 30 mins. Centrifugal separation under the same conditions was implemented, at identical conditions, for phase separation of ZMCA particles and nitric acid. The supernatant was removed the ZMCA particles were placed in the oven for drying at 55^{o}C. During trials of washing on a small scale, SEM images were taken prior to the washing and after to determine the concentration of AC required and the time of the washing.

The washing method required the understanding of the dissolution of CPM under varying conditions. Ammonium carbamate (AC) has been chosen in this synthesis, based on research conducted by (Jiang et al., 2005). This washing reagent is known to dissolve CPM by hydrolysis of the Keggin phosphomolybdate anion (within the CPM structure), to produce $[MoO_4]^{2-}$ and $[PO_4]^{3-}$ ions. The overall reaction proposed is expressed in equation 3.4-6

$$[PMo_{12}O_{40}]^{3-} + 12H_2O \rightarrow PO_4^{3-} + 12[MoO_4]^{2-} + 24H^{+} \qquad \text{3.4-6}$$

The initial breakdown of the kegging complex then leads to the production of ammonia and carbon dioxide. This takes place when the carbamate ions interact with hydrogen ions.

$$24H_2NCO_2^- + 24H^+ \rightarrow 24NH_3 + 24CO_2 \quad \text{3.4-7}$$

Carbamate is known to protonate and forms carbamic acid, which instantaneously decomposes into NH_3 and CO_2 gas. Any unconverted CPM within the sample can be dissolved using AC. This is an effective washing reagent as smaller more soluble anions are formed and the liberation of CO_2 is known to drive the dissolution process under non-equilibrium conditions.

Dissolution of ZM also occurs with AC. Jiang et al., have assumed a dissolution model of ZM with AC. This is expressed by equation 3.4-8

$$ZrMo_2O_7(OH)_2(H_2O)_2 \rightarrow Zr^{4+} + 2[MoO_4]^{2-} + 3H_2O \quad \text{3.4-8}$$

The breakdown of ZM into zirconium and molybdate ions is followed by the interaction of carbamate ions with zirconium, to form a zirconium carbamate complex. This is expressed by equation 3.4-9

$$Zr^{4+} + xCO_3^{2-} \rightarrow Zr(CO_3)_x^{4-2x} \quad \text{3.4-9}$$

It is the formation of the complex which drives the dissolution process. The rate of dissolution is slower than CPM. Dissolution is governed by the thermodynamic energies. The energies are controlled by the manor on which the different chemical bond types interact with the solvent. CPM dissolution breaks down into smaller, soluble components and requires the protonation of the carbamate. Whereas ZM dissolution requires more energy for the zirconium carbamate complex formation. Compared to the components of CPM the ZM disintegrates into less soluble ions. Therefore, the dissolution rate of ZM in AC is a slower process than CPM.

The washing procedure is a key step in the optimisation process for delivering a high quality uniform product. The aim for the washing step is to remove any unconverted CPM. From the study conducted by Jiang et al, it is clear that AC also dissolves ZM. This is not desirable, therefore the AC should be mixed for a limited amount of time. An equilibrium time period is crucial to provide enough time for all the CPM to dissolve before the dissolution of ZM is initiated. Figure 3.4-10 (d) illustrates the effect of exceeding the equilibrium time. The elongated ZMCA particle is surrounded by porous material, this can be assumed to be the initial stages of the ZMCA dissolution process.

3.4.2 Particle characterisation

3.4.2.1 Particle shape

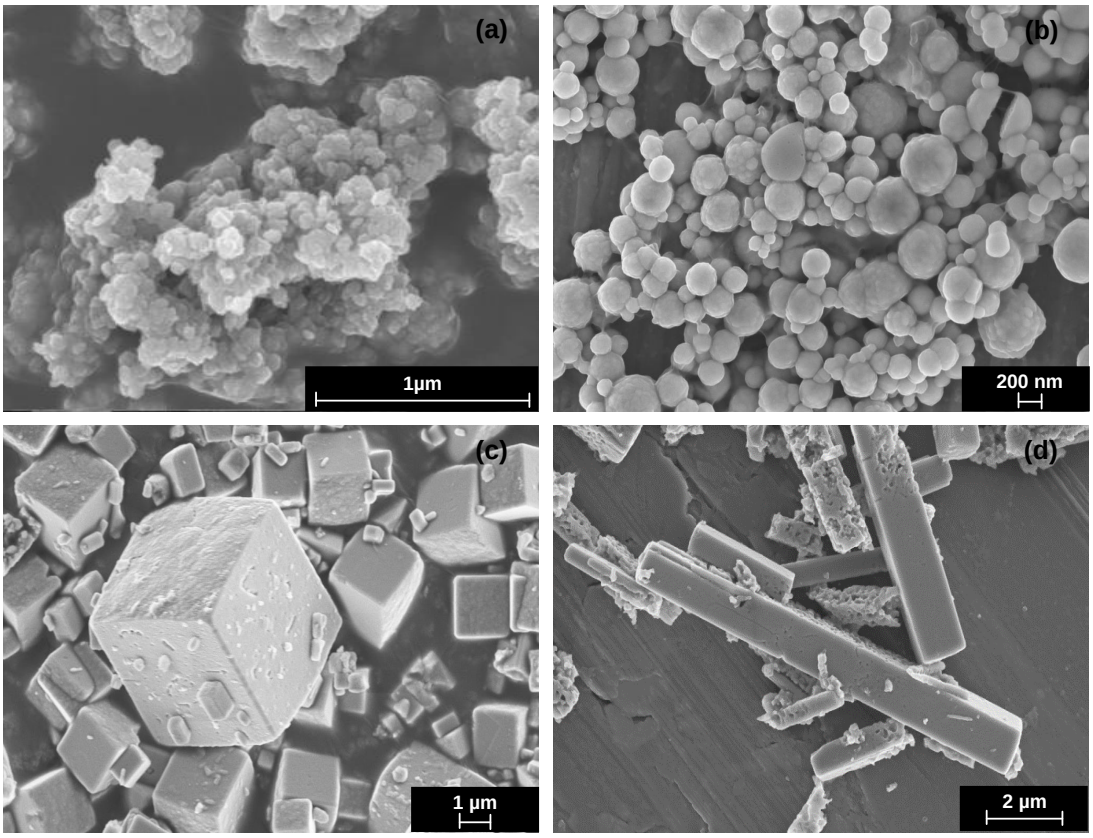

Figure 3.4-11 Scanning electron microscope images of highly active nuclear waste simulants: (a) TiO_2; (b) CPM; (c) ZM; (d) ZMCA.

From figure 3.4-11 (a and b) we see that there are similarities, in terms of both mean size and shape, between the TiO_2 and CPM, with the CPM also consisting of spherical aggregates of smaller primary particles. The images show a size for the agglomerates that is consistent with the Mastersizer® data.

In contrast, SEM images show that the basic particle shape for the ZM samples is cuboidal. Images, Figure 3.4 11 (c and d) of the samples from the normal ZM preparation and morphological manipulated preparation ZMCA. From the images it can be seen that, in general, both ZM and ZMCA crystals are much larger in size than CPM crystals. Individual particle sizes range from 3-4µm for ZM and 2-5 µm for ZMCA.

3.4.2.2 Particle density

The densities of the simulant samples are given in Table 3. The increased density for the ZM and CPM samples when compared to the TiO_2 is

attributed to the incorporation of dense elements such as molybdenum within the simulants and is as expected for these materials.

Table 3 Density values of highly active nuclear waste simulants. Particle density measurements were collected using the Pycnometer.

	TiO_2	CPM	ZM	ZMCA
Density (g/cm^3)	2.85[1]	3.82	3.41	3.41

Comparing the solid properties of the nuclear waste simulants to TiO_2 highlights similarities between TiO_2 and CPM in terms of particle shape; both solids consist of spheroidal aggregate particles that are produced from submicron primary crystallites or particulates. In addition, the mean sizes for these two materials differ only by a factor of 2, although the density analysis (Table 3) highlights that not all particle properties correlate well. In contrast to the general similarities between CPM and TiO_2, the ZM sample has no particle characteristics that correlate with the TiO_2 in terms of particle size, shape or density, and therefore TiO_2 is not an appropriate comparison material for ZM. Additionally, whilst differing in size by a factor of 3, the densities for the CPM and ZM samples are comparable. Information about the effects of particle size may be available therefore through a comparison of these two samples.

3.4.2.3 Particle size

Challenges of particle size analysis occur when considering particulate systems which are non-spherical and polydisperse in size and shape. The mean particle size for a system is dependent on the model which is allocated. This study explores particle size characterisation using a laser diffraction technique and image processing. Particle size distribution using the Mastersizer is illustrated in Figure 3.4-12. The data presented here is an average of 10 repeated measurements, for each particulate system.

[1] The density value obtained for TiO_2 is considerably lower than previously mentioned in literature. The value presented in table 3 is an average value from 3 individual measurements. It is possible to consider the physical powder form of TiO_2, Figure 3.4-11 (a) illustrates aggregated particle. Due to the aggregated nature of TiO_2 powder it is possible to assume that air is trapped between the aggregate pores resulting reduced gas volume. Thus, during the measurement a larger volume is considered, compared to the actual volume of the solid and subsequently leading to a reduced measured density using the volume displacement method.

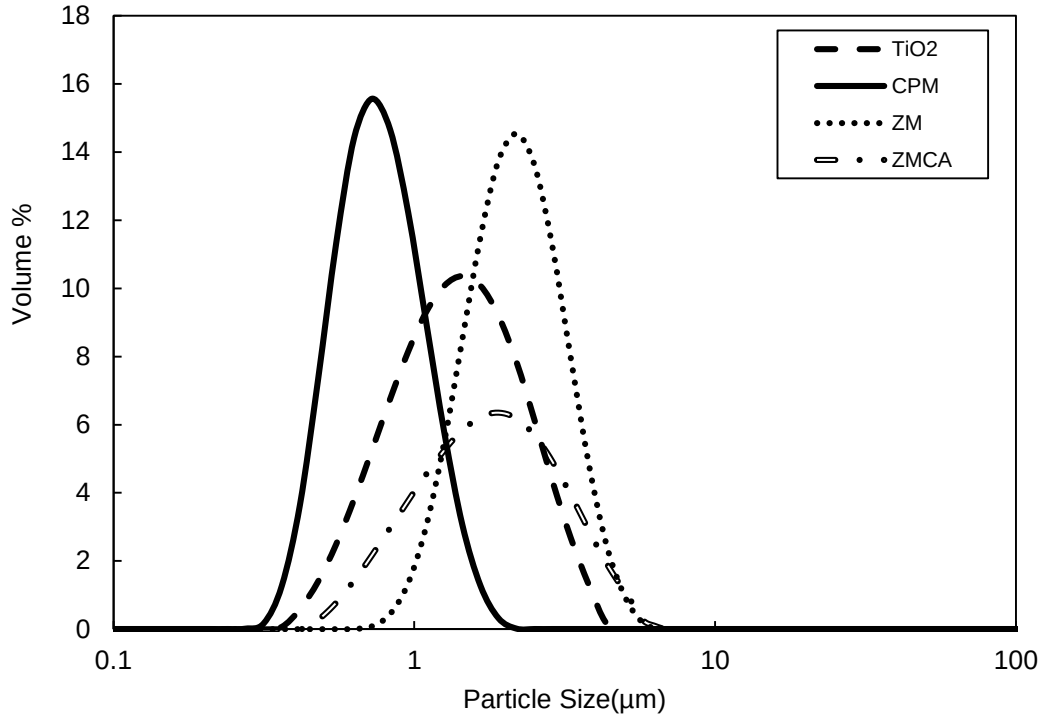

Figure 3.4-12 Particle size distributions for highly active nuclear waste simulants for titanium dioxide (TiO2), zirconium molybdate sol-gel (ZM-sol/gel), caesium phosphomolybdate (CPM), zirconium molybdate (ZM), zirconium citratomolybdate (ZMCA).

Size distribution data in figure 3.4-12 shows clearly that the CPM, TiO_2, ZMCA and ZM exhibit essentially mono-modal size distributions with, respectively, increasing peak mean values of size. Key size data for each sample is provided in Table 4 below.

Table 4 Percentile distribution data of particle size analysis.

	CPM	**TiO2**	**ZM**	**ZMCA**
d (0.1)	0.46	0.63	1.43	0.82
d (0.5)	0.90	1.33	2.31	3.11
d (0.9)	1.10	2.70	3.69	4.63

These data further highlight the relatively narrow distributions for the CPM, TiO_2 and ZM samples. SEM images provide supporting information on particle size as well as allowing an analysis of shape. A close examination of Figure 3.4-11 (a) suggests that the micron-sized TiO_2 particles measured by light scattering consist of fused submicron primary particles. The size of the aggregates seen here is just larger than 1 µm, this complements the particle size data obtained from the Mastersizer®. The apparent shape of the primary particles from the image suggests that they are almost plate-like, with an approximately spheroidal shape for the aggregates.

3.4.2.3.1 Particle size distribution of non-spherical particles

The laser diffraction technique assumes that the particles are perfect spheres and therefore the particle size is reported as volume equivalent sphere diameter. As mentioned in section 3.3.3 there are a number of models which can be applied to obtain a representative particle size distribution.

Image J is a Java-based microscope image processing programme. This software is able to edit, analyse and process SEM images. The particle size can be provided based on the Feret's diameter. This is a measure of size where it considers the distance between two parallel planes in a specified direction. Processing of the initial image requires calibration of the scale bar for conversion from pixels to microns. Particle analysis requires the location of an optimum threshold. The threshold determines the quality of the results. Once the threshold is defined a monochromatic image is produced, the particle size distribution obtained is based on this image. If we consider the analysis Figure 3.4-3 (b), the monochromatic image is illustrated by Figure 3.4-13

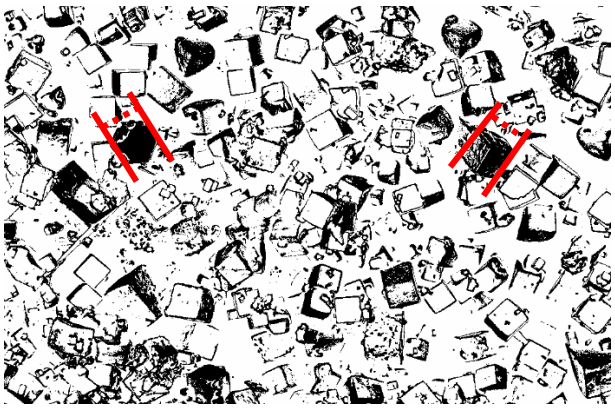

Figure 3.4-13 Image J analysis of cubic ZM particles. The optimum threshold was chosen to produce this monochromatic image. The solid red lines indicate the parallel planes, the dotted red lines indicate the representative diagonal diameter.

The particle size distribution data generated using Figure 3.4-13 did not produce a representative peak mean particle size. As the analysis is based on the Feret's diameter parallel planes are illustrated in Figure 3.4-13. The planes can range from a particular surface of a particle or taken as a diagonal.

An alternative option is to manually obtain the particles parameters. Particle dimensions of interest included the length, width and depth for ZM particles and the maximum length of ZMCA particles. These dimensions were taken for 100 individual particles, as shown in Figure 3.4-14

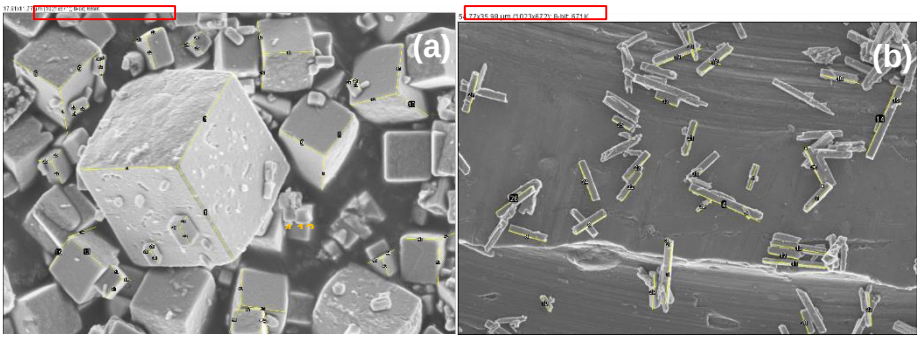

Figure 3.4-14 SEM images of (a) ZM and (b) ZMCA undergoing particle dimension analysis using Image J. Indicated in the red box at top left corner of both images is the calibrated scale bar (a) 17.91 x 11.77 µm and (b) 54.77 x 35.98 µm.

ZM particles have a well-defined three-dimensional structure as illustrated in the SEM images. Obtaining particle edge length in all directions (x, y, z) is therefore feasible. The dimensions were applied to obtain the volume equivalent sphere diameter (D_{volume}), expressed by equation 3.4-10, and the maximum equivalent length of ZM particles.

$$D_{volume} = \left[\frac{6}{\pi} V_{particle}\right]^{1/3} \qquad 3.4\text{-}10$$

This equation expresses the diameter of a sphere with the same volume ($V_{particle}$) as a non-spherical particle. Consider Figure 3.4-14 (a), where the volume of the ZM particle is 65.43 µm^3, this equates to an equivalent sphere diameter of 4.91 µm.

SEM images of ZMCA particles represent the difficulties of obtaining particle parameters in all directions. The visualisation of ZMCA particles in the z-direction is an issue and therefore the volume equivalent sphere diameter could not be applied for this system. Figure 3.4-14 (b) illustrates the measurement of the dominant-particle axis. Thus, the equivalent sphere diameter is referred to the dominant particle length of a non-spherical particle.

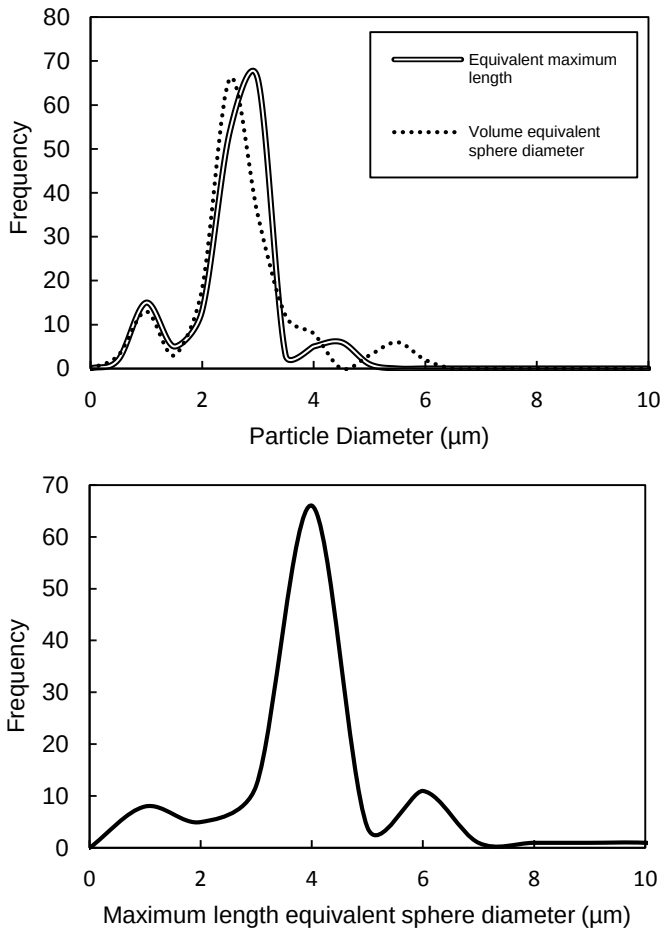

Figure 3.4-15 Particle size distribution of (a) ZM and (b) ZMCA. The data is extracted using Image J processing programme. Number of particles analysed for both systems are 100.

Size distribution data in Figure 3.4-15 shows clearly that the ZM and ZMCA exhibit a multi-modal size distributions. Similar peak mean values of size, with respectively, 3-4 µm. Both particulate systems have a major peak at a much larger size with an extended tail of submicron material, in the range of 0.12-1 µm, and larger material between 5-6 µm for ZM and ZMCA, respectively. This is indicative of a size polydisperse particulate.

In contrast to the laser diffraction technique, the difference in peak mean values for ZM systems are not significant. However, the technique has neglected the submicron particles for both systems. This could be an effect of the finer particles being over shadowed by the larger particles. An alternative explanation is, as illustrated in Figure 3.4-14 (a) the finer particles are located on the surfaces of the larger particle and therefore they are not considered as individual particles. As the Mastersizer is a volume based technique, it is unlikely for the finer particles to be recognised.

Due to the elongated nature of ZMCA particles, it is difficult to represent the particle size as an equivalent volume sphere diameter. Therefore it is

evident from the microscope image analysis that SEM images not only allow particle shape analysis but also allow quantitative analysis to obtain representative particle size distribution for non-spherical particles.

Additionally, Image J analysis carried out on SEM images (see Figure 3.4-10) enabled the calculation of the aspect ratio of ZMCA particles to be ~6.

3.4.2.4 Particle stability

Zeta potential measurements as a function of pH are illustrated in figure 3.4-16. The data is averaged over three repeated measurements for both TiO_2 and ZM systems.

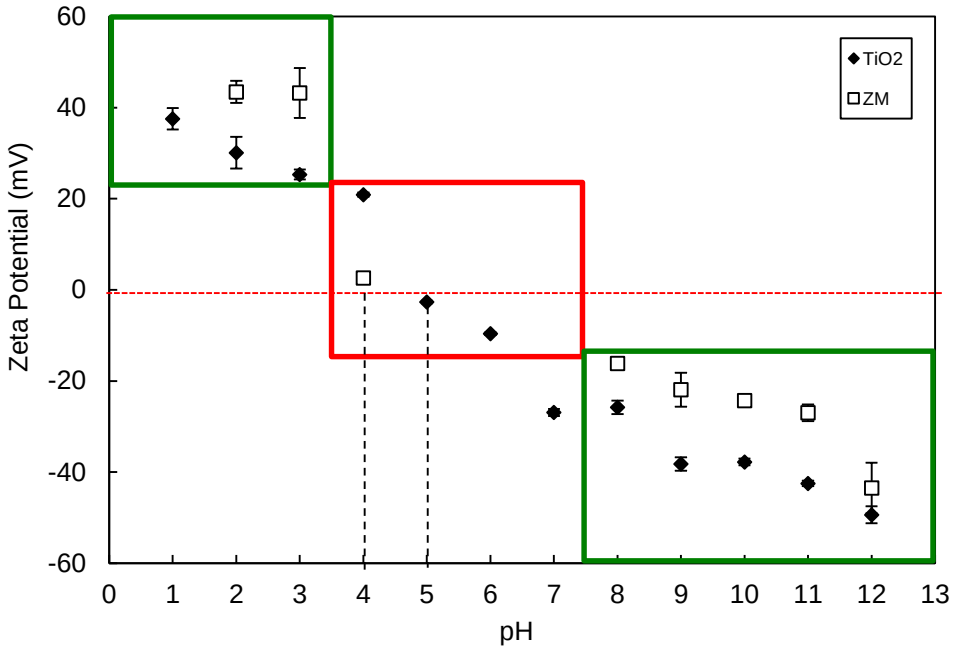

Figure 3.4-16 Zeta potential as a function of pH. The data represents nuclear waste simulant zirconium molybdate (ZM) and titanium dioxide (TiO_2). The zeta potential data was collected using the ZetaSizer.

Across the pH domain both TiO_2 and ZM systems follow an s-shaped curve. This is general for many metal oxide materials (Franks, 2008, Leong and Ong, 2003). There are three key regions from a typical zeta potential curve, indicated by the red and green boxes in Figure 3.4-16.

Particles with large positive/negative zeta potential values create a system where the particles repel each other due to long range repulsive forces, generated from the electrical double layer. This therefore creates a stable dispersion, indicated by the green boxes. As the zeta potential decreases, the particulate system is now dominated by short range attractive forces from the van der Waals forces. This results in the particles to come into contact with each and aggregate, leading to an unstable dispersion, this is

identified by the red box. The point of zero charge (pH_{pzc}) for TiO_2 according to Figure 3.4-16 is around pH 5, this is supported by (Parks, 1965). The pH_{pzc} for ZM particles is around pH 4.

The particle surface of a metal oxide is covered by –OH ions in aqueous media, Yang et al., 2000, expressed the relationship of ionic behaviour as a function of pH by Equation 3.4-11

$$-OH_2^+ \overset{+H^+}{\longleftrightarrow} -OH \overset{+H^+}{\longleftrightarrow} -O^- \qquad 3.4\text{-}11$$

Where the surface charge is a function of the potential determining H^+ and OH^- ions. If the concentration of H^+ ions is raised below the pH_{pzc}, the surface charge or TiO_2 increases due to the protonation of the surface hydroxyl group. This data is also supported by research conducted on zirconia (Briscoe et al., (1998); Khan et al., (2011); Leong and Boger (1991)), titania (Yang et al., 2000; Mikulasek et al., 1997; Leong and Boger, 1991) and alumina (Leong and Boger, 1991) dispersions where the electrostatic repulsions between particles is due to the build-up of the EDL, from ion adsorption on the particle from the background electrolyte.

The natural pH for TiO_2 and highly active nuclear simulants was measured. A pH probe was inserted into a dispersion of 0.1 wt% and a pH value was recorded. Table 5 shows the pH of particles dispersed in DI water.

Table 5 Natural pH of TiO_2 and highly active nuclear waste simulants. Particles are dispersed in DI water.

Simulant	pH
TiO_2	5.35
ZM	2.36
CPM	1.42

The key difference between the nuclear waste simulants and TiO_2 is that ZM and CPM both naturally buffer at a pH of 1, in the stable region. In the case of TiO_2 it naturally buffers at a pH of 5, this is in the range of its pH_{pzc}. In this region the particles are uncharged and unstable causing the particles to aggregate and create an unstable dispersion.

3.4.2.5 Crystalline structure of nuclear waste simulants

Interaction of x-rays with CPM, ZM and ZMCA powder produced a diffraction pattern. Essentially, the fingerprint of each system has been determined through the PXRD technique. The crystal structure of CPM is presented in figure 3.4-17. CPM is identified to crystallise in a cubic lattice with a space

group of *Pn3m*. The lattice parameters were also determined, the unit cell lengths $a = b = c = 11.79^o$ and the angles between them $\alpha = \beta = \gamma = 90^o$. The space group will be described in detail in Chapter 4, Section 4.6.1.

The crystallographic structure of CPM is not publically available in the open literature, therefore indexing of the peaks were required. Using the lattice parameters, the wavelength of the radiation source and the calculation of d_{hkl}, a manual iterative method was used to estimate the 2θ position. The miller indices (*hkl*) were assigned corresponding to the *2θ* position obtained from the XRD pattern.

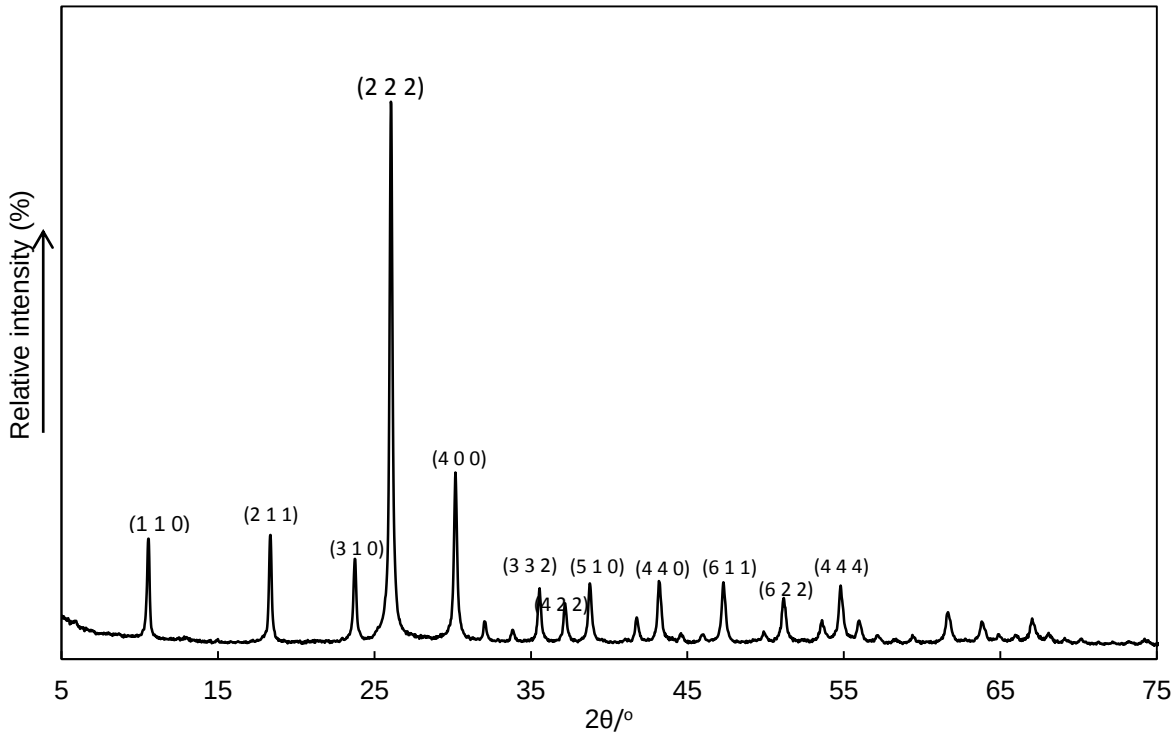

Figure 3.4-17 **X-ray diffraction pattern for caesium phosphomolybdate (CPM)**

An example of this would be to explore a number of *hkl* values i.e. (100), (110), (111), (200) etc. Initial stages involve calculating the interplanar d-spacing, with respect to the crystal system. This is followed by applying the Bragg's law to determine the *2θ* position. For $hkl = (110)$,

$$\frac{1}{d_{110}^2} = \frac{1^2+1^2+0^2}{11.796^2} \rightarrow d_{110} = 8.34\dot{A} \qquad 3.4\text{-}12$$

$$\sin\theta_{110} = \frac{1.54}{2(8.34)} \rightarrow 2\theta = 10.59^o \qquad 3.4\text{-}13$$

The calculation corresponds to the first main peak of the CPM structure. From figure 3.4-17 it can be suggested that the main peaks are visible 10.59^o (110), 18.40^o (211), 23.83^o (310), 26.14^o (222) and 30.27^o (400).

ZM and ZMCA are identified to crystallise as a body-centred tetragonal lattice with a space group of *I4₁cd*. The lattice parameters also determined as $\alpha = \beta = \gamma = 90^o$ and $a = b = 11.45\,\dot{A}$ and $c = 12.49\,\dot{A}$. Figure 3.4-18 illustrates a typical XRD pattern for the ZM and ZMCA particles synthesised and to that of Clearfield and Blessing (Clearfield and Blessing, 1972).

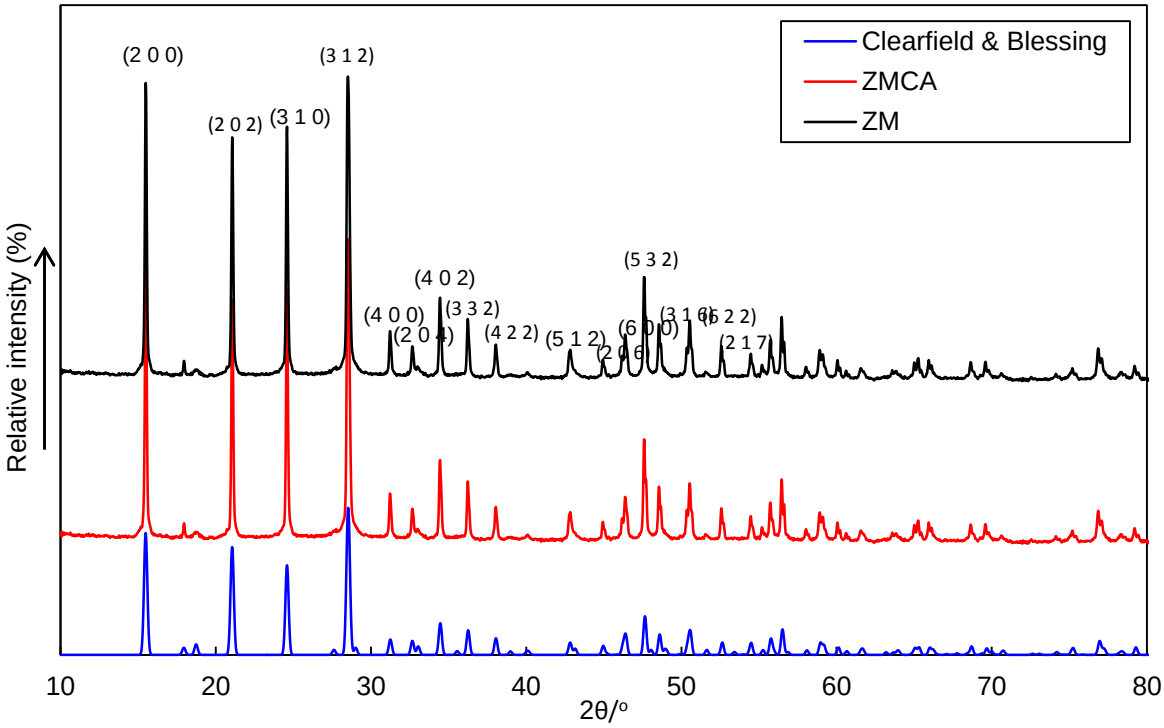

Figure 3.4-18 X-ray diffraction pattern for zirconium molybdate (ZM), zirconium citratomolybdate (ZMCA) and a comparison to zirconium molybdate particles synthesised by Clearfield and Blessing.

From Figure 3.4-18 it can be suggested that the main peaks visible are 15.45° (200), 21.03° (202), 24.56° (310) and 28.46° (312), where the peaks of synthesised ZM are identical to Clearfield and Blessing. The peak indices correlate well with (Fourdrin et al., 2012). In contrast, the peaks are at a slight shift compared to the XRD pattern in this study. The reason for this shift is due to the difference in radiation source. Fourdrin et al employed Co-Kα radiation source, where $\lambda = 1.79\dot{A}$.

The miller indices for each peak was assigned by applying the same method for CPM. The crystallographic parameters obtained from the diffraction pattern which are applicable for ZM crystals have been applied for the indexing. For $hkl = (200)$,

$$\frac{1}{d_{200}^2} = \left[\frac{2^2+0^2}{11.45^2} + \frac{0^2}{12.49^2}\right] \rightarrow d_{200} = 5.725\dot{A} \qquad 3.4\text{-}14$$

$$\sin\theta_{200} = \frac{1.54}{2(5.725)} \rightarrow 2\theta = 15.45^{o} \quad \text{3.4-15}$$

An interesting observation is that the XRD pattern for both ZM and ZMCA are identical. The incorporation of the citric acid additive has no direct effect on the crystal structure. The citratomolybdate complex attaches onto the specific surface and alters the rate of growth of that surface. It does not however change the atomic structure of a particular plane contained within the crystal. Therefore, it is expected that the XRD patterns are identical.

Comparing the diffraction patterns of CPM and ZM, the size of the crystalline material, relative to each other, may be indicated. Large crystallites tend to give rise to narrow sharp peaks. Considering the SEM images and PSD data, the CPM particles has a size peak mean value of ~0.9 µm. Compared to ZM and ZMCA particles, where the size peak mean value is between 3-4 µm. The XRD peaks of CPM and ZM suggest the peak width increases with decreasing particle size. However, it is important to consider that the peak width also increases as a result of variations in d-spacing caused by microstrain.

The number observed peaks is related to the symmetry of crystal, and in the case of ZM there are a large number peaks, indicating low symmetry (8 symmetry operators). The intensities of the peaks relate to the type of atoms present on the planes. The scattering intensities for the x-rays are directly related to the number of electrons in the atom. It is known that that the lighter atoms scatter weak x-rays, whereas, heavy atoms scatter x-rays more effectively. Atoms differ in size, this directly correlates to the difference in interplanar spacing. Thus, in the case of ZM the (2 0 0) plane may contain of Zr and Mo atoms and CPM structures the (2 2 2) plane may contain Cs atoms.

3.5 Conclusions

This chapter highlights key components related to the synthesis, morphology modification and particle characterisation of highly active nuclear waste simulants. The reaction precipitation method enabled the production of CPM, ZM and ZMCA particles on a larger scale.

- Addition of organic additive. Manipulation of particle morphology by addition of citric acid, produces a chemical structure identical to that of ZM particles. The key difference is the transformation of the aspect ratio, from ~1 for ZM particle to ~6 for ZMCA particles.
- Development of cuboidal ZMCA particles. Implementing particle characterisation techniques such as SEM and EDX, during synthesis

and post-synthesis, confirmed the presence of unconverted CPM at the end of the Method 1 synthesis route.

- Application of relevant particle characterisation techniques. Particles properties of nuclear waste simulants such as size, shape density and stability were determined. SEM and Image J analysis determined the particle size of non-spherical particles, averaging over 100 particles for both cubic ZM and cuboidal ZMCA systems.
- Stabilisation. Zeta potential measurements as a function of pH illustrated nuclear waste simulants to be stable at their natural pH of 1, in contrast to unstable TiO_2 dispersions at the natural pH of 5.5 where the dispersion is at pH_{pzc}.

Ultimately, a chemical mechanism has been proposed for the initial production of spherical CPM to cubic ZM and the final step to produce cuboidal ZMCA particles. It is the liberation of the oxomolybdate complex, $[MoO_5]^{2+}$, which determines the overall yield of the final product. Synthesis carried out on a larger scale, 4L, enabled the production of larges volumes for extensive characterisation including particle properties and physical behaviour (i.e. sedimentation and rheology).

This chapter provides the foundation particle and dispersion characterisation. Understanding the influences of the solid-liquid properties on sedimentation and rheology, are key parameters which can be directly utilised for improvements in the nuclear waste treatment engineering process.

4 Morphological prediction of zirconium molybdate

Summary

This chapter considers morphological modelling of zirconium molybdate. Initial calculations of morphology predictions include the anhydrous α & β phases. Preliminary calculations of the hydrated phase and the influence of citratomolybdate complex on growth faces will be discussed.

4.1 Introduction

Molecular modelling techniques allow many industries to understand, in some detail, the solid-state chemistry of particulate materials. A number of theoretical models can be applied to calculate the energy of the systems, intra and intermolecular interactions, predict properties such as density, viscosity and crystal morphology.

HAL solid properties could significantly impact the heat inventory and enhance corrosion if the solids are not maintained in suspension. ZM particles, as seen previously in Chapter 2, crystallise in a cubic morphology. It can be assumed that the particles of a cubic nature are difficult to re-suspend once a settled bed is formed due to the highly dense and packed nature of the particles upon sedimentation (see Chapter 5). This has implications on post-operational clean out strategies and immobilisation of the solids.

In this chapter an atomistic chemical model is defined to enable the prediction of ZM morphology. Molecular modelling techniques allow the understanding of structural formation, surface chemistry and how chemical contaminants have the potential to change crystal morphology. It is however, very complex to model the transmutation of ZM to ZMCA and is beyond the scope of this research programme.

Application of the surface energy calculation method is able to simulate the crystal morphology of ZM. For the purpose of this atomistic model it is assumed that ZM particles are inactive. Zirconium ions (^{95}Zr) are short-lived radionuclide, with a half-life of 63 days, therefore when the HASTs are due to be emptied the Zr radionuclides will have achieved full decomposition.

4.2 Underlying science of crystallography

4.2.1 Crystal lattice in two dimensions

Crystals are composed of ions, atoms or molecules which are repeated at regular intervals (motif) and have the same orientation in three dimensions (Megaw, 1973). The repeating point groups define sets of symmetry operations that leave points, known as lattice points, which are invariant. Symmetry operation considered for 2D lattices include rotational symmetry. Thus highlighting five types of two-dimensional planar lattice types; (i) Primitive oblique; (ii) primitive rectangular; (iii) centred rectangular; (iv) primitive square; (v) Primitive hexagonal.

4.2.2 Crystal lattice in three dimensions

The concept of the two-dimensional can be extended to three-dimensions. It is common to represent a lattice by selecting a portion known as a *unit cell*. A lattice is composed of repeating units of a unit cell, therefore representing a portion of a lattice by a unit cell is convenient, illustrated in Figure 4.2-1

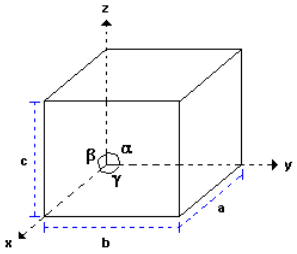

Figure 4.2-1 **Structure of a unit cell.**

Lattice parameters define the overall crystal structure. The direction of the translation vectors of the lattice is defined by the axes, *x, y* and *z*, these are related to the unit cell edge lengths, *a, b* and *c* respectively. Inter axial angles are represented as α, β and γ, these angles are between the cell edge lengths of the unit cell (Wheatley, 1981).

A set of translations which composes a lattice demonstrates how the repetition occurs within the crystal. An assumption that the position of each point is defined by the ends of vectors *(r)*, equation 4.2-1

$$r = ua + vb + wc \qquad 4.2\text{-}1$$

Where *a, b* and *c* are known to be the primitive translation of the lattice (unit vectors describing the lattice parameters) and *u, v* and *w* are integers. A *translation vector* connects the lattice points; for instance in some structures where the pattern is defined, it corresponds to a displacement which leaves the pattern and its surroundings unchanged. It is known as an operator which generates new lattices points where it is at the same distance and in the same direction as the previous ones (Megaw, 1973).

During packing of the unit cells the space must be filled, there are seven different shapes of unit cell, they require the minimum amount of symmetry and are presented in Table 6 (Wheatley, 1981, Megaw, 1973, Bragg and Bragg, 1957).

Table 6 Seven crystal systems and their corresponding axial cell lengths and angles

Crystal system	Axial Angles	Axial Angles
Cubic	$a = b = c$	$\alpha = \beta = \gamma = 90^o$
Tetragonal	$a = b \neq c$	$\alpha = \beta = \gamma = 90^o$
Orthorhombic	$a \neq b \neq c$	$\alpha = \beta = \gamma = 90^o$
Trigonal	$a = b = c$	$\alpha = \beta = \gamma \neq 90^o$
Hexagonal	$a = b \neq c$	$\alpha = \beta = 90^o, \gamma = 120^o$
Monoclinic	$a \neq b \neq c$	$\alpha = \gamma = 90^o \neq \beta$
Triclinic	$a \neq b \neq c$	$\alpha \neq \beta \neq \gamma \neq 90^o$

The seven crystal systems, Table 6, can be combined with *four* different types of unit cell. The four units cells are distinguished with respect to the positioning of the lattice points. They are known as the primitive unit cell, the body-centred unit cell, the face-centred unit cell and the side-centred unit cell.

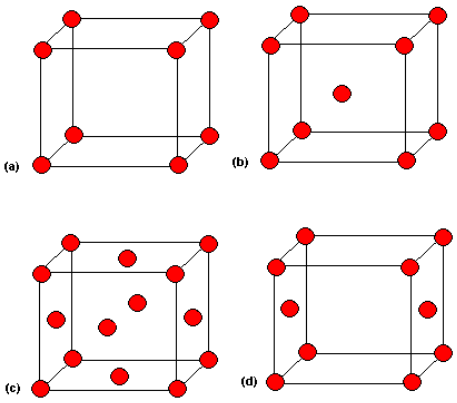

Figure 4.2-2 Four different types of unit cell; (a) primitive, (b) body-centred, (c) face-centred, and (c) side-centred

The primitive cell, Figure 4.2-2 (a) has a lattice point on each corner and is denoted by the symbol *P*. The body-centred cell, Figure 4.2-2 (b), has a lattice point on each corner and one in the centre of the cell and is denoted by the symbol *I.* The face-centred cell, Figure 4.2-2 (c), as a lattice point on each corner and on each face of the cell and is denoted by the symbol *F*. The side-centred cell, Figure 4.2-2 (d) has a lattice point on each corner and two on the opposite of the cell, corresponding to the plane. An A-centred cell will have a lattice point on the *bc* faces. This is denoted by the symbol *A, B* or *C*. When the 7 crystal systems are combined with the four types of lattice, 14 Bravais lattices are formed. In some cases it is not possible to combine some of the lattice cells with the different shapes; this is due to their symmetry.

4.2.3 Symmetry operators

The importance of space groups for crystallography is to determine the structure of the crystal. For instance a structure is built form more than one set of symmetry related atoms, the prototype of each atom should be know; from this an *asymmetric unit* can be established. Therefore in order to build a structure the asymmetric can be originated and allow the space group to operate on it.

4.2.3.1 Point Groups and Space Groups

A three dimensional periodic structure can have any of the ***point-group operators:***

- Inversion symmetry (i). The coordinates of a point (x, y, z) are transformed to the point $(\bar{x}, \bar{y}, \bar{z})$.
- Mirror symmetry (m). The coordinates of a point are reflected through a plane.
- Identity operator (I). The coordinates of a point are unchanged.

Three dimensional periodic structures which contain symmetry such as rotation, inversion and mirror give 32 *point groups*, when translational symmetry is used in conjunction with the point groups, 230 *space groups* are produced (Hall et al., 2005, Bragg and Bragg, 1957).

A combination of a rotational symmetry and translation, a screw axis is formed. An example of a screw axis can be denoted by 2_1, which gives a rotation of ($360^o/2=180^o$) followed by a translation of half the lattice repeat distance, along the direction of the rotation axis. A screw axis thus halves the morphological importance. Consider 2_1 along the b-axis of a cubic lattice, the important faces considered will be {0 2 0} and {0 4 0} and the {0 1 0} and {0 3 0} faces will be neglected.

A mirror symmetry combined with a translation results in a glide plane, denoted by 2/c. This indicates a reflection in a mirror plane perpendicular to a two-fold rotation axis, followed by half the lattice distance along the c-axis.

All the symmetry operators are combined within a crystal it is known as the space group; it is the collection of operations which is attained by situating the translations of the space group elements to zero which is known as the point group. When all these different types of operators are combined there is a total of 230, these are known as the ***space groups*****.** In other words when all the symmetry operators are combined within a crystal it is known as

the space group; it is the collection of operations which is attained by situating the translations of the space group elements to zero which is known as the point group (Hall et al., 2005).

4.2.3.2 Space group Representation

A space group can be represented in two ways; (a) a collection of symmetry elements with its location in the unit cell or (b) a collection of points arranged so that it poses these symmetries.

- The first letter corresponds to the lattice symbol, this is the *Bravais lattice* type (P, F, I, A, B or C)
- The remaining part has relation to the point-group symbol; describes the symmetry of the atoms in the crystal

4.2.3.3 Point group Representation

It is known that the point groups are what controls the external morphology of a crystal. There are 32 crystallographic point groups which are consistent with translational symmetry (where a translation does not change the crystal). There are two systems of symbols which are at present being used; they are known to be presented by Schönfiles and Hermann-Mauguin (Nowacki, 1972). The Hermann-Mauguin notation has been considered and used by the *International Union of Crystallography*; whereas Schönfiles notation is used on group theory.

Table 7 Representation of point groups (Brown and Forsyth, 1973)

Symbol	Meaning
X or $\bar{X}$	Rotation or inverse axis
X2 or $\bar{X}$2	An additional diad exist perpendicular to *X or* $\bar{X}$
Xm or $\bar{X}$m	*m* donates a mirror plane (symmetry plane) on the axis *X or* $\bar{X}$
X/m	Mirror plane perpendicular to the axis *X*
X/mm	A combination of *X/m* and *Xm*
$\bar{X}$m2 or X2m	The symmetry planes contain the axis $\bar{X}$ where the diads are perpendicular to $\bar{X}$

4.3 Molecular modelling techniques and underlying science

Molecular modelling involves mathematical derivations, calculations and predictions (Leach, 2001). Molecular modelling is related to computer simulations, three-dimensional structures are involved so that manipulation of the structures and properties can take place. When utilising a computer programme it is important to take into consideration the atoms involved in the molecule, the positions of the atoms which are known as the coordinates (*x, y, z)*.

It is important to consider the properties of a crystal during molecular modelling. The properties required are essential input parameters for

specific simulations. Information on the crystal structure such as the atomic coordinates, symmetry of the atoms, shape of the crystal and the environment it is contained are all important input parameters. The aim of molecular modelling is to provide information about the behaviour of the crystals such as

- Bond angles, lengths and torsion angles
- Lattice energy, surface energy, molecular energy (these relate to the breakdown of bond energies between the atoms) and activation energy
- Information about the electrons within the orbits, the charge allocated to the atom in different environments
- Morphological predictions

4.3.1 Atomistic force field

The potential energy of ions, atoms, molecules or a solid is a function of independent energy terms. Ultimately, it is dependent on the internal energy of the system. The total potential energy can be divided into two-bodied, three-bodied, four-bodied and non-n bonded terms (Leach, 2001), expressed in Equation 4.3-1

$$E_{Total} = \sum_{n_{bonds}} E_{bonds} + \sum_{n_{angles}} E_{angles} + \sum_{n_{torsions}} E_{torsions} + \sum_{n_{nonbond}} E_{nonbond} \quad \text{4.3-1}$$

The bond energy is a two-body potential which considers the energy between two atoms chemically bonded by a covalent bond. The potential energy associated with bond angle considers the change in bond angle during minimisation. This expression is a three-body potential where the values are dependent on the fractional coordinate of the three independent atoms. The energy required to distort the bond angle from equilibrium is much lower than the energy need to alter a bond angle.

Torsion energy potential takes into account the places containing atoms a, b and c, whereby a magnitude of rotation is required for the second set of planes containing atoms b, c and d become parallel, thus known as the torsion angle, θ_{abcd}. The term also considers m, the type of symmetry in the rotation and A, a parameter related to the Torsion energy and angle.

Non-bonded terms can be expressed commonly by either the Buckingham potential (Buckingham, 1956) (Eq. 4.3-2) or the Lennard-Jones potential (Lennard-Jones and Strachan, 1935) (Eq. 4.3-3), of ionic materials.

$$E_{Buckingham} = A_{ij}\, exp(-B_{ij} r_{ij}) - \frac{C_{ij}}{r_{ij}^6} \quad \text{4.3-2}$$

$$E_{Lenard-jones} = \frac{A_{ij}}{r_{ij}^{12}} - \frac{B_{ij}}{r_{ij}^{6}} \quad 4.3\text{-}3$$

Both non-bonded energy potentials considers the short range van der Waals forces, represented by the second term and the short range electrostatic forces, represented by the first term. Covalently bonded atoms with different electronegativities result in polarisation of the bond, this leads to electrostatic interactions between the atoms. This is expressed by the Columbic term, which is the approximation of the monopoles interacting with other atoms within the same molecule. This is expressed in Equation 4.3-4

$$E_{Colubmbic} = \frac{1}{4\pi\varepsilon_0}\frac{q_i q_j}{r_{ij}} \quad 4.3\text{-}4$$

This term is dependent on the ε_0, permivitity of free space, qi and qj the point charges on atoms i and j and r_{ij} the separation distance between atoms i and j. This term is a representation of short range repulsion attributed by the overlap of the electron clouds. For energy simulations the charge model should be clearly defined, whether it be a formal or partial charge model.

Empirical fitting of potential energy can be carried out using experimental data and using the terms defined. The energy is a function of fractional coordinates on atoms, bond lengths and angles, point charge, atomic mass and radial separation distance between atoms.

4.3.2 Lattice energy calculation

Lattice energy calculation, expressed by 4.3-5, requires the fractional coordinates of all the atoms in the asymmetric unit. The symmetry operator, which is a function of the space and point group, is applied to the coordinates to generate the fractional coordinates of all the atoms in the unit cell. Once the fractional coordinates have been established the bond distances between the atomic pairs can be determined. The final requirement is the assignment of the relevant interatomic potentials and the point charges, Equation 4.3-6.

$$E_{cr} = \frac{1}{2}\sum_{k=1}^{N}\sum_{i=1}^{n}\sum_{j=1}^{n'} V_{kij} \quad 4.3\text{-}5$$

$$V_{ij} = -\frac{A_{ij}}{r_{ij}^{6}} + \frac{B_{ij}}{r_{ij}^{12}} + \frac{q_i q_j}{r_{ij}} \quad 4.3\text{-}6$$

The lattice energy requires the sum all the atoms in the central molecule and then all the atoms of all the surrounding molecules. Where V_{ij} is the interatomic energy between atoms i in the central molecule and j an atom in the k^{th} surrounding molecule, N is the total number of surrounding molecules, n the total number of atoms in the central molecule, n' total

number of atoms in each of the surrounding molecules, A and B are interatomic potential.

4.3.3 Energy minimisation

Energy minimisation is required to provide the optimum molecular geometry; this essential creates a structure at a mechanical equilibrium. This requires the energy to be minimised by the lattice parameters and atomic positions. There are many ways in which energy minimisation can be simulated; with constant pressure where by the lattice parameters and the atomic positions are liable to change; with constant volume allowing the atomic positions to be changed; preserving the symmetry operations.

A numerical approach to define the minimum energy potential is the Newton-Raphson technique. This takes into the hessian matrix of second order derivatives to produce to normal coordinates. Thus scaling the energy gradients in a particular Cartesian coordinate direction and characterising the stationary point as a minimum in the energy potential.

4.3.4 Morphological prediction

4.3.4.1 Bravis-Friedel-Donnay-Harker (BFDH) model

This approach is based on an approximation on the faces that are likely to dominate overall crystal morphology. Initial stages of this theory, proposed by Bravais (Bravais, 1866) and Friedel (Friedel, 1907), stated that the interplanar spacing (d_{hkl}) directly effects the exterior of the crystallographic form. Concluding a greater morphological importance is achieved by a greater interplanar spacing. Equation 4.3-7 is expresses an ideal cubic lattice:

$$d_{hkl} = a\sqrt{\frac{1}{h^2}+\frac{1}{k^2}+\frac{1}{l^2}} \qquad 4.3\text{-}7$$

Donnay and Harker (Donnay, 1937) later expanded on this theory by taking into consideration the crystallographic symmetry. The space group is able to provide the symmetry of a specific crystal. The BFDH model calculates, in rank order, the d-spacing for a range of crystal habit planes and simulates a crystal shape based on the unit cell parameters and the symmetry operators. It is important to consider that this approach does not consider interatomic interactions, bond types, or point charges, all of which have an effect of crystal growth.

4.3.4.2 Surface energy model

Surface energy of crystals can be calculated by

i. Creating a 2-D slab from the bulk
ii. Creating a single surface by employing a two-method region

Region one contains a surface and all layers below it that undergoes significant relaxation. Region 2 contains the rest of the bulk material, it is assumed here that no relaxation occurs and all atoms are fixed and make no contribution to the total energy. The surface energy can be computed using the following expression:

$$E_{surf} = \frac{E_{slab} - E_{bulk}}{A} \quad \text{4.3-8}$$

Where E_{bulk} is the energy of the bulk of the material and E_{slab} is the energy associated with a surface created from the same system and *A* is the total surface area of the surface created. The above expression essentially considers the atom-type and the fractional coordinates of the system. The surface energy is inversely proportional to the overall morphological importance, thus the energy associated is producing equilibrium morphology of a crystal.

4.3.4.3 Attachment energy model

The attachment energy model considers the overall strength of intermolecular interactions between the central molecule and the all the other surrounding molecules. An approach associates the lattice energy, E_{cr}, by applying the following expression:

$$E_{att} = E_{cr} - E_{slice} \quad \text{4.3-9}$$

Where E_{slice} is the slice energy, this considers the summation of all the interatomic interactions between all the atoms in the central molecule contained in the slice and the all the atoms on all the other surrounding molecules within the same slice. Another approach often regards the E_{att} as the energy released when a slab of crystal thickness is incorporated into the crystal lattice. The growth morphology approach assumes the growth rate of a crystal face is proportional to the attachment energy. Thus, the knowledge of the relative growth rates allows the surface distances to be defined and therefore provides the morphology of the crystal.

4.4 Literature review

A key issue in the nuclear industry is to under-pin a chemical model of the HAL waste. Throughout the process operations there are many challenges

that are a result of the properties of the solids, these include blockages, localised heating and corrosion. Internal studies within the nuclear industry have confirmed that ZM solids are a significant contributor to these process issues. It is therefore of importance to develop a chemical model to identify surface chemistry mechanisms, such as ionic binding and co-precipitation to understand and predict possible scenarios of morphological changes in HAL solids during processing. The polymorphic phases of ZM structures are key to define to understand the direct influence of the chemical structure on process plant operations.

Internal NNL reports indicate useful research into the factors influencing ZM formation. The influence of the ZM particle growth with excess uranium in solution has been investigated. Uranium in solution increases the acidity and decreases the growth rate of ZM crystals (Franklin, 1999). Seeding agents were found to also delay the initial precipitation of the ZM crystals (Denniss et al., 2000). Irradiation of the ZM particles indicated negligible effects (Denniss et al., 1999).

Publically available literature on ZM systems has increased over the last few decades, where initial interests included isotropic negative thermal expansion properties. The crystalline structures of materials exhibiting this property are distinctive, the materials include ZrW_2O_8 (Mary et al., 1996, Evans et al., 1996, Evans et al., 1997, Evans et al., 1999), HfW_2O_8 (Evans et al., 1996), ZrV_2O_7 (Korthuis et al., 1995, Evans et al., 1998, Carlson and Krogh Andersen, 2001) and cubic $ZrMo_2O_8$ (Lind et al., 2001). These compounds are composed of rigid MO_4 tetrahedra and/or MO_6 octahedra, these are usually connected by corner-sharing oxygen atoms. The corner sharing atoms give rise to transverse vibrations when the corner-sharing oxygen atoms are excited. The linear formation of Mo-O-Mo is disrupted as the magnitude of vibrations increases and the metal-metal distances decrease, known as negative thermal expansion (Tucker et al., 2005, Evans et al., 1999, Mittal and Chaplot, 1999, Lind, 2012). These are undesired effects as external pressures are caused by internal stresses in materials and therefore could limit potential applications. Therefore, further studies to eliminate thermal expansion become of interest and a desired structure such as cubic $ZrMo_2O_8$ were developed.

High pressure studies of up to 0.6 GPa have been performed on cubic *γ-$ZrMo_2O_8$*, further conventional techniques were implemented to produce a more thermodynamically stable trigonal α-*$ZrMo_2O_8$* (Auray, 1986) and monoclinic β-*$ZrMo_2O_8$* (Klevtsova, 1989, Sahoo et al., 2009). Anderson and

Carlson have carried out extensive research on producing different polymorphic forms of ZM, where two reversible high pressure phase transitions occurred from trigonal α-$ZrMo_2O_8$ to monoclinic δ-$ZrMo_2O_8$ at 1.06-1.11 GPA and from δ-$ZrMo_2O_8$ to triclinic ε-$ZrMo_2O_8$ at 2.0-2.5 GPa (Krogh Andersen and Carlson, 2001, Carlson and Andersen, 2000). Comparison of the structures under high pressures indicated the volume compression for the α-*ZM* and δ-*ZM* structures are similar and are considerably lower than for ε-*ZM* structure. The table below indicates the different polymorphic forms of ZM.

Table 8 Relevant zirconium molybdate polymorphic forms. The polymorphic forms occur at varying external conditions, as indicated in the table.

Polymorph	Crystal System	Authors	Conditions
α-$ZrMo_2O_8$	Trigonal	Auray et al. (1968)	T = ambient
β-$ZrMo_2O_8$	Monoclinic	Klevtsova et al. (1989)	T = ~960K
γ-$ZrMo_2O_8$	Cubic	Lind et al. (2002)	T = 633K
δ-$ZrMo_2O_8$	Monoclinic	Carlson et al. (2000)	P = 1.1 GPa
ε-$ZrMo_2O_8$	Triclinic	Carlson et al. (2000)	P = 2.5 GPa

The structure of α-$ZrMo_2O_8$ is produced from the metastable *γ-$ZrMo_2O_8$* upon prolonged heating conditions at 663 K; kinetically controlled conditions are then required for the transformation to β-$ZrMo_2O_8$.

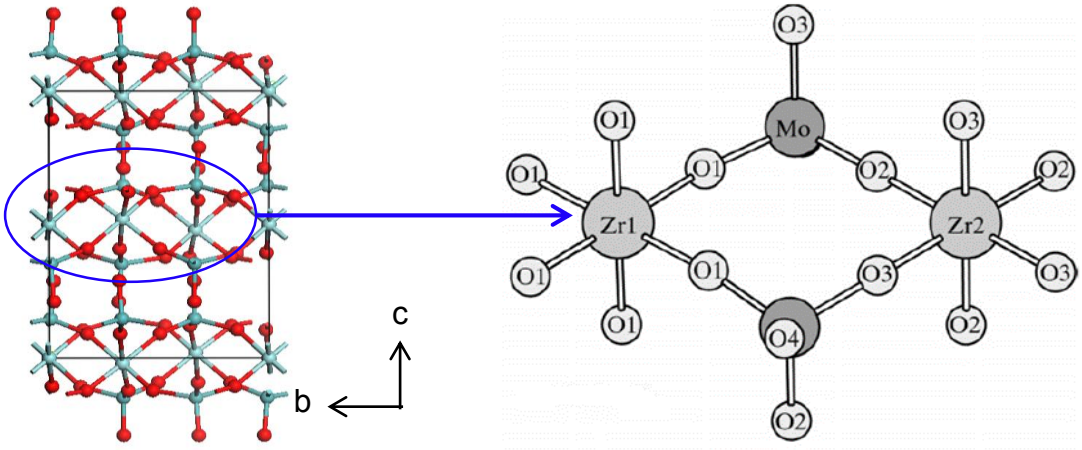

Figure 4.4-1 Crystal structure of α-$ZrMo_2O_8$ illustrating the significance of the interatomic interactions and the resultant layers perpendicular to the c-axis (Auray et al., 1968).

Figure 4.4-1 illustrates α-$ZrMo_2O_8$ structure, initially solved by Auray et al. where layers of ZrO_4 octahedra are linked together by MoO_4 tetrahedra are built perpendicular to the c-axis. Oxygen atoms to three different Zr atoms from the tetrahedral molybdenum group. Description of beta-ZM. This research is interested in exploring the molecular models for both α-*ZM* and β-*ZM* phases.

As mentioned previously in chapter 3, it is believed that the HAL contains the hydrated form of ZM, where synthesis of ZMH were initially based on the Clearfield and Blessing approach. Clearfield et al., initially solved the structure of ZMH (Clearfield and Blessing, 1972). ZMH structure essentially consists of systematically positioned $ZrO_3(OH)_2O_2$ pentagonal bipyramids and $MoO_4(OH)(H_2O)$ octahedral structures, there are directly linked through a Zr-O and Mo-OH bridge, which ultimately holds the structure together. The space group, $I4_1cd$, is polar and therefore the Zr atom is placed on the origin of the asymmetric unit, thus providing a coordinate of 0, 0, 0. An individual unit cell compromises of 8 molecules and thus providing 8 Zr/unit cell, 16 Mo/unit cell and 88 O/unit cell.

A challenge for this model is under-pinning the position of the water and hydroxyl groups. Clearfield et al. have attempted to predict the position of the respective groups, it is assumed the hydrogen bonding provides a secondary role in maintain the structure. The hydrogen bond bridges are identified to create a zig-zag pattern throughout the structure. From the solved structure the O-O atoms which are less than 3 Á were investigated and found the contacts were generated by the space group symmetry to define a three contact O-O-O angles. Further analysis based on this oxygen structure led to the assumption that hydrogen atoms can be placed if

- O(4) atoms are regarded as aquo-oxygen atoms (these atoms are bound to water molecules).
- O(7) act as a bridging hydro-oxygen atoms.

This assumption correlates well with the notion of a zig-zag pattern throughout the structure. The position of the H atoms are still yet to be solved and defined. However, calculations in this research will initiate based on this assumption.

Further studies on the formation of an uncharacterised metastable intermediate polymorph of ZM, known as *LT-$ZrMo_2O_8$*, is explored. Known as the dehydration procedure of ZMH (Allen and Evans, 2003). The overall process is given in Equation 4.3-1

$$ZrMo_2O_7(OH)_2 \cdot 2H_2O \rightarrow LT - ZrMo_2O_8 \rightarrow cubic ZrMo_2O_8 \qquad 4.4\text{-}1$$

This particular study highlights the reversible process of de/rehydration and to also determine the positions of the hydroxyl and water groups. The conceptual mechanism of the process is as follows, in terms of the hydroxyl and water groups

- Loss of H_2O molecules from the MoO_6 octahedra structures.

- Loss of OH and H groups from the ZrO_7 and MoO_5 polyhedra. This also results in the breakage of an O-Mo bond to liberate 6 and 4 coordinate Zr/Mo sites.

Essentially the chains of edge-sharing $ZrO_6(OH)$ is in good agreement with the Clearfield and Blessing assumption that O(7) atoms are the bridging hydro-oxygen, where the bond angles of the O(7) bridge is Zr(2)-O(7)-Mo(1) 106.9º, this is the shortest bridging angle and thus supports the position of the –OH group (Clearfield and Blessing, 1972). Similarly the $MoO_4(OH)(H_2O)$ is in support O(4) atoms is the donor atom of a coordinate water molecule. Both $ZrO_6(OH)$ and $MoO_4(OH)(H_2O)$ structures run parallel to the c-axis (Allen and Evans, 2003).

Simulation studies on ZM structures are limited. However, research on ZrW_2O_8, which is known to be similar in thermal expansion properties to cubic- $ZrMo_2O_8$ have been explored (Pryde et al., 1997, Pryde et al., 1996). This research confirms the mechanism of thermal expansion causing the oxygen atoms from different polyhedra in the structure to compress.

Table 9 Values for the parameters of the short-range pair Buckingham potentials for ZW_2O_8. The values presented are Buckingham potentials for Zr-O (Pryde et al., 1996) and O-O (Sanders et al., 1984).

Atomic interaction		***B***	***ρ***	***C***
		eV	A^6	eV A^{-6}
Zr[4+]	O[2-]	9 x 10^6	0.140000	0.00000
O[2-]	O[2-]	22764.00000	10.000000	27.87900

These values have been derived for thermal expansion material ZrW_2O_8, these are a possible basis for deriving the interatomic potential for ZM structures.

The molecular mechanics calculations in this research are derived from an internal NNL report (NNL, 2013). The aim of this chapter is to employ the derived charges and potentials to predict the morphology of α and β polymorphs. Due to time constraints preliminary calculations of the hydrated ZMH structure will also be investigated. The force field parameters employed are described in the table 10.

Table 10 Fitted force field for anhydrous ZM and hydrated ZM structures. The values have been extracted from the internal NNL report (NNL, 2012).

	Atomic interaction		*A*		*r*	*C*	
			eV	**Kcal mol^{-1}**	**A^6**	**eV A^6**	**Kcal mol^{-1} A^6**
Anhydrous structure	Zr[4+]	O[2-]	976.14229	22510.37730	0.376000	5.65E-08	0.00000131
	Zr[4+]	Zr[4+]	0.00000	0.00000	10.000000	0.00000	0.00000000
	Zr[4+]	Mo[6+]	9279.25295	213984.66910	0.268200	8.93026E-05	0.00205937
	Mo[6+]	O[2-]	1578.10530	36391.97480	0.367500	5.252E-07	0.00001211
	Mo[6+]	Mo[6+]	1191.03253	27465.86420	0.268200	8.93026E-05	0.00205937
	O[2-]	O[2-]	22759.30000	524841.95670	0.149000	2.78895E-05	0.00064315
Hydrated structure	O(H_2O)	Mo[6+]	1578.10530	36391.97480	0.367500	5.252E-07	0.00001211
	O(H_2O)	Zr[4+]	976.14229	22510.33730	0.376000	5.65E-08	0.00000131
	O(H_2O)	O[2-]	22759.30000	524841.95670	0.149000	2.78895E-05	0.00064315

A key assumption that is considered when developing a chemical model for ZMH systems is that they are inactive. Radionuclides of zirconium and molybdenum present in HAL have a short half-life of <4 years.

Though polymorphic research on ZM structures have focused on experimental data collection, where external conditions such as temperature and pressures result in the formation of the various structures, this research focuses on developing a chemical model to predict the external morphology of the α-*ZM,* β-*ZM* and ZMH phases. Crystallographic data is readily available for the solved structures, these will be used for the basis of this research.

4.5 Materials and methods

Various molecular modelling packages have been applied across a wide range of industries to improve the engineering of performing materials, including pharmaceuticals and oil pipe lines. This research aims to implement a number of molecular modelling packages to develop a chemical model to predict the morphology of a highly active nuclear waste simulant, ZM. Analysis at a microscopic scale provides an insight into the atomic interactions and surface properties of the ZM crystals. This chapter will focus on the molecular modelling methods to obtain predicted structures of the two anhydrous ZM polymorphic forms and preliminary predictions of the hydrated structure with incorporation of the citratomolybdate complex.

4.5.1 Crystal structures

All crystal structures are obtained from the Inorganic Crystal Structure Database (ICSD) (FIZ Karlsruhe GmbH 1998). This data base contains over 160 000 data entries and crystallographic information on a variety of inorganic compounds.

4.5.2 Molecular visualisation

Initial modelling includes identification of crystal structure, extraction of key crystallographic data followed by molecular visualisation. MATERIALS STUDIO version 6.5 (Accelrys) was used to visualise the crystal systems. This visualisation software package enables construction and manipulation of crystalline materials. The main tools implemented within the packages includes evaluation of the crystal structure, crystal growth and morphology. The crystal structure obtained from ICSD is converted to a *.cif* and imported into MS and viewed as a 3D-atomistic structure. Once the structure imported the unit cell, bond connectivity and supercell (3 x3) is built, these factor all dependant on the atomic position and symmetry. In the case of the hydrated ZM structure, calculation of the hydrogen bonds is required, this is neglected for both the anhydrous polymorphic forms.

4.5.3 BFDH calculation

Surface chemistry analysis is conducted by cleavage of the main surfaces, determined by the largest d-spacing values. The morphological calculation tool in MS enables analysis to obtain the main surfaces by implementing the BFDH model. The BFDH values can be validated by employing the DRAGON software package.

The Bravais-Friedel-Donnay-Harker (BFDH) (Bravais, 1866, Friedel, 1907, Donnay, 1937) method takes into account the geometry of the crystal lattices; it is assumed that the relative growth rates are R_{hkl} of the crystal faces are inversely proportional to the inter-planar distance d_{hkl}. The main aspect for this method is to present the apparent faces of the crystal which can be represented in the growth planes. DRAGON applies these methods to produce a file with all the important faces of α-glycine crystal. Therefore it can be suggested that the crystal lattice and the symmetry, such as the Bravais lattice and the space group, creates possible growth faces (Bandyopadhyay and Grant, 2000). The required input parameters for important faces to be determined are listed below.

- Input the cell constants (*a, b, c, α, β, γ)*.

- State the maximum wavelength, maximum 2-θ and zero-point, (1.54178 Angstroms, 50 degrees, 0.000 degrees)
- State the space group
- The number of reflections and the multiplicity will be presented, the statement of '*sorting reflections*' should be agreed
- The output number type should be decided and set (0 = TTY (first 10 reflections) + LPT listing)
- The maximum indices (hkl)
- The important faces in descending order of importance i.e. starting with the largest value of the d-spacing
- The d-spacing
- The angle (2-θ)

4.5.4 Lattice energy minimisation

The procedure for lattice energy minimisation requires knowledge of the fractional coordinates of the atoms in an asymmetric unit of the crystal structure. This research employed the software package GULP (Gale, 1993). Implementation of the space group and symmetry operators enables the calculation of the fractional coordinates of all the atoms in the unit cell. The coordinates allow the distance of each atomic pair to be calculated. The overall lattice energy minimisation requires a number of input parameters. The atomistic potential energy model adopted for this research is provided from NNL, the values are presented in table 10. The charge model implemented in the calculations for this research explored both the formal charge and partial charge model, defined in table 11.

Table 11 Formal and partial charges used for lattice energy minimisation and morphology predictions. This table contains values extracted from the NNL report (NNL, 2012).

Species	Formal ionic model	Partial ionic model
Zr[4+]	4	2.7
Mo[6+]	6	4.05
O[2-]	2	-1.35
O(H2O)[*1]	-0.8472	-0.8472
H(H2O)[*1]	0.4236	0.4236
O(OH)[*2]	0.426	0.426
H(OH)[*2]	-1.426	-1.426

*1 charge values obtained from literature for water molecules (Wu et al., 2006) and *2 for hydroxyl group (Gale, 1996, Lewis and Catlow, 1985).

The computational energy summation is a function of the interaction energy between the central and neighbouring atoms, the number of atoms, atom-atom potential, fractional charges on the atoms and the interatomic distances. This procedure is dependent on the constraints defined, the

lattice energy minimisation was performed at constant pressure and temperature. The significance for energy minimisation prior to further calculations, is to provide the location of the optimum molecular geometry.

A typical GULP input file requires a number of keywords (dependant on the type of calculation made), lattice parameters, fractional coordinates, charge model and the interatomic potentials, presented in Figure 4.5-1. Presented in table 11 are a list of keywords used for lattice energy minimisation and surface energy calculations.

Table 12 summary of keywords used for lattice and surface energy calculations. These are all valid keywords for GULP version 4.0 (Gale, 2005)(Gale 2007).

Keyword	Meaning
conp	Perform constant pressure calculation – cell to vary
conv	Perform constant volume calculation – hold cell fixed
efg	Calculate electrostatic electric field gradient
nomod	Do not modify input coordinates
opti	Minimise the energy with respect to geometrical variables
prop	Calculate final properties for final geometry
qok	It is ok to run with non-charge neutral unit cell
pot	Calculate electrostatic site potentials
single	Perform a single point calculation of the energy

```
opti conp qok nomod pres prop pot efg
pressure 0 GPa

title
GULP calculation for Alpha_Auray_ZM
end

cell
10.139 10.139 11.708 90.000000 90.000000 120.000000 1 1 1 1 1 1

fractional
O1 core 0.006700 0.173100 0.100800 -2.000000 1.000000 0.0 1 1 1
O1 core 0.161500 0.497900 0.117800 -2.000000 1.000000 0.0 1 1 1
Mo1 core 0.338910 0.010200 0.149000 6.000000 1.000000 0.0 1 1 1
O1 core 0.352200 0.033300 0.292300 -2.000000 1.000000 0.0 1 1 1
O1 core 0.495900 0.163600 0.081400 -2.000000 1.000000 0.0 1 1 1
Zr1 core 0.333333 0.666667 0.018680 4.000000 1.000000 0.0 1 1 1
Zr1 core 0.000000 0.000000 0.000000 4.000000 1.000000 0.0 1 1 1

Species
Mo1 core 6
O1 core -2
Zr1 core 4

spacegroup
163

accuracy
12.0 4 20

cutd 10.0
buck
Mo1 core O1 core 1578.10530 0.36750 0.000000525000 0.0 10.0
buck
Zr1 core O1 core 976.142290 0.376000 0.000000056500 0.0 10.0
buck
O1 core O1 core 22759.30000 0.14900 0.0000278895000 0.0 10.0
buck
Zr1 core Zr1 core 0.000000 10.00 0.0000000000 0.0 10.0
buck
Zr1 core Mo1 core 9279.25296 0.26820 0.0000893025595 0.0 10.0
buck
Mo1 core Mo1 core 1191.03253 0.26820 0.0000893025595 0.0 10.0
```

Keywords

Lattice cell parameters

Fractional coordinates

Formal charge model

Numerical style space group

Interatomic Buckingham potential model

Figure 4.5-1 Typical input file for energy minimisation. The input file represents the calculation for α-ZM.

The internal energy therefore is a function of the positions of the electrons and nuclei, as simulated by (Gale and Rohl, 2003). The calculation assumes the electrons of the associated atoms are incorporated in a particular force field, denoted by the Buckingham potential. The cut-off point must be clearly defined, which also can be varied, this is important as the interactions between the particles become weaker once the interparticle distance increases. The application of all the above parameters employs the Monte Carlo method, where the simulation searches for a local minimum energy. Once the minimum energy is located, the optimised structure can now be defined.

Energy minimisation enables the calculations and analysis of bulk and surface properties of the crystalline material. This research focuses on the surface properties to predict the overall morphology of the crystal.

4.5.5 Surface and attachment energy calculation

An independent graphical interface programme, GDIS (Fleming and Rohl, 2005) enables the surface construction and structural manipulation of the crystalline material. The crystalline interface is developed by obtaining the important miller indices and thus the d-spacing. Once the surfaces have been identified the surface properties can be calculated in terms of the surface energy, attachment energy and morphological predictions. The overall procedure for morphological prediction is described below.

- BFDH analysis, three software packages can be employed MS, DRAGON and GDIS, the important faces are determined based on the respective d-spacing (all should give exactly the same result).
- Minimisation of the bulk structure. GDIS enables visualisation of the relaxed and unrelaxed states of the crystalline structure.
- Cleavage of the main surfaces from the relaxed bulk structure, surface chemistry analysis can be carried out in MS.
- Cleavage of important surfaces of minimised structure. Ensuring surface dipole of each face is equal to 0 e. Angstroms. Surface relaxation includes ions in Region I and region II to be relaxed until the gradient of the forces approached zero, whilst the ions in region II were held constant.
- Surface dipole ≠ 0. Surface dipoles can be removed by surface reconstruction and thus, atomic displacement. This includes by defining a 3 x 3 transformation matrix and a 3 x 1 translation. This

method can be applied to the bulk structure and the individual surfaces and enables cleavage of a wide range of surfaces without dipoles.

- Once all the relevant parameters have been defined the calculation of the surface properties such as the surface and attachment energies can be calculated.
- Morphological predictions can be obtained for all three methods. The ZM crystal structures for the general BFDH, equilibrium and growth morphologies.

4.6 Results and Discussion

Morphology prediction of two anhydrous zirconium molybdate polymorphs, the stable alpha phase and the metastable beta phase and the hydrated form are presented. It is assumed that it is the hydrated structure present in HASTs.

4.6.1 Crystal and surface chemistry

Analysis of the crystal structure is explored from structure obtained from the ICSD. The main crystallographic parameters obtained for the anhydrous phases are represented in table 13.

Table 13 Crystallographic data available for alpha and beta structures of ZM available from ICSD

Crystallographic parameters	α-$ZrMo_2O_8$	β-$ZrMo_2O_8$
Unit cell lengths (a, b, c)	10.139, 10.139, 11.708	11.424, 7.930, 7.461
Unit cell angles (α, β, γ)	90, 90, 120	90, 122.550, 90
Space group	P-31c (No. 163)	C2/c (No.15)
Number of symmetry operators	12	8
Number of formula units/ unit cell	8	-

Table 13 indicates the key crystallographic data extracted from ICSD for the anhydrous α-ZM polymorph (Auray et al., 1986) and β-ZM polymorph (Sahoo et al., 2009). α-ZM crystallises in a trigonal crystal system, the space group notation indicates a primitive lattice with a 3-fold inversion axis and a centre of symmetry 1-fold axis along c-axis. β-ZM crystallises in a monoclinic crystal system, the space group notation indicates a c-centred lattice with a 2-fold axis perpendicular to the c-axis. Derivation of the symmetry operators will be discussed later in the chapter.

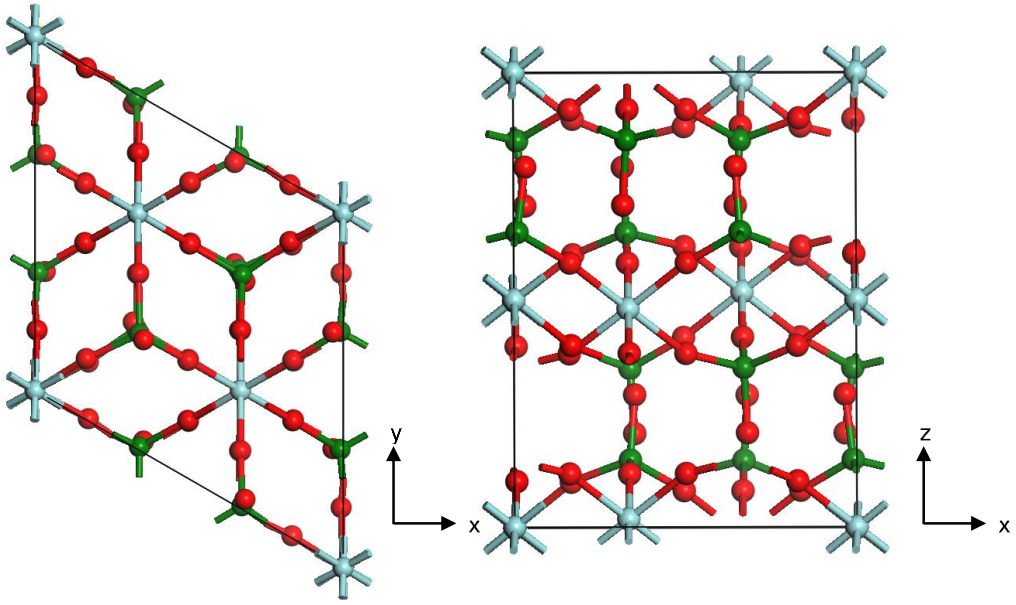

Figure 4.6-1 Unit cell of a-$ZrMo_2O_8$ indicating the atomic structure of a 1x1 unit cell. The crystal structure illustrates of zirconium atoms (light blue), molybdenum atoms (green) and oxygen atoms (red).

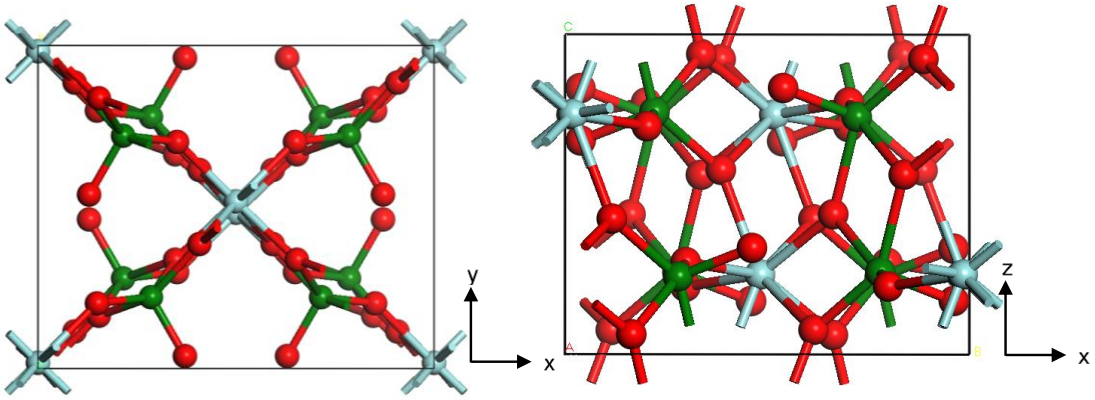

Figure 4.6-2 Unit cell of b- $ZrMo_2O_8$ indicating the atomic structure of a 1x1 unit cell. The crystal structure illustrates of zirconium atoms (light blue), molybdenum atoms (green) and oxygen atoms (red).

Figures 4.6-1 and 4.6-2 represent the crystal structure of both alpha and beta anhydrous phases of ZM. Both phases have the Zr atoms fractional coordinates of (0, 0, 0). The crystal structure also illustrates ZrO_6 octahedra are linked together by MoO_4 tetrahedra. In the case of the α-ZM the crystal structure is built with both subunits linked perpendicular to the z-axis. This phase also indicates the primitive lattice structure of the unit cell, whereby the zirconium atoms are positioned on the corners of the unit cell. Usually primitive lattice structures equate to one lattice point, this is due to corner sharing atoms i.e. 8x(1/8) = 1. The β-ZM crystallises with a side-centred lattice on the c face of the unit cell (a convention of a monoclinic system), where the Zr atoms are located on the side of the lattice cell, illustrated in figure 4.6-2. Crystal chemistry evaluation is important to predict mechanisms

such as ion adsorption and co-precipitation. As the precipitated HAL solids are suspended in HNO_3 solution, there are many isolated ions within the solution. The crystal structures suggest that the bulk contamination is likely to be greater than the surface, as there are more Zr atomic sites located within the bulk, in contrast to the surface. However, it is also important to consider that the contaminants gain access to the bulk during growth during attachment at interfaces where growth is occurring.

4.6.1.1 Surface chemistry of α-ZrMo2O8

Analysis of the α-$ZrMo_2O_8$ crystal structure, by implementing the BFDH model, enables the dominant faces contributing to the overall morphology to be defined. Table 14 indicates the dominant faces of {1 -1 0} and {1 -1 1} to be a major contributor to the overall morphology of α-$ZrMo_2O_8$ crystals.

Table 14 Inter-planar spacing of five important faces of alpha-ZM from the BFDH model. Values are generated in Materials Studio

hkl	Multiplicity	d_{hkl}
{1 -1 0}	6	8.781
{1 -1 1}	12	7.025
{0 0 2}	2	5.854
{2 -1 0}	6	5.070
{1 -1 2}	12	4.871
{2 -2 1}	12	4.111

The surface chemistry for surfaces mentioned in table 14 is illustrated in figures 4.6-3 to 4.6-7.

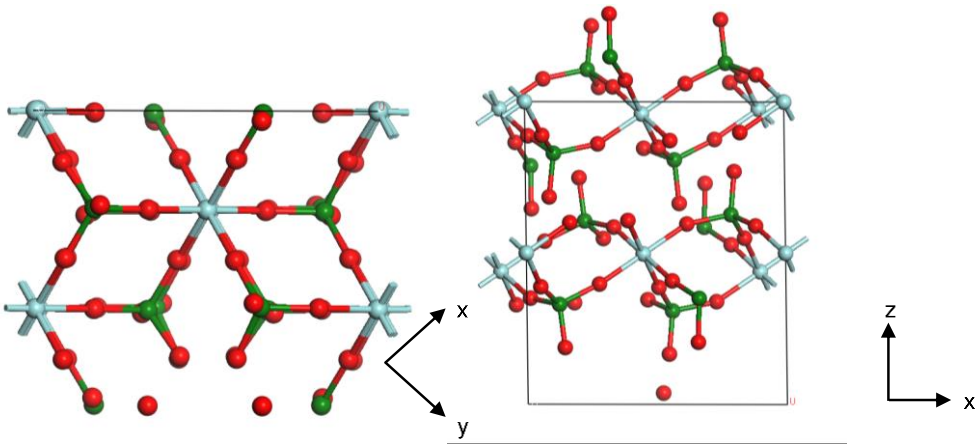

Figure 4.6-3 Projection and Arial view of a- $ZrMo_2O_8$ {1 -1 0} face. This illustrates the surface chemistry of zirconium atoms (light blue), molybdenum atoms (green) and oxygen atoms (red).

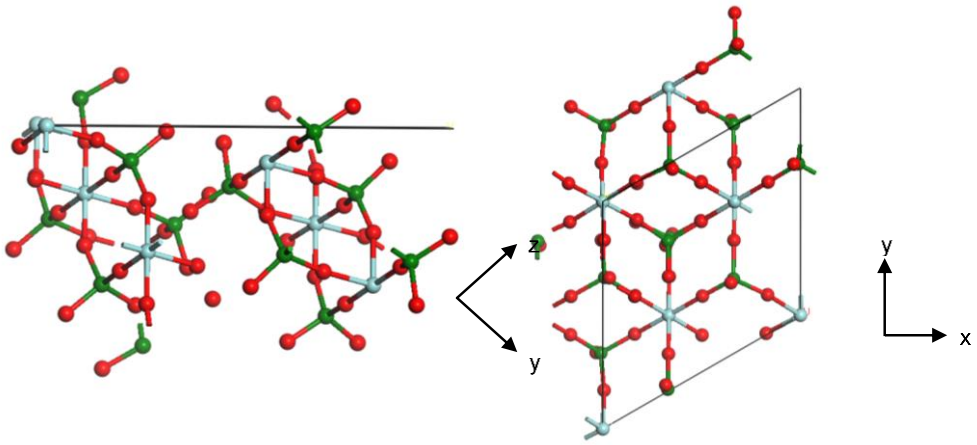

Figure 4.6-4 Projection and Arial view of a- $ZrMo_2O_8$ {1 -1 1} face. This illustrates the surface chemistry of zirconium atoms (light blue), molybdenum atoms (green) and oxygen atoms (red).

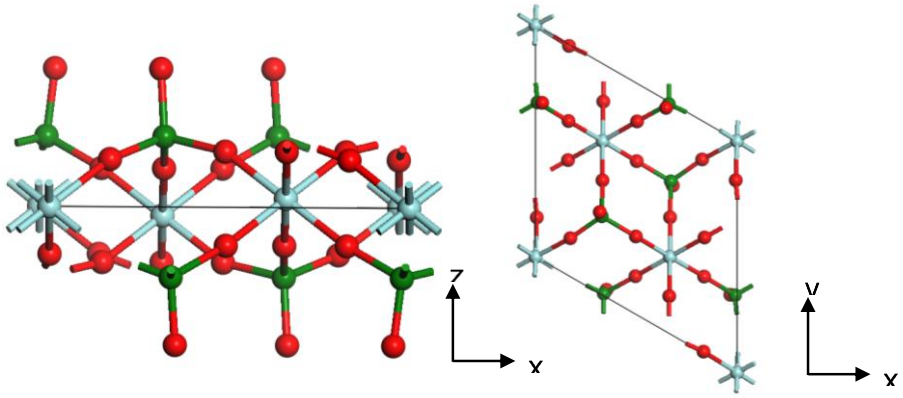

Figure 4.6-5 Projection and Arial view of a- $ZrMo_2O_8$ {0 0 2} face. This illustrates the surface chemistry of zirconium atoms (light blue), molybdenum atoms (green) and oxygen atoms (red).

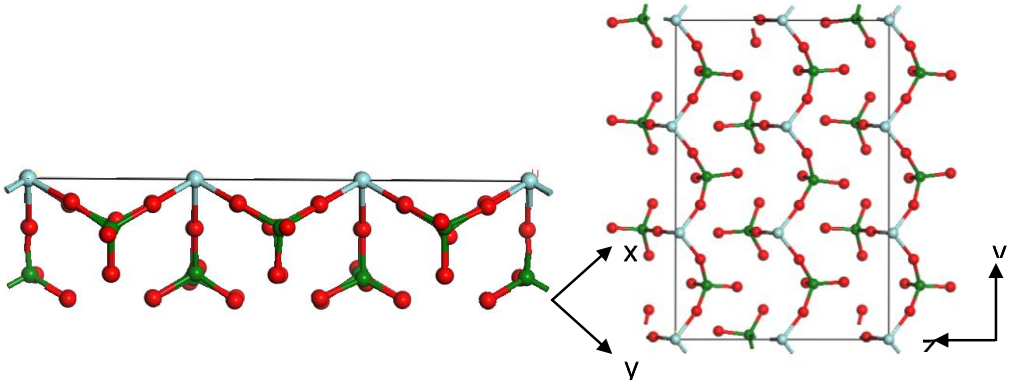

Figure 4.6-6 Projection and Arial view of a- $ZrMo_2O_8$ {2 -1 0} face. This illustrates the surface chemistry of zirconium atoms (light blue), molybdenum atoms (green) and oxygen atoms (red).

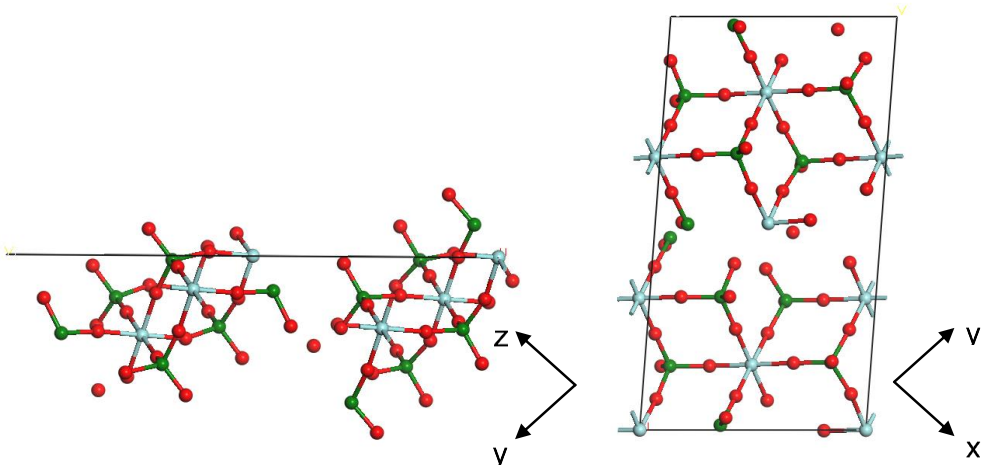

Figure 4.6-7 Projection and Arial view of a- $ZrMo_2O_8$ {1 -1 2} face. This illustrates the surface chemistry of zirconium atoms (light blue), molybdenum atoms (green) and oxygen atoms (red).

Figures 4.6-3 to 4.6-7 allow surface chemistry analysis of the dominant faces. All faces indicate strong anionic-cationic interactions. In particular, the {2 -1 0} face indicates an ordered interplanar chemical structure. The positions of the atoms create an open structure dominated by interionic interactions perpendicular to the y-axis. In contrast to the more densely packed {1 -1 0}, {1 -1 1} and {0 0 2} aces, where strong interatomic interactions are present. The {0 0 2} is the only face to illustrate the protruding Mo and Zr atoms from the surface. The exposure of both Mo, and in particular, Zr sites gives rise to a greater degree of surface contamination. Thus, the {0 0 2} has a significant effect on the growth of the morphology due to readily available Zr and Mo sites.

4.6.1.2 Surface chemistry of β-$ZrMo_2O_8$

Analysis of the β-$ZrMo_2O_8$ crystal structure, by implementing the BFDH model, enables the dominant faces contributing to the overall morphology to be defined. Table 15 indicates the dominant faces of {1 1 0} and {1 1 -1} to be a major contributor to the overall morphology of α-$ZrMo_2O_8$ crystals.

Table 15 Inter-planar spacing of five important faces of beta-ZM from the BFDH model. Values are generated in Materials Studio

hkl	Multiplicity	d_{hkl}
{1 1 0}	4	6.132
{1 1 -1}	4	5.405
{2 0 0}	2	4.836
{0 2 0}	2	3.964
{1 1 1}	4	3.805
{0 0 2}	2	3.158

The surface chemistry for surfaces mentioned in table 15 are illustrated in figures 4.6-8 to 4.6-12.

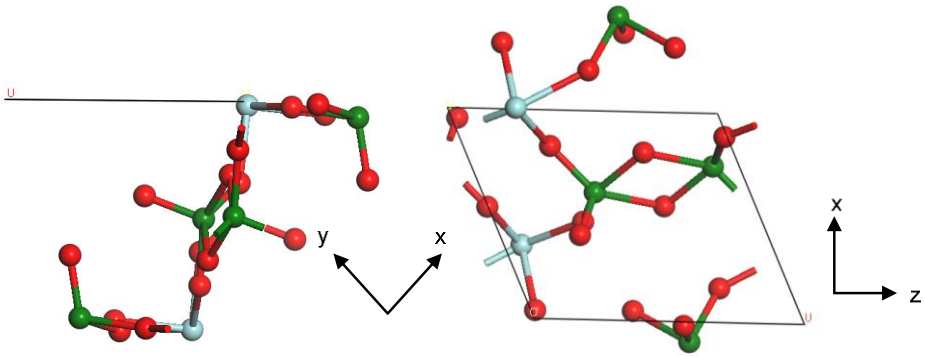

Figure 4.6-8 Projection and Arial view of β-$ZrMo_2O_8$ {1 1 0} face. This illustrates the surface chemistry of zirconium atoms (light blue), molybdenum atoms (green) and oxygen atoms (red).

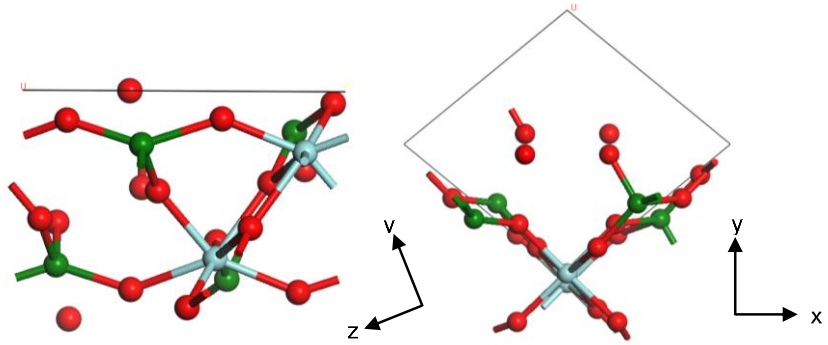

Figure 4.6-9 Projection and Arial view of β-$ZrMo_2O_8$ {1 1 1} face. This illustrates the surface chemistry of zirconium atoms (light blue), molybdenum atoms (green) and oxygen atoms (red).

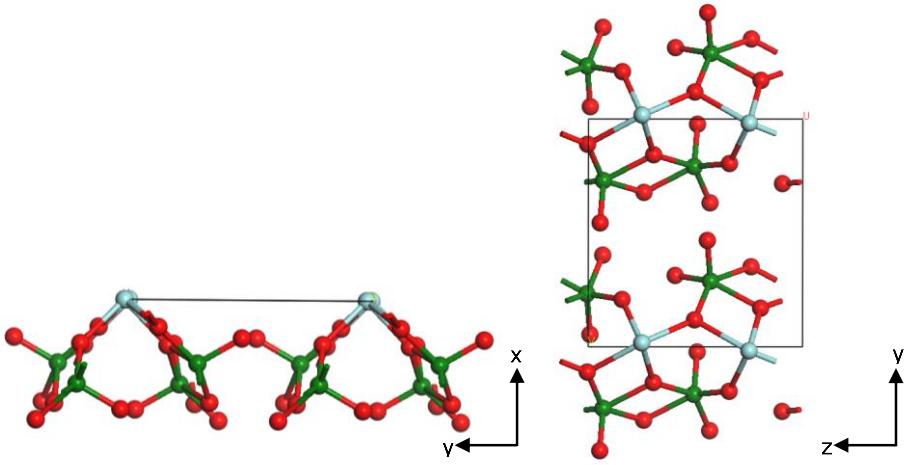

Figure 4.6-10 Projection and Arial view of β-$ZrMo_2O_8$ {2 0 0} face. This illustrates the surface chemistry of zirconium atoms (light blue), molybdenum atoms (green) and oxygen atoms (red).

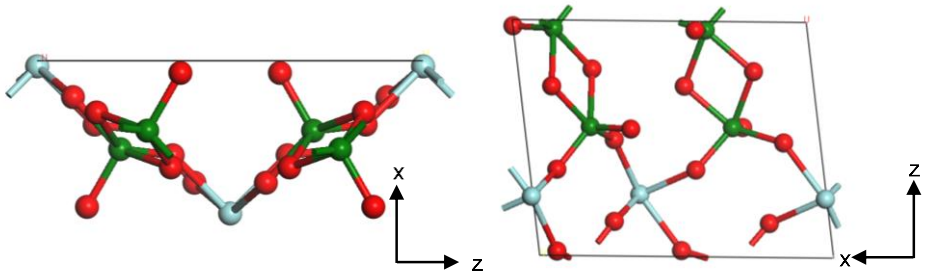

Figure 4.6-11 Projection and Arial view of β-$ZrMo_2O_8$ {0 2 0} face. This illustrates the surface chemistry of zirconium atoms (light blue), molybdenum atoms (green) and oxygen atoms (red).

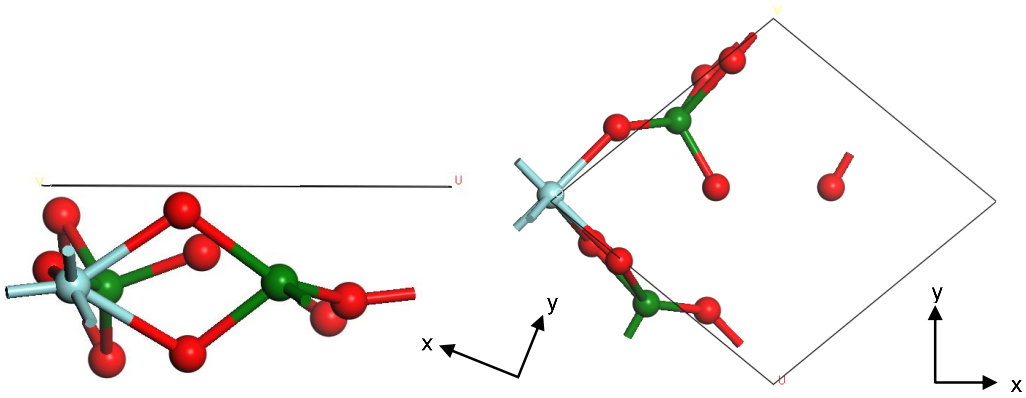

Figure 4.6-12 Projection and Arial view of β-$ZrMo_2O_8$ {0 0 2} face. This illustrates the surface chemistry of zirconium atoms (light blue), molybdenum atoms (green) and oxygen atoms (red).

Figures 4.6-8 to 4.6-12 allow surface chemistry analysis of the dominant faces. In contrast to the α-$ZrMo_2O_8$ phase, the surface chemistry indicate all faces to have fewer interatomic interactions for the β-$ZrMo_2O_8$ phase. In particular, the {1 1 0}, {1 1 1} and {0 0 2} faces illustrate a very open structure with inter-atomic interactions below the surface. The {2 0 0} illustrates a densely packed structure below the surface, dominated by strong interatomic interactions. Through analysis of the surface chemistry it is evident that there are more Zr and Mo sites available in the bulk of the structure, compared to the dominant surfaces.

4.6.2 BFDH prediction using Materials Studio

Morphological predictions for α-$ZrMo_2O_8$ and β-$ZrMo_2O_8$ structures, based on BFDH model is illustrated in Figure 4.6-13.

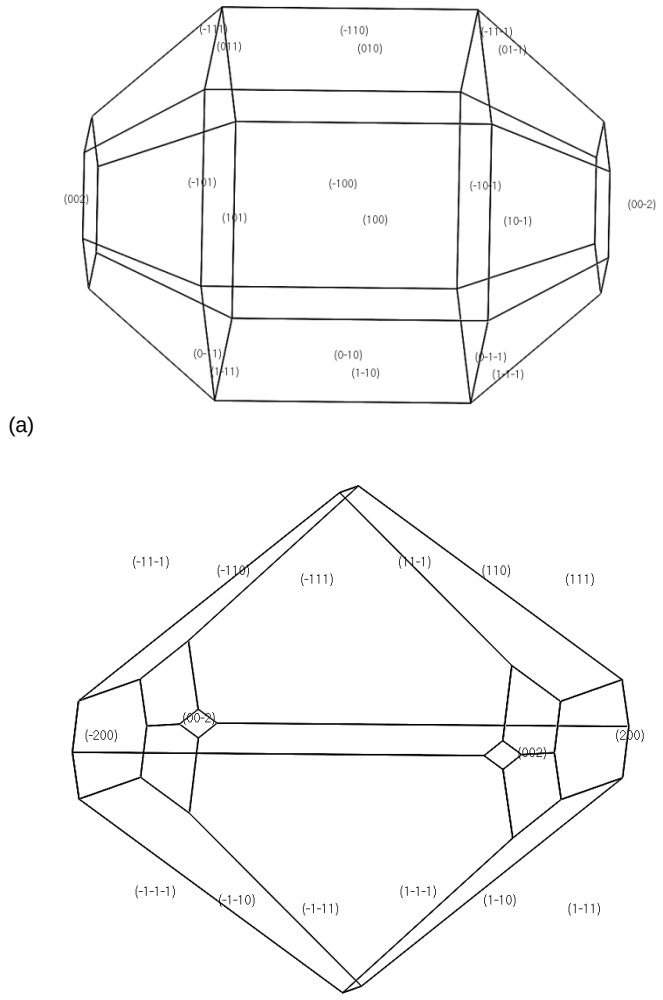

(a)

(b)

Figure 4.6-13 Prediction of the BFDH calculated morphology for both (a) α-$ZrMo_2O_8$ and (b) β-$ZrMo_2O_8$. Structures are predicted using MATERIALS STUDIO.

The morphological predictions based on the BFDH model illustrate for α-$ZrMo_2O_8$ (figure 4.6-13 (a)) crystal structures the dominant faces of {1 1 0}, {1 1 1} and {0 0 2} have the largest surfaces area. Thus, the faces with the largest d-spacing have a significant effect on the overall external morphology of the crystal. The BFDH model predicts the morphology of α-$ZrMo_2O_8$ crystalline structure as a hexagonal prism. Figure 4.6-13 (b) illustrates the morphology prediction for β-$ZrMo_2O_8$ crystal structures, indicating the dominant faces of {1 1 1}, {1 1 0} and {2 0 0} to have the largest surface area. In contrast, the {0 0 2} face illustrating the smallest surface area. The overall BFDH predicts a bipryramidal morphology for β-$ZrMo_2O_8$ crystal structures. Considering the BFDH model assumes greater morphological importance is achieved by greater interplanar spacing, it neglects other important factors. These include the type, number and strength of interatomic interactions and the electron charge density. All of which are considered to have a significant effect during the growth of the crystal.

4.6.3 Lattice energy minimisation

The validity of the force field parameters derived by NNL, presented in table 10, was explored in this research. The aim is to replicate lattice energy values obtained by NNL, once validation is achieved surface and attachment energy calculations can take place. Two input files were created, for lattice energy optimisation, one to replicate the NNL input file with their derived potentials and a second to change the potential values for Zr-O interatomic interaction, from literature (Pryde et al., 1998).

As mentioned in section 4.5.4, the input files consisted of the structural information and the force field parameters. An output file consists of a number of mechanical properties such elastic constants, bulk and Young's moduli and the optimised structural properties including the lattice energy. Initial lattice energy calculations demonstrated challenges during lattice optimisation. Analysis of the fractional coordinates was therefore explored. The original crystallographic fractional coordinates resulted in an error during optimisation stating '*cell volume fell below optimum*' indicating the atomic coordinates are unstable. Therefore equivalent fractional coordinates have been derived by the application of the symmetry operators. Fractional coordinate derivation requires calculation of the equivalent position from the initial coordinates at (x, y, z). This procedure was carried to verify the fractional coordinates were equivalent and in addition to apply the identical asymmetric unit provided by NNL.

All calculations have been carried out using GULP, the lattice energies for un-optimised and optimised structure for both anhydrous phases are presented in Table 16.

Table 16 Lattice energy properties prior and post optimisation for α-$ZrMo_2O_8$ and β-$ZrMo_2O_8$ crystalline phases. The values are compared to previous values produced from NNL and literature (NNL, 2012; Pryde et al., 1998).

		NNL Input		**This research Input**		**Pryde et al. Input (Zr-O)**	
		Unoptimised	Optimised	Unoptimised	Optimised	Unoptimised	Optimised
α-ZM	Lattice energy (eV)	806.44	771.09	806.99	770.94	779.06	728.84
	Lattice energy (kJ/mol)	-308336.63	-310574.13	-308350.43	-310590.23	-311045.39	-313943.47
β-ZM	Lattice energy (eV)	263.05	243.66	262.46	254.95	240.63	213.60
	Lattice energy (kJ/mol)	-101861.86	-103949.47	-101829.78	-104153.92	-103936.45	-106397.19

From Table 16, during the optimisation there is a decrease of 4.56% for α-$ZrMo_2O_8$ and 2.90% for β-$ZrMo_2O_8$. The lowest percentage difference of the β-$ZrMo_2O_8$ phase is indicative of it being the most thermodynamically stable

phase. Structural optimisation requires the closest minimum for a given structure to be obtained, the equilibrium geometry. During this process the change in atomic coordinates defines the overall thermodynamic stability of the phase. Comparing both the alpha and beta phases, the energy gradient during minimisation is greater for the alpha phase thus, indicating the force field implemented is less able to describe the solid structure.

It is evident from Table 16 that there is no significant change of the lattice energy when comparing the values from the NNL report to the values generated by this research. The percentage difference, for α-$ZrMo_2O_8$, for un-optimised structure is 0.06% and for the optimised structure is 0.02%. In contrast, comparing values generated by the Pryde et al. Zr-O potential, this generated a percentage difference of 3.5% for the un-optimised structure and 5.61% for the optimised structure, when compared to this research. It may be assumed the larger percentage difference reported, using Zr-O potential (Pryde et al.,1998), is indicative of the potential extracted a different crystal structure (ZrW_2O_8). The results indicate reasonable validation for the interatomic potentials derived by NNL. The validation of the potentials enables calculation of structural properties, surface and attachment energy calculations and ultimately predicts the morphology of the phases.

4.6.4 Surface and attachment energy morphological prediction

Lattice minimisation is required prior to surface energy cleavage and calculations. This creates a crystalline structure with an optimum energy. Surface energy calculates the equilibrium morphology determined by the minimum of the surface energies for all relevant faces. The overall surface energy calculation is based on the difference between the energy of the surface plane and the bulk energy per unit area. Attachment energy calculates the growth morphology. This is based on the growth rate of the relevant crystal face is proportional to its attachment energy. Thus determining the energy released on attachment of a growth slice to a growing crystal surface.

Surface calculations were carried out using GDIS. This software enables the visualisation of the unit cell before and after minimisation, thus revealing structural differences between the unrelaxed and relaxed state. The calculations were carried out at a constant volume, surface planes were created from the relaxed bulk structure. Visualisation of the relaxed and unrelaxed bulk structure is presented in Figure 4.6-14.

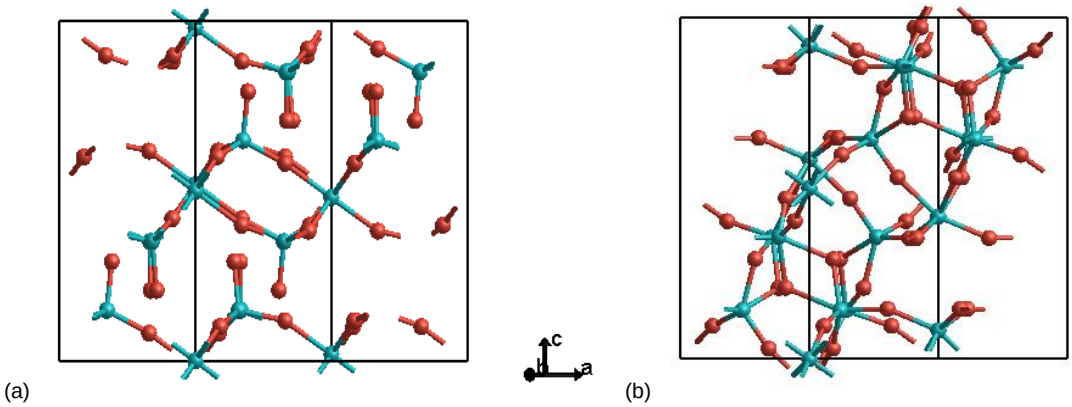

Figure 4.6-14 Crystalline structures of α-$ZrMo_2O_8$ illustrating the structural difference between (a) unrelaxed and (b) relaxed state.

Figure 4.6-14 illustrates the change in the molecular geometry before and after minimisation. Consider the values in table 11, the 4.56% decrease in energy is illustrated in figure 4.6-14(b). The open structure of the α-$ZrMo_2O_8$ provides a low-energy packing platform to obtain the minimum geometric point. The absence of hydrogen bonding within the system also contributes to the high energy difference. Molecules with the absence of hydrogen-bond donors and acceptors provide the overall crystal structure with strong, directional interactions (Day et al., 2004). This therefore produces a structure which minimises with a higher energy difference.

During cleavage of the relevant surfaces extreme surface dipoles were observed. A surface dipole signifies a high energy structure, this is an undesirable characteristic for surface and attachment energy calculations. Surfaces containing a dipole will be neglected during morphology prediction, and thus producing an unrealistic representation of the product. Surface reconstruction has been considered to remove the large dipoles contained on the surfaces. Surface cleavage, post bulk minimisation, produced many surfaces with dipoles. Thus, the application of symmetry operators on atomic positions of α-$ZrMo_2O_8$ has been considered. This procedure requires the manipulation of the transformation (3 x 3) and translational (3 x 1) matrix.

The initial matrix configuration is expressed below

$$\begin{pmatrix} 1 & 0 & 0 \\ 0 & 1 & 0 \\ 0 & 0 & 1 \end{pmatrix} + \begin{pmatrix} 0 \\ 0 \\ 0 \end{pmatrix}$$

Application of this matrix indicated the majority of the surfaces exhibited a surface dipole for {1 -1 0}, {1 -1 1}, {1 -1 2} and {1 0 2} planes. The manipulated matrix is expressed below

$$\begin{pmatrix} 1 & 0 & 0 \\ 0 & 1 & 0 \\ 0 & 0 & 1 \end{pmatrix} + \begin{pmatrix} 3 \\ 3 \\ 3 \end{pmatrix}$$

Application of this matrix resulted in the cleavage of all surfaces without a large dipole. The atomic coordinates with respect to the new matrix is illustrated in figure 4.6-15.

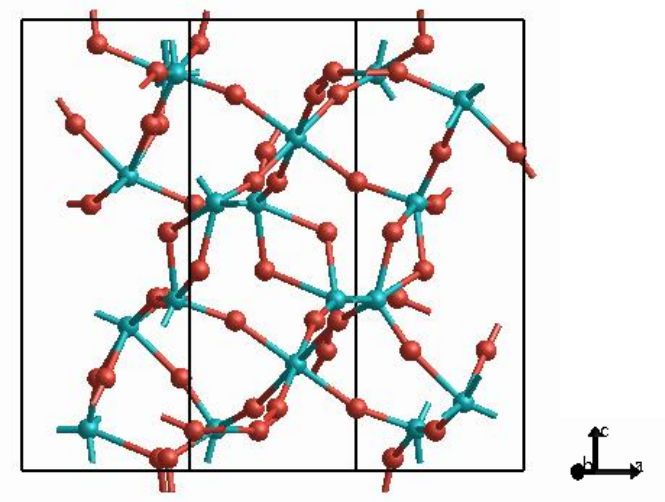

Figure 4.6-15 Crystalline structure of α-$ZrMo_2O_8$ with new translated atomic coordinates after the application of the re-defined matrix.

The re-defined matrix enables the calculation of the surface and attachment energies for the respective planes.

The screen shot of the surface builder for cleaved surfaces of α-$ZrMo_2O_8$ is illustrated in figure 4.6-16, this indicates the production of all relevant surfaces to contain a 0-dipole surface.

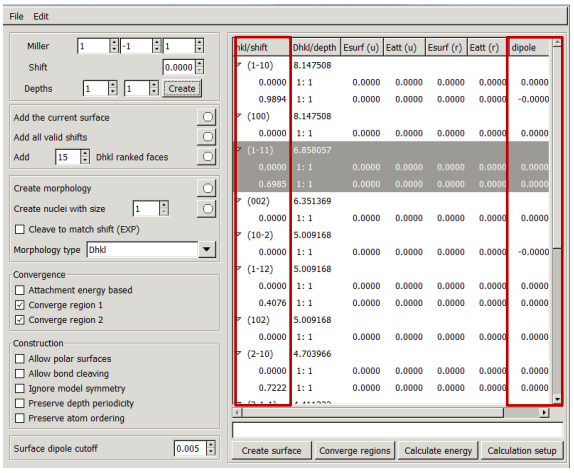

Figure 4.6-16 Screen shot of the surface building technique in GDIS. The relevant surfaces and the dipoles have been highlighted by the red box.

All surfaces as illustrated in Figure 4.6-16 have 0-dipole and therefore lattice energy optimisation and surface energy calculations were explored to ultimately predict the morphology. Figures 4.6-17 – 4.6-22 illustrate the main

surfaces in the unrelaxed and relaxed regions. Geometric optimisation can be visualised indicating the new atomic coordinates at an energy optimum.

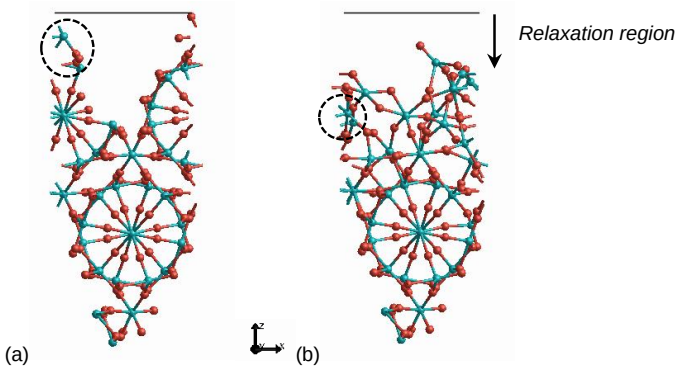

Figure 4.6-17 Cleaved (1 -1 0) surface of α-$ZrMo_2O_8$ illustrating (a) unrelaxed and (b) relaxed state. Surfaces were generated in GDIS. The molecular structure contains Zr atoms(light green), Mo atoms (dark green) and O atoms (red).

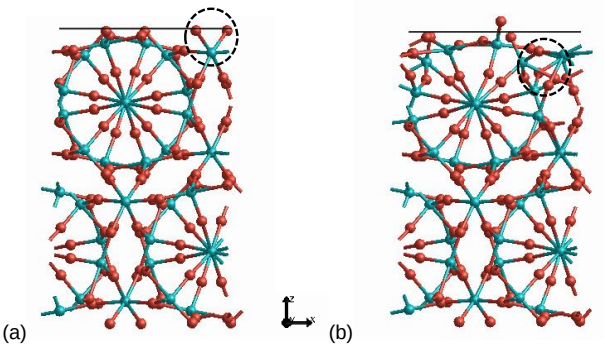

Figure 4.6-18 Cleaved (1 0 0) surface of α-$ZrMo_2O_8$ illustrating (a) unrelaxed and (b) relaxed state. Surfaces were generated in GDIS. The molecular structure contains Zr atoms(light green), Mo atoms (dark green) and O atoms (red).

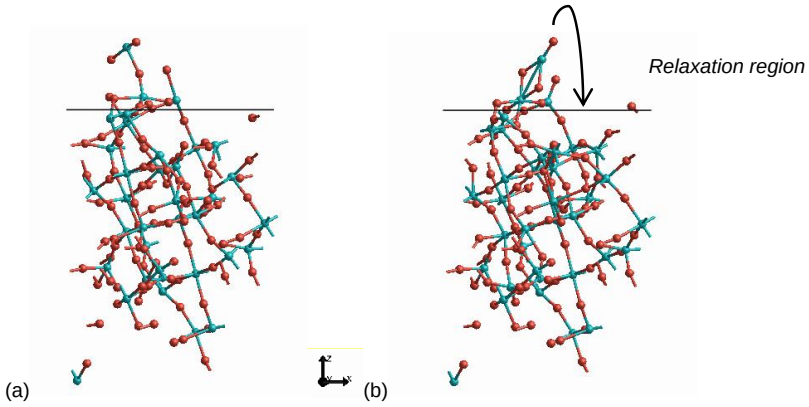

Figure 4.6-19 Cleaved (1 -1 1) surface of α-$ZrMo_2O_8$ illustrating (a) unrelaxed and (b) relaxed state. Surfaces were generated in GDIS. The molecular structure contains Zr atoms(light green), Mo atoms (dark green) and O atoms (red).

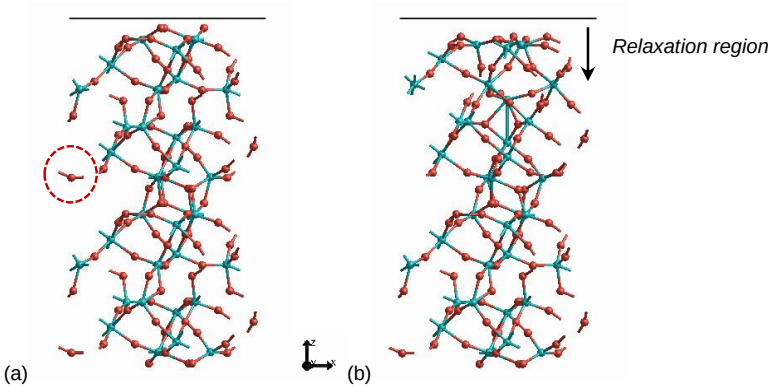

Figure 4.6-20 Cleaved (0 0 2) surface of α-$ZrMo_2O_8$ illustrating (a) unrelaxed and (b) relaxed state. Surfaces were generated in GDIS. The molecular structure contains Zr atoms(light green), Mo atoms (dark green) and O atoms (red).

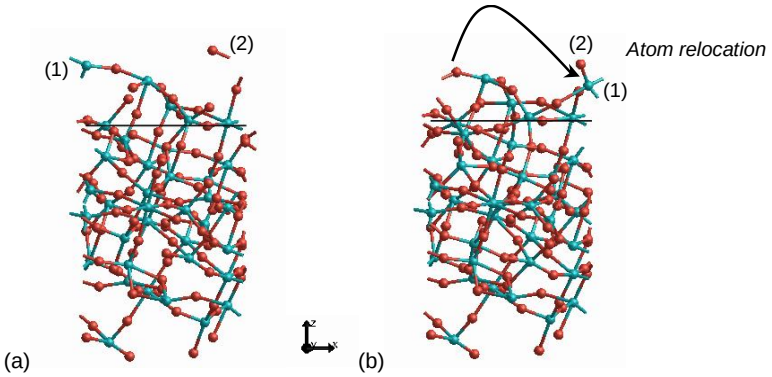

Figure 4.6-21 Cleaved (1 0 -2) surface of α-$ZrMo_2O_8$ illustrating (a) unrelaxed and (b) relaxed state. Surfaces were generated in GDIS. The molecular structure contains Zr atoms(light green), Mo atoms (dark green) and O atoms (red).

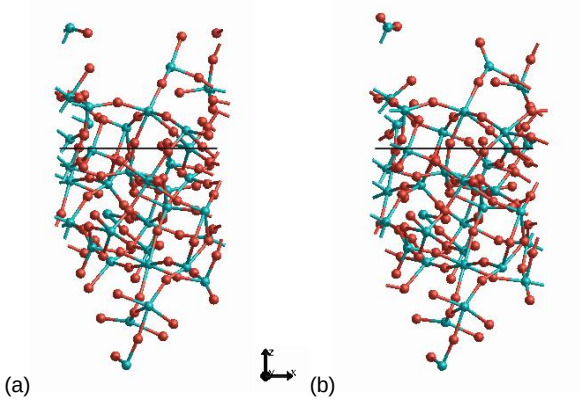

Figure 4.6-22 Cleaved (1 -1 2) surface of α-$ZrMo_2O_8$ illustrating (a) relaxed and (b) unrelaxed state. Surfaces were generated in GDIS. The molecular structure contains Zr atoms(light green), Mo atoms (dark green) and O atoms (red).

Figures 4.6-17 – 4.6-22 illustrate the movement of the atoms located on the surfaces to achieve optimum minimum energy within the structure. The energy difference indicates the stability of the surfaces and therefore can be related to the overall surface and attachment energies. For the α-$ZrMo_2O_8$ phase, the (1 -1 0) surface is illustrates the greatest difference during

relaxation. The increased degree of atomic compression indicates this surface to be the most unstable. The lone oxygen atoms, illustrated in figure 4.6-21, the (1 0 -2) face, create further challenges by increasing the surface dipole. However, during matrix transformation and atomic relocation upon minimisation the effects can be greatly reduced. This can be further analysed by comparing the energy values post minimisation.

Surface and attachment energies for α-$ZrMo_2O_8$ were calculated using GDIS. The energies for both unrelaxed and relaxed surfaces for the relevant faces have been calculated and presented in Table 17.

Table 17 Surface and attachment energies for unrelaxed (u) and relaxed (r) structures for α-$ZrMo_2O_8$. The data have been calculated using GDIS with the re-defined transformation and translation matrix.

hkl/ shift	Dhkl/ depth	E_{surf} (u) (J/m^2)	E_{att} (u)/unit (eV/mol)	E_{surf} (r) (J/m^2)	E_{att} (r)/unit (eV/mol)
(1-10)	8.148	16.9739	-54.4492	0.5322	-56.528
(1 0 0)	8.148	6.5762	-16.0447	1.4569	-16.0652
(1-11)	6.858	18.2724	-94.479	1.7164	-121.375
(0 0 2)	6.351	2.9725	-9.4783	-0.8084	-20.2934
(10-2)	5.009	7.5273	-160.2757	1.2287	-186.1011
(1-12)	5.009	14.9043	-100.5993	4.631	-103.5247
(1 0 2)	5.009	7.5273	-160.2756	1.2287	-186.1011
(2-10)	4.704	13.9547	-49.9425	1.5601	-131.461
(2-11)	4.411	16.2757	-31.4138	2.3012	-66.1264

Table 17 indicates the change in surface and attachment energies for all important surfaces. The table suggests for all relevant faces post minimisation the decrease in surface energies and increase in attachment energies. As expected, surface energy during minimisation for (1 -1 0) face is reduced by ~180%. This is a significant difference, suggesting it is the most unstable region and a low-density packed surface. The values are supported by figure 4.6-17. In contrast to (1 0 0) where there is a ~0.7% decrease. Figure 4.6-18 supports the values, there is a slight change in two oxygen and zirconium atoms. Furthermore, this surface illustrates a high-density packed surface, thus the degree of atomic compression is reduced. Comparing surface energy values of 4.631 J/m^2 and 0.5322 J/m^2 for (1 -1 2) and (1 -1 0) surfaces, respectively, indicates the (1 -1 2) to have the highest surfaces energy and the (1 -1 0) face to have the lowest surface energy. This is supported by figures 4.6-22 and 4.6-17, where the (1 -1 2) have a significant number of protruding Zr, Mo and O atoms. In contrast the (1 -1 0) face has no atoms located on the surface and furthermore, the distance of the plane to the initial section of region is far greater than any of the relevant

surfaces. This relationship suggests the surface energies have great dependence on the interatomic interactions both on the surface of the relevant face and in the bulk.

Morphology predictions for α-$ZrMo_2O_8$ using the BFDH model, calculated surface energies for both relaxed and unrelaxed and calculated attachment energies for both relaxed and unrelaxed are illustrated in figure 4.6-23.

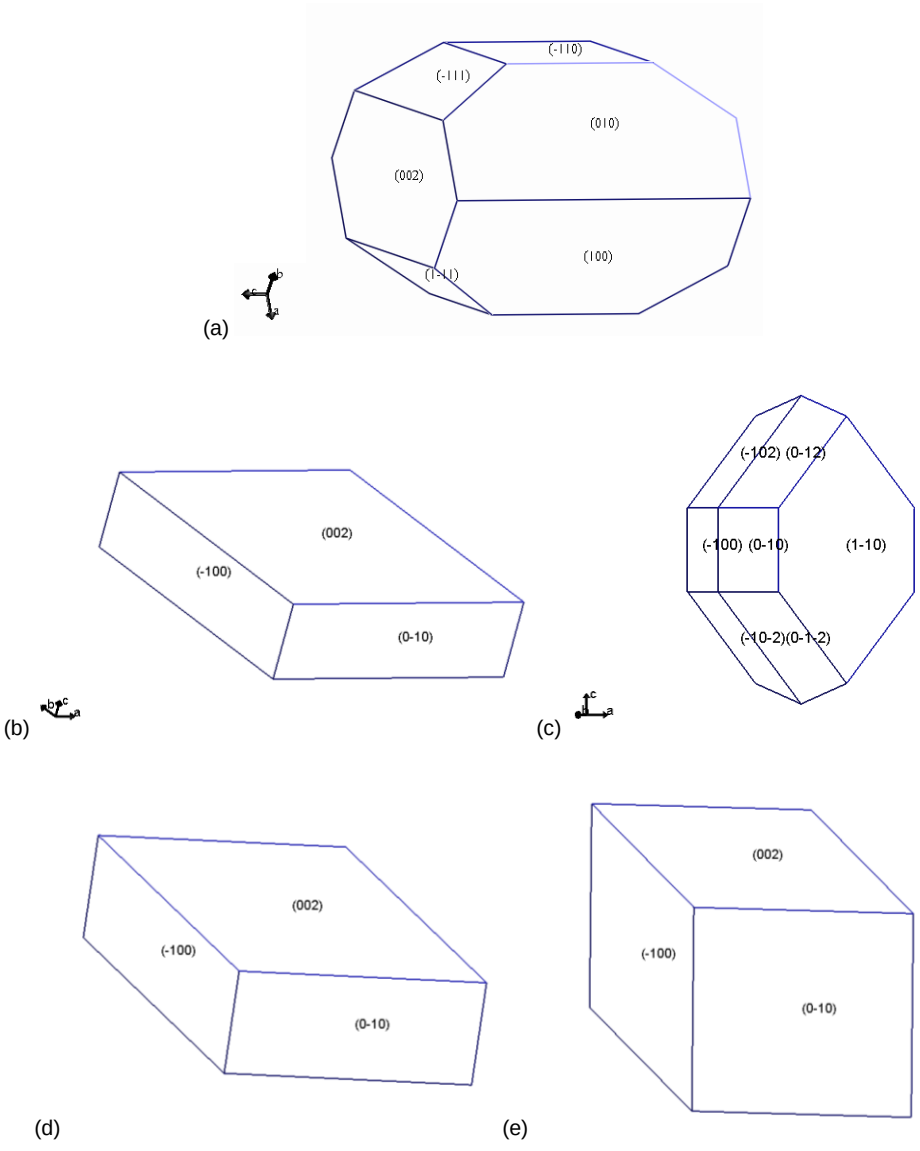

Figure 4.6-23 Morphology prediction of α-$ZrMo_2O_8$ using GDIS. Calculated structures of (a) BFDH, (b) unrelaxed morphology using surface energies (c) relaxed morphology using surface energies, (d) unrelaxed morphology using attachment energies and (e) relaxed morphology using attachment energies.

Figure 4.6-23 illustrates the distinct similarities of all calculated morphologies, all predictions (with the exception of the calculated relaxed surface energy model) illustrates the prominent (0 0 2) face growing along the c-axis. The BFDH is similar to the one predicted by MS, illustrating a

hexagonal prism. Figure 4.6-23 (a) however consider fewer plane and illustrate a hexagonal (0 0 2), similar to the MS BFDH, attached to a bipyramidal structure consisting of (1 1 0), (1 0 0) and (0 1 0) planes growing perpendicular to the c-axis. Unrelaxed surface energy and attachment energy models illustrate a flat cuboidal morphology. The attachment relaxed model predicts a larger cubic morphology. The predicted morphology using the relaxed surface energy predicts a hexagonal bipyramidal prism, neglected the (0 0 2) face. Consider figure 4.6-20 (a), this illustrates the unrelaxed (0 0 2) surface, highlighted in the red dotted circle is a lone oxygen atom. Upon minimisation atomic relocation occurs and is difficult to obtain the new coordinates. It can be assumed the oxygen atom relocation produces the negative surface energy value of -0.8084 J/m^2 which ultimately leads to the neglection of this surface during morphological prediction.

The same procedure was carried out to calculate the morphology for β-$ZrMo_2O_8$ phase using GDIS. Figure 4.6-24 illustrates the unit cell before and after minimisation, thus revealing structural differences between the unrelaxed and relaxed state. The calculations were carried out at a constant volume, surface planes were created from the relaxed bulk structure.

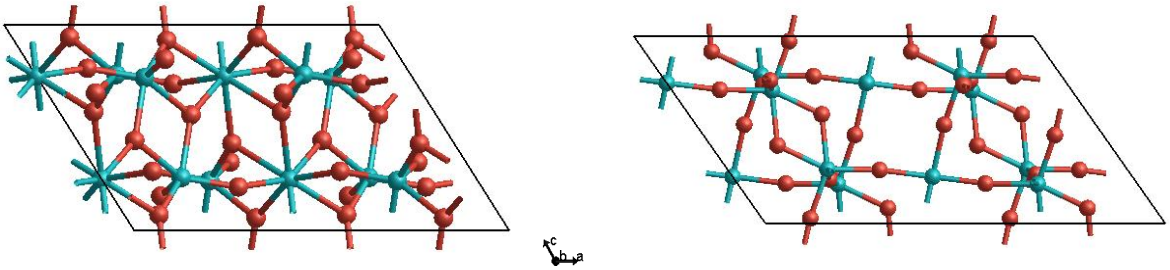

(a) (b)

Figure 4.6-24 Crystalline structures of β-$ZrMo_2O_8$ illustrating the structural difference between (a) unrelaxed and (b) relaxed state.

Figure 4.6-24 illustrates the 2.90% decrease in lattice energy during optimisation. The initial unit cell illustrates a high-density structure, which results in an overall smaller energy decrease when compare to α-$ZrMo_2O_8$. Post minimisation, the structure illustrates a confined and uniform atomic arrangement within the unit cell.

Similarly to α-$ZrMo_2O_8$ structure, surface reconstruction has been considered to remove the large dipoles contained on the surfaces. Surface cleavage, post bulk minimisation, produced many surfaces with dipoles. Thus, the application of symmetry operators on atomic positions of β-$ZrMo_2O_8$ has been considered. This procedure requires the manipulation of the transformation (3 x 3) and translational (3 x 1) matrix.

The initial matrix configuration is expressed below

$$\begin{pmatrix} 1 & 0 & 0 \\ 0 & 1 & 0 \\ 0 & 0 & 1 \end{pmatrix} + \begin{pmatrix} 0 \\ 0 \\ 0 \end{pmatrix}$$

Application of this matrix indicated the majority of the surfaces exhibited a surface dipole for {1 -1 0}, {0 1 -1}, {1 1 -1} and {2 -1 -1} planes. The manipulated matrix is expressed below

$$\begin{pmatrix} -1 & 0 & 0 \\ 0 & -1 & 0 \\ 0 & 0 & -1 \end{pmatrix} + \begin{pmatrix} 0 \\ 0 \\ 0 \end{pmatrix}$$

Application of this matrix resulted in the cleavage of all surfaces without a large dipole. The atomic coordinates with respect to the re-defined matrix is illustrated in figure 4.6-25.

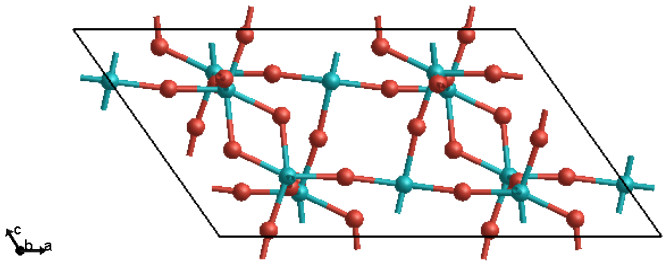

Figure 4.6-25 Crystalline structure of β-$ZrMo_2O_8$ with new translated atomic coordinates after the application of the re-defined matrix.

Figure 4.6-25 illustrates the inversion of the atomic coordinates. The inversion produces a wide range of 0-dipole surfaces for an accurate morphological prediction. Based on the developed fractional coordinates, surface and attachment energy calculations were carried, the results are presented in Table 18.

Table 18 Surface and attachment energies for unrelaxed (u) and relaxed (r) structures for β-$ZrMo_2O_8$. The data have been calculated using GDIS with the re-defined transformation and translation matrix.

hkl/ shift	Dhkl/ depth	Esurf (u) (J/m^2)	Eatt (u)/unit (eV/mol)	Esurf (r) (J/m^2)	Eatt (r)/unit (eV/mol)
1 -1 0	6.3513	6.6083	-72.9159	2.1335	-60.5703
2 0 0	5.8235	6.3749	-2.2644	1.8573	-17.6423
1 1 -1	5.5573	10.7885	-98.8212	2.7511	-19.0822
2-1-1	5.0156	11.5680	-62.6876	2.5593	-80.5340
2 -1 0	4.6173	7.3814	-78.9467	2.5228	-74.6702
2 0 -2	4.0877	11.9772	-29.7354	2.3927	-32.7015
3 -1 -1	4.0204	9.2224	-171.8023	2.2260	-12.4169
1 -1 1	4.0204	7.0285	-93.7259	2.0195	-85.4121
0 2 0	3.7885	3.2406	-18.4401	1.6430	-20.3448

Table 18 presents the calculated surface and attachment energy values for unrelaxed and relaxed structures. Post minimisation the (1 1 -1) face has the highest surface energy value of 2.7511 J/m^2. The lowest surface energy values are 1.8573 J/m^2 and 1.6430 J/m^2 for (2 0 0) and (0 2 0) faces, respectively. This is indicative of lower interatomic interactions on the latter surfaces.

Morphology predictions for β-$ZrMo_2O_8$ using the BFDH model, calculated surface energies for both relaxed and unrelaxed and calculated attachment energies for both relaxed and unrelaxed are illustrated in figure 4.6-26.

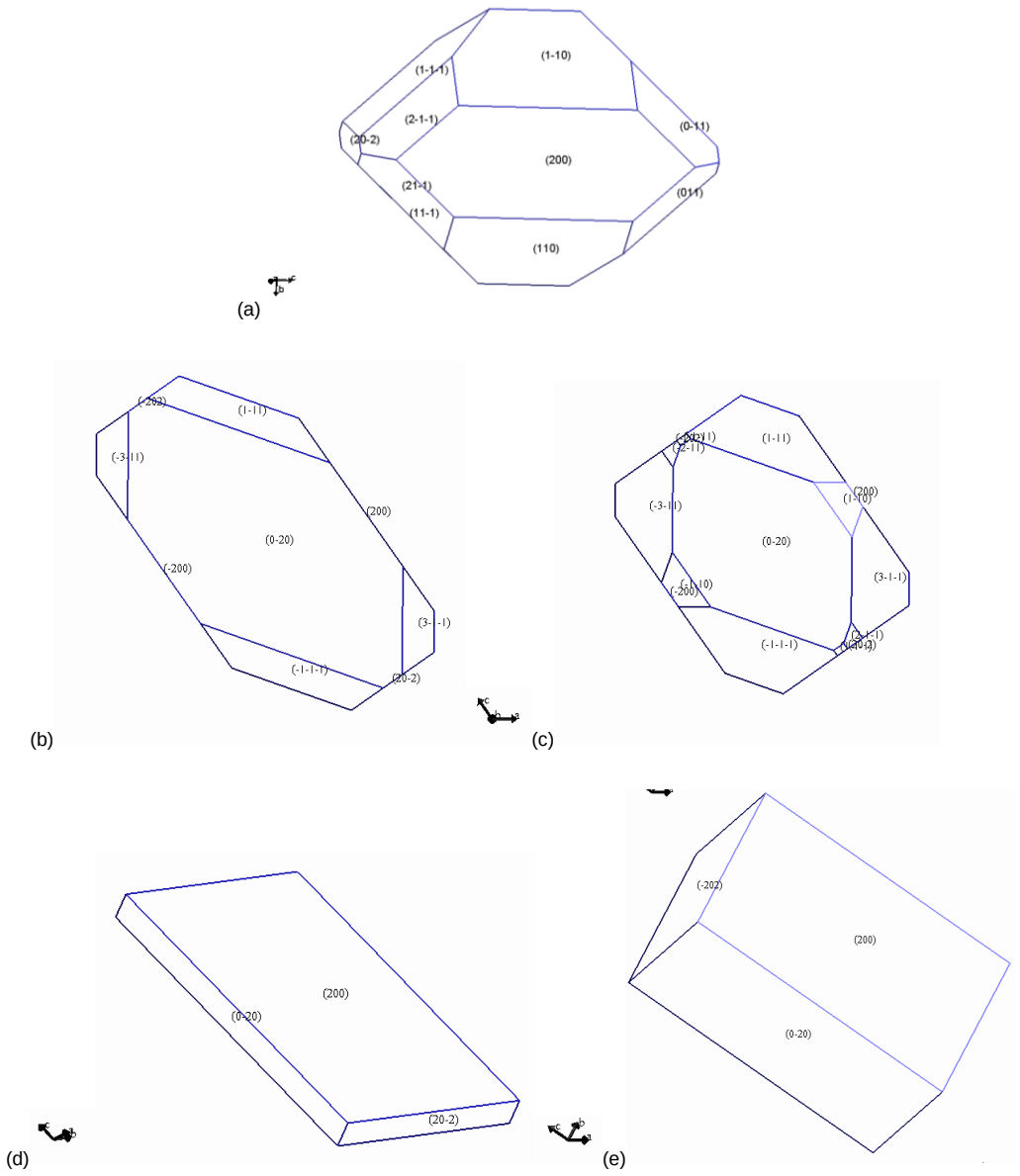

Figure 4.6-26 Morphology prediction of β-$ZrMo_2O_8$ using GDIS. Calculated structures of (a) BFDH, (b) unrelaxed morphology using surface energies (c) relaxed morphology using surface energies, (d) unrelaxed morphology using attachment energies and (e) relaxed morphology using attachment energies.

Figure 4.6-26 illustrates the distinct similarities of all calculated morphologies, all predictions illustrates the prominent face of (2 0 0) growing along the a-axis, (0 2 0) growing along the b-axis and (0 0 2) face growing along the c-axis. The BFDH is similar to the one predicted by MS, illustrating a bipramidal structure. Figure 4.6-26 (a) however considers fewer plane and illustrate a hexagonal (2 0 2) and (2 0 0) planes, similar to the MS BFDH, attached to a structure consisting of (1 1 0), (1 1 1) and (0 1 1) planes growing perpendicular to the c-axis. Surface energy calculations indicate the surfaces with the lowest energy values contribute significantly to the overall morphology of the crystal. Upon minimisation of the surface energy calculation the overall surface area decreases. In particular the (2 0 0) illustrates a large decrease of ~100%. Unrelaxed and relaxed attachment energy models illustrate a flat cuboidal morphology and a larger cuboidal morphology, respectively.

4.6.5 Crystal chemistry of ZMH

Crystallographic data for the hydrated ZM is provided in table 19.

Table 19 Crystallographic data available for hydrated structure of ZM available from ICSD

Crystallographic parameters	$ZrMo_2O_7(OH)_2(H_2O)_2$
Unit cell lengths (a, b, c)	11.45, 11.45, 12.49
Unit cell angles (α, β, γ)	90, 90, 90
Space group	$I4_1CD$ (No. 110)
Number of symmetry operators	16
Number of formula units/ unit cell	8

ZMH (Clearfield et al., 1975) crystallises in a tetragonal crystal system, the space group notation indicates a body-centred lattice with a 4-fold screw axis along the c-axis.

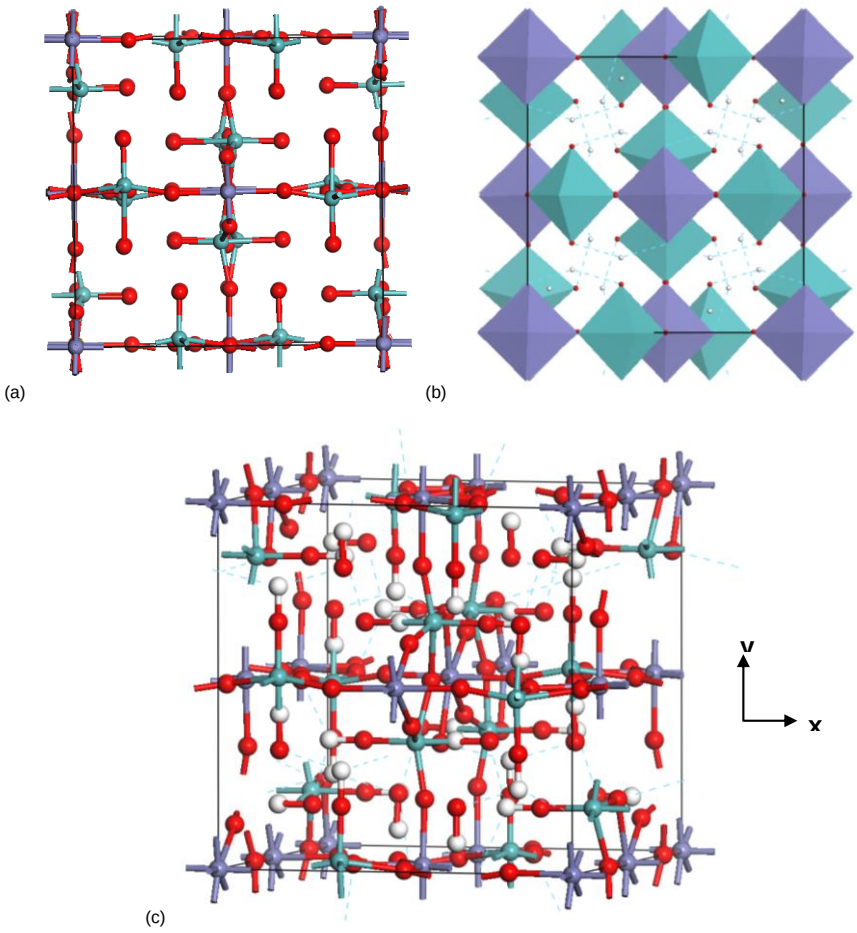

Figure 4.6-27 Crystallographic structure of ZMH obtained from ICSD (Clearfield et al. 1975). The structures illustrate (a) a unit cell without hydrogen atoms (b) polyhedral structure of the ZMH containing H atoms and (c) ball and stick illustration of ZMH containing H atoms. The molecular structure is comprised of Zr atoms (purple), Mo atoms (green), O atoms (red) and H atoms (white).

Figure 4.6-27 (b) illustrates the ZH unit cel consisting of regular ZrO_5 pentagonal bipyramids and MoO_4 tetrahedral bipyramids. It is the Zr-O and Mo-OH bridges which main the strength of the structure. The number molecules/unit cell can be determined be defining the number of Zr atoms located in the unit cell. The location of an atom within the unit cell dictates the overall contribution to the number of molecules. Each atomic location is shared between a number of unit cells and therefore contribute different fractions to the total number of atoms in each cell. Generally there are four main locations which are considered: (1) corner lattice points are shared by eight neighbouring cells and therefore contribute 1/8 to each atom; (2) face centre lattice points share by two unit cells and contribute ½ to each atom; (3) edge centre lattice points shared by 4 units cells and contribute to ¼ to each atom; (4) body centre lattice points are not shared and therefore contribute to one whole atom. Consider the Zr atoms within the unit cell

$$8\ corner\ atoms \rightarrow 8 \times \frac{1}{8} = 1$$

$$4\,edge\,atoms \;\rightarrow\; 4 \times \frac{1}{4} = 1$$

$$10 face\,atoms \;\rightarrow\; 10 \times \frac{1}{2} = 5$$

$$1 body\,atom \;\rightarrow\; 1 \times 1 = 1$$

Considering the calculation of the Zr atomic positions it can be confirmed the total number of Zr atoms within the unit cell is 8 and therefore a total of 8 molecules.

The morphology prediction for ZMH crystal structure implements the BFDH model. The prediction is illustrated in figure 4.6-28, using MS.

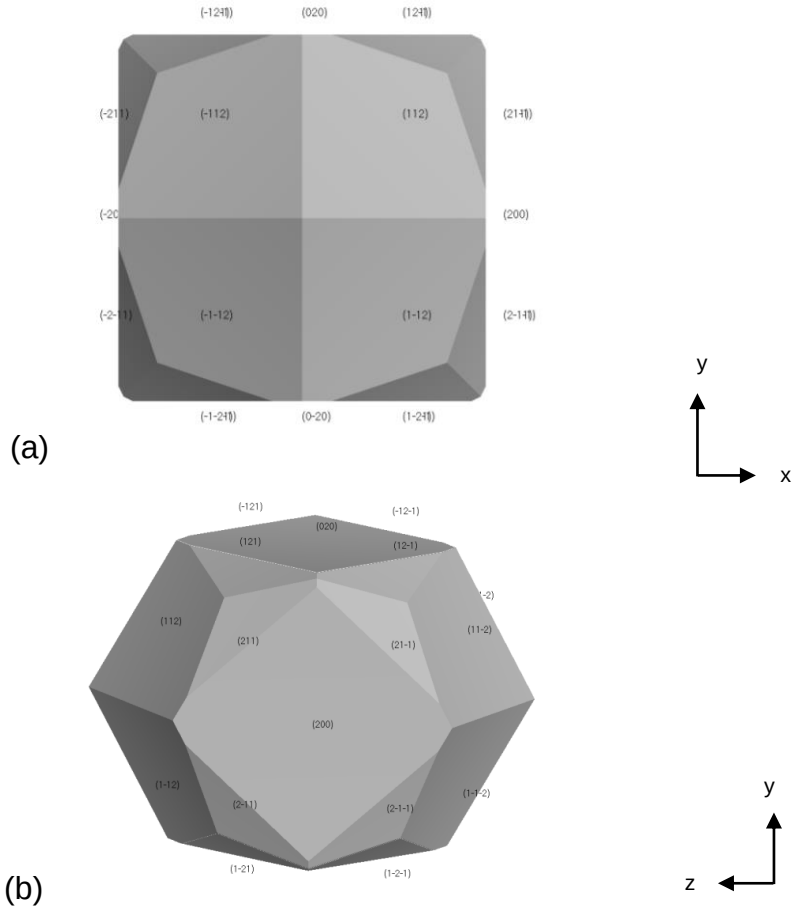

Figure 4.6-28 Prediction of the BFDH calculated morphology for ZMH illustrating the projection along (a) y and x-axis and (b) y and z-axis. Structures are predicted using MATERIALS STUDIO.

The morphological predictions based on the BFDH model illustrate for ZMH (Figure 4.6-28) crystal structures the dominant faces of {2 0 0} and {0 2 0} have the largest surfaces area. Planar faces belonging to the {1 1 2} family, growing along the c-axis illustrates these faces are responsible for the deviation from the cubic morphology. In contrast, the planes {2 0 0} growing along the a-axis and {0 2 0} growing along the b-axis. Thus, projection of the

BFDH model perpendicular to the x-axis indicates an almost cubic morphology.

4.6.6 Effect of citric acid on ZMH morphology

Preliminary morphology predictions on ZMH crystals are explored. As mentioned in Chapter 3, the addition of the organic additive *vis*. citric acid manipulates the ZMH morphology. Thus, this section aims to apply surface chemistry analysis and morphology predications, based on the BFDH model, to validate assumptions made from the experimental data.

The main assumption is the inhibition of growth of a particular surface. It is key to define the main faces which contribute to the growth and thus the morphology of the ZMH crystal. Previously, MS calculated the 6 dominant faces to be {2 0 0}, {-2 0 0}, {0 2 0}, {0 -2 0}, {1 1 2} and {-1 1 2} as shown in figure 4.6-28 (BFDH ZMH). The predicted BFDH morphology does not satisfy the experimental ZMH structures. Further analysis on the growth directions and growth faces, complimented with Space group analysis have led to the determination of the 6 main faces which contribute to the external morphology of ZMH crystals. Consider the SEM image of the cubic ZMH, the relative growth directions and planes are illustrated figure 4.6-29.

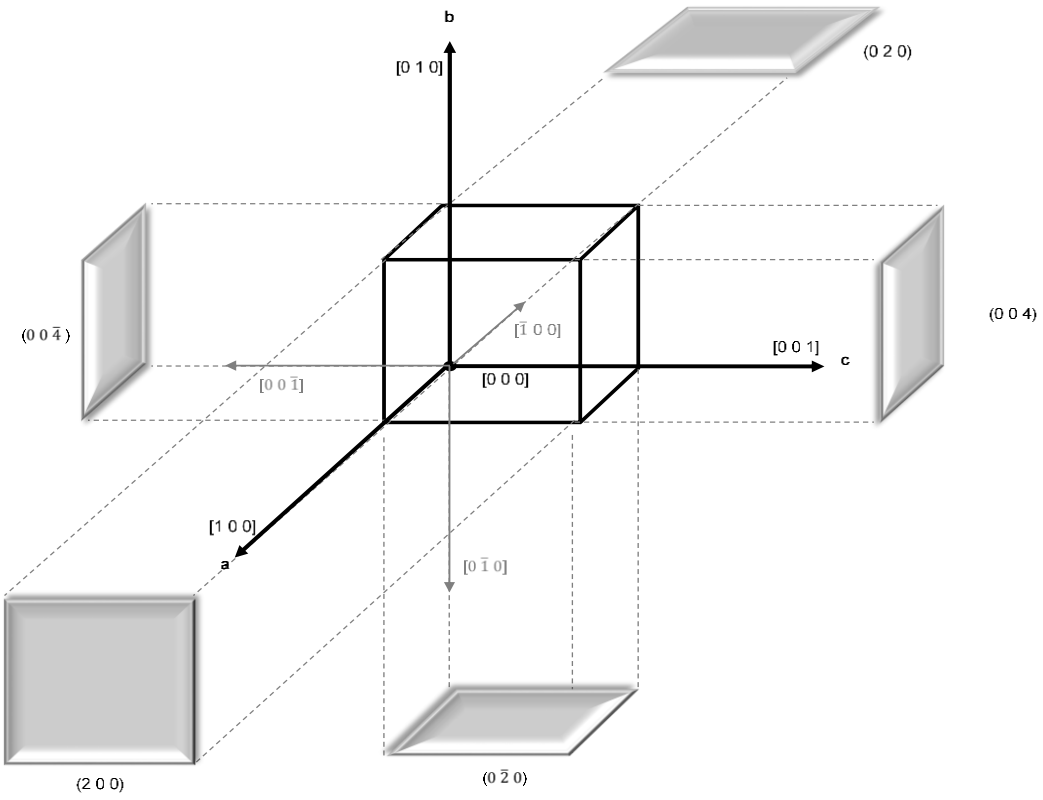

Figure 4.6-29 Growth directions (square brackets) and respective planes (round brackets) for ZMH cubic morphology.

The growth planes illustrated in Figure 4.6-29 have been derived from the space group. The Hermann-Mauguin space group notation for ZMH structure is $I4_1cd$, as illustrated by the XRD patterns both ZMH and ZMCA have identical structures thus the crystallographic parameters remain identical. The space group suggests a body centred tetragonal lattice structure, denoted by I. The object is repeated by the point group symmetry of 4/mm parallel to the c-axis. This is a 4-fold screw axis with an anticlockwise rotation of 90^o, the unit of rotation is $1/4c^o$ parallel to the c-axis. Perpendicular to the a- and b-axis are the c-axial glide planes with a unit translation of $1/2c^o$ in a direction parallel to the c-axis. Perpendicular to the directions 45^o from a- and b-axis and 90^o from the c-axis are the diamond glide planes, with a translation of $1/4a^o+1/4b^o+1/4c^o$. The growth faces have been determined by the four-fold symmetry along the c-axis due to the tetragonal structure, thus denoting growth faces (0 0 4) and (0 0-4), illustrated in figure 4.6-29.

The growths faces were then used for morphology prediction. The software package, MERCURY, calculated the morphology and the respective relative growths rates. The morphology for ZMCA crystals has been predicted through the manipulation of the relative growth rates. The values are presented in table 20.

Table 20 Relative growth rates for dominant surfaces for ZMH and ZMCA structures.

Face	Relative growth rates	
	Natural growth environment ZMH	Addition of organic additive ZMCA
{2 0 0}	17.4672	3.2669
{-2 0 0}	17.4672	3.2669
{0 2 0}	20.2228	4.4216
{0 -2 0}	20.2228	4.4216
{0 0 4}	21.1065	21.1065
{0 0 -4}	21.1065	21.1065

Table 20 suggest the {2 0 0} face is the slowest growth face. Analysis of the surface chemistry for the relevant surfaces validated the assumption that the citratomolybdate complex (Zhou et al., 1997), Figure 4.6-30, is likely to attach onto a particular surface and inhibit growth.

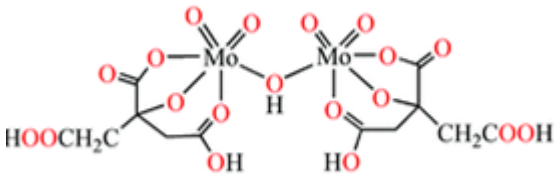

Figure 4.6-30 Chemical structure of the citratomolybdate complex responsible for inhibiting growth of surfaces {2 0 0}, {0 0 -2}, {0 2 0} and {0 -2 0}.

Figure 4.6-30 illustrates the citratomolybdate complex to be a non-centrosymmetric with cis-arrangement of the citrate ligands. The chemical structure allows attachment to specific surfaces, where only the concave part of the complex is available for interaction.

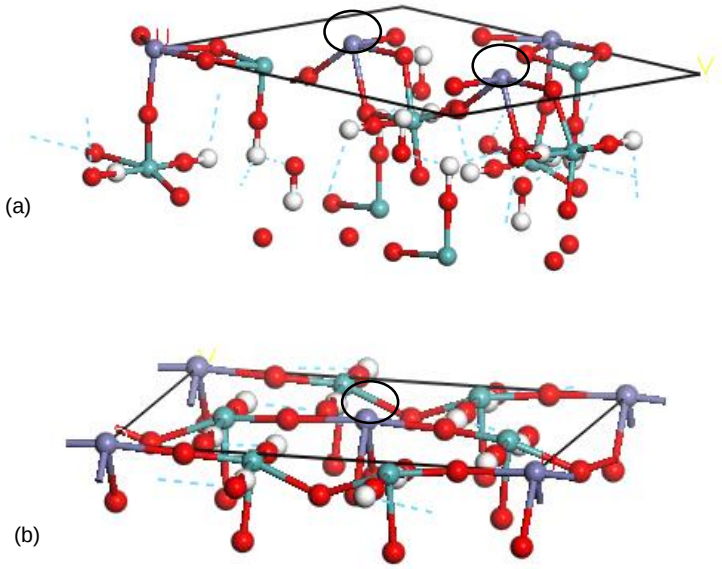

Figure 4.6-31 Cleaved growth surfaces of (a) {2 0 0} and (b) {0 0 4}. The black circles emphasise the availability of Zr sites on each surface.

Figures 4.6-30 and 4.6-31 indicates the citratomolybdate complex and the {2 0 0} and {0 0 4} surfaces. It is evident the inhibition of the {2 0 0} is likely due to a higher number of Zr available sites for the Mo-O-Mo interaction. In contrast to the {0 0 4}, where there is one available Zr site for interaction. The citratomolybdate complex is attaches onto the {2 0 0}, {-2 0 0}, {0 2 0}, {0 -2 0} faces where the growth of all four planes is inhibited, whereas the {0 0 4} and {0 0 -4} faces continue to grow. Thus the relative growth rates have been adjusted accordingly and the morphological predictions are illustrated in figure 4.6-32.

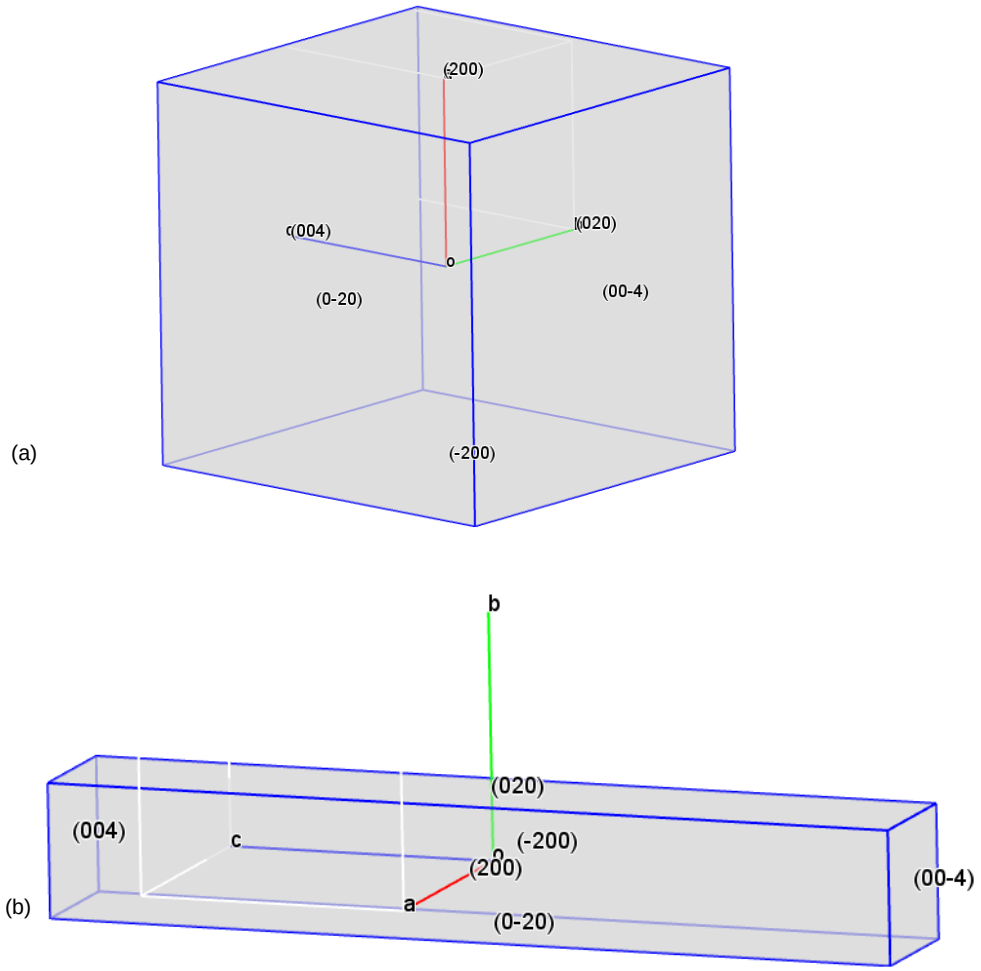

Figure 4.6-32 Morphological prediction of (a) cubic ZMH and (b) cuboidal ZMCA crystals. The BFDH model using MERCURY software was implemented to obtain the predicted structures.

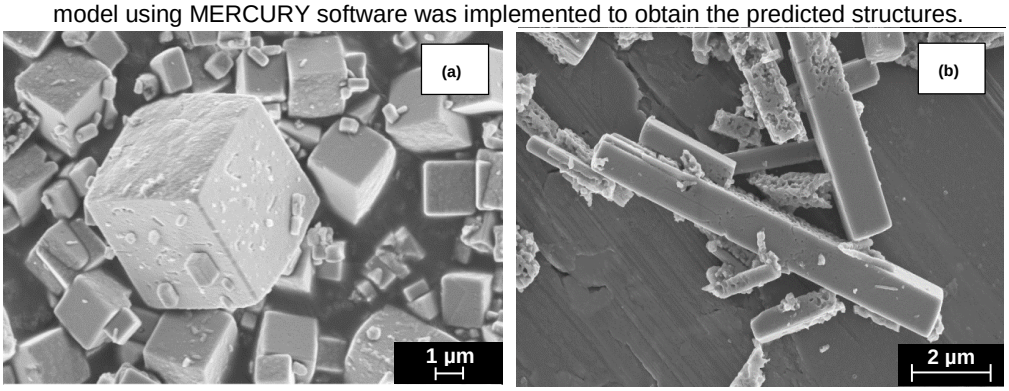

Figure 4.6-33 SEM images of (a) cubic ZM and (b) cuboidal ZMCA crystals. The crystals were obtained by a precipitation reaction (as discussed in Chapter 3).

Predicted morphology of ZMH and ZMCA illustrates (Figure 4.6-32) an excellent agreement with the crystal morphologies obtained through experimentation (Figure 4.6-33). Thus it is evident that application of surface chemistry analysis, growth plane derivation and manipulation of the relative growth rates of the specific forms, is able to validate the assumption made from the experimental data. Addition of the organic additive, citric acid, forms

a citratomolybdate complex. Due to the increased availability of the Zr sites on the {2 0 0}, {-2 0 0}, {0 2 0}, {0 -2 0} faces and the bent angle Mo-O-Mo of the additive complex, the growth of the surfaces are inhibited. The growth of the {0 0 4} and {0 0 -4} in the [0 0 1] and [0 0 -1] direction, along the c-axis continues. Thus, the elongated morphology of cuboidal ZMCA crystals is created.

4.7 Conclusions

This chapter highlights the key parameters required for morphological prediction for highly active nuclear waste simulant, ZM. It is important to define the polymorphs that are likely to be present under specific ambient conditions. High temperature conditions produce monoclinic β-$ZrMo_2O_8$ and cubic γ-$ZrMo_2O_8$. High pressure conditions produce monoclinic δ-$ZrMo_2O_8$ and triclinic ε-$ZrMo_2O_8$. Various methods were implemented to predict the morphology for both anhydrous α-$ZrMo_2O_8$ and β-$ZrMo_2O_8$ phases**.** The polymorph present in the experimental section (see Chapter 3) is the ZMH phase. Qualitative analysis of the ZMH and ZMCA morphological predictions are consistent with synthesised particles in Chapter 3.

- BFDH model. Predicted a hexagonal prism and a pentagonal prism for α-$ZrMo_2O_8$ and β-$ZrMo_2O_8$, respectively. This model considers planes with respect to the d-spacing and therefore neglecting interatomic interactions and charges on each plane. This supports the consideration of a larger number of surfaces on the morphology using this method. Surfaces with the largest d-spacing dominate the overall morphology.
- Surface energy model. Single surface method there the surface and layers of atoms below the surface undergoes significant atomic relaxation. The surface energies are dependent on the type and number of interatomic interactions on the surface. Surfaces with the lowest energy dominate the overall morphology.
- Attachment energy model. Considers the overall energy release on attachment of a growth slice. Surfaces with lowest attachment energy values dominate the overall morphology.

All methods predicted morphologies in agreement. It is possible to suggest the surface and attachment energy methods are more accurate forms of prediction as it considers interatomic and intermolecular interactions and atomic properties. Preliminary morphological predictions for ZMH morphologies relates well to experimental forms. Application of the

symmetry and crystallographic properties enables the determination of the relative growth planes. The manipulation of the relative growth rates of the relevant planes confirmed the assumption made during experimentation. The increased number of Zr sites on the {2 0 0} and {0 2 0} planes increases the probability of the citratomolybdate complex to attach and thus inhibit growth in the x and y directions. Ultimately the change in morphology from cubic ZMH to cuboidal ZMCA is exhibited.

This work has demonstrated a molecular modelling approach to predict the morphology for anhydrous ZM forms. It is believe the ZMH crystals are present in the HASTs. Development from this work enables opportunities to predict the morphology for the ZMH structure. The locations of the water and hydroxyl groups need to be clearly defined for lattice energy optimisation and the morphological prediction using the surface and attachment energy models. It is important to understand the possible mechanisms of radionuclei adsorption which can ultimately to lead morphological change. Change in morphology impacts process plant operations and therefore it is necessary to define the change in crystal chemistry for current processing and POCO of highly active nuclear waste.

The ultimate aim is to link the particle morphology to the sedimentation and rheological properties of the materials. It is the impact of cubic verses cuboidal and the potential to understand how to modify the particle morphology using tailored additives in order to optimise the sedimentation and rheological behaviours. Critically, the behaviour of HAL determines the efficiency and safety of process operations. The influence of particle morphology on key behaviours (sedimentation and rheology) are discussed in Chapters 5 and 6.

5 Influence of particle properties on sedimentation behaviour

Summary

This chapter describes the use of appropriate sedimentation techniques, Turbiscan and Lumisizer, to establish the effect of solid-liquid properties on sedimentation behaviour. This includes particle volume fraction, particle properties, influence of background electrolyte, sediment bed analysis.

5.1 Introduction

HAL solids are known to precipitate from solution during the evaporation process and during storage within the HASTs. The formation of settled beds in the evaporators, storage tanks and pipelines during transport enhance the challenges of spent fuel processing. Localised heat spots which leads to the promotion of corrosion, due to the active Cs^+ radionuclides, compromises the integrity of the infrastructure. Challenges may additionally occur regarding POCO, where transport of residual solids will be required. It is therefore, essential to understand the sedimentation behaviour and in turn inhibit or reduce the settling rate of HAL solids.

This chapter focuses on the influence of particle properties, discussed in Chapter 3, on sedimentation behaviour. Morphology control, to produce ZMCA, is proposed to reduce deposition of particles due to the elongated cuboidal nature. By dispersing in 2M HNO_3, in contrast to DI water, we probe settling behaviours relevant to current processing and associated POCO operations. Two techniques, gravitational and centrifugal settling, will be employed and compared.

5.2 Literature review

5.2.1 Sedimentation fundamentals

Sedimentation is a phenomenon where, in a two phase suspension, the solid particles settle out to create a sediment bed. The sedimentation of particles is important to technology whether it be on an industrial or laboratory scale. For industry, the design of separation equipment requires a good working knowledge of the sedimentation behaviour. Several industrial separation techniques are listed:

- Gravitational clarifier used in water treatment to separate impurities (solid) from water through coagulation and flocculation. The efficiency of the clarifier is increased as the coagulation and flocculation processes cause fine particles to aggregate and form a dense bed upon sedimentation.
- Cyclones to separate particles from gas or liquid streams with a combination of gravitational and centrifugal forces, commonly used in food processing. A typical process involves the removal of water from liquid foodstuff such as tomato juice (Sassi, 1996).
- Gravimetric API separator to remove oil and suspended solids from waste water effluents of petrochemical plants. The design standards

of this separator are published by the American Petroleum Institute (API)(Beychok).

Sedimentation analysis is governed by fundamental criteria of the measurement and suspension arrangement within the sedimentation vessel. Homogeneity of particles within suspension across the sample matrix, particle concentration and the force field applied (gravitational or centrifugal) are key parameters for sedimentation analysis.

5.2.1.1 Particles falling under gravity through a fluid

Sedimentation requires the understanding of the contribution of forces which resist the motion of any particle through a fluid under gravity. Stokes law (Stokes, 1851) defines the relative motion of spherical particles in a fluid under gravity. Three forces which are acting on the sphere are the drag force (F_d) of the fluid (acting upwards), the buoyancy effect (F_b) which is the weight of the displacing fluid (acting upwards) and the gravitational force (mg) (acting downwards). By combining the forces and the volume of the sphere an equation can be derived to obtain the overall settling velocity of the particle. The summation of the forces acting on a particle:

$$F_b + F_d = mg \qquad 5.2\text{-}1$$

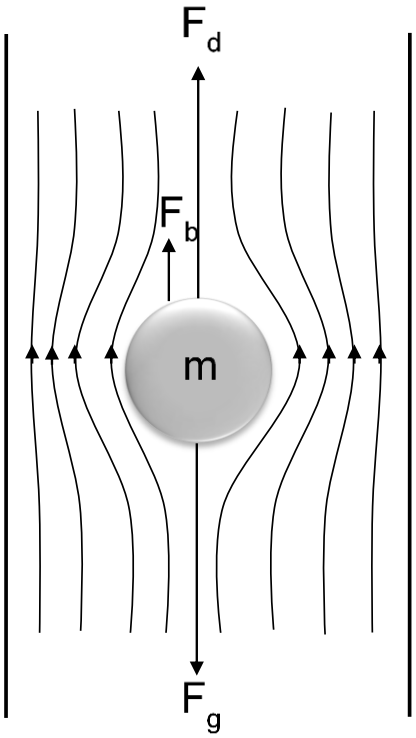

Figure 5.2-1 The image illustrates the forces contributing to the motion of a spherical particle in a fluid in the laminar region under gravity.

Figure 5.2-1 illustrates the applied drag force applied by the surrounding, incompressible fluid acting on the falling particle. The drag force defines a dependence on the Reynolds number which considers the inertial and viscous forces within a volume of fluid. At high Re number, the inertial forces disrupts the fluid flow field and this results in turbulent flow. A low Re numbers, the fluid flow field is undisrupted and uniform, thus creating a laminar flow. Consider a free settling particle with a low velocity, relative to the surrounding fluid, the derivation of the drag force in the laminar region (Re<0.1) (Macmillan, 2010, Stokes, 1851) can be defined as

$$F_d = 6\pi\mu U d \qquad 5.2\text{-}2$$

Where μ is the fluid viscosity, *U* is the velocity of the sphere relative to the fluid and *d* is the diameter of the sphere.

The buoyancy force requires the mass density of the fluid (m_{df}) and the gravitational acceleration:

$$F_b = m_{df} g \qquad 5.2\text{-}3$$

The volume of sphere can be taken into account and manipulate the above equation:

$$v_{sphere} = \frac{4}{3}\pi r^3 \qquad 5.2\text{-}4$$

Where *r* is the radius of the sphere. Due to the fact that $m = \rho \times v$ the buoyancy force equation can be represented by

$$F_b = m_{df} g = \frac{4}{3}\pi r^3 \rho_{fluid} g \qquad 5.2\text{-}5$$

Combining the equations which portray the force, equation can now be expressed as

$$\frac{4}{3}\pi r^3 \rho_{fluid} g + 6\pi\mu U d = mg \qquad 5.2\text{-}6$$

Initial conditions of a spherical particle falling from rest under gravity will exhibit high velocities as the shear drag is relatively small. The drag force forces increases as the particle continues to accelerate, hence reduce the acceleration. Ultimately a force balance is achieved when the acceleration is zero and thus a terminal velocity is attained and expressed in Equation 5.2-7 by the Stokes law (Stokes, 1851)

$$U_T = \frac{2r^2\left(\rho_{sphere} - \rho_{fluid}\right)g}{9\mu} \qquad 5.2\text{-}7$$

From Stokes law the sedimentation of a particle is dependent on the solid properties such as the density; the fluid properties such as the viscosity,

density and the interparticle interactions as well as the solute-solvent interactions.

Fully understanding the behaviour of sedimentation requires knowledge of the issues involved (Russel et al., 1989, Bernhardt, 1994, Franks, 2008)

- The effect on the settling velocity when the volume fraction is varied.
- The contribution of interparticle interactions when the volume fraction is varied.
- Particle properties
- Fluid properties
- Temperature

Centrifugation provides an enhanced force field for sedimentation to occur (Ambler, 1961). Force is represented as $F = ma$, where *F* is the force (N), *m* is the mass (kg) of particle and *a* is the acceleration (m/s^2) this represents the gravitational force. Centrifugal force is expressed as $F = \omega^2 r$ where ω is the angular velocity (radians) and *r* is the radius of rotation (m).

Key assumptions of the Stoke's law consider smooth, rigid and spherical particles; low particle concentration such that no wall effects are accountable for; particles are in the laminar regime (Re < 0.2); no temperature influence. Particle characterisation techniques in Chapter 3 define HAL waste to contain non-spherical charged particles, where the overall stability of the suspension is dictated by the concentration of H^+ and OH^- ions. HASTs store HAL under controlled agitation systems. Currently each jet ballast is fired for 80 s, the full cycle for firing all 7 ballasts is ~30 mins. As considerable force is applied the flow field around the particles during sedimentation becomes complex as it deviates from the laminar region. Considering the complexities of the HAL solids and storage conditions it is expected the settling behaviour will deviate from classical the Stokes regime and enter the hindered settling regime.

5.2.2 Settling regimes

A typical settling test requires the analysis of a solid-liquid interface as a function of time. There are four main sedimentation regimes that describe the behaviour of the settling particles from suspensions. A batch settling test allows the determination of the distinct settling regimes where the change in height of the solid-liquid interface as a function of time is monitored. The settling of particles depend on:

- The characteristics of the particles, whether they are discrete or flocculating.
- The concentration of particles in suspension, creating either a dilute or concentrated suspension.

The characteristic determine which regime the particles settling in, as illustrated by Figure 5.2-2.

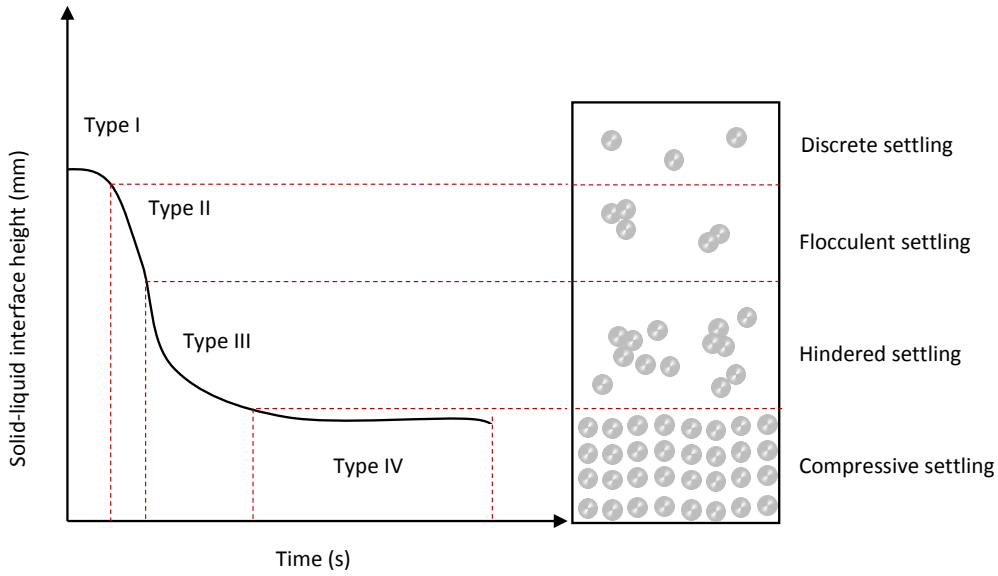

Figure 5.2-2 Key settling regimes of particles in a dispersion

Type I, known as the discrete settling region. In this region the settling of particles occur in a dilute suspension where the particle have no tendency to change size and shape, under gravity with time. The particles settle as individual bodies and do not interact with neighbouring particles.

Type II, known as flocculent settling. This region is dependent on particle properties (size, shape and density), the degree of aggregation and size polydispersity of the particulate system. Aggregation of particles may occur in this region, the particle collision frequency is directly proportional to the concentration of solids and the level of turbulence encountered by the system. Very high turbulence promotes particle aggregate break-up as well as aggregation. A number of factors depend on the promotion/break-up of aggregation including the strength of interparticle forces, orientation of the particles, relative velocities of particle prior to collision and particle size. In size polydisperse systems, large particles with higher settling velocities surpass smaller particles with smaller velocities, thus creating a dispersion where segregation and sedimentation occur. Systems containing particle

agglomerates have higher settling velocities in this region, compared to un-aggregated systems.

Region III, known as the hindered settling region. The solids concentration here is high enough that particle-particle interactions are significant, which in turn dominates the behaviour of the settling interface. At high particle concentration the strong cohesive forces and/or particle effects, such as particle shape, are able to restrict the movement of the particles. These effects are able to cause significant displacement of fluid, which interfere with the velocity flow field around the neighbouring particles. The particles in the region settle together creating a distinct interface between the clarified liquid and the settling particles.

Region IV, known as the compressive settling region. The solid density is extremely high in this region. The high solid concentration provides a partial mechanical support for the particles above. At this point the mass of particles create a compressed bed above the gel-point and undergo mechanical compression as they settle further. The degree of compression is dependent on the particle properties. The rate of settling in region IV is extremely slow. The compressive function is expressed as

$$H_t - H_\infty = (H_o - H_\infty) e^{m(t-t_o)} \quad \text{5.2-8}$$

Where H_t signifies the height of solids at time *t*, H_∞ is the height of solids at infinite *t*, H_o is the height at initial *t* and *m* is a constant.

Allain et al. (Allain et al., 1995) studied the effect of the change in volume fraction on aggregation and sedimentation behaviour. The main aim of the research was to look at the coupling of aggregates in colloidal systems and see if it influences the settling of the solids. It is suggested in their research that there are three behaviours which the colloidal system undertakes with respect to change in volume fraction.

Behaviour one, at low volume fractions *cluster deposition* is identified. At first the sample shows a well dispersed turbid suspension and after time the particles form aggregates/clusters and tends to settle. Different sizes of aggregates are formed, the larger ones settle more rapidly and, as these larger aggregates settle they entrain smaller aggregates which therefore also settle at the same time. This suggests that all though there is a range of settling velocities of individual aggregates within the suspension, the system behaves uniformly due to the entrainment of the smaller aggregates.

Behaviour two, at higher volume fractions *collective settling* is identified. This is where the aggregates form a gel where collapse of the interface occurs.

The research has found the distinction between the two behaviours in terms of volume fraction, Φ* ≅ 3×10^{-3} distinguishes itself from cluster deposition and collective settling. Behaviour three, where above a certain volume fraction, Φ** ≅ 5×10^{-2}, the particles do not settle.

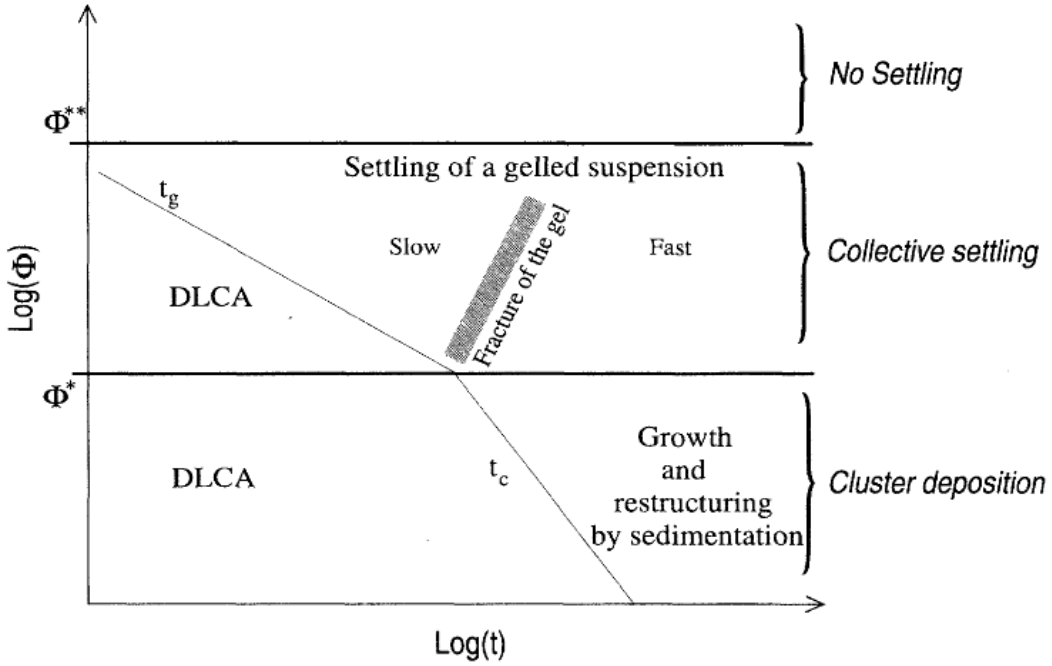

Figure 5.2-3 A graphical representation of distinct mechanisms which takes place when the volume fraction is varied as a function of time; gel time (t_g) and cluster time (t_c) are shown with respect to the behaviour (Allain et al., 1995).

Figure 5.2-3 illustrates the various settling regimes as function of volume fraction. Aggregation is an important factor to consider in colloidal systems, research have identified that the Brownian diffusion of clusters controls the growth rate, therefore it is suggested that diffusion limited cluster aggregation (DLCA) is a plausible model to support this.

As described by Allain et al. (Allain et al., 1995), the sedimentation rate depends on the mechanisms formed by the particles, for instance cluster deposition or collective settling. This suggests that interparticle interactions have an effect on the sedimentation rate. The shape of the particle size distribution can be determined by the sedimenting interface. A sharpe interface suggests that there is a narrow distribution of particle diameters, whereas a broadly spread interface suggests a polydisperse system. There are three factors which takes place which effect the sedimentation interface as proposed by Hassen et al., (Hassen and Davis, 1989)

- Polydispersity of particles
- 'self sharpening effect' of particle concentration

- Self induced hydrodynamic particle diffusion, where fluctuating of particle settling velocities takes place due to hydrodynamic interactions

All these factors relate the sedimentation rate to the interactions of neighbouring particles, if the particles form a large interface the sedimentation rate increases.

5.2.2.1 Hindered settling function

A real dispersion under gravitational settling differs greatly from the behaviour predicted by the Stokes law. Stokes law is based on the free fall of individual particles.

There have been many theoretical and experimental studies carried out to define a hindered settling function for monodisperse systems in a laminar flow (Barkena et al., (1973); (Garside and Al-Dibouni, 1977, Davis and Acrivos, 1985, Davis and Birdsell, 1988). A common function used, is determined by Richardson and Zaki (Richardson and Zaki, 1954)

$$U_o = U_t(1-\emptyset)^n \qquad 5.2\text{-}9$$

This is a mathematical expression for hindered settling velocity, U_o, and considered a correction term for free settling velocity, U_t. This is an empirical relation between settling velocity and solid volume fraction, $\emptyset$. A variable constant, *n*, is dependent on the particle Reynolds number and the vessel diameter. Hindered settling functions describe the reduction in particle velocity with increasing particle concentration. This behaviour is due to

- Interactions of neighbouring particles.
- Fluid flow around the particle. The upward flow created by the downward settling of the particle.

The values for *n* can differ depending on the particle size and the Reynolds number. Table 21 indicates the change in *n* with flow behaviour

Table 21 Values of *n*, a variable constant depending on the Particles Reynolds number. The table is extracted from (Holdich, 2002)

Particle Re Number	*n*
< 0.2	4.65
<0.2 <Re'<1	4.35 $Re'^{-0.03}$
1 <Re'<200	4.45 $Re'^{-0.1}$
200<Re'<500	4.45 $Re'^{-0.1}$
Re'>500	2.39

An empirical value of *n=4.65* is suggested for monodisperse spherical particles in the laminar region of flow.

Suspensions used in industry are known to have wide distributions of size, shape and density, known as polydisperse systems. In initial studies of determining the hindered setting function, Garside et al., (Garside and Al-Dibouni, 1977) designated an empirical value of *n=5.1*. This showed to be in excellent agreement with spherical particles with a low Re number. However, when applied to a polydisperse system, poor agreement to the hindered settling function was expressed.

Many studies have proposed modifications to the Richardson-Zaki hindered settling function, for polydisperse systems (Davis and Birdsell, 1988, Davis and Gecol, 1994, Cheung et al., 1996, Mirza and Richardson, 1979, Masliyah, 1979, Patwardhan and Tien, 1985). A study conducted by Selim et al. (Selim et al., 1983)complements the Richardson-Zaki equation with a correction function including the density of the fluid ρ_f and particles ($\rho_i \; and \; \rho_i$, density of species *i* and *j*, respectively). This equation is expressed in equation 5.2-10

$$U_o = (1 - \emptyset)^{n-1} \left(\frac{\rho_i - \rho_m}{\rho_j - \rho_f}\right) \qquad 5.2\text{-}10$$

The mixture density is a function of the total volume fraction of particles and fluid density. A well-known theory of predicting the sedimentation velocity in polydisperse dilute systems was developed by Batchelor et al., (Batchelor and Wen, 1982)

$$U_o = 1 + \sum_{j=1}^{N} S_{ij} \emptyset_j \qquad 5.2\text{-}11$$

A dimensionless sedimentation coefficient, S_{ij}, is a negative function of the particle radius ratio (a_i/a_j) and the reduced density ratio ($\rho_j - \rho_f / \rho_i - \rho_f$). Therefore the objective of this theory is to account for the wide distribution of particle size and densities within a dispersion. This model is in good agreement for dilute mono- and bidisperse colloidal and non-colloidal dispersions (Al-Naafa and Selim, 1992, Davis and Birdsell, 1988). However, this neglects hydrodynamic effects and has poor agreement with concentrated dispersions. Davis et al (Davis and Gecol, 1994) proposed a hindered settling function with no empirical parameters for concentrated polydisperse systems. The model is expressed in equation 5.2-12

$$U_o = (1 - \emptyset)^{-S_{ij}} (1 + \sum_{j \neq 1} (S_{ij} - S_{ii}) \emptyset_j) \qquad 5.2\text{-}12$$

This model is an extension of the Batchelor model. The sedimentation coefficients are determined from data provided by Batchelor and Wen

(Batchelor and Wen, 1982). It also reduces to the Richardson-Zaki equation for monodisperse systems. This model has good agreement with bidisperse, dilute and concentrated systems.

Davies et al (Davies et al., 1975) expressed the derivation of parameters to describe the hindered settling function. All though the *n* parameter is a beneficial indication to describe the effect of an increase particle volume fraction in reducing the sedimentation rate, the initial porosity indicates an advantage in describing the hindered settling function. Highly hindered systems corresponds to the initial porosity converging to the upper limit of unity, whereas *n* diverges indefinitely to large values.

The study conducted by Davies suggests that hindered settling of silica and china clay suspensions is not only a function of particle volume fraction but also the range and intensity of interparticle interactions, high particle surface potential and fluid properties. Particle-liquid cohesion reduces the effect of density of the solid, which results in the solvated particle-solvated particle repulsion. Reduction in the settling velocity is established as a result of electrostatic repulsions preventing particle-particle cohesion. Factors influencing the hindered settling functions

- High dispersion polarity. An increase in polarity and particle volume fraction increases the effect of reducing the settling velocity.
- Formation of aggregates. Ionic solids form aggregates with the addition of electrolytes, this reduces the solid surface charge density and enhances van der Waals attractive forces. Aggregation of particles promotes particle settling velocity.
- Formation of aggregates increase the particle volume in the compressive settling region. Difficulties in solid-liquid separation under gravity can arise.

A number of experimental techniques have been devised to determine the hindered settling function. A common method is to prepare a sample, involving agitation to homogenise the suspension and to monitor the settling interface in a laboratory measuring cylinder. Once a clear solid-liquid interface is identified, it can be assumed that the sample is in the hindered settling regime. The rate of the settling interface with time can also be extracted.

Davies et al (Davis and Birdsell, 1988), employed a laser transmission technique where the particle volume fraction can be determined at any location within the solid-liquid. The fluid and spherical glass particles were

dispensed in a rectangular vertical glass vessel, with particle concentration range from 0.0003-0.15 vol%. The He-Ne laser beam passed through the suspension, where the application of the Beer-Lambert Law allowed the relation of light absorbency to the calculation of particle volume fraction. The settling velocities of the particulate systems decreases linearly with increasing particle concentration, this is based on the pair-wise interactions. The Richardson-Zaki expression agreed well for the hindered settling velocity of the monodisperse suspensions at the top of the dispersion. The best fit in regression was found when the exponent n = 4.9 for smaller particles and n = 5 for the slightly larger particles.

5.2.3 Effect of particle properties on sedimentation

Settling velocity is a result of several forces acting on a particle in a fluid, as mentioned earlier in the chapter. The drag force depends on the particles' relative speed to the fluid. Therefore, the particle size, shape and density affect the particle settling velocity. Consider a dispersion containing a large dense particle suspended in water (particle density > fluid density). The larger the particle the greater the gravitational force acting upon it. The buoyancy force is a function of the volume of the particle, where it is equal to the water displaced by the particle with an equal volume of the particle. As the particle size and density increases the gravitational force exceeds this buoyancy force creating a net gravitational force. As the downward gravitational force increases, acceleration of the particle and the drag force acting on the particle also increases. For particles of the same density but different size, the settling velocity of the larger particle will always be greater. Similarly, for particles of the same size but different density, the settling velocity of the denser particle will be greater.

Theoretical and experimental studies have been carried out to determine the effects of particle properties on settling velocities of dispersions. It is also important to consider that both particle and fluid properties affect the settling behaviour. Vesaratchanon et al. (Vesaratchanon et al., 2008) conducted sedimentation experiments in a cylindrical flat-bottom glass tube with a length of 40 mm and a diameter of 12 mm. The effects of particle size and shape on the sedimentation rate were explored. Particle interactions play an important role in the behaviour of the suspension, thus when the size of the particle changes the interactions between the neighbouring particles also change. When the size of the particle increases the interactions become less significant and the sedimentation rate increases. Larger particle have a

lower amount of particles present per unit volume, therefore the osmotic pressure is reduced. The results suggested that the particle shape does affect the sedimentation rate to some degree. The ellipsoidal shape showed to have the slowest sedimentation rate, followed by spherical and cylindrical.

Interactions of silica colloids were studied by defining the extent of van der Waals attraction of uncharged particles using a dynamic light scattering technique (Donselaar and Philipse, 1999). The larger particles of silica particles exhibit smaller van der Waals forces in contrast to the smaller silica particles. Conclusions were made that the decrease in sedimentation velocity, due to van der Waals attractive forces. These findings are concentration dependant.

Particle interactions are known to play a significant role in the overall settling velocity. Various studies conducted to determine the impact of aggregate size and surface charge on stability, aggregation and sedimentation (French et al., 2009, Dunphy Guzman et al., 2006, Badawy et al., 2010). Comparison of titanium dioxide and titanium nanotubes on aggregation and sedimentation was conducted by Liu et al (Liu et al., 2013). This study highlights the influence of pH and ionic strength on sedimentation behaviour. An increase in pH values leads to aggregation, where particle size increases from a mean particle size of 20 nm to 1000 nm. The aggregation mechanism not only depends on the pH strength but also on the particle shape, where the spherical TiO_2 particles readily form aggregates, compared to the TiO_2 nanotubes. The increase in ionic strength also promoted aggregation, due to the compression of the electric double layer. The TiO_2 nanoparticles with the smallest surface area and highest point of zero charge pH value, lead to aggregation of the smallest size, this resulted in reduced settling velocities. In contrast to the larger TiO_2 nanotubes, where aggregate size exceed 1000 nm and the pH_{pzc} was much lower. This enhanced the settling velocities.

Whilst monodisperse and spherical particles are well characterised settling systems, dispersions containing complex heterogeneous (size polydisperse) and asymmetrical particles remain poorly understood. Settling velocities of non-spherical particles are affected, for example, by oscillation of the particle to attain an equilibrium orientation. As a result, the settling velocity of non-spherical particles, relative to a spherical particle having an equivalent volume or surface area, is reduced. This is a result of an increase in resistance during sedimentation (Komar and Reimers, 1978, Syvitski et al., 1991). Komar et al, suggest particles with a high degree of asymmetry results in unstable settling behaviour, justified by the use of orientation

averaging. Considering a disc-shaped particle, where he shape effects on settling velocities are promoted. The averaged drag force ($\overline{F_D} = 6d\mu v$), considering all orientations, defined by a combination of the drag force for broadside ($F_D = 8d\mu v$) and edgeside orientations ($F_D = (\frac{16}{3})d\mu v$) (Allen, 1997).

Experimental studies conducted by Konert et al., (Konert and Vandenberghe, 1997) calculated the equivalent sphere diameter of a 7 µm clay-plate to be 2 µm. This study highlighted the settling behaviour of rod-like particles, with an aspect ratio of 17.4, using magnetic resonance imaging (MRI). This monitored the time evolution of height profile during a batch sedimentation, as a function of particle volume fraction. MRI results indicated rod-like particles increased the hindered settling effects compares to spherical particles. The effect also increased with increasing particle volume fractions (Turney et al., 1995).

Settling of fibrous particles in a fluid have been commonly studied, emphasising on the complex settling behaviours compared to spheres (Shin et al., 2009, Salmela et al., 2007, Jianzhong et al., 2003, Stover et al., 1992, Zhang et al., 2013). Previous research suggests the settling velocity depends on the aspect ratio. Qi et al (Qi et al., 2014) assessed the influence of aspect ratio on settling velocity and orientation of fibres using a laser diffraction technique. The aspect ratio has influence on the vertical settling velocity and orientation during flow, stating that ~60% of the particle of long aspect ratio have unstable orientation. This results in rotation of particles causing a wide range of horizontal velocities, contradicting the conclusions of Lin et al. Reduction of settling velocities is created by the greater instability of the higher aspect ratio longer particles, compared to shorter particle with the same diameter.

Cylindrical shaped particles are known to impact separation processes. Gabitto et al. (Gabitto and Tsouris, 2008) developed the terminal velocity of free-falling cylindrical particles. Stating the aspect ratio as an appropriate empirical parameter to account for the shape factor. Calculation of the Re number increased with increasing values of aspect ratio, ranging from 1.5 to 100. The base of the settling cylindrical particles create a three-dimensional flow, the fluid flow differs with different aspect ratio. The flow effects decrease as the aspect ratio increases, therefore reducing the settling velocities.

In contrast Lau et al (Lau et al.) considers the calculation of the dynamic shape factor as a suitable parameter of flow. The shape factor is a function

of the forces acting on the particle, Re number, drag coefficient, particle and fluid properties. For spheres $X = 0.98$, cubes $X = 1.03$ and for cuboids and cylinders are found to be functions of the aspect ratio. This is due to the dependence of change in orientation in flow. The settling velocities for cuboids and cylinders with smaller aspect ratios is reduced. The dominant particle-axis is observed to be perpendicular to the direction of flow, regardless of its starting position. This equilibrium orientation increases the drag flow due to the larger projected area in the direction of flow (Hazzab et al., 2008, Becker, 1959).

Ilic et al. (Ilic and Vincent, 1994) explored the effect of particle shape on the sedimentation rate, three groups of shapes were created by the results. Firstly, particles with symmetrical ends and fall vertically have the highest settling velocities. Secondly, particles with asymmetric ends (one flat and one with a point) have moderate settling velocities. Thirdly, shapes which have both ends that are flat and fall normal have the lowest settling velocities. This suggests the direction of which the particle is falling and the symmetry of the shape are also important factors contributing to the settling velocity of the particles.

5.2.4 Sedimentation studies related to the nuclear industry

Sedimentation studies in the nuclear industry are of great importance for the design of facilities regarding safe storage, transport and immobilisation of HAL. Research that is available to a wider audience in the open literature is limited. However, a number of studies have been carried out on both laboratory and larger scales in the UK.

Initial studies were carried out on nuclear waste simulants at a laboratory scale by Mason et al (Mason, 2005). This study highlighted the influence of particle properties on nuclear waste simulants upon sediment bed consolidation to increase opportunities for process optimisation, in particular the re-suspension system. Nuclear waste simulant suspensions included simulant 1 containing only cubic particles and simulant 2 contains a mixture of spherical and cubic particles, they are represented of Magnox fuel types; simulant 3 containing only spherical particles and simulant 4 containing only cubic particles, they are represented of Oxide fuel types. Sedimentation behaviours extracted from the Lumisizer technique illustrated settling velocities for simulant 1 (cubic particles) to reduced when compared to simulant 3 (spherical particles) (Mason, 2005). This indicates, strongly cohesive spherical particles have reduced drag force acting on them,

therefore increased settling velocities. Research conducted by Mason et al., has initiated opportunities to further understand the properties and behaviours of highly active nuclear waste, in particular this PhD research.

The majority of research within the nuclear industry in the UK has been focused on empirical measurements on a laboratory scale, as briefly mentioned. Currently, active HASTs have a maximum capacity of 140 m^3 and direct measurement of the contents is challenged by the radioactive nature. Based on he challenges, NNL have developed an inactive replication of a HAST, with capacity of ~60 m^3, illustrated in Figure 5.2-4.

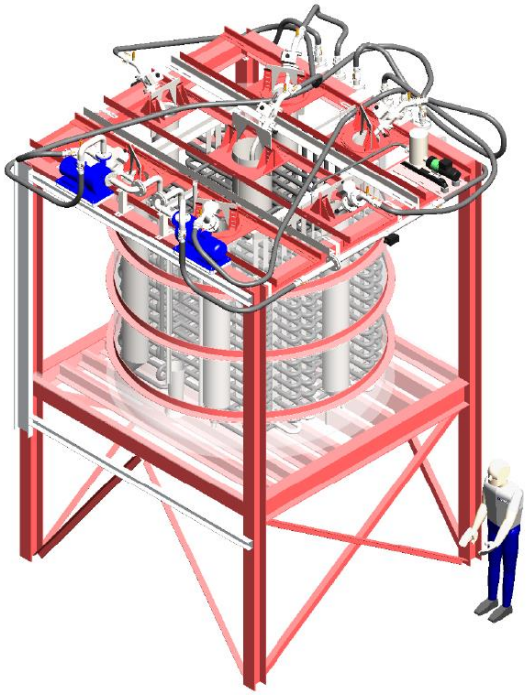

Figure 5.2-4 Schematic of the 60 m^3 inactive HAST (Bux et al., 2013).

Current studies have proposed *in situ* measurements for sedimentation analysis. Bux et al. (Bux et al., 2013), apply an acoustic backscatter system (ABS) to characterise settling behaviours of nuclear simulant. The backscattered data enables analysis of solids concentration and sediment bed depths. This technique has been applied in previous studies for concentrated glass suspensions and TiO_2 mineral oxide suspensions (Thorne and Hanes, 2002, Hunter et al., 2012). Bux et al., (Bux et al., 2013) highlights of the importance of the agitation systems. The sediment bed analysis from the backscatter data indicated a full cycle run of the jet ballasts resulted in the decrease of sediment bed thickness. Concentration sample obtained supported the re-suspension mechanism within the HASTs, providing a higher dispersed solid concentration.

Impinging liquid jets are used widely, in particular in the nuclear industry, UK. The erosion of the sediment bed is studied to understand and improve the waste treatment strategy (Hunter et al., 2013). Previous studies have been conducted to understand the resuspension of consolidated multiphase waste (Hamm et al., 1989, McArther, 2005). Understanding of the settling and the re-suspension behaviour is a key part of the nuclear waste management, in situ studies and jet ballast studies on nuclear waste analogues such as TiO_2, barium sulphate and in the case of US research ammonium based compounds. Research in this field is crucial for the forefront of this research, where inactive simulants representative of the solids contained in the HASTs, which is able to be scaled up from the laboratory scale to 60 m^3 for empirical measurements.

5.2.5 Literature review conclusions

Defining sedimentation behaviour is fundamental for designing engineering facilities. It is evident publically available literature on characterisation of realistic nuclear waste simulants and the effect of their particle properties on process plant operations is limited. The literature that is available considers nuclear relevant process operations, such as the jet ballasts, on particles which are not directly relevant to the HAL solids. Thus, this research aims to define the key particle properties of inactive HAL solids to answer fundamental questions on the physical behaviour of the solids and the key parameter which ultimately dictates the change in behaviour.

Sedimentation behaviour under gravitational centrifugal force will enable characterisation of a homogeneous dispersion and sedimentation bed compaction to determine the re-dispersion behaviour of the HAL solids. Morphological manipulation which produces particles of identical chemical structure with differing aspect ratio i.e. ZM and ZMCA, facilitates the understanding of desirable process optimisation conditions. Together with a comprehensive particle property characterisation and determination of sedimentation behaviour will aim to contribute to broaden the knowledge of process plant operations determined by HAL solid-liquid properties, which will lead to an improved nuclear waste treatment strategy.

5.3 Materials and methods

Dispersed phases of synthesised CPM, ZM and ZMCA particles were used for sedimentation studies and compared to TiO_2. The continuous phases included DI water and 2M HNO_3. The sedimentation rate as a function of

volume fraction was determined using gravitational and centrifugal techniques.

5.3.1 Turbiscan

In this device, the dispersion is placed in a cylindrical glass measurement cell and turbidity measurements are taken through its entire length to establish a sedimentation or creaming velocity under gravity. An electro luminescent diode is the light source in the near infrared region (λ_{air}=880nm). There are two optical sensors: one is a *transmission sensor,* where light is transmitted through the sample, at 180º from the incident light source; and, a *backscattering detector,* where the light is backscattered by the sample, which is at 45º from the incident radiation. The length of the sample is scanned and an optical reading of the transmission and backscatter data is acquired, this presented as the light intensity % as a function of sample height in mm. Data can be collected at pre-set times after an initial trace is recorded. The main components of the multiple light scattering technique are illustrated in Figure 5.3-1.

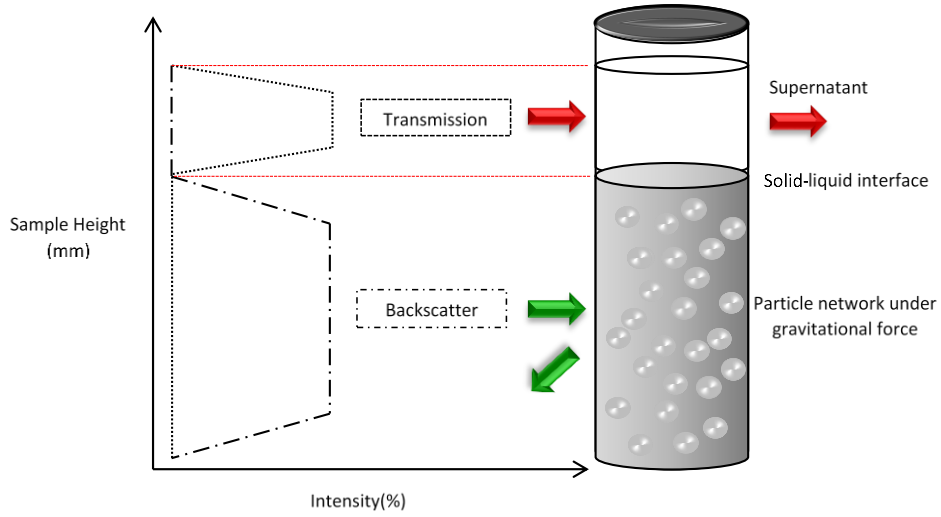

Figure 5.3-1 Schematic representation of the Turbiscan showing the data interpretation from the light source penetrating through the sample into a graphical illustration. The Turbiscan sample cell dimensions has an internal diameter of 30 mm and an initial sample height of 42 mm.

In a typical experiment, a dispersion was filled up to the height of the holder which is ~20mL or 42mm. The sample was placed into the Turbiscan via the opening at the top of the instrument. For each volume fraction, the sample was left to run for 3.5 h and the data was collected every 2 minutes.

5.3.2 Lumisizer

A Lumisizer® (L.U.M. GmbH, Berlin, Germany) was also employed here as an alternative route to determine the sedimentation rate and to allow further information about the sediment bed to be obtained. This device also determines sedimentation information using transmitted light through a measuring cell as a function of height in the cell and time. A key difference between the two techniques is that the Turbiscan® measures the settling rate under gravitational force whereas the Lumisizer® employs a centrifugal force. The main advantages of employing the Lumisizer® are that more than one sample can be measured simultaneously (12 samples), the temperature at which the sample is measured can be easily adjusted, the maximum speed of the centrifuge can be controlled up to 4000 rpm, and the quantity of material is relatively low (400 µL). Key components of the centrifugal technique are illustrated in Figure 5.3-2.

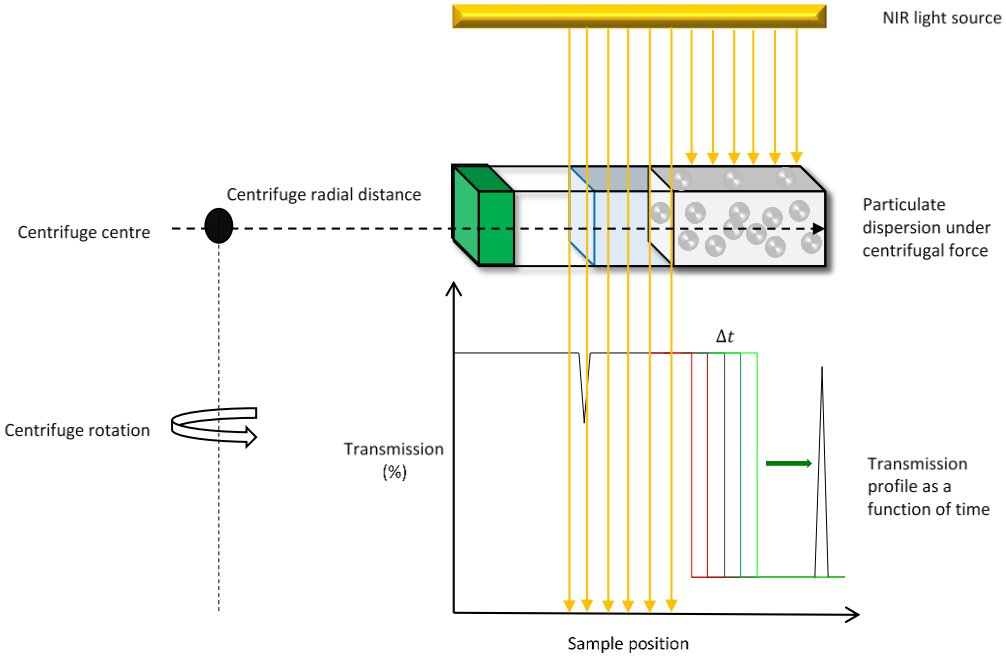

Figure 5.3-2 Schematic representation of the Lumisizer showing the data interpretation from the light source penetrating through the sample into a graphical illustration. The Lumisizer sample cell dimensions has an internal diameter of 8 mm and initial sample height of 22 mm.

In a typical measurement here, an aliquot of 400 µL was extracted using a syringe from a 10 mL stock suspension and transferred into a polyamide (PA) cell. The cell was then loaded into the Lumisizer® for analysis and 250 profiles were collected at intervals of 300 s for all particulate systems at 1000 rpm.

5.4 Results and discussion

5.4.1 Stokes free-settling

Estimated free-settling (U_t) values for TiO_2 and HAL simulants are presented in Table 22. The values have been obtained using the average particle size data from Chapter 3.

Table 22 Estimated values of free-settling rates for TiO2 and highly active nuclear waste simulants.

Particle system	Vt [m/s]		Vt [mm/s]	
	Water	Nitric Acid	Water	Nitric Acid
TiO2	$1.93x10^{-6}$	$1.11 x10^{-6}$	0.001935	0.0011094
CPM	$1.86 x10^{-6}$	$1.07 x10^{-6}$	0.00186	0.0010668
ZM	$1.18 x10^{-6}$	$6.75 x10^{-6}$	0.011821	0.0067516
ZMCA	$1.18 x10^{-6}$	$6.75 x10^{-6}$	0.011821	0.0067516

Figure 5.4-1 illustrates the influence of fluid properties on free-settling rates. The free-settling rates of the particles falling under gravity considers flow through water with a density of 1000 kg/m^3 and viscosity of 0.001 Pa.s, and flow through nitric acid with a density of 1070 kg/m^3 and viscosity of 0.0017 Pa.s.

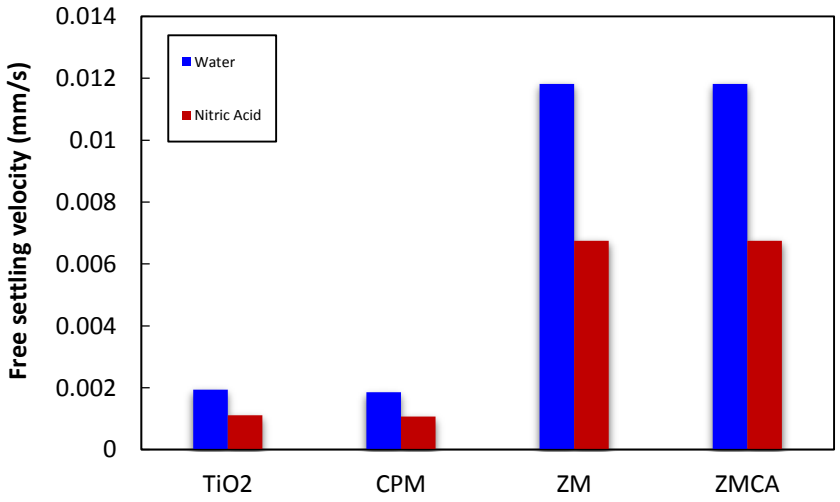

Figure 5.4-1 The data represents a comparison of estimated free-settling rates for TiO2 and highly active nuclear simulants dispersed in water and nitric acid.

From Figure 5.4-1 it is evident increase viscosity and density of nitric acid significantly reduces the free-settling rates of all particulate systems. Comparing TiO_2 and CPM dispersions, the increased free-settling rates for CPM is a result of higher particle density, albeit TiO_2 has a larger particle size. Figure 5.4-1 also illustrates the dependence of particle size of free-settling rates, where ZM and ZMCA dispersions have the fastest settling rates compare to TIO_2 and CPM dispersions.

The validity of the Stokes' law is limited to spherical, rigid particles, low particle concentration and laminar flow, thus discrepancies between the estimated values (Table 22 and Figure 5.4-1) and the experimental data is expected. The addition of electrolyte concentration on particle surface charge, discussed in Chapter 3, influences the stability of the dispersions. The influence of particle shape is unaccounted when calculating the free-settling rates, this is illustrated in Figure 5.4-1, where the free-settling rates for both ZM and ZMCA are identical. The experimental settling data collected in this thesis is expected to deviate from the calculated free-settling values, as it is predicted the sedimentation is also governed by particle properties such as surface charge and shape.

5.4.2 Gravitational force

The combination of particle size, shape and density will obviously lead to different settling properties for the different systems. Turbiscan® profiles illustrated in Figure 5.4-2 represent the settling behaviour of each particulate system. Sedimentation analysis used the backscatter profiles, as shown below. In these plots, the x-axis indicates the position of the sediment interface in the cell, where the initial position is at 42 mm. The y-axis indicates the backscattered intensity.

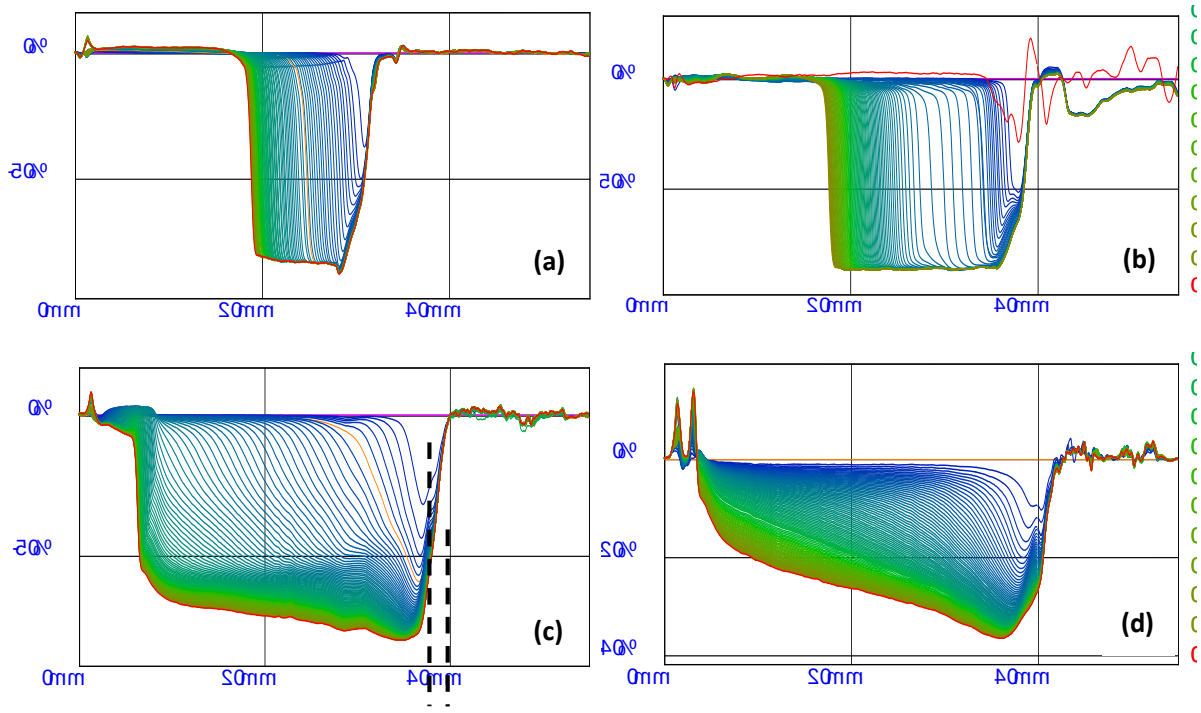

Figure 5.4-2 Sedimentation profiles of nuclear waste simulants at 6 vol%: (a) Titanium dioxide; (b) caesium phosphomolybdate; (c) zirconium molybdate; (d) zirconium citratomolybdate. All particulate systems have been dispersed in DI water. The data collected using the Turbiscan.

Figure 5.4-2 indicates distinct settling properties, expressed through the change in shape of the profiles. Migration from the top of the sample (at 42 mm RHS of the profiles) to the bottom of the sample (LHS of the profiles) leads to a progressive increase in particle concentration, thus increase in backscatter signal. The uniform settling behaviour of TiO_2 and CPM dispersions, where both dispersions exhibit a linear settling rate with definitive solid-liquid interface, can be explained by the similarities in particle properties. Both particulate systems are relatively monodisperse with and overall spherical aggregate size of ~1 µm. The uneven settling profiles of ZM and ZMCA dispersions illustrate the effect of size polydispersity within the systems. Figure 5.4-2 (c) and (d) indicate at any given time the backscatter signal is detected over a range of different heights. For example, indicated by the dotted lines in Figure 5.4-2 (c), at $t = 2\,mins$ the backscatter signal occurs over 3 mm (from 38-35 mm). The backscatter variation over height indicates initial settling of the larger ~3 µm particles, followed by the finer submicron particles. Thus creating a dispersion where both segregation and sedimentation occur.

The solid-liquid interface migration is important to define for sedimentation analysis using the Turbiscan®. As illustrated in Figure 5.4-3 to 5.4-6, all settling curves and sedimentation rates were extracted from backscatter profiles, due to low transmission profiles of ZM and ZMCA dispersions. Thus, backscatter analysis was implemented for direct comparison of sedimentation behaviour for all particle systems. Obtaining settling curves from backscattered profiles required all profiles to be set in reference mode (i.e. subtraction of the reference profile from all other profiles) to emphasise variation of the solid-liquid interface as a function of time. Reference mode selection was followed by phase thickness calculation, this required setting of a threshold. Optimum threshold at half of the backscatter intensity of the final profile across the initial and final solid-liquid interface was developed. Implementation of the optimum threshold parameters enabled representative sedimentation behaviours of all particulate systems to be analysed.

In Figures 5.4-3 to 5.4-6 settling data for the nuclear waste simulants (CPM, ZM and ZMCA) and the metal oxide (TiO_2) are given as a function of particle volume fraction. The data shown here were collected using the Turbiscan, where the settling front was analysed using the backscatter detector. The volume fraction range for CPM, ZM and ZMCA is from 2-14 vol% and for TiO_2 the range is 2-10 vol%.

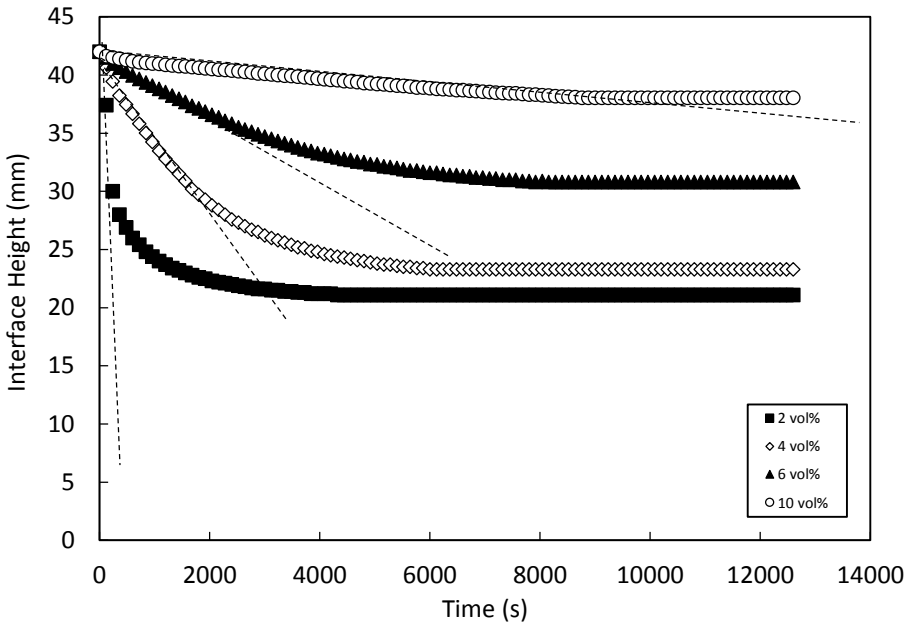

Figure 5.4-3 Settling curves of TiO_2-H_2O dispersions as a function of volume fraction. The data illustrate the final height of sediment bed and sedimentation rate (indicated by the dotted line).

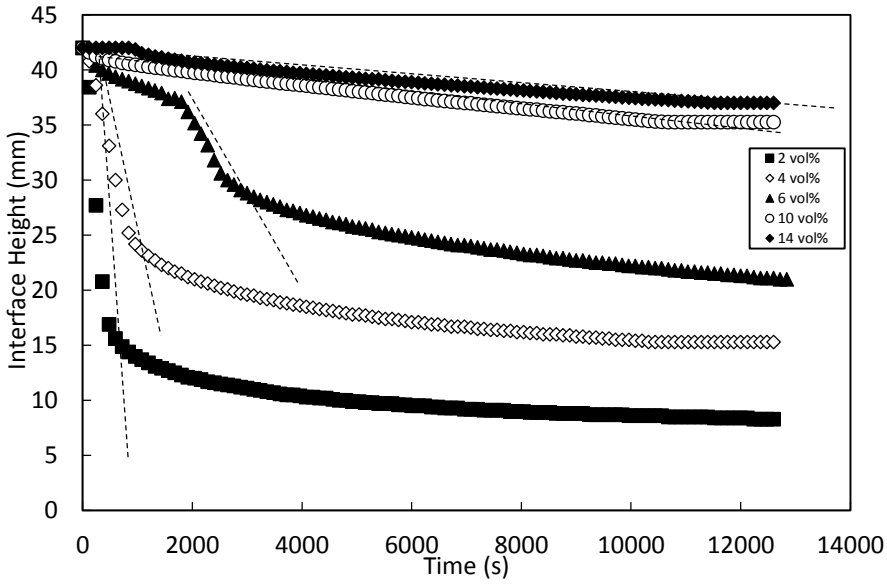

Figure 5.4-4 Settling curves of highly active nuclear waste simulant CPM-H_2O dispersions as a function of volume fraction. The data illustrate the final height of sediment bed and sedimentation rate (indicated by the dotted line).

For the TiO_2 sample (Figure 5.4-3) a complex settling behaviour is observed. For the lowest concentration, a rapid initial settling interface was measured which suggests lower hindered settling effects within the TiO_2 at this concentration. However, the final settled volume fraction in this case is considerably greater than was seen for the CPM (Figure 5.4-4) sample at an equivalent volume fraction. At 4 vol%, there is a significant reduction in the initial settling rate, which also appears to be non-linear, along with a much greater sediment height, once again, than was seen for the CPM. It is believed that these complex settling effects may stem from interactions

between the voluminous sediment bed and the approaching settling front, leading to a non-distinct settling front. At 6 vol%, the settling is even more retarded, while at 10 vol% there is almost no evidence of suspension settling. These data suggest that at these higher concentrations the TiO_2 is forming a self-supporting and space filling network, with aggregates interacting in a matrix across the whole of the measurement cell.

For the CPM suspensions, there appears to be three distinct sedimentation behaviours as a function of volume fraction. For volume fractions below 6 vol%, a hindered settling process is apparent. Above 6 vol% little or no sedimentation is seen which suggests, again, a space filling aggregated particle network is forming over the sample cell volume (similar to TiO_2). However, at 6 vol% three distinct sedimentation behaviours are apparent from figure 5.4-4. The initial strongly hindered settling suggests a space-filling network is present. Beyond some critical induction time, the system yields and a consolidation of the particle network takes place. It maybe assumed that, in this case, the colloidal network progressively builds up an internal stress during the induction time as a result of localised rearrangements within the network, and this, in turn, ultimately leads to the collapse of the sediment front (Bartlett et al.). In the final stage, a compaction of the particle network takes place and is consolidated towards an equilibrium height.

Figures 5.4-5 and 5.4-6 illustrate the settling curves of ZM and ZMCA dispersions, respectively.

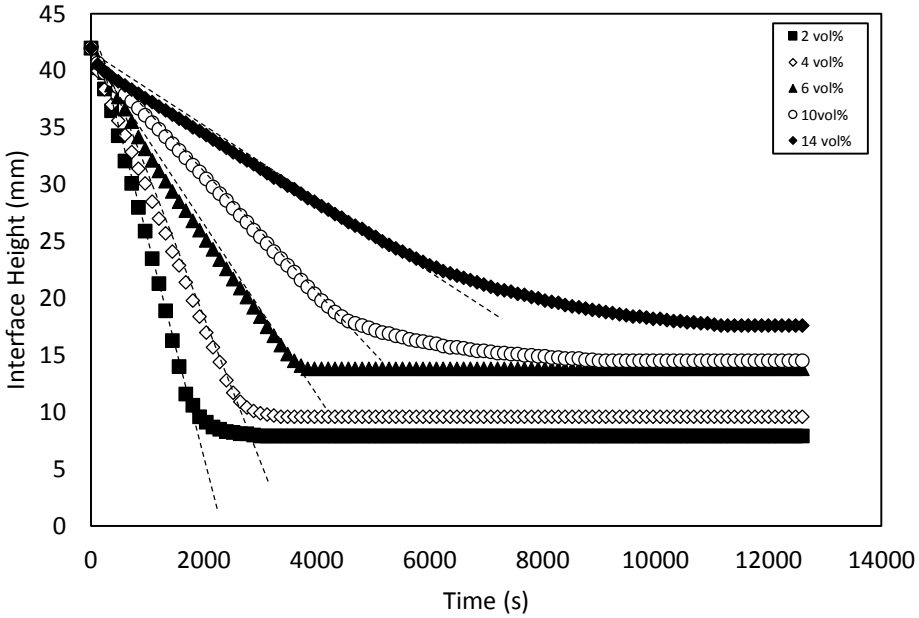

Figure 5.4-5 Settling curves of highly active nuclear waste simulant ZM-H_2O dispersions as a function of volume fraction. The data illustrate the final height of sediment bed and sedimentation rate (indicated by the dotted line).

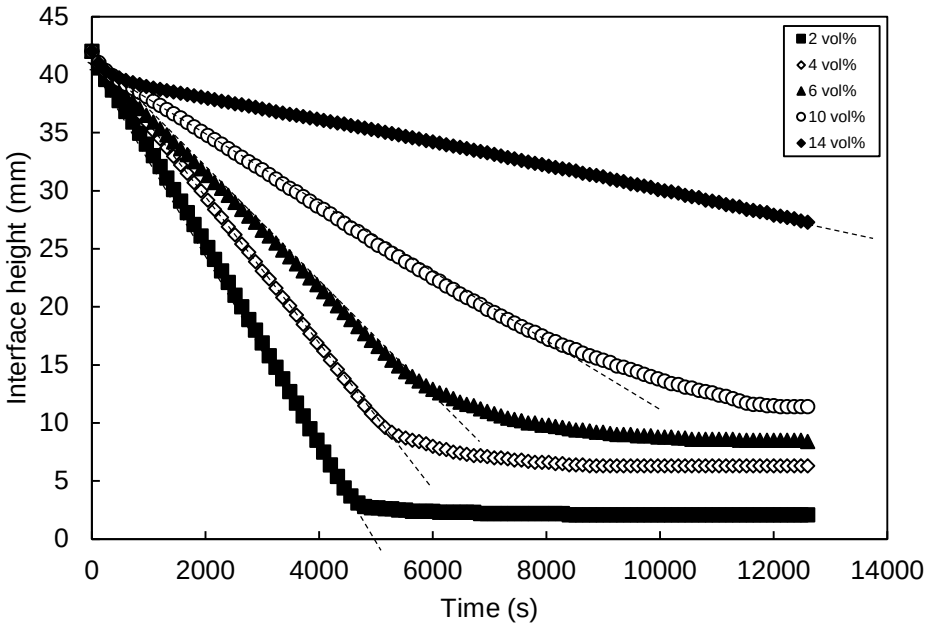

Figure 5.4-6 Settling curves of highly active nuclear waste simulant, ZMCA-H_2O dispersions as a function of volume fraction. The data illustrate the final height of sediment bed and sedimentation rate (indicated by the dotted line).

The settling data for the ZM and ZMCA particles is considered here first (Figures 5.4-5 and 5.4-6). After a short initial induction period (t < 300s), where any turbulence from initial mixing is dissipated, the sediment interface is seen to progress in a linear fashion with time for all volume fractions. This is normally indicative of hindered settling. For samples with a volume fraction ≤ 6% for ZM systems and ≤ 4% for ZMCA systems, a transition to a second regime is seen after some finite time when the sediment bed compresses from the fluid pressure, and only a small change in the sediment height is then seen over extended times. As the concentration is increased, the initial rate of settling reduces and the time for sediment consolidation increases. Indeed, ZM particulate systems for 10 and 14 vol% this second zone is not reached within the 4000 s. For ZMCA particulate systems the second zone is not reached for all volume fractions within the 4000 s. This is indicative of reduced settling velocities of ZMCA systems.

Comparison of space-filling network across the sample matrix of TiO_2 when compared to the ZM sample are likely due to a highly aggregated state of the TiO_2, which leads lower density sediment beds. In fact, the cubic and cuboidal nature of ZM and ZMCA may lead to highly compact sediment, which is consistent with the very low final bed heights for the ZM systems.

The changes in the initial settling rate with particle concentration are presented in Figures 5.4-3 to 5.4-6 where we can see that, in general, for all

suspensions, as the volume fraction of the particles in water increases, the sedimentation rate decreases, as expected. Hindered settling functions are based on collective particle interactions and settling particles are influenced and the rate reduced by neighbouring particles (Vesaratchanon et al., 2008, Kumar et al., 2000).

5.4.2.1 Effect of particle properties

To better correlate the settling behaviour of the four species, the average initial linear settling rates (in mm/s) for each species and each concentration (as shown by the dotted lines in Figures 5.4-3 to 5.4-6) were directly compared across a large concentration range, and are shown together in Figure 5.4-7.

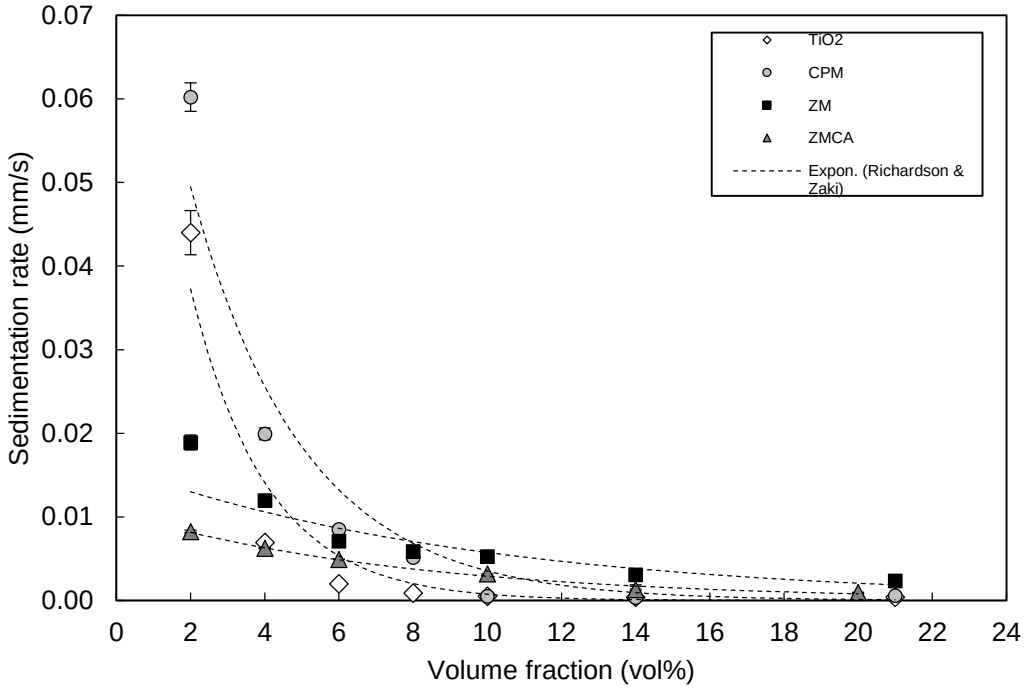

Figure 5.4-7 Sedimentation rate as a function of volume fraction. The data represents nuclear waste simulants (CPM, ZM and ZMCA) and TiO_2 suspensions, the particles are dispersed in DI water. The data represented here are calculated from the backscatter information generated from the Turbiscan.

An empirical correlation between the settling velocity and the particles volume fraction is expressed by the Richardson and Zaki equation (Equation 5.2-9), discussed in section 5.3.1.1. For the nuclear waste simulants and TiO_2 particulate systems, this correlation shows good agreement with the experimental data. Where the variable constant *n* is a function of the particles Reynolds number.

Table 23 resents data of the fitted parameters using the Richardson and Zaki equation. Initial fits were carried out by using calculated free-settling rates in table 22, using Solver in Excel. As the suspensions being tested are

within the laminar region and consist of micron-sized particles, thus a value of *n=4.65* was initially implemented.

Table 23 Fitted parameters of the Richardson and Zaki equation to TiO2 and highly active nuclear waste simulants.

Particle system	U_t (mm/s)	n	MSE
TiO_2	0.1149	51	1.04E-05
CPM	0.1257	39	1.21E-05
ZM	0.0156	9.48	6.07E-06
ZMCA	0.01	11.43	5.59E-08

The free-settling velocities extracted from the experimental data, by implementing the Richardson-Zaki fit, indicates an order of magnitude higher velocities for TiO_2 and CPM dispersions in contrast to the estimated free-settling velocities (Table 22). ZM and ZMCA systems show to be consistent with the estimated values. It is evident the fitted values for *n* are significantly higher than expected. In some cases *n* has been found to be as high as 6.5 due to Brownian motion (Batchelor, 1972, Di Felice, 1999), 5.5 (Bürger and Tory, 2000).

A correlation considering *n* to be a function of particle shape and size and Re number was developed by Maude and Whitmore (Maude and Whitmore, 1958). The generalised equation of the Richardson and Zaki relationship is expressed in Equation 5.4-1

$$ln(u) = ln\, u_0 + n\, ln\varepsilon \qquad 5.4\text{-}1$$

Where U_0 is the free settling velocity, $\varepsilon = 1-\phi$ is the porosity. The plot of *ln(u)* vs. *ln(ε)* gives a linear relationship where the intercept of the y-axis gives the free-settling velocities and the gradient gives the *n*. This relationship will therefore be able to validate the values obtained for the fitting parameters U_0 and *n*.

Figure 5.4-8 illustrates the Maude-Whitmore relationship for TiO_2 and highly active nuclear waste particles dispersed in water. The data indicates a linear increase in ln (u) as a function of porosity, thus illustrating the hindered settling region where this is a great dependence on bulk volume fraction.

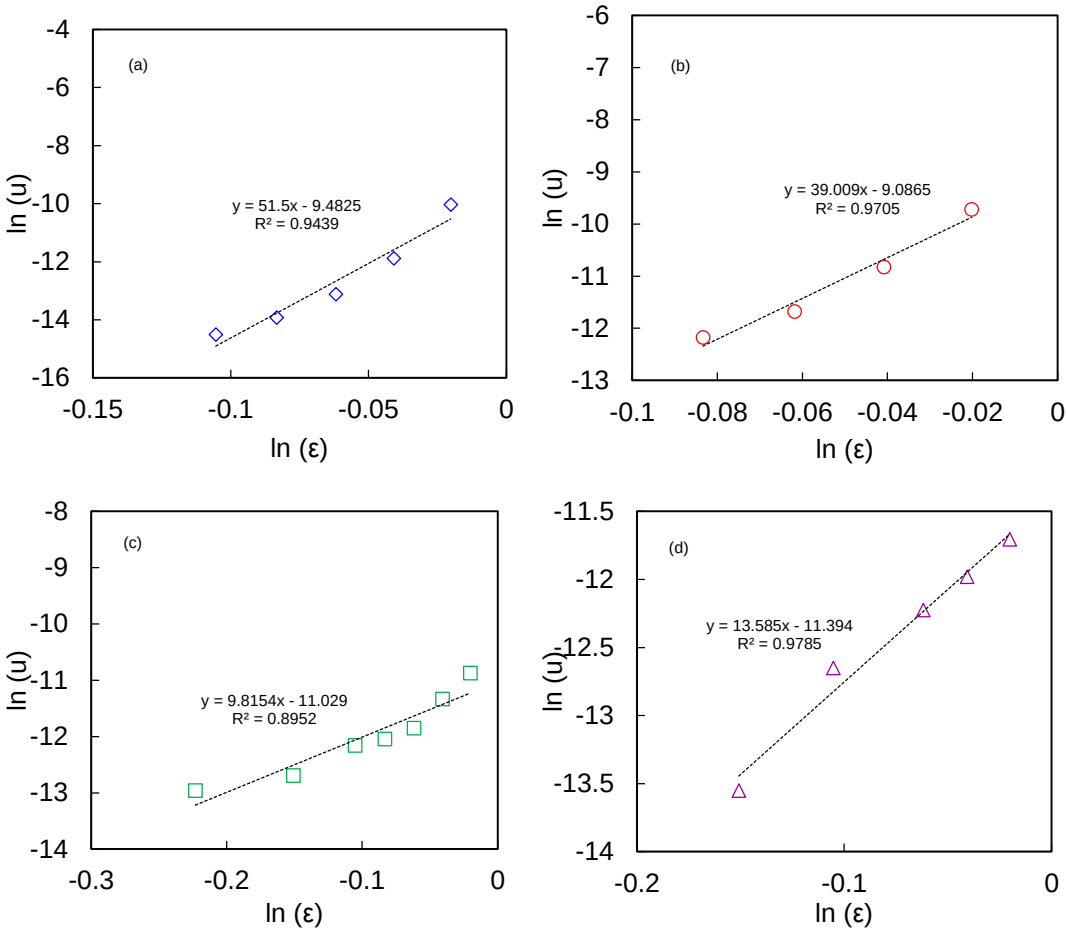

Figure 5.4-8 This data represents Ln(u) vs. Ln(ε) plot of (a) TiO2, (b) CPM, (c) ZM and (d) ZMCA dispersions.

Figure 5.4-8 illustrates excellent fits for the hindered settling region indicates free-settling velocities of 0.076 mm/s for TiO_2, 0.113 mm/s for CPM, 0.016 mm/s for ZM and 0.011 mm/s for ZMCA dispersions. Similar to the fitted values of the free-settling velocities using the Richardson-Zaki correlation, ZM and ZMCA correspond well to the initial estimated free-settling values in Table 22. Similarly, the TiO_2 free-settling velocities are lower than CPM using the Maude-Whitmore correlation which is in agreement with the initial Stokes values. This indicates the dependence of particle density on the terminal velocity.

In both cases, the free-settling constant obtained using the Richardson-Zaki fit and the extrapolation of the straight line using the Maude-Whitmore correlation, indicate TiO_2 and CPM values to exceed the actual free-settling velocities by orders of magnitude. This is indicative of, in particular, TiO_2 systems to be aggregated, which is supported by the zeta potential data (see Figure 3.4-16). Also indicating the porosity of the aggregates increase with bulk concentration. The extremely large *n* value for TiO_2 ($n = 52$) relate to the effect on the particle properties on hindered settling, where the degree

of aggregation has dominating effects. Comparing ZM ($n = 10$) and ZMCA ($n = 14$) particles, the larger *n* value for ZMCA dispersions indicates the influence of aspect ratio on the hindered settling.

From Figure 5.4-8 each particle type displays an approximate exponential decrease in settling rate with increased concentration (as would be expected for hindered zone settling behaviour) although the rates are different for each species (not shown) and there are critical differences in particular between ZM/ ZMCA and the other particles. Comparing CPM to TiO_2 firstly, the CPM has higher settling rates for all concentrations above 2 vol%, consistent with it having a greater particle density. Interestingly, for 2 vol% the measured settling rates are similar, and it is thought that this may be explained by increased hindered settling effects in the CPM system within this lower concentration threshold. Such heightened hindered effects maybe from differences to aggregate shape or orientation altering the interaction with the up-flowing liquid.

More importantly, there are key differences between the ZM/ZMCA and CPM samples, which are less easy to explain. As the ZM crystals are significantly larger (and have a similar density to CPM) one would expect correspondingly a faster settling rate. However, it is important to consider the effect of particle size on particle-particle interactions. As the particle size increases the influence of particle-particle interactions decreases. This is a consequence of the reduced number of particles per unit volume, therefore resulting in decreased fluid exclusion. This is consistent with Vesaratchanon et al. (Vesaratchanon et al., 2008), where an increased latex particle size from 500 nm to 1000 nm indicated slower settling velocities for the larger particle. Although the settling rate at high volume fractions (above 6 vol%) appear to be slightly above the CPM, at low to moderate volume fractions it is significantly lower. From Figure 5.4-8 it appears that above 6 vol% a space filling network is present and this strongly influences the overall sedimentation behaviour. This relationship suggests particle size is not a dominant factor influencing the overall settling rate, thus a greater understanding in additional particle properties is required.

Particle shape is, of course, a potential influence on this behaviour, as non-spherical particles change their orientation during sedimentation and therefore affect the overall velocity of the particles. Comparing ZM and ZMCA settling velocities, it is apparent from figure 5.4-7 that ZMCA have

reduced velocities. The aspect ratio (A_r) calculated for ZM and ZMCA are ~1 and ~6, respectively.

Particles with a larger aspect ratio will change orientation during sedimentation, in order to achieve its most stable position which minimises the drag force. However, further studies have been carried out by Fan et al. and Lau et al. and they suggest this may not be the case. Elongated particles tend to oscillate during sedimentation with varying orientation. Orientation is defined as the angle between length of the prominent axis of the particle to the direction of flow (Lau et al.). The most stable form is when the particle is horizontal, i.e. perpendicular to the direction of flow (Lau et al., Fan et al., 2004).

It can be assumed during sedimentation ZMCA particles will change orientation and oscillate around the stable horizontal orientation. The equilibrium orientation is affected by the particle concentration; this will be discussed further. Comparing the settling velocities to ZM particulate systems, the elongated ZMCA particles typically settle at a larger angle of tilt. This results in reduced settling velocities and increased drag effects. The shape effects are further enhanced by the end effects, where from the SEM images in Chapter 3 indicate ZMCA particles have flat, square edges. These types of particles are likely to yield against the direction of flow, producing increased angle of tilt (away from $\theta = 90^o$). These shape effects could be a result of the large extensional stresses at the corners of the particles (Liu and Joseph, 1993).

Furthermore, Liu et al have looked at the change in orientation as function of particle concentration (Liu and Joseph, 1993)**.** At lower volume fractions the angle of tilt is at its minimum where the cylindrical particle will settle with the major axis of the particle perpendicular to the direction of flow. At higher volume fractions the cylindrical particle orients itself where the major axis of the particle is parallel to the flow. This suggests that the drag on the particle at high volume fractions is reduced. Figure 5.4-8 indicates settling velocities for any particulate system ≤ 6 vol% are influenced by particle orientation due to concentration effects. Consider ZMCA and CPM particulate systems, above 6 vol% the settling velocities are increased for the elongated ZMCA particles. Where, at higher concentrations the ZMCA particles orient themselves in the direction of flow to maximise the space-filling network across the sample matrix.

It can be suggested from the settling studies of nuclear waste simulants that particle shape effects dominate the observed settling velocities. The order of settling velocity with respect to shape is sphere > cube > cuboid. This suggests particle particles that are symmetrical in all directions have higher settling velocities compared to asymmetric particles. This is consistent with studies carried out by Ilic et al and Lui et al (Ilic and Vincent, 1994, Liu and Joseph, 1993).

Differences between ZM and CPM suspensions post-settling were analysed in an attempt to further understand the low apparent settling rate of the ZM particles. Specifically, it felt that reduced settling rates within the ZM systems may also be down partially to the influence of particulate fines. Figure 5.4-9 provides images of the ZM and CPM suspensions after a 3hr 30min settling period, and was used as a visual aid to compare the systems.

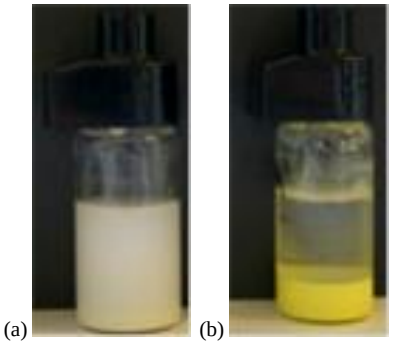

Figure 5.4-9 This image illustrates the nuclear waste simulant suspensions of (a) ZM and (b) CPM after a settling period. The suspensions are shown to be in the Turbiscan sample holder, both suspensions have an initial concentration of 6 vol% and all experiments have been carried out at ambient temperature.

These dispersions indicate that the CPM particles settle out fully and form a definitive sediment bed. ZM suspensions, however, display a residual milky appearance which indicates incomplete settling. Further characterisation of ZM suspensions was undertaken by extracting an aliquot of both the supernatant and sediment to analyse using the Mastersizer®. The data are presented in Figure 5.4-10.

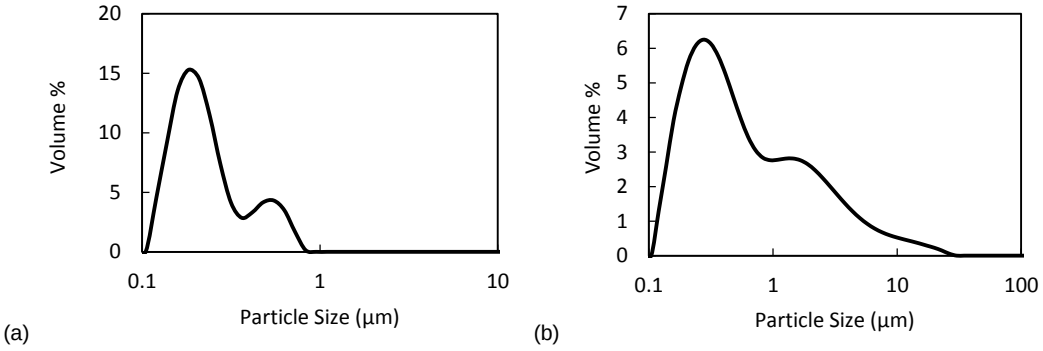

Figure 5.4-10 Size distribution data of zirconium molybdate suspension (a) supernatant (b) supernatant and sedimentation bed. The size distribution data was obtained using the Mastersizer.

Figure 5.4-10 (a) suggests the supernatant contains fine particles of 0.18-0.48 µm. For the sediment bed, the size distribution is within the range of 0.18-2.73 µm. This suggests that ZM suspensions are more size polydisperse than was apparent from the initial sizing data given in Figure 3.4-12, in Chapter 3. It is clear, from figures 5.4-9 and 5.4-10, a significant fraction of slow settling fine particles are left in suspension.

Factors which influence the hindered settling functions are the extent of size polydispersity, particle concentration and self-induced hydrodynamic interactions (Hassen and Davis, 1989). For size polydisperse ZM suspensions, the distinctive feature of this system is segregation and sedimentation, this results in areas of different particle concentration. It can be suggested that the Turbiscan is largely monitoring the sedimentation of the larger 3µm ZM particles and neglecting the finer sub-micron particles which are still left in suspension. This is supported by the particle size data in figure 5.4-10 (b). The figure gives the particle size measurements after the 3.5 hr settling period where by a sample of the sediment bed was taken and shows the larger 3 µm ZM particles have settled out over a period of time and formed a sediment bed. However, although segregation is clearly occurring over time, it is possible at higher particle concentrations the ZM fines are enhancing the hindered settling effects within the system through interactions with the larger particle fragments, leading to a further retardation of the settling rate, from that expected for a suspension of only large particles. Furthermore, it may be presumed that the large scale segregation could potentially affect the orientation of the larger particle during sedimentation.

5.4.2.2 Effect of electrolyte concentration

To explore the effects of a change in the fluid properties, the nuclear waste simulant materials and titanium dioxide sample are dispersed in 2M HNO_3. The choice of medium is of direct relevance to the legacy nuclear waste storage tanks. Data for the solid-liquid interface migration as a function of time was detected using a Turbiscan. The volume fraction range chosen for TiO_2 and CPM is 2-10 vol%, and for the ZM it is 2-20 vol%, Figures 5.4-11 to 5.4-13. A change in fluid properties enables a better understanding of the influence of particle-particle interactions on sedimentation behaviour. In addition, it is of key interest for the nuclear industry to gain an understanding for current processing, as the HAL solids are stored in 2-3M HNO_3.

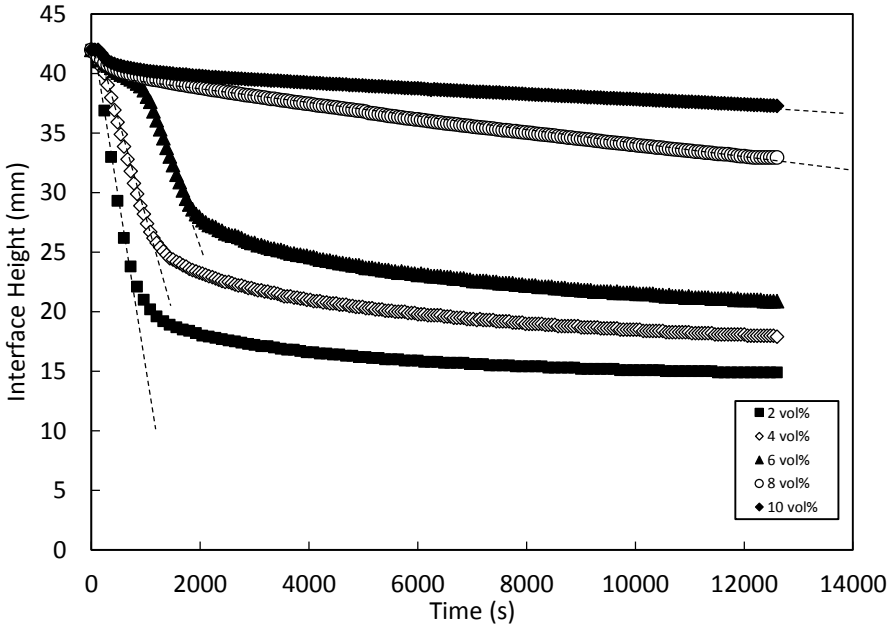

Figure 5.4-11 Settling curves of TiO-HNO_3 (2M) dispersions as a function of volume fraction. The data illustrate the final height of sediment bed and sedimentation rate (indicated by the dotted line).

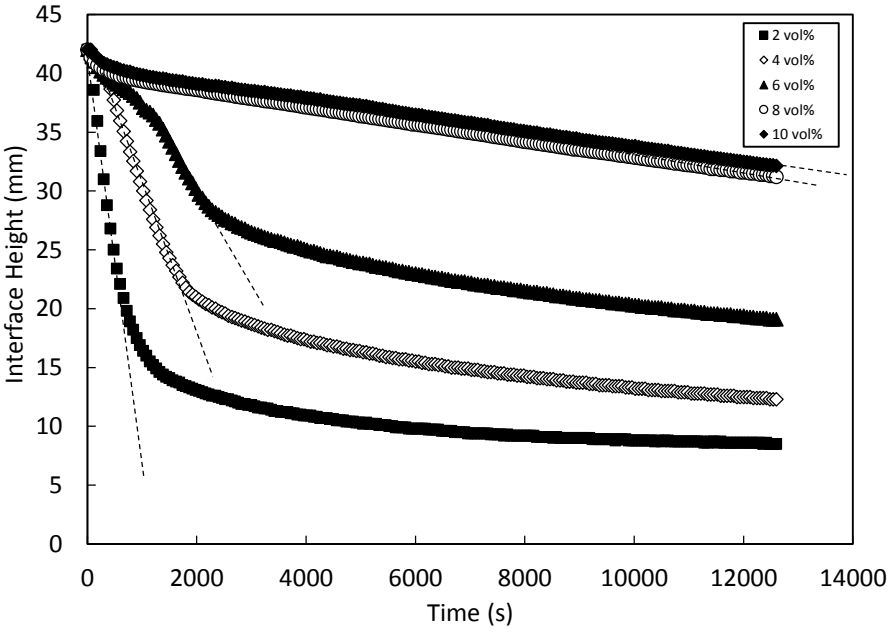

Figure 5.4-12 Settling curves of highly active nuclear waste simulant, CPM-HNO_3 (2M) dispersions as a function of volume fraction. The data illustrate the final height of sediment bed and sedimentation rate (indicated by the dotted line).

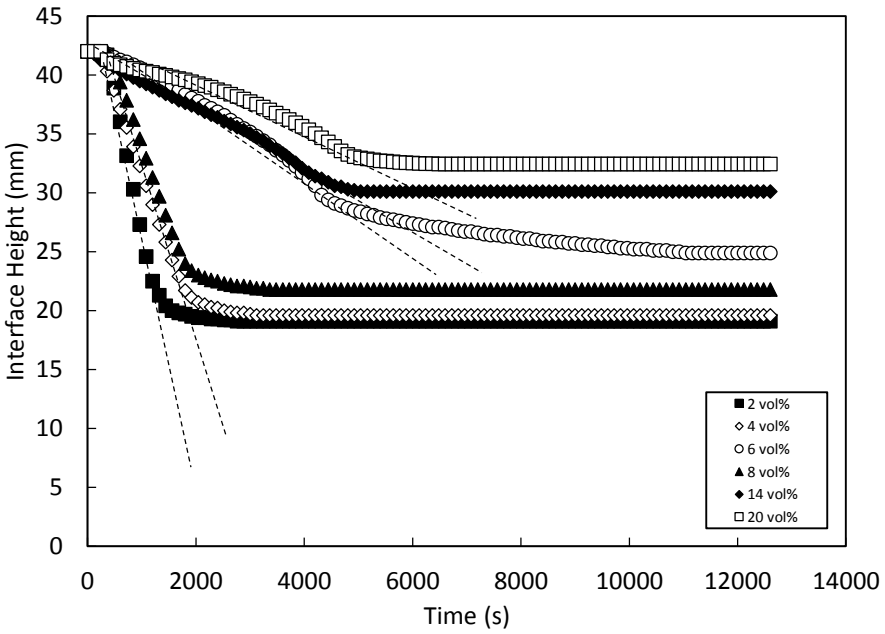

Figure 5.4-13 Settling curves of highly active nuclear waste simulant ZM-HNO_3 (2M) dispersions as a function of volume fraction. The data illustrate the final height of sediment bed and sedimentation rate (indicated by the dotted line).

Figures 5.4-11 to 5.4-13 illustrate the settling curves of TiO_2, CPM and ZM as a function of volume fraction. Both TiO_2 and CPM particulate systems appear to have three distinct settling behaviours with respect to particle volume fraction. This is similar to CPM particulate systems dispersed in water. Gravitational settling occurs ≥ 4 vol% within ~2000 s followed by bed consolidation, for both systems. At 6 vol%, a space filling network is formed within 1000 s of the time being tested, this is followed by yield and collapse of the suspension >1000 s. This relates well to Figure 5.4-4. TiO_2- and CPM-HNO_3 suspensions > 8 vol% exhibit no change in height of the solid-liquid interface over time, therefore considered a stable suspension. In contrast, ZM suspensions exhibit gravitational settling followed by bed consolidation for each volume fraction within the tested range.

Free-settling calculations, illustrated in Figure 5.4-1, indicate reduced free settling velocities due to increased density and viscosity fluid properties of nitric acid. However, EDL compression, due to increased H^+ concentration, suggests particles may lead to aggregation and thus a possible increase in settling velocities. Thus, in contrast to water, it is expected by altering fluid properties this will lead to competing behaviours and collectively results in complex sedimentation behaviour.

Figure 5.4-14 correlates the sedimentation rate (mm/s) of the solid-liquid interface as a function of volume fraction for each particulate systems. The experimental data is fitted using the Richardson and Zaki empirical

expression, it shows to be in good agreement. The overall shape effects show expected relationship, where the sedimentation rate behaviour is illustrated, in Figure 5.4-14, as cubes < spheres.

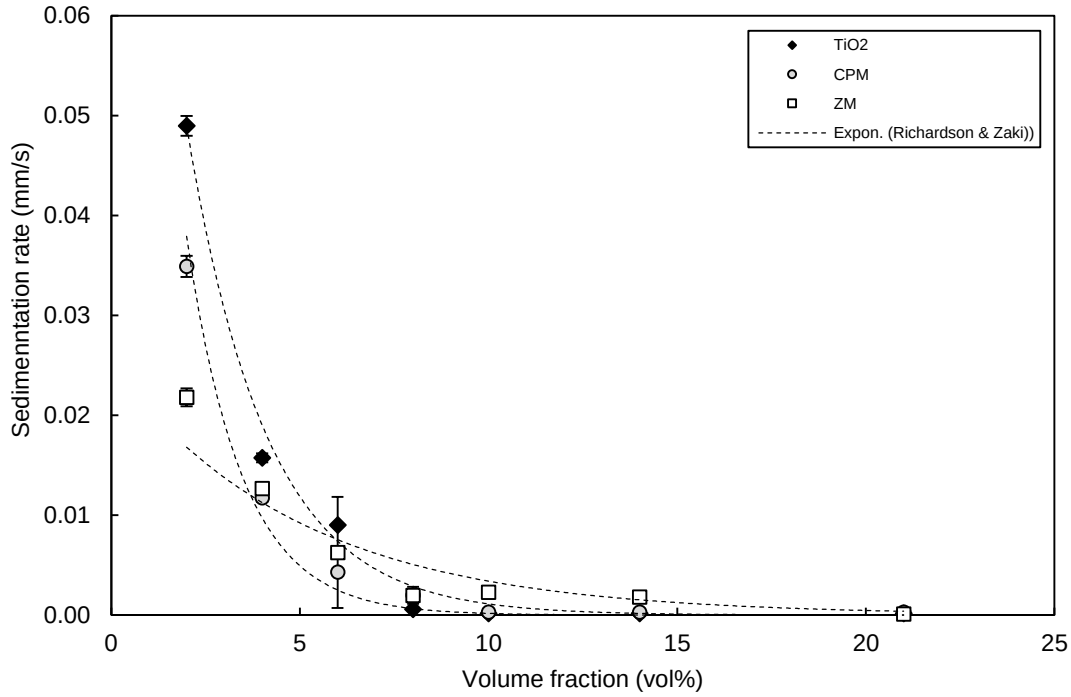

Figure 5.4-14 Sedimentation rate as a function of volume fraction. The data represents nuclear waste simulants (CPM and ZM) and TiO_2 suspensions, the particles are dispersed in nitric acid. The data represented here are calculated from the backscatter information generated from the Turbiscan.

Comparing the settling velocity data in Figure 5.4-14 to that in Figure 5.4-7, where the particles are dispersed in water, we see that the settling velocities for CPM particles in nitric acid are significantly reduced at any given volume fraction. In contrast, TiO_2 particles exhibit increased settling rates when dispersed in nitric acid. ZM particles have consistent settling velocities whether dispersed in water or nitric acid. The fitting parameters U_T and *n* are presented in Table 24 for TiO_2 and HAL simulants dispersed in 2M HNO_3.

Table 24 Fitted parameters of the Richardson and Zaki equation to TiO_2 and highly active nuclear waste simulants dispersed in nitric acid.

Particle system	U_t (mm/s)	n	MSE
TiO_2	0.117	44	3.00E-06
CPM	0.123	61	1.12E-06
ZM	0.019	15	1.04E-05

Figure 5.4-14 illustrates experimental data fitted to the Richardson-Zaki estimate, using Solver. Table 24 represents much higher values of the fitted parameter *n*. Such high values of this parameter are uncommon, previous

literature values have indicated values of *n* such as 12.59 (Been and Sills, 1981).

As mentioned in section 5.4.3 the linearised expression by Maude-Whitman was also implemented to obtain *n* values. Figure 5.4-15 illustrates the *ln(u)* vs. *ln(ε)* for TiO_2 and HAL simulants in 2M HNO_3.

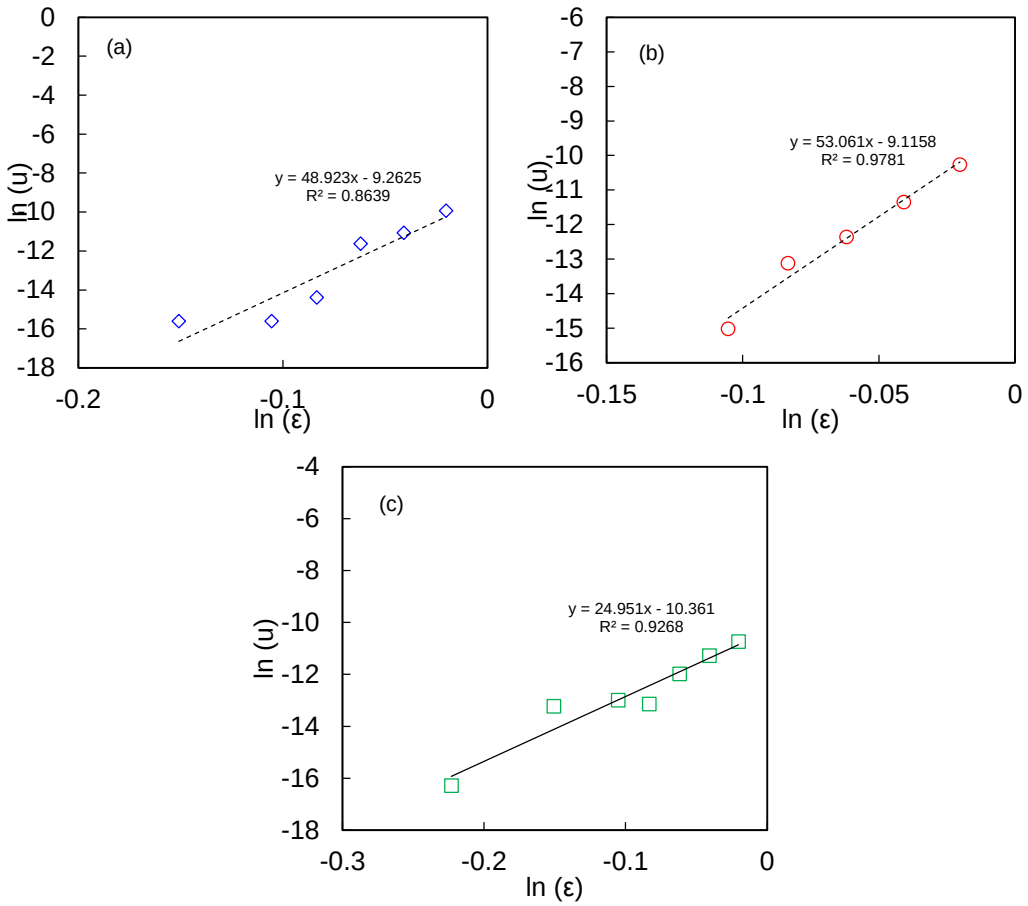

Figure 5.4-15 This data represents Ln(u) vs. Ln(ε) plot of (a) TiO_2, (b) CPM and (c) ZM dispersed in nitric acid.

Figure 5.4-15 illustrates excellent fits for the hindered settling region indicates free-settling velocities of 0.095 mm/s for TiO_2, 0.109 mm/s for CPM and 0.031 mm/s for ZM and dispersions. TiO_2 free-settling velocities are higher than CPM using the Maude-Whitmore correlation in contrast to the initial Stokes values. The straight line extrapolation of the *ln(u)* vs. *ln(ε)* plot produces extremely high *n* values of 49 for TiO_2, 53 for CPM and 25 ZM. Values of n for CPM and ZM in HNO_3 are considerably higher than in H_2O suggesting both systems are aggregated. In contrast, TiO_2-HNO_3 dispersions illustrate increased free settling and a lower *n* value when compared to TiO_2-H_2O dispersions. As the experimental and estimated values are in good agreement, the Richardson-Zaki and Maude-Whitman correlations provide reliable methods to determine values of *n*. However, it is

assumed the high values of U_t and *n* indicate aggregated systems. Therefore, the models do not consider the limited fluid exclusion due to aggregate formation.

Figure 5.4-14 illustrates the influence of fluid properties on contrasting settling rates. Reduced settling velocities could be due to the increased density (1500 kg/m^3) and viscosity (2.5 cP) properties of nitric acid. According to Stokes law, sedimentation is governed by particle size and density as well as the fluid density and viscosity, as illustrated in Figure 5.4-1. By dispersing the particles in nitric acid the density difference between the phases have been minimised. In addition, increased fluid viscosity further increases the resistance against the particles in motion. Considering the change in properties, this is a viable reason for the reduced settling velocities for CPM particles when dispersed in nitric acid. However, the explanation is inconsistent for TiO_2 suspensions. It is expected for both particles to have similar settling behaviours due to their similar mean particle size and shape.

Interparticle forces can be manipulated by controlling the concentration of H^+ and OH^- ions. For a given system a change in pH controls the surface charge of particles between separated particles. Electrolyte concentration controls the diffusive cloud of counter ions. The electrostatic potential decays exponentially with increasing distance from the shear plane. Deybe double layer thickness is inversely proportional to the decay constant. Therefore, for CPM-HNO_3 suspensions, high electrolyte concentrations escalates the decay of the electrostatic potential barrier and reduces the thickness of the EDL. At high enough concentrations, the EDL collapses resulting in domination of van der Waals attractive forces over repulsion. This causes the CPM particles to aggregate.

An interesting similarity illustrated by Figures 5.4-14 and 5.4-7 indicates for aggregated TiO_2-H_2O and CPM-HNO_3 suspensions the settling rate is reduced. Indeed, the free-settling calculations indicate reduced velocities in nitric acid for both CPM and TiO_2 dispersions, governed by the fluid properties. However, in the case of TiO_2 dispersions in water and nitric acid suggest differences in the aggregation mechanism. Consider zeta potential measurements (Figure 3.4-16), where TiO_2-H_2O suspension is at pH_{pzc} causing aggregation of particles within the suspension. In contrast, TiO_2-HNO_3 dispersions exhibit aggregation due to an increase in electrolyte concentration. Therefore, it is considered settling velocities obtained are of aggregated TiO_2-H_2O and TiO_2-HNO_3 suspensions. The increased settling

velocities of TiO_2-HNO_3 is inconsistent when compares to the free settling velocities. It is therefore expected for TiO_2 to exhibit the lowest overall settling velocity due to lower solid density and increase in fluid properties. Thus, it is possible to assume that there are alternative governing factors which govern the sedimentation behaviour.

Various research have been carried out, whereby the mean particle size increases due to aggregation and therefore results in increased settling velocities (Velamakanni and Lange, 1991, Liu et al., 2011, Godinez and Darnault, 2011). The findings of this research supports the DVLO theory, this is further supported by the calculation of the hydrodynamic diameter, discussed in section 5.4.2.3, to assume particles are aggregated due to their environment. It is evident complex behaviours occur in aggregate systems. Therefore it is proposed that settling velocity of aggregated systems, under gravitational force, is dependent on the ***aggregation mechanism***, ***aggregation structure*** and ***particle volume fraction***.

The structural network of the particle built across the sample matrix is key to determine the overall settling velocity of the system. The degree of exclusion of inter-aggregate fluid is a function of the aggregate arrangement. Figure 5.4-16 illustrates the particle network of an aggregated and non-aggregated system.

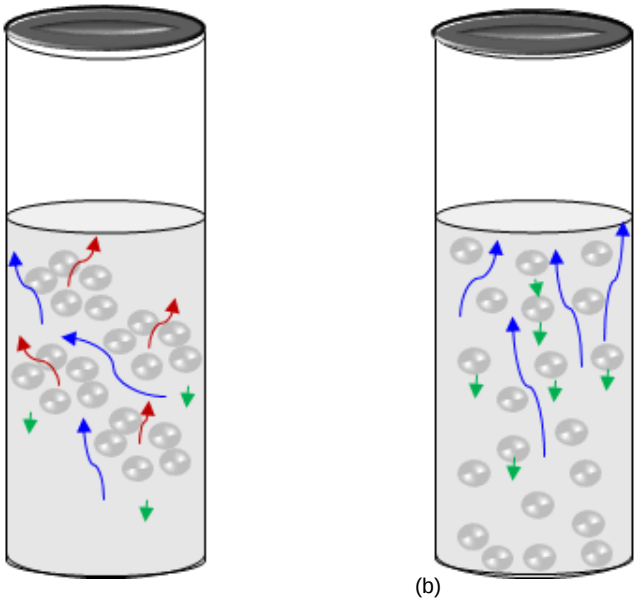

Figure 5.4-16 Particulate structural model for (a) aggregate formation and (b) non floc-aggregate systems. The blue arrows indicate fluid exclusion. The green arrows indicate direction of migration. The red arrows in (a) indicate fluid exclusion of intra-aggregate fluid exclusion.

Figure 5.4-16 illustrates the reduction in fluid exclusion in an aggregated system (Figure 5.4-16 (a). There are two main mechanisms of fluid exclusion: (i) exclusion of inter-aggregate fluid between the aggregates

moving closer to each other; (ii) exclusion of intra-aggregate fluid. The latter resulting in reduced settling velocities. Initial stages involve aggregates that are space filling, irregular shaped spheres to reduce the rate at which the fluid is excluded, the drag forces are increased and initial settling velocities are reduced. In particular cases, particle volume fraction dependant, as settling proceeds the aggregates combine and arrange themselves into a vertical column (almost acting as a cylinder). This therefore is a plausible explanation to support the reduced settling velocities of aggregating systems.

5.4.2.3 Hydrodynamic diameter

The hydrodynamic diameter of each particulate system was calculated using the Stokes law extended to concentrated dispersions (Mills and Snabre, 1994)(Stokes, 1949).

$$d_{Hydrodynamic} = \sqrt{\frac{18\mu V_s}{(\rho_p - \rho_c)g} \cdot \frac{\left[1+\frac{(4.6\emptyset)}{1-\emptyset^3}\right]}{1-\emptyset}} \qquad 5.4\text{-}2$$

This relationship considers the viscosity of the continuous phase (μ), the settling velocity (V_s), density of the particle and the continuous phase (ρ_p and ρ_c) and the particle volume fraction (∅). The data is plotted below, in Figure 5.4-17, where the hydrodynamic diameter of each particulate system was calculated in water and nitric acid as a function of particle volume fraction.

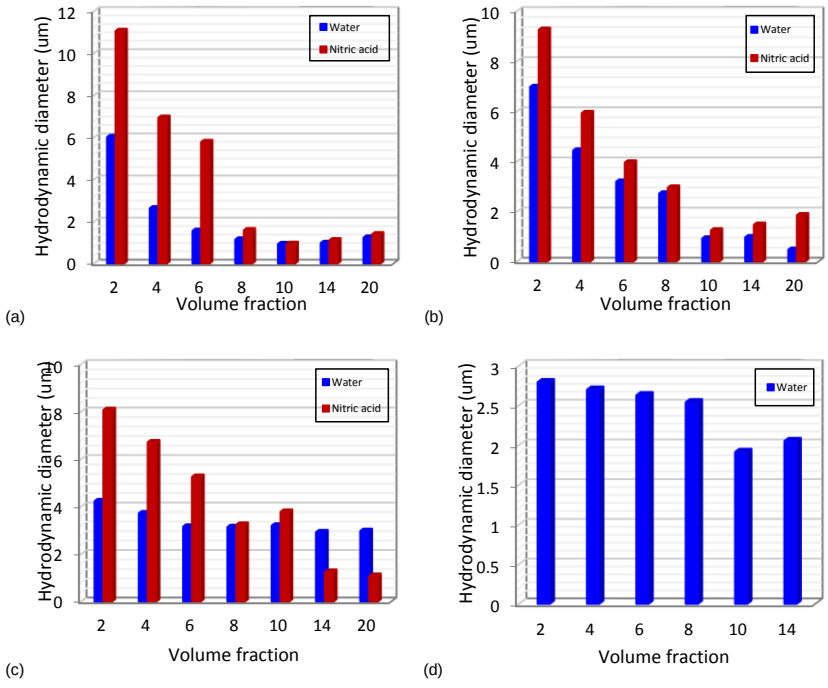

Figure 5.4-17 Hydrodynamic diameter calculated for (a) TiO2, (b) CPM, (c) ZM and (d) ZMCA dispersed in water (blue) and nitric acid (red).

Consider TiO_2 and CPM particles where the particle size decreases with increasing particle concentration, from 2-20 vol%. Both particulate systems show to increase in particle size when dispersed in nitric acid. In contrast, ZM and ZMCA particle have similar particle size with increasing volume fraction when dispersed in water. Similarities in CPM and ZM suspensions show the particle size to increase when dispersed in nitric acid, this is indicative of the aggregation of particles. This is consistent with the DVLO theory, where the increase of background electrolyte depletes the electrostatic potential barrier causing the particles to aggregate, thus the increase in overall particle size. The average particle size of ZM and ZMCA is calculated to be in the range of 2.5-4 µm, which is broadly consistent with the Mastersizer data and Image J analysis, Figure 3.4-15.

Considering the zeta potential data, Figure 3.4-16, where the TiO_2 particulate system is illustrated to be at pH_{pzc} when dispersed in water. In this region the particles are unstable and aggregated which leads to an increase in particle size when dispersed in water than in nitric acid. However, Figure 5.4-17 (a) also indicates aggregation when TiO_2 is dispersed in nitric acid. Therefore, considering the settling data in both water and nitric acid, Richardson and Zaki fits and the Stokes hydrodynamic diameter correlation it is likely both particle dispersions are aggregated. The extent of particle aggregation is dependent on the particle surface charge and thus results in complex sedimentation behaviour.

Calculation of the hydrodynamic diameter for TiO_2, CPM and ZM-HNO_3 suspensions show increase particle diameter with an increase in volume fraction. The particle size increase effectively suggests the hindered settling effects have not been considered. Thus the extrapolated stokes correlation of the hydrodynamic diameter is not applicable for the aggregated systems.

5.4.2.4 Equilibrium sediment height

The Turbiscan® has the ability to emphasise the difference in settled bed structures, as illustrated in the settling curve data. The equilibrium height of the sediment may also be related to the shape of the particle. It is expected for both TiO_2 and CPM to have similar particle bed structure due to their similarities in size and shape. The influence of particle shape can be determined by calculating the mean particle volume fraction in the sediment bed. The initial volume fraction (ϕ_o), initial height of interface (H_o) and the equilibrium height of the sediement (H_{Eq}) these are key parameters required to calculate the particle volume fraction in the consolidated bed. This can be calculated using the following expression:

$$\bar{\emptyset} = \emptyset_o \frac{H_o}{H_{Eq}} \qquad 5.4\text{-}3$$

Figure 5.4-18 represents the relationship of the change in sediment bed particle volume fraction as a function bulk volume fraction (0.02-0.14) for TiO_2 and simulated HAL solids.

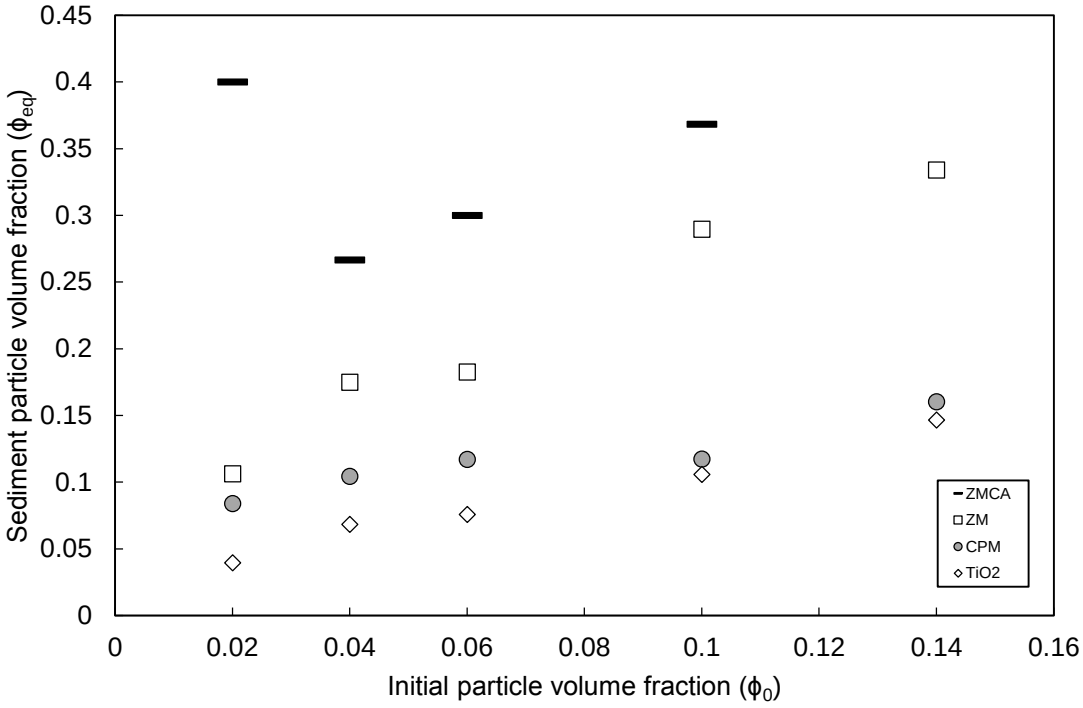

Figure 5.4-18 The data indicates the sediment particle volume fraction as a function of bulk volume fraction. The data represents nuclear waste simulants (CPM, ZM & ZMCA) and TiO_2 suspensions, the particles are dispersed in DI water. The data represented here are calculated from the backscatter information generated from the Turbiscan.

Figure 5.4-18 illustrates a non-linear relationship between the calculated particle volume fraction of the consolidated bed and bulk particle volume fraction. Each particulate system indicates the dependence of the bulk particle concentration on the final consolidated bed particle volume fraction. At any given bulk volume fraction ≥ 0.14, the highest particle volume fraction is demonstrated by ZMCA dispersions, and the lowest is demonstrated by TiO_2 dispersions. Additionally, TiO_2, CPM and ZM systems illustrates consistent ϕ_{eq} with increasing ϕ_o, until ϕ_o reaches 0.1 where the transition from a hindered settling region to a compressive region occurs.

Aggregated TiO_2 particles and spherical CPM particles sediment into a loosely packed bed, thus higher equilibrium heights are obtained after the settling period, compared to ZM and ZMCA particles. The larger equilibrium bed for TiO_2 supports the highly aggregated nature of the particles. The cubic shape of ZM may allow these particles to settle into compact, dense sediment creating a uniform, stacked bed. In comparison, the cuboidal

ZMCA settles into a compact bed with the highest sediment bed volume fraction due to the elongated nature of the particles at ϕ=0.02. Bulk volume fractions, 0.04-0.1, exhibit lower ϕ_{eq} than a bulk volume fraction of 0.02, albeit ϕ_{eq} increases within increasing ϕ_o. It may be assumed from Figure 5.4-18 that at low ϕ_o the ZMCA particle fall into a flat packed bed and at higher ϕ_o the ZMCA particles have arbitrary orientation during sedimentation and thus leading to a randomly orientated ZMCA sediment bed. Thus suggesting the final sediment bed volume fraction is dependent on the initial bulk volume fraction, where the orientation of the ZMCA particles become important. This is consistent with settling behaviours illustrated in Figure 5.4-7, where at lower bulk volume fractions ZMCA particles are orientated with the dominant particle-axis perpendicular to the direction of flow. At higher bulk volume fractions the ZMCA particles orient themselves parallel to the direction of flow, thus leading to a lower ϕ_{eq}.

The particle volume fraction in the ZM and ZMCA sediment is much higher compared to CPM. This suggests that the energy required to re-suspend these solids will be much higher than that of the CPM solids. It can be assumed that the particles in the ZMCA settled bed have more contact points with other particles and create more inter-particle forces and thus more energy is required to break the structure of the bed. Based on the equilibrium height it can be assumed the ZMCA particles sediment into a flat packed bed, where face-to-face contact of the dominant particle axis, evident at low particle volume fractions. In the case of CPM the lower volume value suggests that the particles are further apart from each other, resulting in few inter-particle forces and therefore lower energy is required to re-suspend these solids. Chapter 6 discusses the influence of particle properties in sediment bed re-suspension. The rheological parameter, yield stress, can determine the stress required in order for full flow of the solids to occur.

5.4.3 Centrifugal force

An alternative method to observe the settling rate, with an accelerated driving force, is the Lumisizer®. By using a centrifugal driving force, any particulate fines that would not settle under gravity will be accounted for in settling data. The transmission profiles in Figure 5.4-19 represent suspensions of 6 vol% with a speed of 1000 rpm, for the CPM, ZM and ZMCA and TiO_2 particles. The sedimentation rate of each particulate system and the height of the sediment bed can be estimated from measuring the

increase in transmission at the settling front border with the clear supernatant.

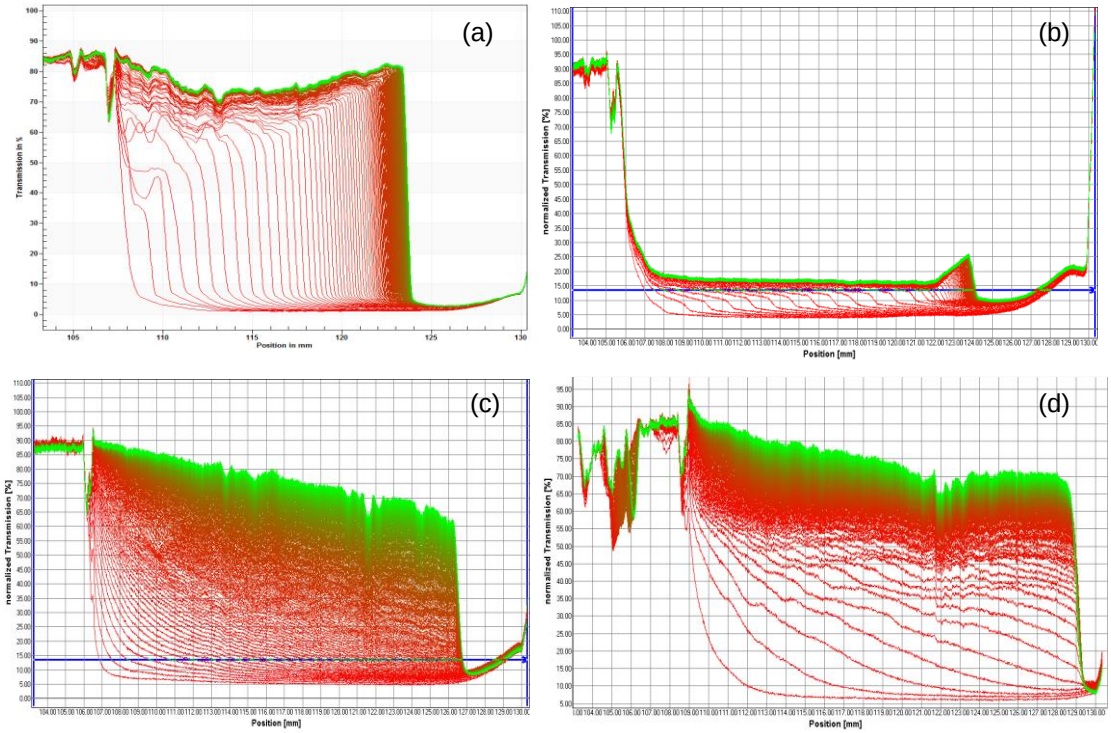

Figure 5.4-19 Sedimentation profiles of nuclear waste simulants at 6 vol% at 1000rpm: (a) TiO_2; (b) CPM; (c) ZM; (d) ZMCA. All particulate systems have been dispersed in DI water. The data represented was collected under centrifugal force using the LumiSizer.

Distinct settling properties are illustrated through the shape of the transmission profiles. TiO_2 dispersions settling with a uniform settling behaviour, under centrifugal force, due to its monodisperse and relatively spherical particle shape. It appears CPM dispersions to have reduced light transmission through the sample. This is suggestive of the particles adhering to the inside of the PC sample holder. This therefore interferes with the degree of light passing through the dispersion. Both ZM and ZMCA dispersions indicate the effect of size polydispersity, where it is evident from the profiles segregation of the dispersion occurs. The profiles properties are consistent with the backscatter data obtained from the Turbiscan.

The extinction profiles were collected using STEP^{TM}-technology (Space and Time resolved Extinction Profiles). Settling curves are obtained by assigning an appropriate threshold of 20% for all profiles. This threshold allows extraction of reliable velocity profiles for comparative studies for each particulate dispersion.

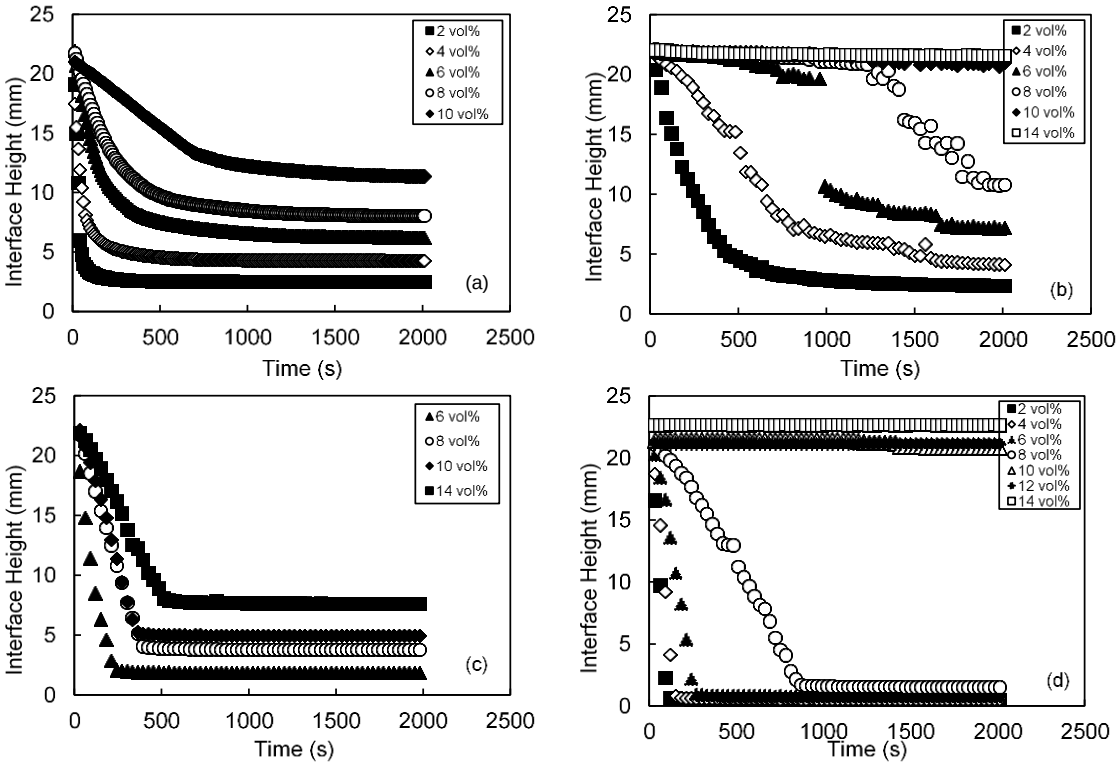

Figure 5.4-20 Settling curves of (a) TiO_2, (b) CPM, (c) ZM and (d) ZMCA dispersed in DI water as a function of volume fraction. The data presented was collected using a centrifugal force technique using the Lumisizer, over a period of 30 mins, at 1000 rpm.

Figure 5.4-20 illustrates the change in interface height as a function of time. Particulate systems, TiO_2, CPM, ZM and ZMCA, show a linear regressing profile as a function of volume fraction. This is indicative of gravitational settling, the change of the interface from initial to consolidated height. Settling curves extracted from raw profiles with low transmission profiles for CPM produces unsystematic settling data, as illustrated in Figure 5.4-19 (b). This supports the deviation from the linear regressing profile indicated by the other simulants.

The sediment bed height for the TiO_2 is considerably larger than for the ZM and ZMCA samples (Figure 5.4-20 (a)) which is consistent with the Turbiscan data (Figure 5.4-3). Given the constant starting volume fraction of solids, this confirms the presence of an open voluminous sediment, a feature that is indicative of aggregate formation. The ZM has a consolidated bed height that is larger than the ZMCA, which is consistent with its bulky cubic nature creating more interstitial gaps, but it is still markedly denser than the much smaller TiO_2. Figure 5.4-20 (d) illustrates two key features for ZMCA dispersions, at low volume fraction $\geq 8vol\%$ typical gravitational settling is apparent at higher volume fraction $\leq 10vol\%$ the dispersion approaches the gel-point. As the particle volume fraction of ZMCA increases the particle-particle interactions become prominent and the fluid exclusion becomes

restricted. At high particle concentration the elongated ZMCA particles tend to align themselves along the dominant particle-axis. At this point the particles become highly ordered across the sample matrix and thus creates a liquid crystalline solution, as illustrated in Figure 5.4-20 (d) $\leq 10vol\%$.

As illustrated by Figure 5.4-6, the gel-point of ZMCA dispersion is established at $\leq 14vol\%$. In contrast, Figure 5.4-20 (d) indicates ZMCA dispersions exhibit the gel-point at a lower particle volume fraction, $\leq 10vol\%$. Section 5.4.2.1 concludes the orientation of cuboidal ZMCA particles is dependent on the initial particle volume fraction. At low initial particle volume fractions, ZMCA particles tend to settle with the dominant particle-axis perpendicular to the direction of flow, at high initial particle volume factions, ZMCA particles create a disorganised network as the particles restrict the movement of neighbouring particles, as illustrated in Figure 5.4-21.

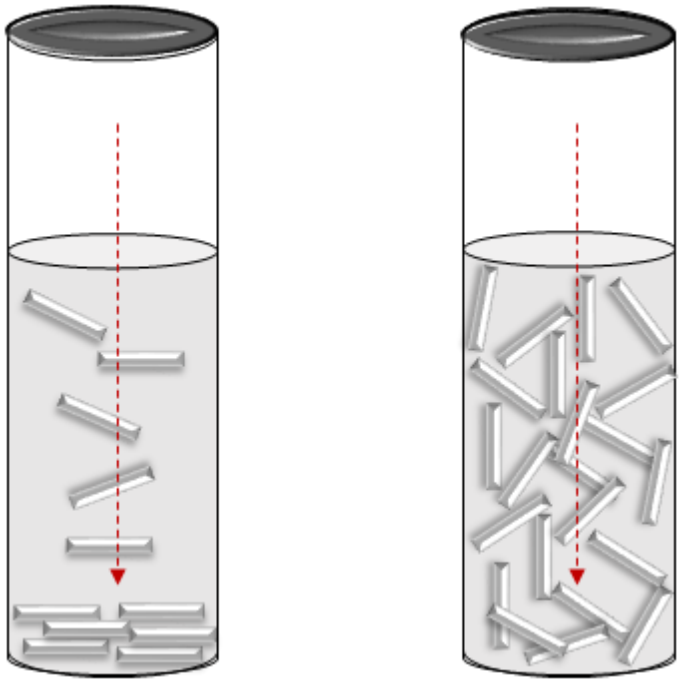

Figure 5.4-21 Cuboidal ZMCA particle orientation as a function of initial particle volume fraction; (a) Dispersions is at a low volume fraction indicating dominant particle-axis perpendicular to the direction of flow and (b) dispersions at a high particle volume fraction indicating dominant particle-axis parallel to the direction of flow.

It may be assumed the gel-point defined at a lower initial particle volume fraction for ZMCA dispersions from the Lumisizer data is a result from the diameter of the sample cell. Figure 5.4-21 illustrates the dimensions of the Turbiscan and Lumisizer sample holders. The restricted movement of particles is further enhanced by decreasing the diameter of the sample cell.

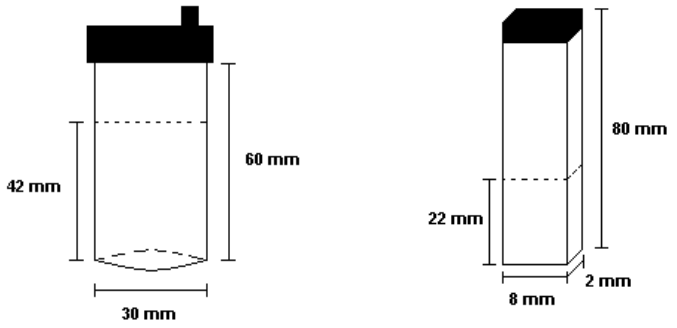

Figure 5.4-24 Dimensions of the sample holders for each sedimentation technique (a) Turbiscan sample cell with an internal diameter of 30 mm and an initial sample height of 42 mm (b) Lumisizer sample cell with an internal diameter of 8 mm and initial sample height of 22 mm

Figure 5.4-22 illustrates the Turbiscan to Lumisizer ratio is 15:1. The wall effects within in the Lumisizer measurement cell is enhanced, the reduced volume leads to the cuboidal ZMCA particles to bridge across the sample matrix and thus establish a gel point at lower concentrations compared to the larger volume provided by the Turbiscan measurement cell. Thus, the walls of the measurement cell affect the structure of internal particle network which is enhanced as the diameter of the measurement cell is reduced (Buratto et al, 2014). Furthermore, the Turbiscan data neglects the finer particles in suspensions, the sediment height calculated from Figure 5.4-6 is of the larger 3 µm particles for ZMCA dispersions, thus underestimating the gel-point. The gel-point of a dispersions is governed by the particle properties, initial volume fraction and dimensions of the sample cell.

The Lumisizer® has the ability to provide some insight on the difference in the settled bed structure which different particle samples form. Relating this to the HASTs the ZM particles are likely to settle and form compact bed which suggests that the energy required to re-suspend these solids will be much higher than that of the CPM solids. It can be assumed that the particles in the ZM settled bed have more contact points with other particles and will therefore create stronger interparticle forces and thus more energy will be required to break the structure of the bed. In the case of CPM the bed structure suggests from figure 5.4-20 (b) that the particles are further apart from each other, this results in few interparticle forces and therefore lower energy is required to re-suspend these solids.

Key settling velocity data extracted from the sedimentation profiles are illustrated in figure 5.4-23. The centrifugal velocities were converted to gravitational force to correlate to better correlate to the Turbiscan data. The transmission profiles were obtained during centrifugation at 1000 rpm, this corresponds to a relative centrifugal acceleration $(\propto = (1.118 \times 10^{-5}) \times$

$rpm^2 \times R$) of 127 x g. The radial (*R*) position at the bottom of the sample cell is 114 mm. Thus,

$$V_{@1g,1\times g} = \frac{V_c}{RCF} \qquad 5.4\text{-}4$$

The calculated sedimentation velocities are illustrated below.

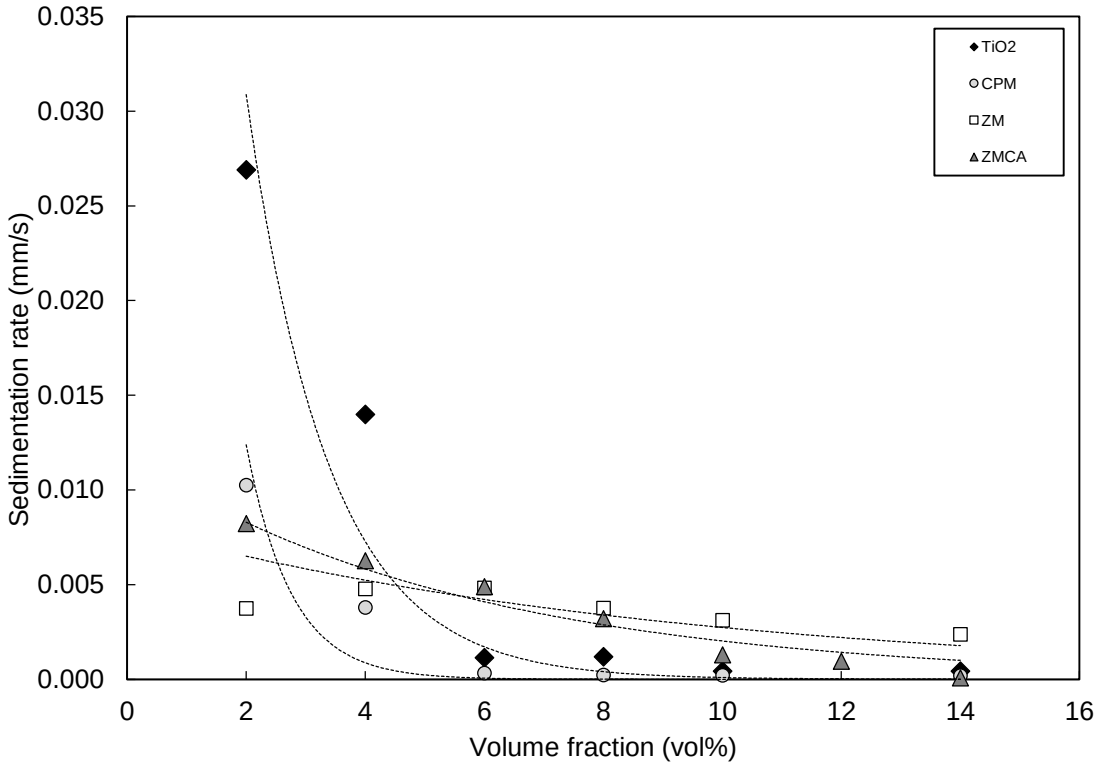

Figure 5.4-25 Sedimentation rate as a function of volume fraction. The data represents nuclear waste simulants (CPM, ZM & ZMCA) and TiO_2 suspensions, the particles are dispersed in DI water. The data represented here are calculated from the backscatter information generated from the Lumisizer.

Figure 5.4-23 indicates CPM and TiO_2 to have the fastest settling rate and the ZMCA and ZM, once again, to have the slowest. The settling velocity for all dispersions was calculated using the linear region of the settling curve. Dispersions ≥6 vol% indicate particle shape and volume fraction effects for ZMCA particles, as observed in the Turbiscan data. ZM dispersions appear to be settling in the free settling region, independent of neighbouring particles. However, this seems to be inconsistent with previous data.

The TiO_2, CPM, ZM and ZMCA sedimentation data is broadly consistent with the data collected using the Turbiscan®, and indeed the applied centrifugal force in the Lumisizer may additionally accelerate the particulate segregation that is occurring within the ZM samples. It is noted that settling data is estimated in both the Lumisizer® and Turbiscan® by measuring the large transmission increase at the supernatant boarder with time. If high levels of segregation are occurring, larger particles may settle quickly within the

dispersion zone, and not therefore be measured in the transmission increase of the supernatant boarder. Therefore, it is assumed the measured settling rates for ZM may be slower, because such light scanning techniques that focus only quantifying the change in supernatant boarder are not suited to measuring polydisperse suspensions which do not settle in hindered modes.

One of the main challenges of this research is the quantity of material available for experimental analysis. Sedimentation tests on a larger scale potentially involve manual extraction of sedimentation data by measuring the change in height between the supernatant and the particle interface as a function of time. Despite this technique reducing wall effects, it is not a feasible option for the material of study due to the large quantity of material required. As the Turbiscan is specific one type of sample holder (dimensions mentioned previously) further studies on the effect of the variation of sample holder diameter on sedimentation behaviour is not possible for this technique. As these particles have broadly similar particle size and the same volume fractions are studied it can be suggested that the wall and end effects are similar for each particulate system. Hence, the data are internally self-consistent.

5.5 Conclusions

This chapter highlights the key solid-liquid properties which influence the sedimentation behaviour of the nuclear waste simulants. The sedimentation data indicates the settling behaviour is governed by a number of factors

- Particle properties such as size and density influence the settling behaviour to a certain extent. However, particle morphology is a dominating influence on the sedimentation behaviour. Increased aspect ratio of the ZMCA particles oscillate during sedimentation to achieve an equilibrium position, the rapid movement of the particles increase the drag flow acting on the particles and thus a reduction in settling properties.
- Particle volume fraction, at high particle content interparticle interactions becomes increasingly influential. Particle orientation of ZMCA particles are determined by the increase in particle volume fraction.
- Particle network across the sample matrix. This is influenced by the particle properties (size & morphology) and the fluid properties (salt concentration). The aggregation network formation becomes influential as a function of volume fraction.

It is important to consider the rate of fluid exclusion as a means of characterising the sedimentation behaviour. The equilibrium height enables analysis of the impact of particle shape on consolidation of the sediment bed. Particle aggregates create and open bed compared to dense compact beds created by cube and cuboid shaped particles.

The application of these behaviours to the current storage, transportation and immobilisation of the highly active nuclear waste can be determined. The HAS tanks store the waste in controlled agitation conditions, airlifts and jet ballasts. Taking into account the results of this study, the agitation systems will need to be tailored to the diverse sedimentation profiles of the particulate systems. Manipulation of particle morphology by addition of an organic additive increases the aspect ratio of ZM systems. This has desirable effects for transportation through pipes, decreasing the changes of depositions to occur in pipes and thus eliminating corrosion of pipe lines through a decrease in blockages.

Two sedimentation techniques, Turbiscan and Lumisizer, demonstrate consistent behaviours. One of the challenges this research encountered was the quantity of material available for behavioural studies. As previously mentioned, the synthesis of the nuclear waste simulants are time consuming and costly. The key advantages the Lumisizer provide are small sample volume required for measurement, 12 samples measured at any one time and analysis of high particle concentration. Despite the advantages, the Turbiscan provides relevant sedimentation data to the HASTs, as measurements are carried out under gravitational settling.

6 Influence of particle properties on rheological behaviour

Summary

This chapter describes the influence of particle properties, particle shape and size, on rheological behaviours, inclusive of flow behaviours and rheological parameters, shear yield stress and compressive yield stress. HAL dispersions below and above the gel-point will also be considered in this chapter. This Chapter will highlight key results from Chapters 3 & 5 and link them directly to rheological behaviours.

6.1 Introduction

It is of continuing interest to further improve nuclear waste treatment strategies. The previous chapters have covered the characterisation of chemical and physical behaviour for HAST/HAL relevant nuclear waste simulants. Relevant rheological data for these simulant materials is critical to developing strategies for storage, immobilisation and transportation of the HAL. This study highlights the flow behaviour of the HAL solids and two rheological parameters, yield and compressive yield stress.

A research highlight is to consider the particle morphology manipulation of ZM systems to produce ZMCA systems (Chapter 3) to assess the direct effect of particle morphology on rheological behaviour. Furthermore, this research aims to demonstrate the advantages of employing a vane tool geometry to characterise the flow behaviour of complex HAL dispersions. Ultimately, the aim of this chapter is to link the chemical and physical properties of HAL, as discussed in Chapters 3 and 5, to the measured rheological parameters. This may allow empirically predictive approaches to manage the highly active nuclear waste materials.

6.2 Literature review

The term '*Rheology*' was proposed by Bingham and published by the American Society of rheology in 1929 (Barnes et al., 1989, Barnes, 1995). Rheology is the study of flow behaviour of fluids and the deformation of matter under an applied stress. It is by employing well-defined rheological techniques that direct measurements of viscosity for structured fluids are conducted. Examples of structured fluids include polymer solutions, emulsions and dispersions. The flow properties of liquids play a significant role in our daily lives, from the blood flowing around our bodies, the viscosity of the liquids we use as toiletries, to the properties of the liquids we consume.

Understanding rheology contributes significantly to process development. Measurement of, for example, viscosity behaviour is valuable in predicting flow-ability, pump-ability and handling of the material during the key process operations. An example of direct assessment requires the knowledge of the extent of how viscous the material is i.e. a high viscosity dispersion requires more power to pump, compared to a low viscosity dispersion. The knowledge of this rheological behaviour is useful for pump and pipe line engineering design.

This research project is focused on the properties of highly active nuclear waste suspensions and sludge. Chapter 3 focused on determining particle properties and Chapter 5 assessed the influence of the interparticle interactions, governed by the defined particles properties and particle volume fraction, on sedimentation behaviour of HAL solids. This chapter will now consider the effect of applied stress to the microstructure of the flowing suspension, and thus determined the properties that govern the behaviour of the fluid flow field around the interacting particles.

A key highlight of this research is to assess the flow behaviour of HAL dispersions, this links directly to the flow of HAL through the tank upon jet re-suspension and also assessing the pumping power required for HAL pipeline transport. Yield stress studies are able to confirm the difficulties of re-suspending the HAL sediment. Both shear and compressive yield stress behaviours exist in the systems, however are dominated by the shear yield. The presence of compressive yield behaviour occurs in the impingement jet region where there is a presence of significant pressure force acing down as well as shear forces acting laterally.

6.2.1 Rheological definitions

There are a number of definitions which are frequently used in relation to flow behaviour and the measurement of flow behaviour (Barnes et al., 1989, Goodwin et al., 2000)

- Shear stress (σ). Stress is known to be the force divided by the area of application; however shear stress is a component of stress which is tangential to the area where the force is applied. It is measured in Pascals (Pa).
- Shear strain (γ). When a stress is applied to a material it is evident that deformation will occur, this is considered to be relative deformation in shear.
- Shear rate ($\dot{\gamma}$). This is the change of deformation of the material per unit time. It is measured in (s^{-1}).
- Viscosity (μ). This term is known to be a property of a fluid where the resistance of flow occurs. The resistance of deformation occurs with increasing rate of deformation, this can be expressed as an equation where it expresses that the shear stress is divided by the shear rate, $= \frac{\sigma}{\gamma}$. It is measured in Pa.s.

- Yield Stress (σ_y). The stress required for a material to plastically deform. It is measured in Pascals (Pa).
- Compressive yield stress ($P_y(\phi_{eq})$). Stress applied until a point where the particle network has sufficient strength to prevent further collapse, measured in (kPa).

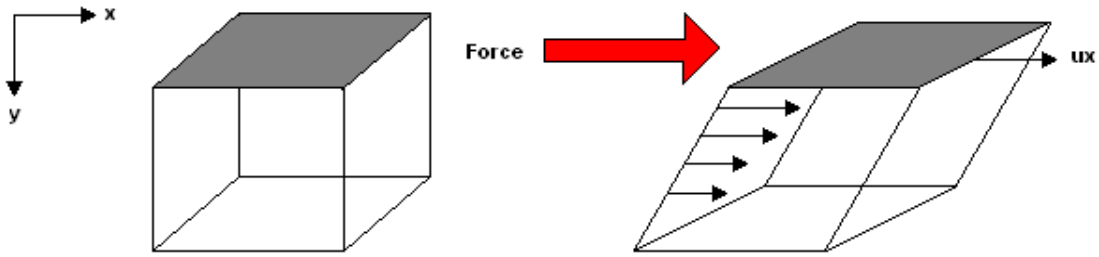

Figure 6.2-1 A simple shear deformation diagram showing the effect of applying shear stress (σ=F/A) to a material giving rise to velocity gradients known as the shear rate ($\dot{\gamma} = V/h$).

As illustrated in Figure 6.2-1 the top plate shows to be moving at a constant velocity where the stress is identified as the force per unit area and the strain to be the change in length of the deformation.

6.2.2 Newtonian behaviour

Rheological behaviour of the fluids can be expressed as two equations which consider the viscous fluid (Equation 6.2-1) and the elastic solid (Rychlewski, 1984) (Equation 6.2-2)

Newtonian fluid model: $\sigma = \eta\gamma$ 6.2-1

Hookean solid model: $\sigma = G\gamma$ 6.2-2

Where *G* is the shear modulus, η is the viscosity coefficient and γ is the shear rate. Hooke's law displays the ideal behaviour of a solid whereby the deformation of materials occurs and instantaneous recovery is observed. A Newtonian liquid is where the flow is persistent with constant application of stress.

A Hookean solid experiences application of stress on the surface of the solid which causes deformation to occur, after deformation has occurred the deformed state is persistent with the application of stress. Linear behaviour in colloidal systems is rare to come across, the application of large stress sand strains will diverge from the above equations (6.2-1 and 6.2-2).

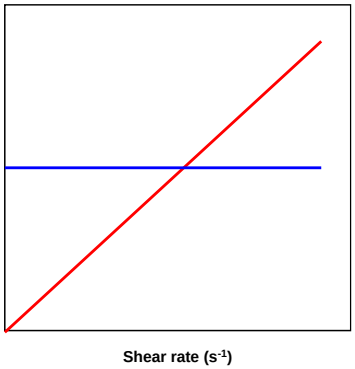

Figure 6.2-2 The blue line shows viscosity as a function of shear rate and the red line shows shear stress as a function of shear rate, this represents Newtonian behaviour fluid

Figure 6.2-2 illustrates Newtonian flow where the viscosity is constant over the applied shear rate, this indicates that the fluid independent of the forces acting upon the solid matter.

6.2.3 Non-Newtonian behaviour

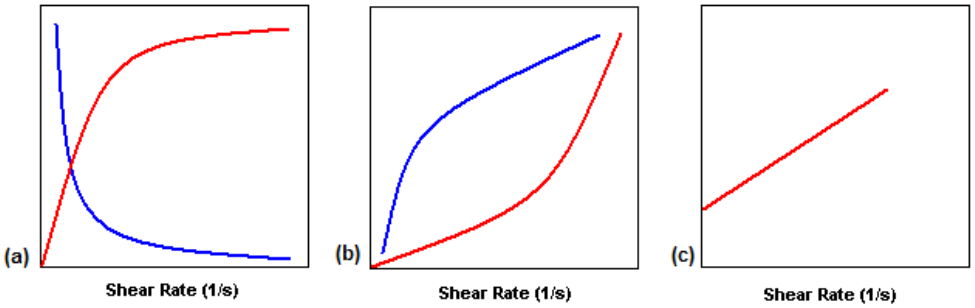

Figure 6.2-3 Different types of flow curves showing non-linear behaviour of fluid flow. The blue line shows viscosity as a function of shear rate and the red line shows shear stress as a function of shear rate; (a) Shear-thinning flow (b) Shear-thickening flow (c) Bingham Plastic flow

Figure 6.2-3 (a) illustrates a decrease in viscosity with increasing shear rate, this is a *shear-thinning* fluid. Such flow may be due to the breakdown of aggregates in a suspension, where large clusters of particles are separated in the low field producing less resistance to that flow and a corresponding thinning of the fluid. Alternatively, a re-arrangement of particles in a suspension can also produce shear-thinning behaviour.

In the opposing case where the viscosity increases with increasing shear rate, the fluid is said to be *shear-thickening*, as illustrated in Figure 6.2-3 (b). This behaviour is typical for dispersions at high particle volume fraction. Shear-thickening dispersions exhibit *dilant* flow behaviour. At low shear rates the continuous phase acts a lubricant between two dispersed particles, at high shear rates the fluid is excluded out of the interstices between the particles, thus creating densely packed particles.

Bingham plastic fluids are fluids where a particular stress must be applied in order for flow to occur, the stress which must be overcome and is known as the *yield stress,* illustrated in Figure 6.2-3 (c). This is a viscoplastic fluid which illustrates a linear relationship between shear stress and shear rate. Once yield stress is achieved the material can exhibit all three flow behaviours, Newtonian, shear-thinning and shear-thickening.

6.2.4 Mathematical models representing rheological flow behaviour

A typical rheological flow curve is a function of applied shear stress over a wide range of shear rate. Consider shear-thinning behaviour, at very low shear rates the viscosity is constant (μ_0). As the shear rate increases initially, the viscosity decreases, this is usually illustrated by a linear regression on a log-log plot. At high enough shear rates the curve will plateau, where the viscosity becomes effectively constant (μ_∞). Both μ_0 and μ_∞ are the limiting Newtonian viscosities and are connected by the power-law region. There are many mathematical models which are able to describe all the features described. The simple equations relate the viscosity and shear rate with a number of empirical parameters, illustrated in Figure 6.2-4.

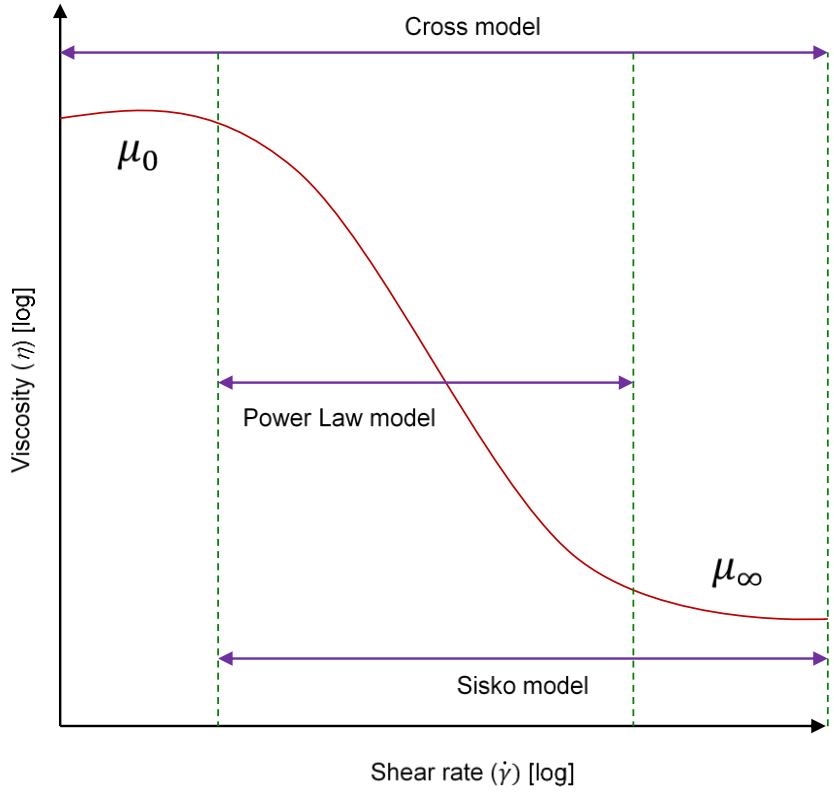

Figure 6.2-4 A graph illustrating a typical shear-thinning flow behaviour. Empirical models, Cross, Power law and Sisko, represent the flow behaviour as a function of shear rate.

Figure 6.2-4 illustrates all three distinct regions of a shear-thinning flow curve, the Cross model is an appropriate model. Cross (Cross, 1965) developed an equation to describe the viscosity

$$\frac{\mu-\mu_\infty}{\mu_o-\mu_\infty} = \frac{1}{1+(K\dot{\gamma})^m} \qquad 6.2\text{-}3$$

Where K is a dimensionless parameter of time (usually $\dot{\gamma}$ at *1 s*$^{-1}$) and m is another dimensionless fitting parameter. Commonly this model is used to describe non-Newtonian fluids where the value of *m* determines the extent of shear-thinning; when $m \to 0$, this defines more Newtonian liquids and when $m \to 1$ it defines more shear-thinning liquids.

For most structured liquids at high shear rates the Cross model simplifies to equation 6.2-4 (Barnes, 2000)

$$\mu = \mu_\infty + \frac{\mu_0}{(K\dot{\gamma})^m} \qquad 6.2\text{-}4$$

The measurement range on occasion neglects both the lower and higher shear rate regions of the curve, leaving the power-law region (Khalili Garakani et al., 2011, Reiner, 1926). In this case the power law model is viable to describe the behaviour

$$\mu = k\dot{\gamma}^{n-1} \qquad 6.2\text{-}5$$

Where *k* is the consistency coefficient and *n* is the power law index. This model provides good analysis for fluids that show shear-thinning behaviour, for a power fluid with 0<n<1 the viscosity decreases as the shear rate increases. Shear-thinning behaviour tends to increase when the value is closer to zero. This law is adequate enough to describe various types of non-Newtonian fluids.

6.2.5 Rheological techniques for flow behaviour

It is important to determine the rheological behaviour of slurries, whether it be for mining waste, sewage sludge, nuclear waste slurries, coal slurry, or a multitude of other examples. An ability to predict flow behaviour can be used to improve industrial processes and/or reduce potential hazards.

Shear rheometry may be divided into two groups, where shear is generated by two methods (Larson, 1999, Macosko, 1994): drag flows (concentric cylinder, cone/plate and parallel plate), in which shear is produced between

a moving and a fixed solid surface. Pressure driven flows (capillary), in which shear is created by a pressure difference over a closed channel. Figure 6.2-5 illustrates the key components of a drag flow rheometer.

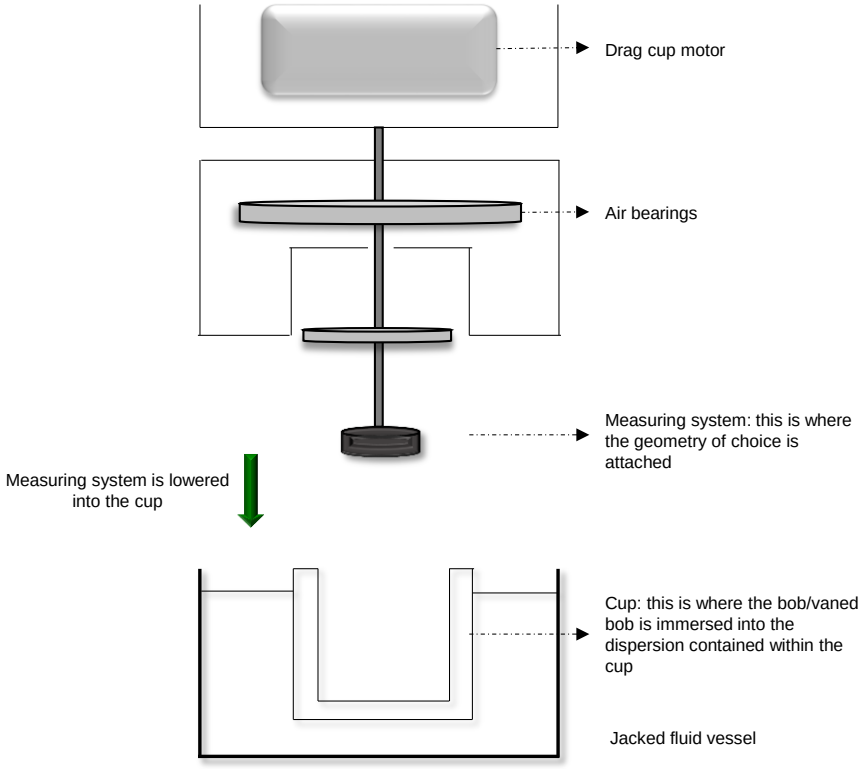

Figure 6.2-5 Schematic diagram of the Bohlin C-VOR rheometer

The capillary rheometry technique implements a pump to force fluid through a capillary. The volume flow rate and the pressure gradient in the region of the fully developed flow are measure to determine the shear viscosity. Capillary rheometers are designed for characterising polymer melts at high shear rates, from 10 to 10 000 s^{-1}. This technique was first proposed by Cogswell (Cogswell, 1972b, Cogswell, 1972a) and then by Binding (Binding, 1988). Two main sources of error are associated with this technique and are described as end and wall errors. End errors are a result of pressure loss (Nguyen and Boger, 1992), optimised methods implemented can eliminate these effects (Bagley, 1957, Jastrzebski, 1967). Wall slip are categorised in two effective groups: particle migration resulting in the formation of a liquid layer (Blair, 1958, Jastrzebski, 1967, Barnes, 1995, Cheng, 1984, Seshadri and Sutera, 1968) and concentrated solids flowing through smoothed walls of the capillary tube (Vinogradov et al., 1978).

The concentric cylinder, first developed by Couette (Couette, 1890) measures the steady shear properties of suspensions. It is simple to operate and available at a low cost. This system consists of an outer, stationary

cylinder and an inner rotating cylinder. The suspension if placed into the cup and the bob is immersed into the suspension, the fluid will surround the bob. The concentric cylinder geometry is a widely used technique for viscosity measurement, for example in colloidal science and food science (Annable et al., 1993, Nindo et al., 2007, Gonçalves and Lannes, 2010) .

Darby (Darby, 1985) established limitations of the concentric cylinder related to the fluid model, the gap width and the shear stress relative the yield stress. Other sources of error include end effects, modification of the cylinder end by altering the shape eliminates the end effects (Van Wazer, 1963, Highgate and Whorlow, 1969, Princen, 1986, Mooney and Ewart, 1934). Wall slip effects are enhanced for smooth cylinders, small gap and low shear rates (Barnes, 1995, Cheng, 1984, Cheng and Richmond, 1978), roughened surface of the geometry surfaces are able to eliminate the wall effects (Barnes, 1995, Dobson, 1975).

The cone-plate geometry is widely used (McKinley et al., 1991, Crawley and Graessley, 1977, Skarja et al., 1997, Geiculescu et al., 2014, Nechyporchuk et al., 2014), however it is only suitable for material with high viscosity. Mooney and Ewart (Mooney and Ewart, 1934) first designed the cone and plate geometry, this was further developed by (Jobling and Roberts, 1959) and consists of a stationary flat plate and a rotating cone. Limitations with high viscosity suspensions include separation of two phases, this increases with increasing cone diameter, decreasing cone angle and decreasing gap size (Vinogradov et al., 1978, Magnin and Piau, 1990, Whorlow, 1980, Macosko, 1994).

All geometries, to some extent, exhibit measurement limitations in terms of end effects and wall effects. The ends effects are expressed in terms of an additional shear flow at the bottom of the rotating cylinder. The effects can be minimised by changing the bottom of the cylinder to a conical shape. Considering the angle of the cone, this optimisation ensures the shear rate is similar at the bottom of the cylinder to that of the gap on the sides. Wall effects can decrease the true viscosity values; the severity of this is dependent on the particle concentration of the suspension i.e. at high particle content.

The vane device has been tailored to improve upon the weaknesses that the concentric cylinder poses, in terms of wall slip. The vane consists of four blades attached to a cylindrical shaft, when immersed into the sample

results in minimal damage to any material structure for a solid-liquid system. The vane has been developed for the purpose of yield stress measurement; however, this research aims to demonstrate that by fully understanding the suspension properties the vane tool can provide reliable flow behaviour responses. The assumption of this technique is that as the vane rotates the suspension surrounding it produces a cylindrical surface.

6.2.5.1 Mathematical validation of the cup / bob and cup / vane geometries

The concentric cylinder (bob) and vane geometries are illustrated in Figure 6.2-6.

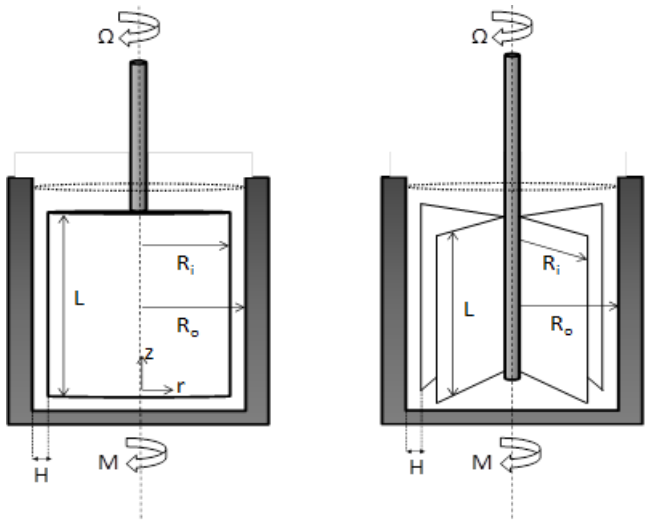

Figure 6.2-6 Schematic of (a) concentric cylinder geometry and (b) vaned bob geometry. This illustrates the outer cylinder with an inner radius of Ro which is known as the cup and the inner cylinder with an outer radius Ri known as the bob, the torque of the inner cylinder (M), the angular displacement at steady rotation (Ω_i), the gap size (H) and the length of the inner cylinder (L).

The torque on the inner cylinder is estimated from the angular deflection of the wire. The sample is placed in the outer cylinder and the inner cylinder is immersed into the suspension. The volume (*V*) of the sample placed in the gap between the two cylinders is expressed in Equation 6.2-6

$$V = \pi LH\{H + 2R_i\} \qquad 6.2\text{-}6$$

The large surface area drives a larger torque for a given sample, compared to any other geometry. The analysis of absolute values relates the shear stress to the torque measurements and the shear rate to angular velocity. Considering the flow of a fluid confined between the rotating inner cylinder at Ω_i the following assumptions can be applied to this measuring system (Macosko, 1994)

- Steady, laminar, isothermal flow
- Negligible gravity and end effects
- Symmetry in angular displacement
- Well defined boundary conditions

Based on the assumptions the working equations of motion in a cylindrical flow can be defined. The stress contribution across the gap between the cylinders can be defined as

$$\frac{M_i}{R_i} = \tau_{\theta r}(R_i) 2\pi R_i L \qquad 6.2\text{-}7$$

Rearrangement of this equation in terms of shear stress gives the expression, if the torque is measured on the inner cylinder

$$\tau_{\theta r}(R_i) = \frac{M_i}{2\pi R_i^2 L} \qquad 6.2\text{-}8$$

If the torque is measured on the outer cylinder

$$\tau_{\theta r}(R_o) = \frac{M_o}{2\pi R_o^2 L} \qquad 6.2\text{-}9$$

The shear stress at the bob is determined by dividing the torque by the surface area of the inner cylinder. Some rheological instruments which employ the concentric cylinder have the outer cylinder rotating and the inner cylinder is kept in a static condition. For the purpose of this study, the working equations will be expressed as a function of the inner rotating cylinder. The local shear strain and rate can now be calculated, the shear strain for narrow gaps (where the curvature is neglected) is expressed in Equation 6.2-10

$$\gamma(\kappa = \frac{R_i}{R_o} \geq 0.99, \bar{R} = \frac{R_o + R_i}{2}) = \frac{\theta \bar{R}}{R_o - R_i} = \frac{\Omega t \bar{R}}{R_o - R_i} \qquad 6.2\text{-}10$$

Where θ is the angular displacement of the rotating cylinder and $\bar{R}$ is the mid-point between the cylinders. When $\kappa > 0.5$, the shear stress of the outer cylinder is 91% of that at the inner cylinder, therefore it is well known that the shear rate changes across the gap. The shear rate can be evaluated from the components of the rate deformation tensor in cylindrical coordinates (*r,* θ, *z*); the derivative is obtained by applying the gradient velocity tensor (∇v).

$$|2D_{r\theta}| = \dot{\gamma} = \frac{\partial v_\theta}{\partial r} - \frac{v_\theta}{r} = r\frac{\partial}{\partial r}\left(\frac{v_\theta}{r}\right) = r\frac{\partial \Omega}{\partial r} \qquad 6.2\text{-}11$$

To express the above shear rate equation as a function of $\tau_{\theta r}$:

$$\dot{\gamma} = \left| r\frac{\partial \Omega}{\partial r} \right| = 2\tau_{\theta r}\frac{d\Omega}{d\tau_{r\theta}} = 2\tau\frac{d\Omega}{d\tau} \qquad 6.2-12$$

Integrating the equation for a rotating inner cylinder and a stationary outer cylinder gives the force balance:

$$\Omega = \frac{1}{2}\int_{\tau_{R0}}^{\tau_{Ri}} \dot{\gamma}\frac{d\tau}{\tau} \qquad 6.2\text{-}13$$

Therefore, differentiating with respect to $\tau_{\theta r}$, the true shear rate at the bob for a power law fluid can be expressed as:

$$\dot{\gamma}(R_{i)} = \frac{2\Omega_i}{n\left(1-\kappa^{-\frac{2}{n}}\right)} \qquad 6.2-14$$

Where,

$$n = \frac{dlnM_i}{dln\Omega_i} \qquad 6.2-15$$

This relation is assumed true for all shear rates present in the annular gap (for 0.5 < κ <0.99).

Based on the assumption that a cylindrical flow is created around the vane blades, the working equations of motion are identical to the concentric cylinder geometry. Wall slip, jamming of particles (large particles) and sample fracture are key issues experienced by the cup and bob geometry at high particle volume fraction and are eliminated by implementing the vane geometry. The vane tool, therefore is the measurement tool of choice for flow behaviour and yield stress data for this research.

6.2.5.2 Vane and Cup technique for flow rheology

Research attempting to describe flow behaviour of suspensions with the vane tool is limited. As described previously, the concentric cylinder and the cone plate are common methods implemented for flow behaviour. Further studies include flow behaviours of linear elastic solids (Sherwood and Meeten, 1997, McFarlane et al., 2005), non-Newtonian shear-thinning fluids (Cheng et al., 2011, Torres et al., 2013, Barnes, 1997) and viscoelastic solids (Sasaki et al., 2004).

Rheology is an important concept for many industrial applications. Currently there are five main areas where the vane is implemented to characterise rheological properties, these include flow behaviours and direct yield stress measurements. Successful implementation and evaluation using the vane

geometry to inorganic colloidal dispersions have been reported. Key areas included the effect of pH on rheology, depletion interaction and effect of solid loading (Benna et al., 1999, Leong et al., 1996) Ramakrishan et al., (1996)). The food industry has effectively studied viscosity flow curves and yield stress of tomato puree, thixotropic behaviour and flow of molten chocolate (Yoo and Rao, 1994, Xuewu et al., 1996, Wilson et al., 1993, Zhang et al., 1998). Environmental studies also consider the flow of soil debris (Scotto di Santolo et al., 2010).

Within the assumed cylinder of the vane it is considered slight or no shearing takes place. The suspension is instead sheared outside the virtual cylinder whose dimensions are dictated by the vane blade tips. Research analysing clay suspensions by Barnes et al., (Barnes and Carnali, 1990) compared the vane to an equivalent concentric cylinder. Both rheological flow curves illustrated no deviation in the Newtonian region, at high shear rates, however, the vane reduced the effect of slip. To further eliminate the slip effects Barnes (Barnes, 2000) developed an improved version of the vane geometry for flow behaviour, in which roughening of the outer cylinder or covering the inner vane with a gauzed basket. Magnin et al (Magnin and Piau, 1990) also suggested the slip at the wall is dependent on the size of the roughness. Therefore suggesting the rougher the tool, the more reliable the results, due to a greater reduction in slip.

Challenges associated with employing a vane to determine the flow behaviour include the diameter of the vane and the shear rate distribution. It is assumed the shearing occurs at a radius equal to the blades, therefore the sample extracted from the dispersion is equal to the diameter of the vane. Dzuy et al., (Dzuy and Boger, 1985) (Dzuy and Boger, 1983) 1983, oppose this assumption and considers the volume extracted is slightly larger than the vane diameter. A key limitation is the use of low solid volume fraction dispersions i.e. low viscosity where dominance of inertial effects alters flow lines (Barnes and Nguyen, 2001). Overestimation of the viscosity is a consequence of this behaviour, where the enhancement of turbulence from the vane tips at high shear rates is a critical limitation (i.e. extra energy is dissipated into the system due to the flow distortions).

Daniel et al (Daniel et al., 2008) explored the vane rheology of cohesionless glass beads, the torque which maintains continuous rotation of the vane was measured as a function of vane immersion depth (10 mm and 90 mm) and rotational speed. An increased vane immersion lead to an increased torque,

however, reliable data is produced when the entire vane is immersed. An issue has been stated by this research, the regions where particles begin to mobilise with an immersed vane show to have implications on the final results.

Particle migration, also known as fracture at the edge of the blades is renowned issue for rheological measurement. This occurs with most geometries for example, using the parallel plate, dispersions have a tendency to be ejected from the edges. Stickel et al, (Stickel and Powell, 2005, Stickel et al., 2009) have hypothesised the dominant forces are direct contact of the particles, once shear flow is induced the particles collide and slide over one another. Once the forces combine they form particle-depleted regions at the boundary. A comparison made by this research for the two geometries, parallel plate and vane, concluded the torque measurement is an improved technique for higher solids volume fraction at high shear rates.

The use of magnetic renaissance (MRI) provides a greater understanding of the challenges of particle migration. Further to Daniel et al (Daniel et al., 2008), MRI of the vane tool has been carried out by Ovarlez et al (Ovarlez et al., 2011). By imaging, it has been identified that a non-cylindrical slip layer is produced. This fluid occurs at the interface between the sheared material and the material between the blades of the vane. The non-cylindrical slip layer is due to the change in trajectories on the non-colloidal particles at the edges of the blade. Therefore as stated by Nguyen et.al (Nguyen and Boger, 1992), that the slip is almost negligible when employing the vane, should be re-considered. From the imaging there is a clear indication that slip is an important factor and that the vane does not prevent slip when employing large particles.

Limited research on rheological characterisation of nuclear waste simulants proves difficult to under-pin a well-defined rheological methodology. Technique development for this research relies on implementing the cup and vane geometry. The outcomes of this research project will be useful for the characterisation of other nuclear waste slurries and may contribute to the design of a more effective nuclear waste treatment strategy.

6.2.6 Mathematical models representing yield stress

The *Bingham model* (Bingham, 2007) represents the solid during full flow of a fluid, the solid shows elastic properties until a certain point, where the

stress has reached a critical value where the plastic property is dominant. The model is expressed as:

$$\sigma - \sigma_y = U\dot{\gamma} \qquad 6.2\text{-}16$$

Where *U* is the plastic viscosity, it can be represented as the gradient of the curve produced when plotting a stress vs. strain rate graph. No flow occurs until a stress is achieved, the flow then begins immediately at a specific rate, this depends on the properties of the material, the stress at which the flow is initiated is known as the yield stress (Whorlow, 1980, Barnes et al., 1989)[i]. Above the yield stress, the shear rate is directly proportional to the shear stress.

The *Casson model* represents fluids where the yield stress is taken into consideration and low shear viscosity (Barnes et al., 1989, Casson, 1959), expressed in Equation 6.2-17

$$\sqrt{\sigma} = \sqrt{\sigma_Y} + \sqrt{k\dot{\gamma}} \qquad 6.2\text{-}17$$

This produces flow curves similar to that of *Herschel-Bulkley model* (Huang and Garcia, 1998). This type of model is employed by the Brookfield viscometer.

The *Herschel-Bulkley model* is expressed in Equation 6.2-18

$$\sigma = \sigma_Y + k\dot{\gamma}^n \qquad 6.2\text{-}18$$

This represents behaviour of fluids where the flow curve shows a non-linear relationship above the yield stress. From the expression above, this model combines the power law model with the yield stress.

Both Bingham and Herschel–Bulkley models are illustrated in Figure 6.2-7.

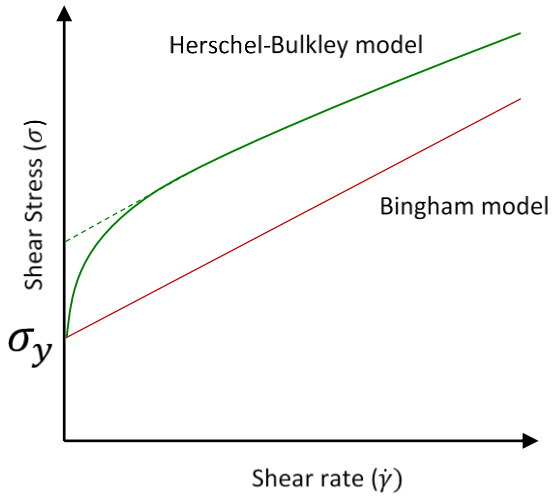

Figure 6.2-7 Graphical representation of steady state flow curves representing Bingham plastic and Herschel–Bulkley models.

6.2.7 Measurement technique for yield stress measurement

Yield stress is defined as the stress at which a material changes from its elastic state to plastic deformation. Barnes and Walters have created an argument to state that 'yield stress only defines what cannot be measured' therefore suggesting that given a long period of time, any material will eventually flow and the yield stress is a value produced due to instrument limitations (Barnes and Walters, 1985, Metzner, 1985, Hartnett and Hu, 1989).

6.2.7.1 Indirect Methods for Yield Stress Measurements

Indirect methods involve extrapolation of shear rate-shear stress data from high shear flow conditions to zero shear rate. A common procedure is to extend the flow curve to low shear rates, until the shear rate is zero, the intercept of the curve at a certain point on the y-axis is the yield stress, as illustrated in Figure 6.3-4. This is a simple technique when the data produced is linear. However when nonlinear flow curves are produced a polynomial equation should be fitted to the data and then the shear rate should be extrapolated to zero. Extrapolation of flow curves can also be carried out by applying appropriate flow models mentioned in Section 6.2.4.

6.2.7.2 Direct Methods for Yield Stress Measurements

A *stress relaxation method* can be used to determine the yield stress. Here, a fluid is sheared at a constant rate or applied stress and then it is rapidly stopped. The stress which is left at equilibrium is expressed as the yield stress (Tiu and Boger, 1974, Povolo et al., 1996a, Povolo et al., 1996b).

Fischer et al (Fischer et al., 1961) have developed a procedure where increasing values of stresses were applied to the fluid until deformation of the material occurred, removal of stress was followed by observing the relaxation of the fluid with time. Bohlin et al (Bohlin et al., 1980)state that the cone-plate geometry is suitable for the stress relaxation measurements.

Creep/creep recovery testing is measuring the slow deformation of a material under a constant stress (Magnin and Piau, 1987, James et al., 1987, Hansen and Williams, 1987). Effectively the test records data from the moment the stress is applied and gives a measure of the elastic, viscoelastic and viscous components of the material. A range of stresses applied produces the response curves which demonstrate the transition from the elastic components to viscoelastic and then finally if a large enough stress is applied the viscous components will be shown. Recovery of the material can also be measured, as illustrated in Figure 6.2-8, this illustrates the deformation state of the material and how the material recovers over time after a particular stress has been applied.

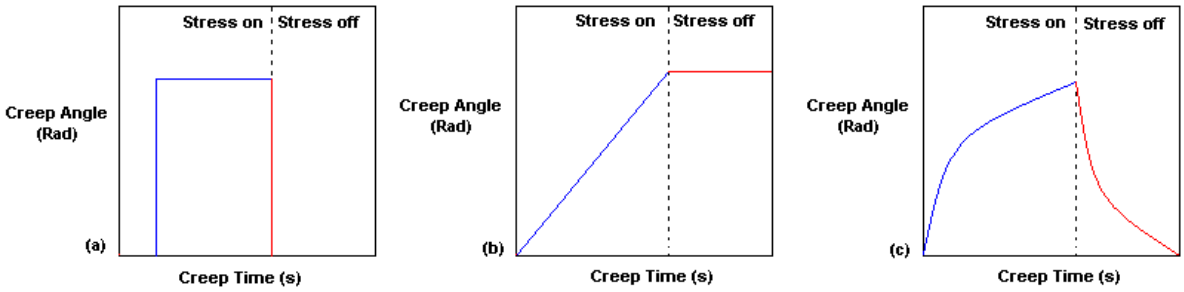

Figure 6.2-8 Response curves showing the creep (blue line) and the recovery of the material (red line). Graph (a) shows the material has pure elastic components, graph (b) shows the material has pure viscous components and graph (c) shows the material has viscoelastic properties

Figure 6.2-8 illustrates typical response curves, at stresses below the yield stress is the fluid behaves like an elastic solid, where instantaneous recovery is exhibited upon stress removal (Figure 6.2-8 (a)). At stresses above the yield stress it is possible to completely break the structure of the material removing all elastic properties of the fluid. This results in a pure viscous flow with no recovery upon removal of stress (Figure 6.2-8 (b)). When the material possesses both elastic and viscous components, it is known as a viscoelastic fluid, where recovery over time occurs (Figure 6.2-8 (c)).

The *vane method* is commonly used in many recent studies of yield stress, due to minimal material disruption during vane immersion and reduced wall

slip (Dzuy and Boger, 1983, Buscall et al., 1993, Turian et al., 1997, Nguyen and Boger, 1992, Liddel and Boger, 1996, Krulis and Rohm, 2004, Stokes and Telford, 2004, Nehdi and Rahman, 2004, Tabuteau et al., 2007, Nguyen et al., 2006).

The vane measures the yield stress of a suspension as it records the torque-time response curves. The yield stress can be calculated from an equation relating the geometry of the tool to the maximum torque, T_m (Dzuy and Boger, 1983, Nguyen et al., 2006)

$$T_m = \frac{\pi}{2} d^3 \left(\frac{l}{d} + \frac{1}{3}\right) \tau_y \qquad 6.2\text{-}19$$

Where d is the diameter of the vane tool, l is the length of the vane tool and τ_y is the yield stress. The vane technique exhibits a lower yield stress value (viscoelastic properties) and an upper yield stress value (viscous properties). Nguygen et al (Nguyen et al., 2006) interprets the higher yield stress as the overall yield stress.

6.2.8 Compressive yield stress measurement

During sedimentation, the compressive yield stress plays an important role in the consolidation stage of concentrated dispersions. The compressive yield stress can be defined as the application of a lateral stress to a given microstructure until no further collapse of the structured sediment bed is possible. Compressive rheology was first described by Buscall (Buscall, 1982) and later developed the multiple-step equilibrium sediment height technique with White (Buscall and White, 1987). Alternative techniques have been developed to determine the compressive yield stress. These include pressure filtration (Green et al., 1998, Green and Boger, 1997, Channell and Zukoski, 1997, Channell et al., 2000), drying consolidation (Brown and Zukoski, 2003) and osmotic pressure (Garrido et al., 2003).

The classic work of Tiller et al. defines filtration resistance as the variation of flow rate with respect to the distance through a filter cake (Tiller and Shirato, 1964). The study revealed two key parameters to model the formation and compressive stages of filtration, known as the specific cake resistance and the solids pressure. A key difference between the filtration technique and that of the Buscall and White technique is that the later focuses on specific material properties independent of their application. In contrast, Tiller et al. model filtration processes as a function of solids pressure vs the void fraction, subsequently followed the specific cake resistance as being defined as a function of applied pressure (dependant on mechanical conditions). All

though this classical approach links the solids pressure and specific cake resistance from filtration to all modes of compressive de-watering, i.e. fundamental links between sedimentation, filtration and centrifugation, the centrifugation technique has advantageous aspects. For example, implementing the Lumisizer, this allows 12 simultaneous measurements with small material quantities to be carried out. Furthermore, the centrifugal compressional tests strongly correlate to the compressional network in the HAST's, where the particle network is broken down by the large volume of fluid acting on the particle bed.

Essentially the compressive yield stress is determined by the yield of fluid exclusion from the sediment bed under an applied pressure. Mechanical techniques are directly applicable for analysing fluid exclusion during sedimentation. This research employs the Lumisizer® for the extended analysis of sediment bed consolidation from the tracking of the solid-liquid interface. Compressive rheology has been studied on colloidal particles such as Latex, silica, alumina, zirconia and bauxite residue (Buscall and White, 1987, Buscall, 1982, Green and Boger, 1997, Green, 1997). The key highlight of compressional rheology research indicates the compressive yield stress is dependent on the particle volume fraction, irrespective of particle system.

This research focuses on the theory developed by Buscall et al., (Buscall and White, 1987), where the initial and equilibrium compressive yield stress are determined. Under a constant centrifugal force the particle dispersion is expected to form a sediment bed over time with a well-defined height, this is the initial compressive yield stress. An initial change in rate of the sediment bed considers parameters such as the initial particle volume fraction, settling rate of an isolated particle, compressive yield stress when the volume faction is 0 and the volume fraction dependant on the hindered settling factor. It is the latter parameter which considers the hydrodynamic interactions, this is influenced by the increase in volume fraction due to sedimentation. A plot of $-(1/g)(dH/dt)$ against $(\Delta\rho g\phi_o H_o)$ which gives a gradient equal to $-IP_y(\phi_o)$, therefore the initial compressive yield stress can be determined.

The equilibrium compressive yield stress is determined once an initial bed is created. The force balance between the particle network strength and the applied centrifugal force determines the height of the sediment bed. The sediment height will change with increasing force with dependence on the formation of the particle network, this is known as the compressive yield

stress at equilibrium. Once the particle network as achieved the equilibrium position, the compressive yield stress at each equilibrium position can be calculated by the mean approximation (Buscal et al., 1987)

$$P_y(\emptyset_{eq}) = \Delta\rho g \emptyset_o H_o \left(1 - \frac{H_{eq}}{2L}\right) \quad \text{6.2-20}$$

Which considers the density difference, $\Delta\rho$, the centrifugal force applied, g, initial volume fraction and height, $\emptyset_o H_o$, equilibrium sediment height, H_{eq}, and the radial distance from the centre of the centrifuge to the bottom of the bed. This is a function of the particle volume fraction at each compressional height and is determined by the following equation

$$\emptyset_{eq} = \frac{\emptyset_o H_O \left[1 - \frac{1}{2L}\left(H_{eq} + g\frac{dH_{eq}}{dg}\right)\right]}{\left(H_{eq} + g\frac{dH_{eq}}{dg}\right)\left(1 - \frac{1}{2L}\right) + \left(\frac{H_{eq}^2}{2L}\right)} \quad \text{6.2-21}$$

Equation 6.2-21 is governed by the change in sediment bed height and applied centrifugal force. During compression the particle structure becomes stronger as the density increases, this behaviour and the stored elastic energy is amplified with increasing particle volume fraction. Therefore determining the compressive yield stress with the compressive sedimentation technique is dependent on the centrifugal force applied, particle properties and suspension chemistry. This method has been successfully implemented on polystyrene particles where the increase in background electrolyte concentration produced aggregates and in turn produced a step-wise compressive profile, in contrast to a stable particle dispersion (Yow and Biggs, 2013).

It is important to consider the difference in shear and compressive yield stress. Shear yield stress is the minimum stress applied for full deformation of a dispersion to occur. This is a result of opposing forces, the stress applied and the material, along parallel planes across the matrix of the sample. Compressive yield stress is the stress limit which leads to failure of a material. This is a result of stress exerted on a material by an external applied load, this acts as a length reduction of the material along the axis of the applied load. Both deformation stresses are governed by the ability of the particle network to accommodate the elastic strain, which is a function of interparticle interactions whereby bonds are distorted, broken and reformed (Zhou et al., 1999, Zhou et al., 2001, Grote et al., 2001, Channell and Zukoski, 1997).

6.2.9 Effect of particle properties on rheological behaviour

Suspensions of particles in a liquid medium are wide available. Industrial sectors including the food, cosmetic, ceramic, oil and pharmaceutical involve, in abundance, multiphase systems which are processed as suspensions. The control of the flow properties of such suspensions is key for a successful manufacturing process. Ultimately, the ability of controlling flow properties requires the knowledge of suspension rheology. The rheology of particle suspension is a complex function of its physical properties and the interaction of the suspended particles. Key factors which govern the flow properties include particle volume fraction, size, shape, surface properties, spatial arrangement of particles and bulk flow field.

A number of studies establishing the influence of particle size on flow behaviour have revealed the reduction in particle size increases the overall suspension viscosity (Kawatra, 2012, Mangesana et al., 2008, Chang and Powell, 1994, Chun et al., 2011, He et al., 2007). The higher number of finer particles results in more interparticle interaction and thus a greater resistance to flow. In contrast, various studies have concluded the increase in particle size increases the overall suspension viscosity (Clarke, 1967, Mangesana et al., 2008, De Bruijn, 1942). The increase in particle size creates a greater inertia on interaction, thus the energy dissipated increases the suspension viscosity.

The presence of a particle will alter the velocity distribution in a flowing liquid, the extra energy dissipated is directly proportional to the increase in viscosity. Einstein (Einstein, 1905) predicted the shear viscosity using the viscous dissipation produced by the flow around a sphere, expressed in equation 6.3-22

$$\mu = \mu_s(1 + \frac{5}{2}\emptyset) \qquad 6.2\text{-}22$$

Equation 6.2-22 considers the fluid viscosity μ_s, volume fraction ϕ and the intrinsic viscosity [μ]. The intrinsic viscosity is taken to be $\frac{5}{2}$ for spherical rigid spheres (Einstein 1911), and will vary with the nature of the particle. The Einstein formula is however only valid for dilute suspensions, enough that the flow around one particle is not influences by the presence of a neighbouring particle. Further studies considered the hydrodynamic interaction, where two spheres leads to a contribution that is proportional to ϕ^2, three-body hydrodynamic interactions produces a ϕ^3 term (Batchelor, 1977, Larson, 1999). An empirical expression which is widely used to describe the concentration dependency on the viscosity of a suspension is

expressed by the Krieger-Dougherty (KD) (Krieger and Dougherty, 1959) expression

$$\mu = \mu_s \left(1 - \frac{\emptyset}{\emptyset_m}\right)^{[\mu]\emptyset_m} \quad \text{6.2-23}$$

Equation 6.3-23 considers the viscosity as ϕ approaches the maximum-packing fraction $\emptyset_m$ for suspensions of spherical or non-spherical particles. The parameters, $[\mu]\ and\ \emptyset_m$, of the equation are related to the particles properties, such as size and shape, and are tabulated by Barnes et al (Barnes et al., 1989).

Spherical dispersions are well understood and the research available in the open literature is in abundance, however non-spherical particles introduce a number of other influencing factors. The additional effects include: (i) local flow field changes around a non-spherical particle, (ii) particle orientation; (iii) particle interactions are greatly influenced by shape, where the degree of interactions will be higher for non-spherical particles, at any given volume fraction. All these factors will have diverse effects on the contribution to the overall suspension viscosity.

The motion of spheroidal particle in shearing flow and the surrounding fluid have been described by Jeffery (Jeffery, 1922). The spheroidal particles contain a dominant axis, *a-axis*, where the particle of motion is defined by the orientation of the axis to the direction of flow. Two main concepts of motion can be described: (i) the a-axis is aligned parallel to the flow, the motion is steady with a constant rotation rate; (ii) the a-axis is aligned perpendicular to flow, this is where particles tumble 'end over end'. The motion of the particles a-axis is periodic and is referred to as a 'Jeffery's orbit' (Jeffery, 1922). The rate of orientation is directly affected as the aspect ratio deviates from unity, for rod-like particles the rate of particle rotation is reduced when the dominant particle-axis parallel to flow, and increases when it is perpendicular to flow. Jeffery orbits have been identified for rod-like and disk particles (Hur et al., 2011, Vincenzi, 2013, Zheng et al., 2011, Trevelyan and Mason, 1951, Goldsmith and Mason, 1962).

The tumbling and translational motion of rod-like particles, under an applied shear field, converts the motion into thermal energy and thus dissipates the energy into the system. The energy dissipated influences the contribution of the overall suspension viscosity. Motion of the rod-like particles is influenced by the particle concentration, Doi and Edwards (Edwards and Doi, 1986) have visualised four concentration regimes based on the number density of rods (ρ_N).

i. **Dilute solution ($\boldsymbol{\rho_{N1}}$).** The concentration of the rods is such that the spacing between the particles is larger than the dominant particle-axis (*L*). The rods are able to rotate freely without being influenced by neighbouring rods. Rotation about the centre of mass of the rod must be around L^3. Interactions are rare.

ii. **Semi-dilute solution** ($\boldsymbol{\rho_{N2}}$). As the particles of rods increase the number of interparticle interactions increase and thus their rotational motions become restricted. The excluded volume is neglected as the particles overlap into the excluded volume and this the spatial distribution of the rods are unaffected. Hydrodynamic interactions between particle become important which lead to rotary diffusion of particle orientation (Stover et al., 1992, Rahnama et al., 1995).

iii. **Concentrated region ($\boldsymbol{\rho_{N3}}$).** At higher particle concentrations the system exhibits rotational and volume exclusion restrictions. The increase in particle concentrations substantially modifies the spatial arrangement of the particles where particle-particle interactions become important (Powell, 1991, Djalili-Moghaddam and Toll, 2006, Pabst et al., 2006).

Research interest on the influence of particle morphology on rheological behaviour has increased over the years. Spherical particles are well understood systems, (Hone et al., 2000, Chan and Powell, 1984, H. M. Laun, 1992, Chandler, 2010, Chadwick et al., 2002, Batchelor, 1977, Choi and Krieger, 1986). It is the deviation from the ideal sphere morphology which produces diverse behaviours that is of interest. Figure 6.2-9 illustrates the morphology of particles previously studied to understand suspension rheology behaviour.

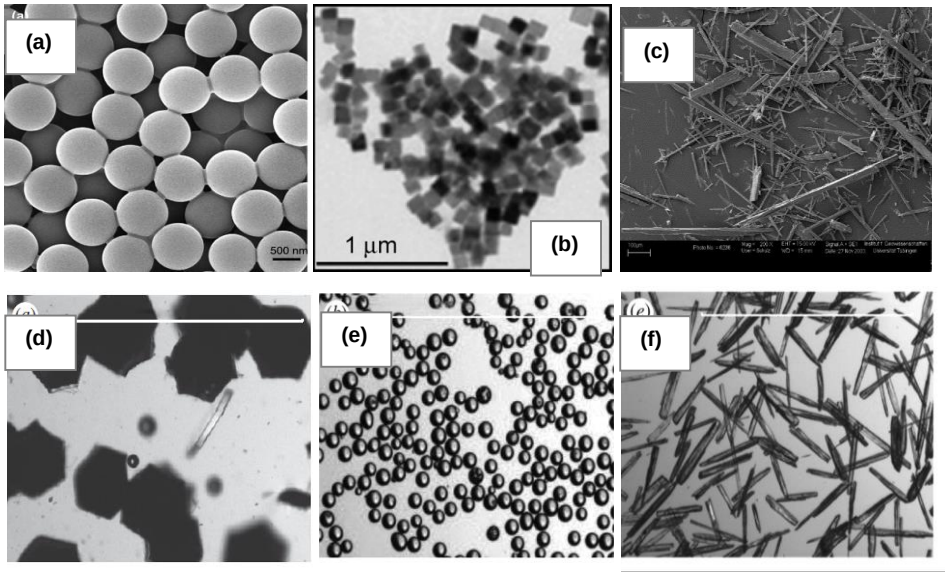

Figure 6.2-9 SEM images of particles currently used in literature to determine the suspension rheology of non-spherical particles (a) spherical latex particles (Chan and Powell 1984), (H. M. Laun 1992), (Hone, Howe et al. 2000)(b) cubic cobalt oxide nanparticles (Vickers, Archer et al. 2009); (c) Wollastonitie fibres (Pabst, GregorovÃ¡ et al. 2006); (d) ultra-fine art glitter; (e) monodisperse glass beads; (f) Wollastonite. SEM images d-f are extracted from (Mueller et al., 2009)

Figure illustrates 6.2-9 (a) Latex suspensions, a well defined system. Studied have explored the influence of particle volume fraction, where high viscosities are exhibited at high particle volume fractions due the particles approaching a close-packed condition, with little free volume between the particles, thus increasing the extent of shear-thinning behaviour (Hone et al., 2000, Chan and Powell, 1984, H. M. Laun, 1992). Rheological characterisation of cubic particles is uncommon, the latest study on this type of systems has been carried out by Vickers et al (Vickers et al., 2009) on cobalt oxide particles (Figure 6.2-9 (b)). At intermediate and high particle volume fraction the dispersion exhibited shear-thinning and shear-thickening behaviour. It was claimed at higher shear rates the shear-thickening behaviour was a result of shear-induced particle-particle collisions and possible formation of hydroclusters. It was not, however, considered that the shear-thickening behaviour could be a result of secondary flow effects, a measurement limitation due to the choice of geometry.

Mueller et al (Mueller et al., 2009) discussed the systematic dependence of particle aspect ratio on the extent of shear-thinning behaviour. Particle higher aspect ratio (Figure 6.2-9 (f)), rotate more rapidly as they tumble in shearing flow, compared to spherical particles (Figure 6.2-9 (e)), where they slide past one another rapidly. This behaviour is supported by Gunes et al (Gunes et al., 2008) the highlight of the study considered modification of the aspect ratio on the same material particles. Flow-induced alignment of spheroidal haematite occurred during extreme flow conditions (high shear

rates), they packed to form planar, stacked structures and orientated in the direction of flow. Similar behaviours have previously been reported on carbon nanotube and fibre suspensions (Hobbie et al., 2003, Iso et al., 1996).

Rheological behaviour of concentrated dispersions can also be controlled by regulating the net interparticle forces. Various studies on mineral oxide suspension indicate as the pH of the solution deviates from the pH_{pzc} the extent of shear-thinning and yield behaviour decreases (Yang et al., 2001, Liddell and Boger, 1994, Zhou et al., 2001, Scales et al., 1998, Johnson et al., 2000, Khan et al., 2012, Penkavova et al., 2011, Leong et al., 1993, Leong et al., 1995). Addition of electrolyte concentration compresses the EDL causing aggregation. The aggregate size increases with increasing electrolyte concentration, this in turn increases the degree of shear-thinning behaviour and yield stress (Chen and Russel, 1991, Kelessidis et al., 2007, Heath and Tadros, 1983, Tadros, 2011, Zhou et al., 2001).

Interest in research on the effect of particle shape on rheological properties is certainly increasing. As mentioned throughout this section, spherical particles are well understood systems, research on arbitrary shapes and the effect on rheological parameters have been determined. This research aims to perform rheological characterisation on highly active nuclear waste simulant suspensions with particles of varying degrees of anisometry and varying particle volume fraction, in two suspending fluid mediums with varying electrolyte concentrations.

6.2.10 Rheology in the nuclear industry

Rheological characterisation of complex suspensions focuses on various systems including polymeric, colloidal, and concentrated mineral oxide suspensions, as mentioned in Section 6.3.4. The control of the rheological properties of slurries for waste treatment have been well defined for many industries including pharmaceuticals, coal and paint processing (Bouyer et al., 2013, Feng et al., 2014, Figliuzzi et al., 2012). Nuclear waste slurries impose unique characteristics, which differ from typical pharmaceutical, coal and other industrial waste slurries, including high pH salt concentration, high temperature, broad particle size- and shape-distribution, varying particle volume fraction, varying chemical composition between each waste tanks and the most challenging condition is the level of radiation. These parameters govern rheological behaviour, as mentioned in Section 6.3.4,

and thus control of such parameters will enable safe, efficient and economic processing of highly active nuclear waste.

Only limited research on the rheological properties of highly active nuclear waste sludge/slurry is available in the open literature. The nuclear waste research field is currently dominated by studies from the US, the waste tanks at the Hanford site, Washington (Chang and Smith, 1996a, Smith et al., 2000, Chun et al., 2011, Zhao et al., 2012, Kay et al., 2003). Chun et al (Chun et al., 2011) explored the effect of particle size distribution and the addition of modifiers to improve the efficiency of nuclear waste treatment. Two simulated nuclear waste slurries consisted of ~5 µm and ~17 µm, respectively. The apparent viscosity and yield stress values (45.5 Pa and 4.7 Pa, respectively) is influenced by the hydrodynamic interactions and the number if interparticle interactions within the slurry, thus a reduction in particle size increases the viscosity and yield stress.

The use of rheological modifiers such as poly-glycols and surface active polymers have been found to significantly reduce the viscosity and the yield stress of nuclear waste slurries (Kay et al., 2003, Chun et al., 2011, Chang and Smith, 1996a). Other factors influencing the rheological properties include the change in pH strength, where the viscosity and yield stress decrease with decreasing pH (Tracey et al., 1996, Chang and Smith, 1996a). Nuclear waste slurries at pH_{pzc} exhibited anti-thixotropic behaviours, suggesting formation of aggregates (Chang and Smith, 1996b, Smith et al., 2000).

Mason et al (Mason et al 2005), explored the effect of particle shape on yield stress of highly active nuclear waste suspensions. The suspensions were categorised into two waste fuel types, mentioned in Chapter 5, Section 5.3.2.1. The study highlighted suspensions containing cubic particles endure weak cohesion between the solids particles, this is reported by the low yield stress data of 19 Pa. In contrast suspensions which contain spherical particles exhibited a much higher yield stress of 65 Pa.

The complex nature of the nuclear waste sludge/slurries create challenges to control rheological properties. Research conducted in this field indicate the governing factors, pH, electrolyte, size and shape control are key to controlling the rheological properties for efficient and economic nuclear waste treatment strategy.

6.2.11 Closing remarks on literature review

It is evident from the literature search that there are areas where there is limited research, this PhD thesis will contribute to these areas. In the nuclear industry there are many challenges to overcome in order to provide reliable information. The amount of heat generated and radiation are the main issues, however, with intensive research alternative methods have been created to analyse the material which are the products of the nuclear fuel cycle. From the reports provided by the European commission and the ONR it is clear that there are concerns related to the waste management strategy, this research aims to provide reliable data from nuclear waste simulants and thus have a broader knowledge of the hydrodynamic properties, which will lead to an improved nuclear waste treatment strategy.

Research on particle characterisation of nuclear waste slurry/solids have shown to be limited. Furthermore, the characterisation of nuclear waste has mainly taken place outside of the UK. The majority of the literature involves slurry characterisation in the US at the Hanford site in Washington. Rheological measurements are important for industries such as pharmaceuticals, food and cosmetics as well as the nuclear industries, the information that is provided by the measurements indicate the flow behaviour of the waste. The geometry effects the overall measurements and thus the selection of the appropriate geometry is important. The particle size and shape impact the behaviour of the suspension; this will in turn affect the hydrodynamic properties. The literature search suggests that information on the size/shape of particles effecting rheological measurements is limited.

This thesis will employ reliable techniques to characterise nuclear waste simulants. The simulants are representative of the waste material contained at the Sellafield site in Cumbria. Rheological techniques will be given careful consideration to obtain consistent and reliable data by selecting the appropriate geometry. In depth investigation will take place to explore the effect of particle shape and size on parameters such as rheology and sedimentation. Therefore this thesis will aim to broaden the knowledge of nuclear waste slurries by characterising the solids and discover properties which affect the flow behaviour. It is suggested that a greater understanding of nuclear waste slurries is an important factor which will contribute to an improvement of nuclear waste treatment strategy.

6.3 Materials and methods

6.3.1 Flow behaviour

The Bohlin C-VOR Rheometer (Malvern Instruments Ltd., UK) was employed to obtain rheological flow curves for highly active nuclear waste suspensions with varying particle volume fraction, electrolyte concentration and varying degree of particle anisometry. Rheological characterisation were carried out on synthesised CPM, ZM and ZMCA, as discussed in Chapter 3 Sections 3.3.1-3.3.3 and on pre-bought TiO_2 characterised in Chapter 3 section 3.4.

The measurement protocol is key to determine reliable rheological characterisation of nuclear waste simulant dispersions. Nuclear waste dispersions are complex, as they contain non-spherical particles and there is an extent of size polydispersity. The knowledge of key parameters is required to obtain a representative rheological behaviour. They are a follows

- Particle properties. Define particle size, aspect ratio and density.
- Suspension volume fraction. Define the particle concentration, whether the dispersion is in the dilute, semi-dilute or concentrated region. To clarify the dominating interactions.
- Surrounding fluid. Is the fluid Newtonian or non-Newtonian.
- Varying PSD. Define whether the system is size monodisperse or polydisperse. Size polydispersity can lead to segregation.
- Stability of the dispersion. Particle migration during the rheological measurement should be avoided.

Particle properties of each dispersion, through particle characterisation techniques as discussed in Chapter 3. From the sedimentation data in Chapter 5, it is apparent segregation as well as sedimentation occurs in ZM and ZMCA dispersions. Initial studies used low volume fraction dispersions < 20 vol%, to characterise the flow behaviour. However, for segregating ZM and ZMCA systems, repeatability and reproducibility tests indicated that size polydispersity has a clear effect. For example, once the sample is subjected to repeat measurements, the larger ~3 µm particles settled out and thus the repeat measurement was carried on the finer particles. Measurements on these particle systems < 20 vol% also suggested no significant difference between dispersions of varying particle volume fraction. Thus, the aim was to eliminate segregation effects to avoid rheological characterisation which is not representative or reliable.

Segregation is associated with the stability of the dispersion and can be controlled by working above the gel-point. The gel-point of each particulate dispersion can be obtained by considering data taken with the Turbiscan, discussed in Chapter 5. The equilibrium height at which the sediment front no longer settles further is caused by a space-filling particle network: This is known as the gel-point. Therefore, a minimum volume fraction can be obtained for each dispersion at which we would not expect any settling to occur. This can be used as the minimum volume fraction to carry out reliable and relevant rheological characterisation. Time constraints were also considered based on the settling in Chapter 5, Section 5.4.1, where the larger particles settle within 30 mins ($\emptyset = 0.02$, ZM). As a typical rheological measurement, without a repeat run, takes ~40 mins, the gel-point > 20 vol% was considered.

Once the solid-liquid properties are defined, a selection of the measurement geometry is required. This selection is dependent on all the parameters discussed above and determines the quality and the reliability of the rheological measurements of the complex dispersions.

A cup & bob geometry is suitable for low viscosity suspensions, i.e. low volume fraction suspensions; a vane tool is more suitable for high viscosity suspensions, i.e. high volume fraction suspensions. Therefore, in this work, titanium dioxide suspensions of between 6-12vol% were examined using a cup & bob geometry, whilst for suspensions of between 15-21vol% the vane geometry was used. Nuclear waste simulant dispersions of between 6-20 vol% are considered here to be low volume fraction suspensions and correspondingly, for these, a cup and bob was employed. Above the gel-point, at between 20-50 vol%, the vane was employed.

For measurements using the cup & bob, the volume of material required is ~15 mL. Samples were prepared in 20 mL vials and a 20 mL pipette was utilised to extract 15 mL of the suspension for transfer to the cup. For dispersions above the gel-point, a 14 mm diameter (V14) vane tool was used with a smooth finished 37 mm cup (C37), which requires ~40 mL of material. In these cases, samples were prepared in 50 mL vials and transferred to the cup prior to the measurement. In all cases, the bob/vane is immersed into the particulate fluid within the cup. The cup is thermally insulated within the rheometer and the temperature was maintained at 20˚C for all experiments reported here.

The data reported here were collected using a Bohlin C-VOR stress-controlled rheometer. When carrying out an experiment, a range of stress values is chosen and systematically applied by the rheometer; the resultant shear rate under a given stress is then recorded. The stress range used was adjusted to account for the different baseline viscosities of the sample dispersions. For example, for TiO_2 in water below the gel-point a stress range of 0.01-100 Pa was used whereas for CPM and ZM dispersions below the gel-point a stress range of 0.01-10 Pa was more appropriate. For dispersions above the gel-point, a stress range for CPM of between 1-300 Pa was used and for ZM or ZMCA dispersions the range was 0.1-50 Pa. The choice of stress values allows a direct comparison of the change in viscosity behaviour for each particulate dispersion across a similar resultant shear rate range.

Each experiment was run over a period of 30 mins where data was collected at a rate of 1 sample per 40 s, the time also includes thermal equilibrium. Determining the time allocation is key for the dispersion to reach steady state prior to each data point measurement.

6.3.2 Yield stress measurements

6.3.2.1 Torque-time method

A Brookfield DV-II Pro Viscometer was employed to measure the yield stress of TiO_2 suspensions as a function of volume fraction. The Brookfield measures the torque-time response, where the rate of rotation is constant and produces a distinct peak after the elastic deformation region. The calculation of yield stress from the torque requires the dimensions of the vane and the torque input which is calculated from 100% torque.

After the instrument has been zeroed the suspension should be prepared and transferred to a 300ml cylindrical glass beaker which is then placed on the adjustable platform. The positioning of the sample is crucial as the vane is immersed into the sample by bringing the sample up to the vane. A vane tool V72 is appropriate for volume fractions 6-18vol%, and the V73 tool is used for volume fractions > 21vol%. A higher viscosity sample is less sensitive to vanes as it ensures it does not exceed the maximum torque. Once the suspension is in place the measurement of the yield stress can begin.

This technique required a total volume of 300 mL to carry out yield stress measurements. However, the vane blades have indents at approximately half-way down their longer side, this allows for measurements in a smaller volume of suspension. Thus, two sceneries were explored: (i) using 300ml of material and the full vane; (ii) reducing the amount to 200ml, 150ml and 100ml using full-half a vane (as appropriate).

6.3.2.2 Creep/Creep recovery method

There are five main ways in which the Bohlin instrument can be used to measure the shear yield stress which include creep testing, oscillation, stress ramp, strain ramp and rate ramp. Rate ramp method is limited as the rheometer operates in a stress-controlled mode. This research is focused on creep testing to obtain the yield stress. An alternative method is considered due to the challenges faced by the quantity of material available. Approximately 40 mL of material is required for yield stress measurement. The V14 and C37 geometry was used as this surpassed the diameter of the cup to be twice the diameter of the vane criterion. Creep tests were performed at increments of 10 Pa, further tests were run for greater accuracy at increments of 1 Pa, until the sample yielded. The creep tests were run for 30 s with data collected at a rate of 1 point per second. To further support the yield determination of the creep tests, a creep recovery method was implemented. Creep recovery tests involved the removal of the stress after 60 s, the recovery behaviour of the sample was recorded for a further 100 s.

6.3.3 Compressive yield stress measurements

Compressive yield stress measurements were carried out in a Lumisizer® 611, the basic technique fundamentals is discussed in Chapter 5. For compressive bed studies an application of increasing g-force to the sample was carried out. 400 µL of 6 vol% nuclear waste dispersions were transferred to a poly carbonate disposable cell. The dispersions were subjected to a force of 500 rpm for 3 hours, this allowed an initial packed bed to be formed. During this period transmission profiles were collected every 5 mins. Subsequently the centrifugal field accelerated by 500 rpm every 30 mins, during this period transmission profiles were collected ever 60 s. Figure 6.3-1 illustrates the experimental set-up and key parameters for yield stress calculation.

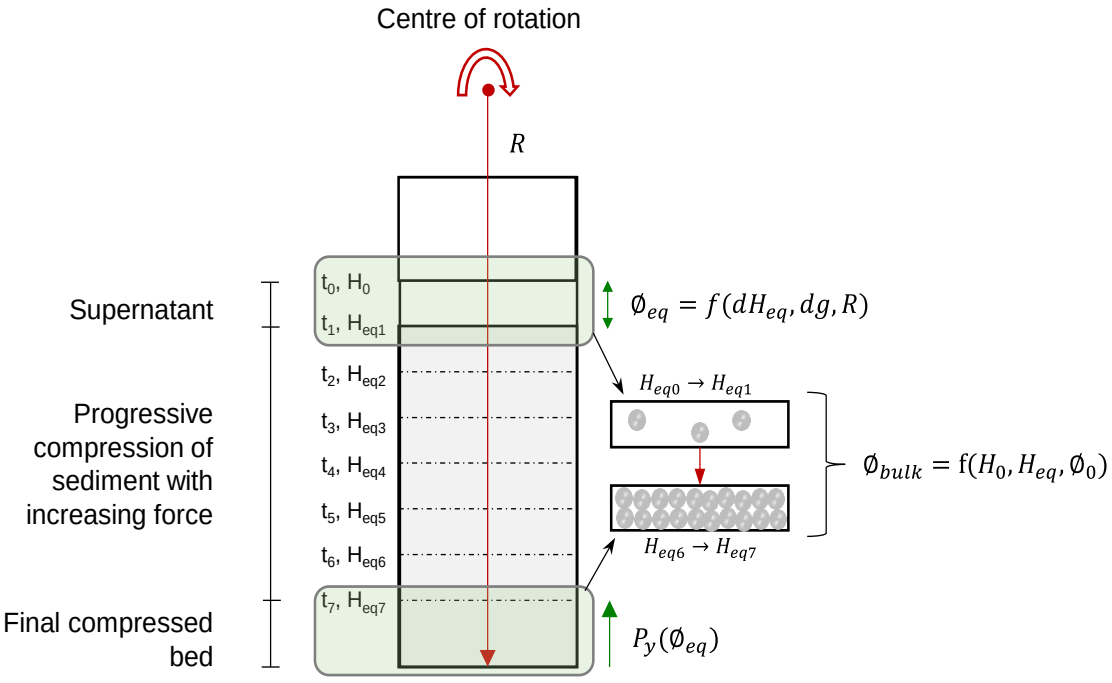

Figure 6.3-1 Schematic illustration of centrifugation coordinate systems (a) raw compressive profile indicting each step change with respect to change in applied centrifugal field and change in sediment height; (b) Key parameters for compressive yield stress calculation.

Initial calculations were conducted by calculating the equilibrium bed height (H_{eq}) at each position, with respect to the centrifugal field applied. The height of the meniscus (H_m) and the compressed sediment height (H_c) were extracted from the raw profile to determine the distance (dH_{eq}) travelled from the initial height. A sample calculation is presented of CPM. Key parameters determined from the raw profile were $H_m = 105.91\ mm$ and $H_c = 118.51\ mm$, at 1000 rpm. Thus the height of the sediment bed was calculated using the following methodology.

$$dH_{eq} = H_c - H_m = 118.51 - 105.91 = 12.60\ mm$$

Given the initial height of the sample is 22 mm, H_{eq} can be determined

$$H_{eq} = H_0 - dH_{eq} = 22 - 12.60 = 9.40\ mm$$

The H_{eq} was determined for each centrifugal field from 500 to 4000 rpm. Calculation of the volume fraction change during consolidation can be determined by considering H_{eq}, H_0 and the initial volume fraction (ϕ_0).

$$\emptyset = \emptyset_0 \frac{H_0}{H_{eq}} = 0.06 \frac{22}{9.40} = 0.14$$

Thus the compressive yield stress can be determined using the below equations, where the mean approximation value as a function of particle volume fraction at equilibrium height was calculated using the following methodology

$$\emptyset_{eq} = \frac{0.00132\left[1 - \frac{1}{2 \times 0.114}(0.0094 + 0.00276)\right]}{\left((0.0094 + 0.00276)\right)\left(1 - \frac{1}{2 \times 0.114}\right) + \left(\frac{0.0094^2}{2 \times 0.114}\right)} = 0.108$$

$$P_y\left(\emptyset_{eq}\right) = 2822 \times 127 \times 0.108 \times 0.022\left(1 - \frac{0.0094}{2 \times 0.114}\right) = 818.11\ Pa$$

The centrifugation technique allowed the compressive yield stress to be determined from the calculation of equilibrium sediment height at a number of applied centrifugal fields.

6.4 Results and discussion

6.4.1 Flow Behaviour

6.4.1.1 TiO_2 and CPM below the gel-point

Further insight into the behaviour of the simulant materials was obtained from rheological measurements. Standard flow curve data for the TiO_2 sample is given, as a function of volume fraction, in Figure 6.4-1. These baseline data were used to provide information on the preferred type of measurement geometry to be used here.

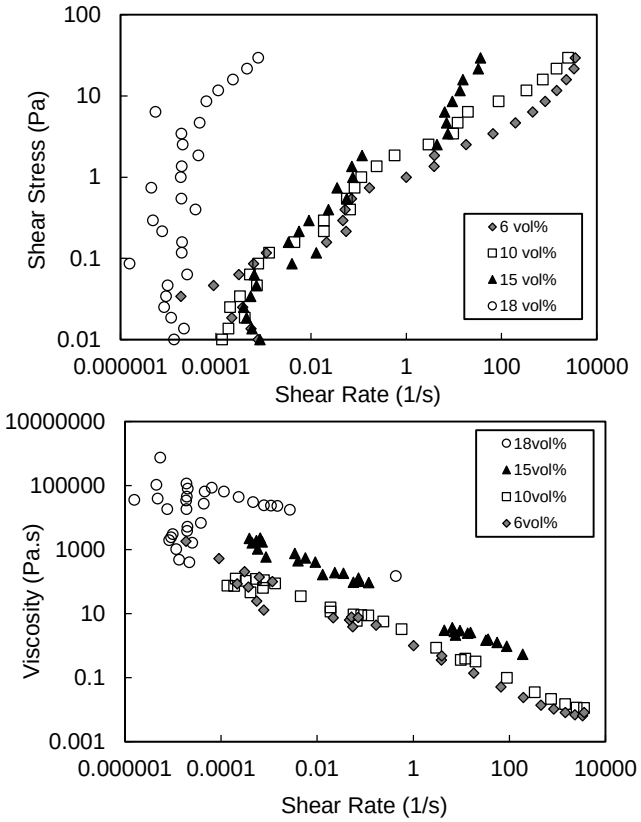

Figure 6.4-1 Flow behaviour of TiO_2 as a function of volume fraction; (a) shear stress as a function of shear rate, (b) Viscosity as a function of shear rate. The rheological data has been collected using the Bohlin C-VOR rheometer, for 6-15vol% the cup & bob was employed to obtain the flow curves and for 18 vol% the vane tool was used to obtain the flow curve.

We can see immediately from the data that TiO_2 suspensions are strongly shear-thinning fluids (Turian et al., 1997, Q.D. Nguyen, 2006), with a large reduction in viscosity as a function of shear rate. In general, we also see that as the volume fraction is increased the low shear viscosity increases, as expected.

Initially, the vane tool was employed for all rheology measurements. However, this tool is known to produce unreliable results for suspensions with low viscosities (Nguyen and Boger, 1992). As an alternative, a cup and bob system was used for flow curve data for suspensions of 6 – 10 vol%. The larger surface area of this tool provides greater sensitivity at low viscosity and, as a result produces more reliable data (Darby, 1985). The vane tool was employed for suspensions of 15 – 18 vol%. Generally, to obtain reliable data when using the Bohlin Rheometer it is important to select the geometry on the basis of its sensitivity to the viscosity of the suspension of interest.

The low shear region of the data in Figure 6.4-1 (b) (from 18 vol% in particular) suggests the presence of wall slip; this is seen as a region of high

noise in the data, please refer to section 6.2.5 on how wall slip effects were reduced. Roughened geometries were not readily available for this research, thus the data presented (in particular TiO_2 systems) have an element of slip built in. It is also known that the ratio of the vane diameter to that of the cup is an important factor to avoid slip, a cup that is twice the diameter of the vane tool gives the best possible rheological data (Dzuy and Boger, 1985, Nguyen and Boger, 1992). The vane tool used for these experiments was the V25 (vane tool diameter of 25 mm) and the cup was C37 (cup diameter of 37 mm).

Initial rheological data for the CPM sample at a range of volume fractions and in two different mediums, water and nitric acid, are given in Figure 6.4-2. 2 M nitric acid was used here to replicate conditions in the HASTs, where HAL solids are suspended in nitric acid during storage. During POCO, water will be employed to wash the tanks, therefore it is important to understand the behaviour of the solids in both mediums.

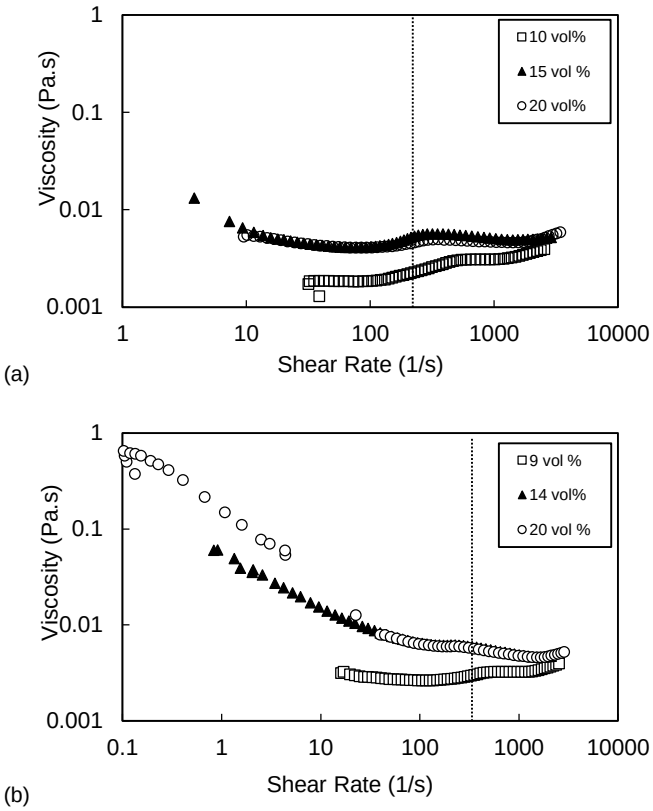

Figure 6.4-2 Viscosity as a function of shear rate for (a) caesium phosphomolybdate in water and (b) caesium phosphomolybate in nitric acid. Both of the curves have been obtained using the Bohlin C-VOR rheometer and employing the cup & bob geometry.

From Figure 6.4-2, we see immediately that a change in the medium strongly affects the rheological behaviour of the dispersions at equivalent volume fractions of solids. Figure 6.4-2 (a) suggests at lower shear rates

(approximately between 10 and 300 s^{-1}) there is a Newtonian plateau, deviation from this plateau occurs at shear rates exceeding 300 s^{-1} due to secondary flow affects (Laun, 1984). Secondary flows are dependent on the geometry employed, these flows occur with cup/bob and Mooney-Ewart geometries. Both these geometries contain an inner cylinder, at high shear rates inertial forces create an axisymmetric secondary flow, known as vortices. An increase in particle concentration enhances the vortex flow (Zirnsak and Boger, 1998).

In general, the viscosities of the TiO_2 samples are much higher than the CPM at the same volume fraction of solids in water (compare Fig 6.4-1 (b) to 6.4-2 (a)). One explanation for these differences in viscosity could be the surface charges of the particles and the overall colloidal stability. In aqueous systems, the surface charge is known to be dependent on the pH, as discussed in Chapter 3.4.2. The samples here at a pH of 5.5, this is located within the range of the iep and therefore the TiO_2 particles may well be aggregated. This would be consistent with a higher overall viscosity of the samples tested here. This also suggests that the CPM sample is not close to its iep the particles have a high charge and are therefore colloidally stable (See Chapter 3).

Comparing the two data sets for the CPM we see that the viscosity in water is considerably lower than in nitric acid. High acid levels will result in a pH reduction as well as an increase in the concentration of background electrolyte. The latter will definitely drive a decrease in stability and an increase in aggregation (see Chapter 5). This is consistent with the increased viscosity of the suspensions. Similar behaviours have been observed whereby the increase in background electrolyte of nuclear waste simulants causes particles to aggregate, hence shear thinning behaviour is exhibited (Smith et al., 2000, Chang and Smith, 1996a). Secondly, the viscosity of the nitric acid itself is higher than water, which may account also for a portion of the increase.

6.4.1.2 Effect of particle properties on flow behaviour above the gel-point

Direct comparison of the influence of particles properties on flow behaviour have been investigated. All flow curves have been obtained above the gel-point (≥ 20 vol%), to eliminate segregation effects of both ZM and ZMCA systems. The highly active nuclear waste simulants are dispersed in DI water. The change in viscosity as a function of shear rate for each

particulate system with varying particle content, 20-50 vol%, as been recorded and analysed. The resultant flow curves are illustrated in figure 6.4-3. All flow curves have been obtained using the vaned bob geometry where by a V14 in a C37 was employed.

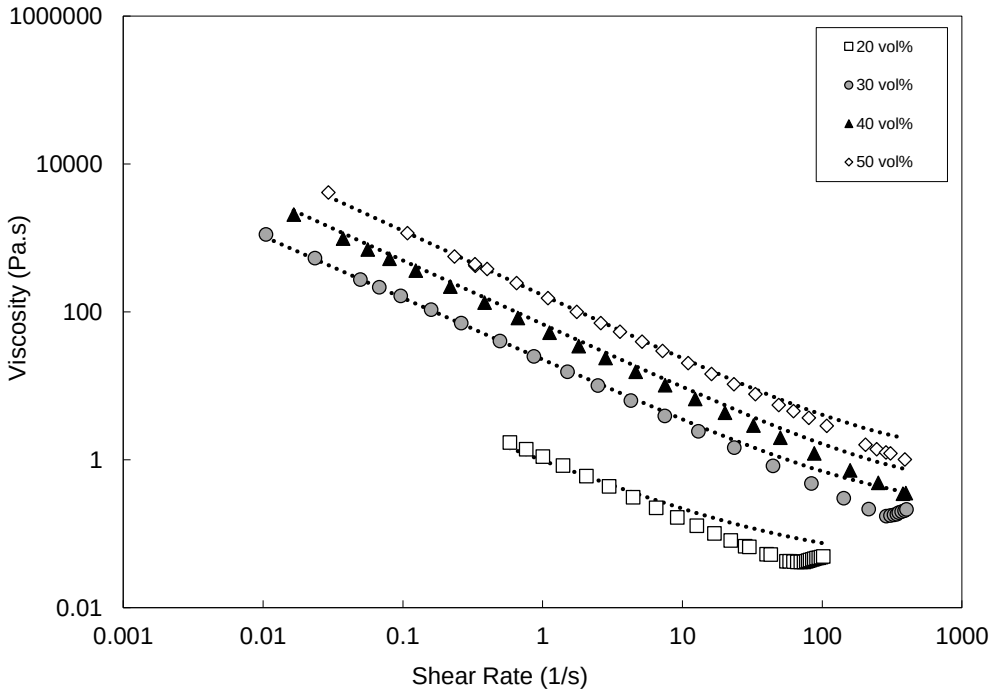

(a)

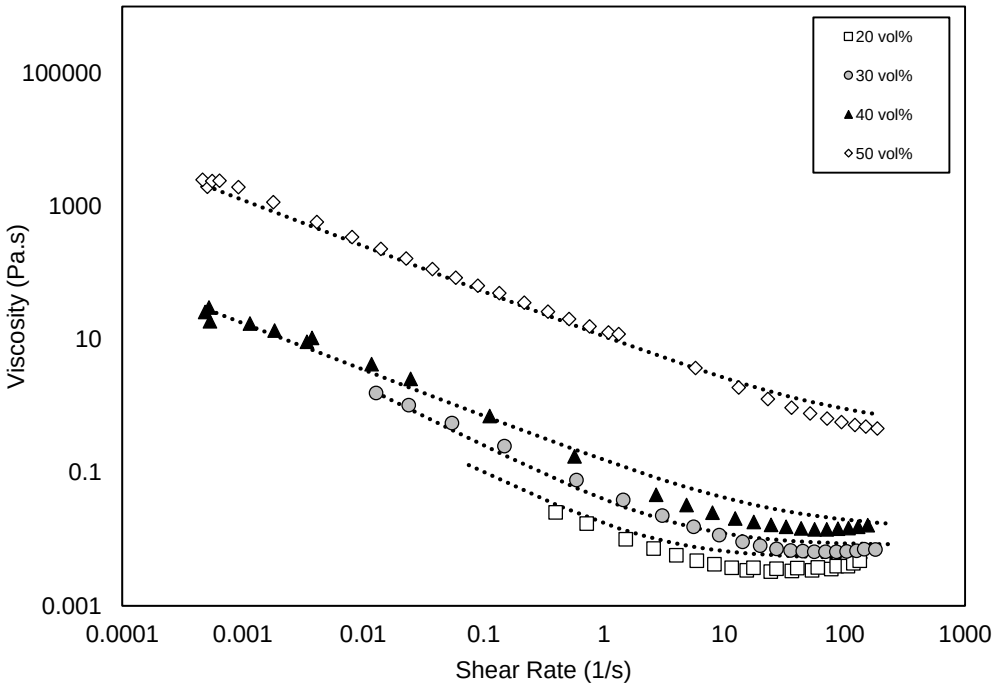

(b)

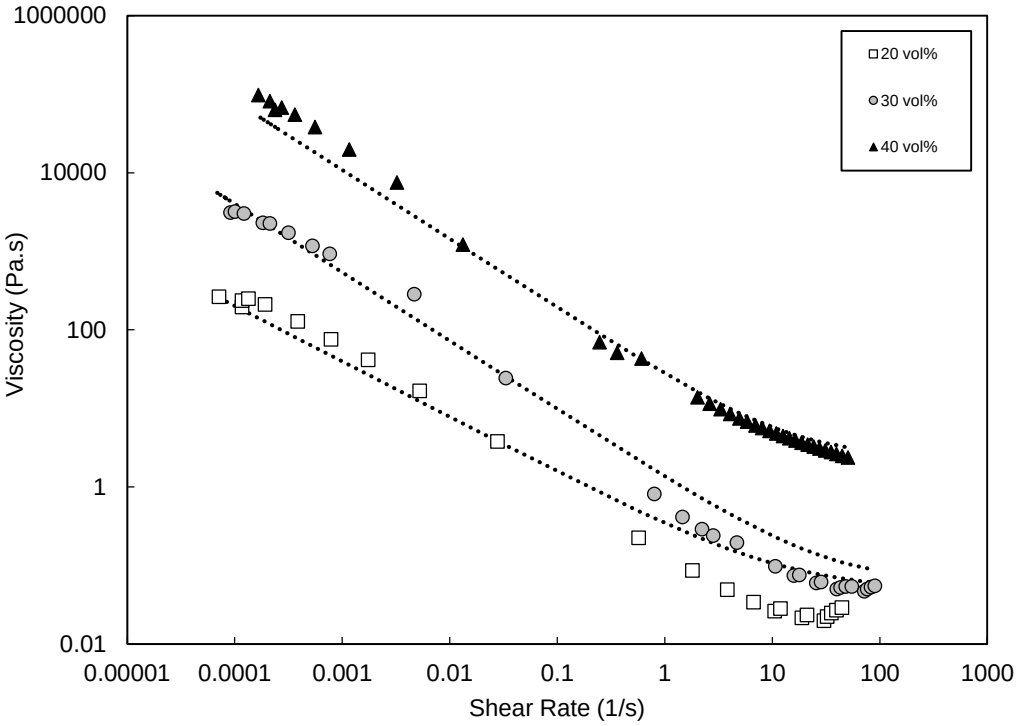

(c)

Figure 6.4-3 Flow behaviour of highly active nuclear waste simulants (a) CPM, (b) ZM and (c) ZMCA dispersed in DI water, all suspensions are above the gel-point. The data represents the change in viscosity as a function of shear rate, with varying particle content. All flow curves have been obtained using the vaned bob geometry.

The data in Figure 6.4-3 shows shear-thinning behaviour for all the nuclear waste stimulants tested here. Such behaviour is consistent with a breakdown in suspension structure driven by hydrodynamic forces as the shear rate increases. Initial viscosity values are related to the number and the strength of bonds and thus the structural nature of the 3D gel. The rate of shear-thinning is possibly related to how the particles align in the flow. Final viscosity values are related to the effective volume fraction in the flow, and thus considering the effect of particle shape.

Comparing Figures 6.4-3 (a) and (b) where the effect of particle size is evident. Viscosity values are orders of magnitude higher for the sub-micron, spherical CPM particles compared to the larger, cubic ZM particles. This is purely due to the greater number of particle-particle interactions per unit volume for CPM systems. Comparing ZMCA particles, Figure 6.4-3 (c), to ZM particles, Figure 6.4-3 (b) the direct effect of shape can be determined. Figure 6.4-3 (c) illustrates the viscosity values, of ZMCA, to be orders of magnitude higher than Figure 6.4-3 (b). Particles with higher aspect ratio rotate at a variable speed, it is the tumbling motion (end-over-end) of the particle which increases the energy dissipated and in turn increasing the viscosity of the suspension. When the system is subjected to shear, the

elongated ZMCA particles rotate more rapidly as they tumble in flow. The increase in viscosity values for ZMCA suspension is a result of the diversion of streamlines in flow as they are re-directed by the particles due to the tumbling motion.

Viscosity of a material according to the rate at which it is sheared provides important information about the processing and performance under applied stress. Processes such as stirring, dispensing and pumping all require a variety of applied stress, this is relevant information for current processing and POCO for the HASTs. Low shear rates are indicative of materials during storage conditions such as sedimentation, segregation and structure orientation. As described in Section 6.2.4 a typical flow curve consists of three regions, two Newtonian regions and a power-law region. From the data illustrated in Figure 6.4-3 it can stated that all the highly active nuclear waste simulants are materials which have a true yield stress, where they exhibit infinite viscosity values at shear rates approaching zero. Compared to materials such as polystyrene spheres and charged poly(styrene-ethylacrylate) copolymer spheres (Krieger, 1972, Laun, 1984) where zero-shear viscosity is apparent, indicative of non-yield stress materials.

It is also evident from Figure 6.4-3 that a definite relationship as a function of volume fraction is illustrated. As expected, the degree of shear-thinning is increased as the particle content is increased. Challenges discussed using the cup-bob geometry for ZM systems, discussed in Section 6.3.1, have been overcome by using the vane-cup geometry. Flow curves have been successfully fitted to the Cross flow model of yoghurt, mudflow rheology and granular dispersions, where by an adaptation of vane tool measurement enabled viscosity characterisation (Krulis and Rohm, 2004, Laigle and Coussot, 1997, Coussot, 2007). All flow curves of CPM, ZM and ZMCA particles dispersed in water have been successfully fitted to the simplified Cross model and Carreau flow models (Cross fit is illustrated in figure 3.5-3). The simplified Cross model, expressed in Equation 6.3-2 is applied for most structured fluids, where it is multiplied throughout by the shear rate. The flow parameters, a constant parameter (K) and the flow index (n), were determined using the Cross model for HAL dispersions of spherical, cubic and cuboidal particles with varying particle volume fractions. The data was fitted using Solver in Excel to obtain the fitting parameters for the best fit. K is closely related to the apparent viscosity that is extracted from the experimental viscosity vs. shear rate data and n is related to the extent of shear-thinning. The key rheological fitting data is presented in Table 25.

Table 25 Cross flow parameters for HAL dispersions above the gel-point.

Particle system	Volume fraction	Fitting parameters		R^2
		K (Pa.s)	*n*	
CPM	0.2	0.98	0.62	0.988
	0.3	24.14	0.79	0.995
	0.4	62.45	0.83	0.997
	0.5	172.65	0.82	0.996
ZM	0.2	0.023	0.28	0.882
	0.3	0.097	0.46	0.972
	0.4	0.561	0.49	0.995
	0.5	14.046	0.63	0.991
ZMCA	0.2	0.63	0.65	0.991
	0.3	1.072	0.84	0.997
	0.4	57	0.89	0.998

The flow parameters for each dispersion show to increase with increasing volume fraction, thus indicating the dependence on relative viscosity on particle volume fraction as a function of shear rate. Flow index behaviour indicates the extent of shear-thinning behaviour, where the approach to unity increases with increasing particle volume fraction. The increase in *n* is attributed to the increase in inter-particle interactions.

Based on the successful fitting of flow models and the production of reliable rheological results, this research considers the vaned bob to be an appropriate geometry for flow property characterisation of complex dispersions.

To better correlate the influence of particle properties the viscosity values, at 1 s^{-1}, have been extracted and plotted as a function of particle volume fraction, as illustrated in Figure 6.4-4. The infinite viscosity values at low shear rates and secondary flow effects of the geometry at high shear rates create an uncertainty in the absolute values extracted for the dependence of viscosity on volume fraction to be determined. Thus, the extracted viscosity values have been extracted at ~1 s^{-1} due to the fact all systems indicate a flow behaviour in the power-law region, where the change in viscosity as a function of volume fraction is consistent at any given shear rate (Figure 6.4-3).

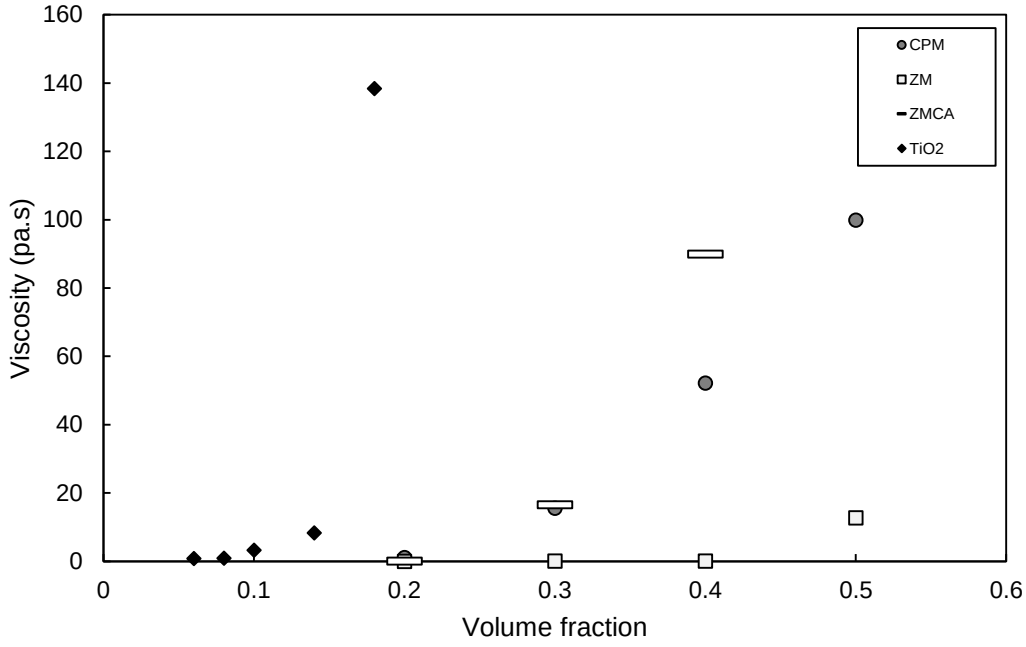

Figure 6.4-4 Viscosity data (at 1 s^{-1}) obtained for TiO_2 and highly active nuclear waste simulants, as function of particle volume fraction. All particles are dispersed in DI water.

The data have been fitted to the K-D equation (Krieger, 1972), expressed in Equation 6.4-1. The K-D expression quantifies the concentration dependence on viscosity, as a function of particle properties.

$$\mu = \left(1 - \frac{\emptyset}{\emptyset_{max}}\right)^{[\mu]\emptyset_{max}} \qquad 6.4\text{-}1$$

Where $[\mu]$ is the intrinsic viscosity and $\emptyset_{max}$ is the maximum packing fraction. As illustrated in figure 6.4-4, elongated ZMCA particle have higher viscosity values than spherical CPM and cubic ZM particles. This expression indicates that the shape of the particles influences the exponential, maximum packing fraction and the intrinsic viscosity. The intrinsic viscosity ultimately indicates the contribution of the interparticle interactions to the dispersion viscosity. As the particle become non-spherical, $\emptyset_{max}$ decreases and the $[\mu]$ increases. Typically, the increase of $[\mu]$occurs at a faster rate than $\emptyset_{max}$ decreases, this therefore results in an overall increase in the exponential as the particle becomes non-spherical.

The K-D equation enables a comparison to the experimentally determined viscosity values. Senapati et al (Senapati et al., 2009) have developed a linearised form of the semi empirical K-D model as expressed in equation 6.4-2

$$\ln(\mu) = -[\mu]\emptyset_{max} \ln\left(1 - \frac{\emptyset}{\emptyset_{max}}\right) \qquad 6.4\text{-}2$$

A plot of $ln(\mu)\ vs\ ln(1-\frac{\emptyset}{\emptyset_{max}})$ generates a linear relationship where the gradient determines the exponential $[\mu]\emptyset_{max}$, and thus $[\mu]$. This relationship is illustrated in figure 6.4-5.

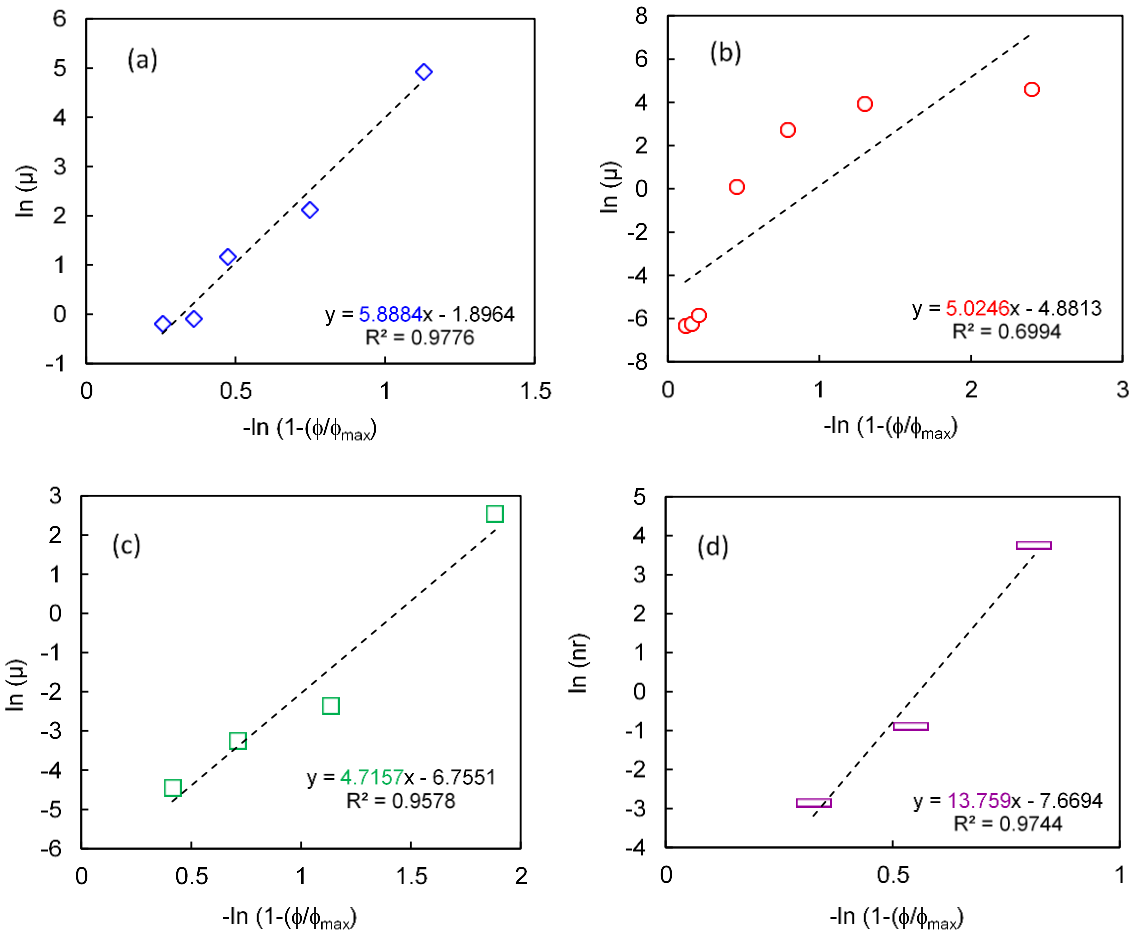

Figure 6.4-5 A linearised form of the Kreiger-Doughtery equation. The data represents the K-D fits for (a) TiO_2, (b) CPM, (c) ZM and (d) ZMCA. All particles are dispersed in DI water.

Figure 6.4-5 illustrates a linear regression for TiO_2 and HAL dispersions. The gradient of the line demonstrates the value for the exponential. CPM deviates from the continuous regressive profile i.e. two distinct regions are illustrated. Figure 6.4-5 (b) illustrates a profile for systems below the gel-point (≤ 20 vol%) and above the gel-point (≥ 20vol%). As the particle volume fraction increases the particles become limited in movement and thus restricting fluid exclusion, at this point the viscosity becomes infinite. Addition of particles to a CPM dispersion progressive builds a colloidal network where the strength and number of interparticles increases, ultimately increasing the intrinsic viscosity, as illustrated in Figure 6.4-5 (b).

Key data extracted and presented in Table 26 from Figure 6.4-5 are exponential values of spherical and non-spherical TiO_2 and HAL dispersions.

The values were obtained by fitting experimental data to the linearised form of the Krieger-Dougherty equation.

Table 26 Comparison of exponential values obtained from fitting the Krieger-Dougherty equation, the values were obtained from a table cited in 'An Introduction to Rheology' (Barnes et al., 1989)

Literature					This research				
Particulate system	**[μ]**	**ϕ_{max}**	**$[\mu]\phi_m$**	**Reference**	**Particulate system**	**[μ]**	**ϕ_{max}**	**$[\mu]\phi_m$**	**R^2 Value**
Submicron spheres	2.70	0.71	1.92	de Kurif et al. (1985)	***TiO_2***	22.62	0.26	5.89	0.9957
TiO_2	5.00	0.55	2.75	Turian et al. (1977)	***CPM***	9.16	0.55	5.03	0.9295
Laterite	9.00	0.35	3.15	Turian et al. (1977)	***ZM***	8.01	0.59	4.72	0.9449
Glass rods	9.25	0.27	2.50	Clarke (1967)	***ZMCA***	19.11	0.72	13.76	0.9575
Glass fibres (Ar=7)	3.80	0.37	1.41	Giesekus (1983)					

From Table 26 good correlations can be made by comparing CPM values to TiO_2 values from Turian et al (Turian et al., 1997). It has been assumed that CPM particles are similar in size and shape to TiO_2 particles and thus, the maximum packing fraction of CPM was taken to be 0.55.

Mueller et al. (Mueller et al., 2009) proposes an equation to calculate the maximum packing fraction of non-spherical particle with $A_r \geq 1$, for ZM particles where the literature is limited for cubic systems, the initial fitting parameters was calculated by the following expression

$$\emptyset_{max} = \frac{2}{0.321A_r + 3.02} \qquad 6.4\text{-}3$$

Which gives values of 0.59 and 0.35 for ZM and ZMCA systems, respectively. In particular for ZM systems, $\emptyset_{max}$ value obtained using Equation 6.4-3, showed good agreement as illustrated in Figure 6.4-5 (c). Additionally, the $\emptyset_{max}$ value correlates well with the compressive yield stress calculations, Section 6.4.3. In contrast the calculated value, using Equation 6.4-3, showed poor agreement to the linearised expression and thus $\emptyset_{max} = 0.35$ for ZMCA particles was neglected. Thus, the $\emptyset_{max}$ value was taken from the compressive yield stress calucations, where $\emptyset_{max} = 0.72$.

Furthermore an empirical relationship for non-spherical particles was proposed by Mueller et al. (Mueller et al., 2009) to calculate the intrinsic viscosity

$$[\mu] = \frac{8{A_r}^2}{45lnr} \qquad 6.4\text{-}4$$

Where *r* is the particle size and calculates $[\mu] = 10.36$ for ZMCA systems.

The K-D fits in agreement with the highly active nuclear waste simulants, the fit to TiO_2 dispersions indicates a larger than estimated $[\mu]$ value of 29 and $\emptyset_{max} = 0.26$. According to the K-D fit the overall increase in the exponential is due the large intrinsic viscosity value. The K-D relationship indicates for suspensions where the intrinsic viscosity is high the maximum packing fraction approaches low values. The K-D approximation validates the maximum viscosity measurements for TiO_2 dispersions at pH_{pzc}. The high viscosity values are a result of the electrophoretic mobility approaching its' minimum limit, caused by the depletion of the EDL.

The experimental data therefore agrees with the theoretical application whereby the overall dispersion results in an increase in viscosity as the contained particles deviate from an ideal sphere, illustrated by the comparison of ZMCA to CPM particulate dispersions. In contrast, the lowest viscosity values have been obtained for ZM particles, this may be due to the lower number of interparticle interactions per unit volume when compared to CPM particles. Comparing ZM to ZMCA, the increase in $[\mu]\emptyset_{max}$ indicates the dependence on the dispersion viscosity on particle aspect ratio, which results from the dependence of $\emptyset_{max}$.

6.4.1.3 Effect of electrolyte concentration on flow behaviour

The influence of background electrolyte concentration on TiO_2 dispersions was investigated. Figure 6.4-6 illustrates the concentration of electrolyte ranging from 1-2M HNO_3 as a function of varying particle volume fraction, compared to Figure 6.4-1 where TiO_2-H_2O dispersions are at pH_{pzc}. Addition of background electrolyte alters the dynamics of the particle network, indicated in Figure 6.4-6.

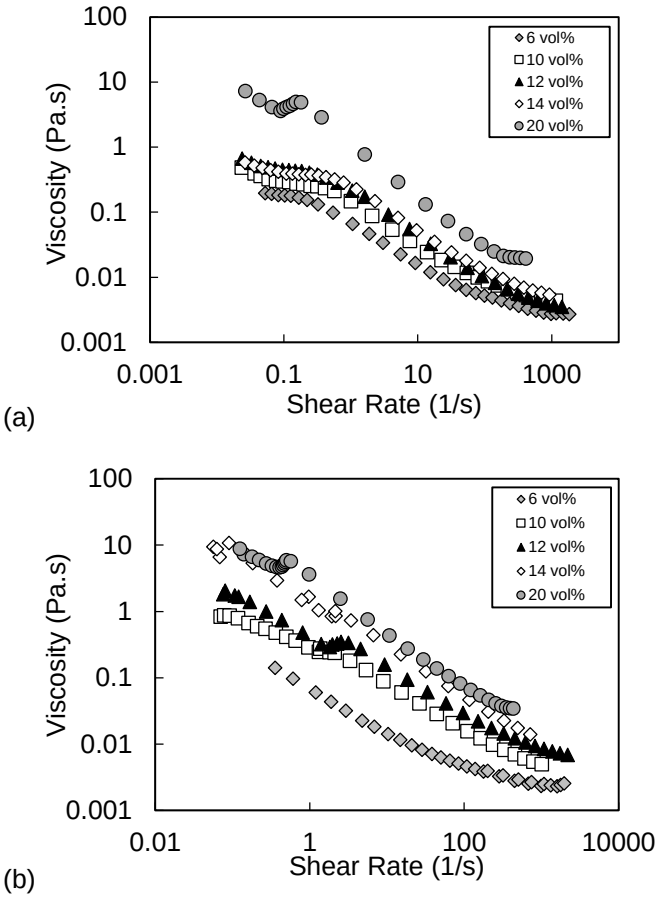

Figure 6.4-6 Flow behaviour TiO_2 dispersed in (a) 1MHNO_3 and (b) 2M HNO_3, The data represents the change in viscosity as a function of shear rate, with varying particle content. All flow curves have been obtained using the cub and bob for 6-14 vol% and the vaned bob geometry for 20 vol%.

Figure 6.4-6 illustrates apparent shear thinning behaviour for both dispersions of TiO_2 in 1M HNO_3 (Figure 6.4-6 (a)) and in 2M HNO_3 (Figure 6.4-6 (b)). Two regimes are identified within these dispersions, Newtonian and power law. Figure 6.4-6 (a) illustrates at any given volume fraction the dispersions approach the low shear rate limiting value of viscosity, this is associated with the first Newtonian region of a flow curve where $\mu_0 = \lim_{\dot{\gamma}\to 0} \mu$. At shear rates ≥ 1 s^{-1}, the dispersions enter the power law region. At high shear rates ≥ 200 $s^{-}1$, 20 vol% TiO_2 dispersions at 1M HNO_3 approaches the second Newtonian region where $\mu_\infty = \lim_{\dot{\gamma}\to \infty} \mu$. A key element of the data presented in Figure 6.4-6 is the reduced viscosity of TiO_2-HNO_3 dispersions, where it appears TiO_2 particles to be less aggregated in acidic environments. This is supported by sedimentation studies, where TiO_2-HNO_3 showed increased settling rates compared to TiO_2-H_2O, thus both sets of flow behaviour data (Figure 6.4-6) and sedimentation data (Chapter 5, Figure 5.3-12) are indicative of reduced aggregation in TiO_2-HNO_3 dispersions. This data is also supported by research conducted on zirconia (Briscoe et al., 1998, Khan et al., 2012, Leong, 1997, Leong et al., 1991), titania (Yang et al., 2001, Mikulášek et al., 1997, Leong et al., 1993) and alumina (Leong et

al., 1993) dispersions where the electrostatic repulsions between particles is due to the build-up of the EDL, from ion adsorption on the particle from the background electrolyte. Hence, resulting in a dispersion exhibiting a low viscosity.

From Figure 6.4-1, at the natural pH of TiO_2, the dispersions exhibit maximum viscosity values due to the system being at a $pH_{pzc.}$ Consider the zeta potential measurements (Figure 3.4-16), above the pH_{pzc} for TiO_2 dispersions where the magnitude of electrophilic mobility increases with increasing H^+ ion concentration. Thus, further supporting the reduced viscosity values of TiO_2 dispersions in 1 and 2M HNO_3 illustrated in figure 6.4-6.

The Influence of electrolyte concentration at varying concentrations between 0.5-2 M HNO_3 as a function of particle volume fraction, was also studied for the CPM (Figure 6.4-7) and ZM (Figure 6.4-8) simulants. The HAL solids are currently dispersed in ~2 M HNO_3 within the HASTs. The electrolyte concentration is expected to vary during POCO as the propose method to clean the tanks is with water. Thus, understanding the flow behaviour during POCO is required to obtain optimum conditions for processing.

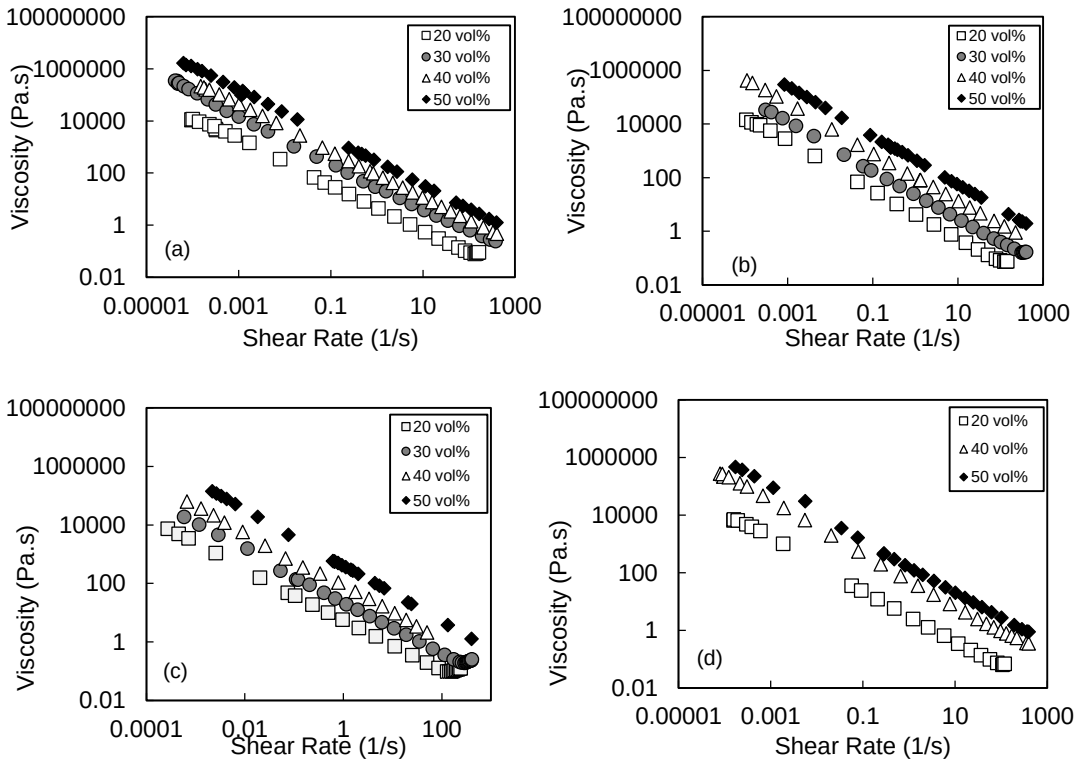

Figure 6.4-7 Flow behaviour of caesium phosphomolybdate with varying electrolyte concentration (a) 0.5M HNO_3, (b) 1M HNO_3, (c) 1.5M HNO_3 and (d) 2M HNO_3, all suspensions are above the gel-point. The data represents the change in viscosity as a function of shear rate, with varying particle content. All flow curves have been obtained using the vaned bob geometry.

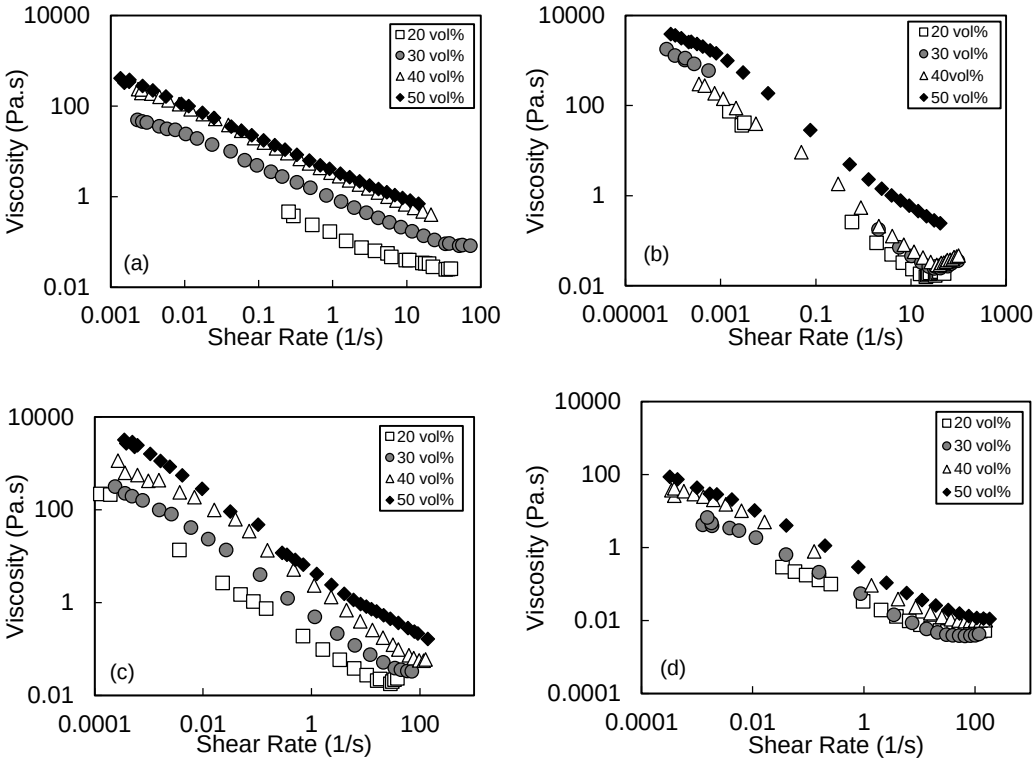

Figure 6.4-8 Flow behaviour of ZM with varying electrolyte concentration (a) 0.5M HNO_3, (b) 1M HNO_3, (c) 1.5M HNO_3 and (d) 2M HNO_3, all suspensions are above the gel-point. The data represents the change in viscosity as a function of shear rate, with varying particle content. All flow curves have been obtained using the vaned bob geometry.

Figure 6.4-7 indicate the extent of shearing-behaviour to be increased when CPM in particular are dispersed in nitric acid, in comparison to behaviour in water (see Figure 6.4-3). An increase in background electrolyte is responsible for the depletion of the electrostatic potential barrier, creating a particle network which is dominated by net-interparticle attractive forces. This mechanism is illustrated in Figures 6.4-7 and 6.4-8 where there is a significant increase in viscosity values for the CPM, but relatively less so for the ZM. The results are consistent with the setting studies (Chapter 5, Section 5.5.1.2), where there is a degree is aggregation in CPM-H_2O dispersions (evident from SEM image in Chapter 3, Section 3.4.2, Figure 3.4-11), to which the extent of aggregation is further enhanced by the addition of electrolyte concentration. The sedimentation studies indicate reduced sedimentation in the CPM-HNO_3 due to the space filling network created by the aggregates. In contrast, ZM systems exhibit slight/no aggregation when dispersed in H_2O or HNO_3, which is also consistent with sedimentation studies.

The pronounced shear-thinning behaviour, for CPM-HNO_3 is due to the attractive particle network. At low shear rates the particle network is broken down into particle clusters, where fluid is trapped in the space between the

clusters, thus resulting in high viscosity values. A combination of increasing shear rates and dominance of hydrodynamic forces the particle clusters are broken down, releasing more fluid and therefore reducing the viscosity.

To better illustrate the effect of electrolyte concentration on flow behaviour, Figure 6.4-9 (a) and (b) represent the influence of increasing the H^+ ion concentration from 0.5-2 M by dispersing the CPM and ZM particles in HNO_3.

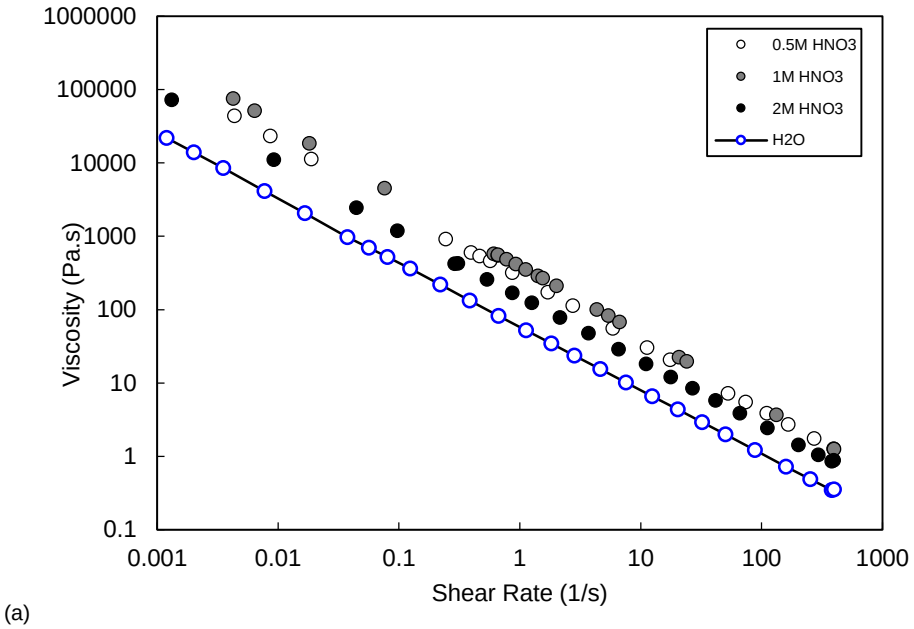

(a)

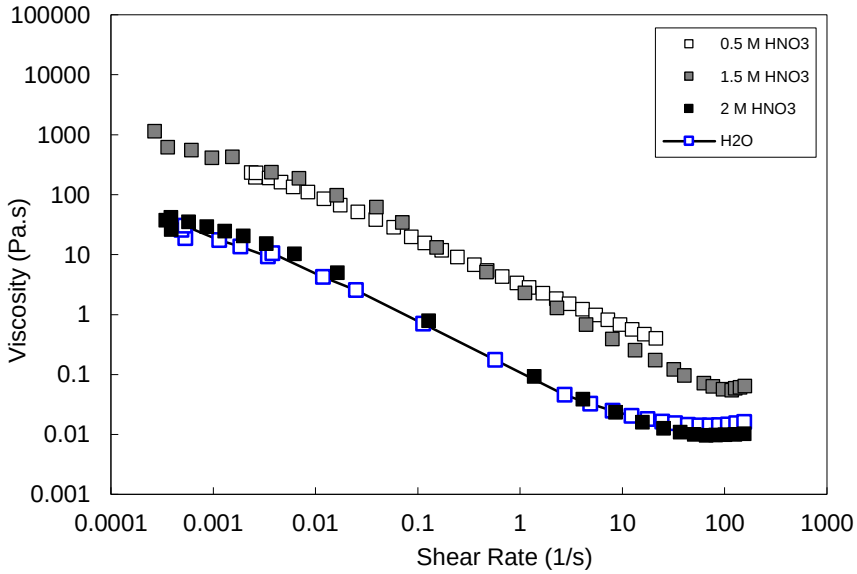

(b)

Figure 6.4-9 Flow behaviour of (a) CPM and (b) ZM dispersed in varying electrolyte concentrations from 0.5 to 2M HNO_3. The data represents both suspensions at 50 vol% and 40 vol% for CPM and ZM systems, respectively, and were obtained using the vaned bob geometry.

Figure 6.4-9 (a) illustrates CPM dispersions have a minor change in viscosity as electrolyte concentration increases. In contrast, ZM dispersions illustrate (Figure 6.4-9 (b)) an obvious change in behaviour as electrolyte concentration increases (from water to 0.5 M HNO_3). However, comparing ZM-H_2O to ZM-HNO_3 (2 M) dispersions, the change is viscosity is negligible, this is supported by sedimentation studies by comparing Figures 5.4-7 to 5.4-14, of the two dispersions where no change is also observed, thus indicating no evidence on aggregation in ZM systems.

Figure 6.4-9 (b) does, however, illustrate the increase in viscosity when the electrolyte concentration is increase to 0.5 M HNO_3, this behaviour occurs until a critical point. Once the dispersion enters the 2M HNO_3 region a large decrease in viscosity is exhibited. This behaviour is indicative of dispersion re-stabilisation through either an increase in zeta potential or the dominance of short-range repulsive forces. Consider the latter, it is believed that the hydrated counter-ions are responsible for the short range repulsion. The counter-ions prevent the particles coming into direct contact, this causes repulsion of particles and therefore a decrease in viscosity. This behaviour is consistent with research conducted by Chang et al, where by the viscosity of alumina slurries dramatically decreases at large concentrations of electrolytes. The hydrated counterions are attracted to the positively charged alumina surfaces and therefore create a hydrated potential barrier. This barrier only occurs when the amount of salt added is sufficient enough to produce the hydrated layer and to decrease the electrostatic potential barrier, so that the particles are in closer contact (Velamakanni et al., 1990, Pashley, 1981, Yilmaz et al., 2007) Chang et al., 2004. The third potential is of interest in many fields, Padmanabhan et al have investigated specific ion adsorption to enhance the short range repulsive forces. The surface composition of alkali-halide solutions were investigated. Short-range repulsions were enhanced with the addition of iodide ions, compared to chloride ions. The Iodide ions are more strongly attracted to the particles surface than chloride ions (Padmanabhan et al., 2007).

An interesting comparison to conduct is the influence of shape on the aggregation mechanism at high electrolyte concentration. Rheological data for cubic ZM and elongated ZMCA is illustrated in Figure 6.4-10.

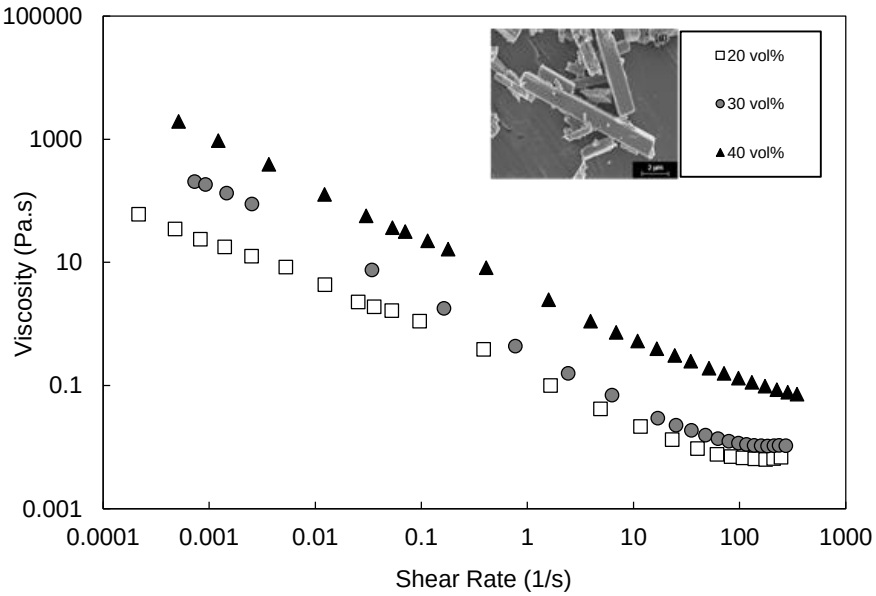

Figure 6.4-10 Flow behaviour of ZMCA dispersed in 2M HNO_3 all suspensions are above the gel-point. The data represents the change in viscosity as a function of shear rate, with varying particle content. All flow curves have been obtained using the vaned bob geometry. SEM images are provided of cuboidal ZMCA.

Figure 6.4-10 shows ZMCA particle dispersed in 2M nitric, where the viscosity is largely decreased in relation to the behaviour in water (Figure 6.4-3). This is an interesting and significant contrast to the acid behaviour of either CPM or cubic ZM. It is assumed that in this case enhanced aggregation of the rod-like particles in acid actually reduces the suspension viscosity, due to the preference for face-to-face contact. It can be assumed that rod-like particle tend to align along the major particle-axis, creating a face-to-face contact (Litchfield and Baird, 2006, Blachier et al., 2014, Teh et al., 2009). Low shearing tends to promote the aggregation. The orientation of the aggregated rod-like particles align themselves parallel to the direction of flow. This reduces the tumbling motion of individual rod-like particles that are present when the suspension is stable in water and thus, reduces the viscosity.

6.4.2 Yield stress

Understanding the transportation properties of HAL is key for successful processing of nuclear waste. As previously mentioned, this research focuses on the influence of particle properties, with complex chemical structure on rheological behaviour. A parameter which is of great interest is the shear yield stress. It is a key parameter to define the strength of a sediment bed.

Defining the yield is important not only for the HASTs but also for other areas within the Sellafield site. Many of the legacy wastes are stored within

ponds/silos. The waste within these ponds contain various types of material ranging from Magnox sludge from corroded fuel to organic wastes. The understanding of the yield stress, the minimum amount of shear stress required to induce flow, is a key application for a number of areas within the nuclear industry. HAL is stored in 2M HNO_3 within the HAST, the application of jet ballasts and air lifts (complex system) are able to re-suspend and maintain the solids in suspension. This section explores the energy required to re-suspend the settled bed of HAL solids and a number of parameters which affect the re-suspension. Yield stress measurements were performed on all highly active nuclear waste simulants and TiO_2 dispersions using two techniques, torque-time and the creep/creep recovery. The influence of particle properties and electrolyte concentration is explored in this research.

6.4.2.1 Torque-time method

The Brookfield viscometer produced a maximum torque% for each volume fraction. The calculation of yield stress from the torque requires the dimensions of the vane and the torque input which is calculated from 100% torque. A number of experiments have been conducted with this instrument, this involves varying the amount of material used, and therefore a range of total material is 100-300g.

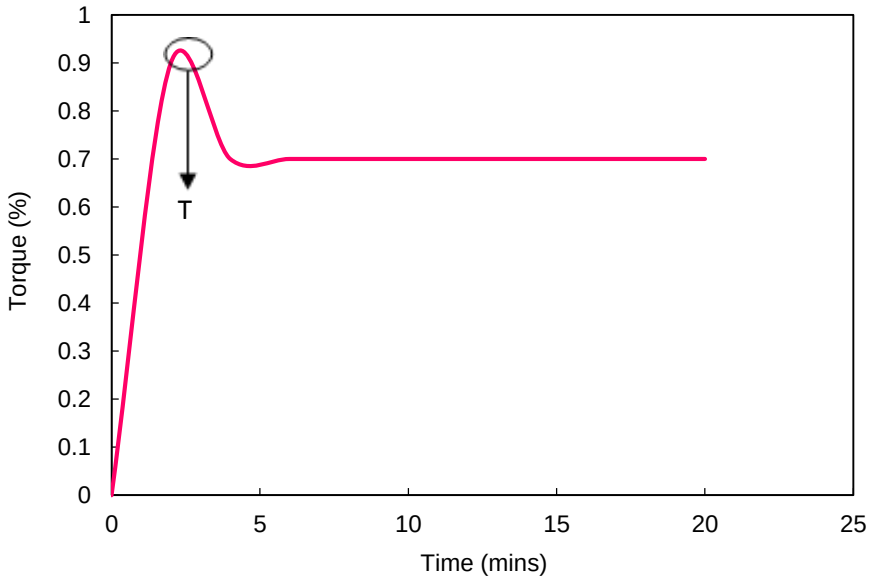

Figure 6.4-11 A graph illustrating the torque-time response obtained from the Brookfield Viscometer. The data represents the response of 6 vol% TiO_2 dispersed in DI water. The circle at the peak of the data represents the maximum torque achieved for that particular suspension.

The calculation is an example for 6 vol% TiO_2, the vane which was employed was the V72. Figure 6.4-11 illustrates the maximum torque exhibited by 6 vol% TiO_2 dispersion to be 0.9%, where 100% torque is

57496 dyne-cm. The maximum torque can be calculated with these known parameters, as expressed below

$$M = \frac{Torque\ \%}{100} \times 100\%\ Torque\ = \frac{0.9}{100} \times 5749 = 517.464\ [\text{dyne} - \text{cm}] \quad 6.4\text{-}5$$

There are many rheological models for yield stress fluids which are related on the type of instrument/geometry implemented. The torque exerted as a function of time is illustrated in Figure 6.4-11. At 0.9% indicates the maximum point at which the dispersion is considered to yield along the cylindrical surface created by the vane blades. Based on the Figure 6.4-11 and the calculation of the maximum torque (*M*) the yield stress can be calculated with the knowledge of the vane dimensions, the radius (*Rb*) and the length (*L*), as expressed in Equation 6.4-6

$$\sigma = \frac{M}{2\pi\ Rb^2\ L} \times 0.1\ = \frac{517.464}{2\pi \times 1.0835^2 \times 4.333} \times 0.1\ = 1.619\ Pa \quad 6.4\text{-}6$$

This calculation was carried out for the torque % measured with the Brookfield at a range of volume fractions 0.06-0.2. Figure 6.4-12 illustrates a plot portraying the yield stress as a function of volume fraction.

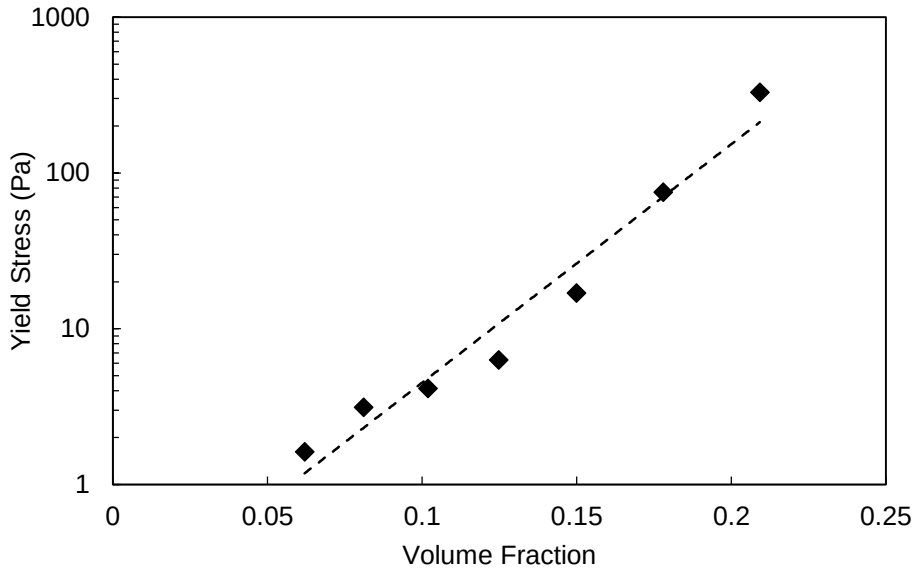

Figure 6.4-12 The relationship of yield stress of TiO_2 suspensions and the variation of volume fraction

It can be suggested from Figure 6.4-12 that as the volume fraction increase the yield stress of the suspension also increases. As the yield stress corresponds to the stress essential for the transition of the material from its elastic state to its plastic state, this figure suggests that at a greater volume fraction the stress required for complete deformation of the material is far greater than what is required when considering a low volume fraction.

This essentially can be explained by the particle-particle interactions within each suspension, for instance at high volume fractions the particle content within the suspension is higher which causes the interparticle forces to be stronger than that of the suspensions lower volume fractions. Therefore the stress needed to break the bonds, is greater for suspensions with high particle content. However, Figure 6.4-12 also illustrates a slight deviation from the linear trend at low volume fraction, $\emptyset \leq 0.12$, where the titania suspensions are below the true gel-point. The interactions at low particle concentrations of the aggregated particles are insufficient to produce a space filling network and thus deviating from the linear relationship.

Figure 6.4-12 coincides well with the research carried out by (Nguyen et al., 2005) where the yield stress as a function of solid weight (wt%) of TiO_2 dispersions was explored. The similar trend where the yield stress increases with the weight fraction suggests that the results produced by this technique are reliable.

The amount of material used for this particular measurement is 300g (total mass), therefore the maximum amount of solid material required is 150g. This is a substantial amount of material, as mentioned in previous chapter the quantity of material available is limited. The manufacturing of the highly active nuclear waste simulants is not only expensive but also time consuming.

6.4.2.2 Creep and creep recovery method

Creep and creep recovery method is a stress-controlled method. A constant stress is applied over a fixed period of time and resultant creep angle is recorded as a function of time. All creep/recovery measurements were conducted with V14 immersed in C37. Figures 6.4-13 to 6.4-15 illustrate the creep angle as a function of time, with a range of applied stress for CPM, ZM and ZMCA dispersions with varying particle content from 20-50 vol% for CPM and ZM and 20-40 vol% for ZMCA, respectively.

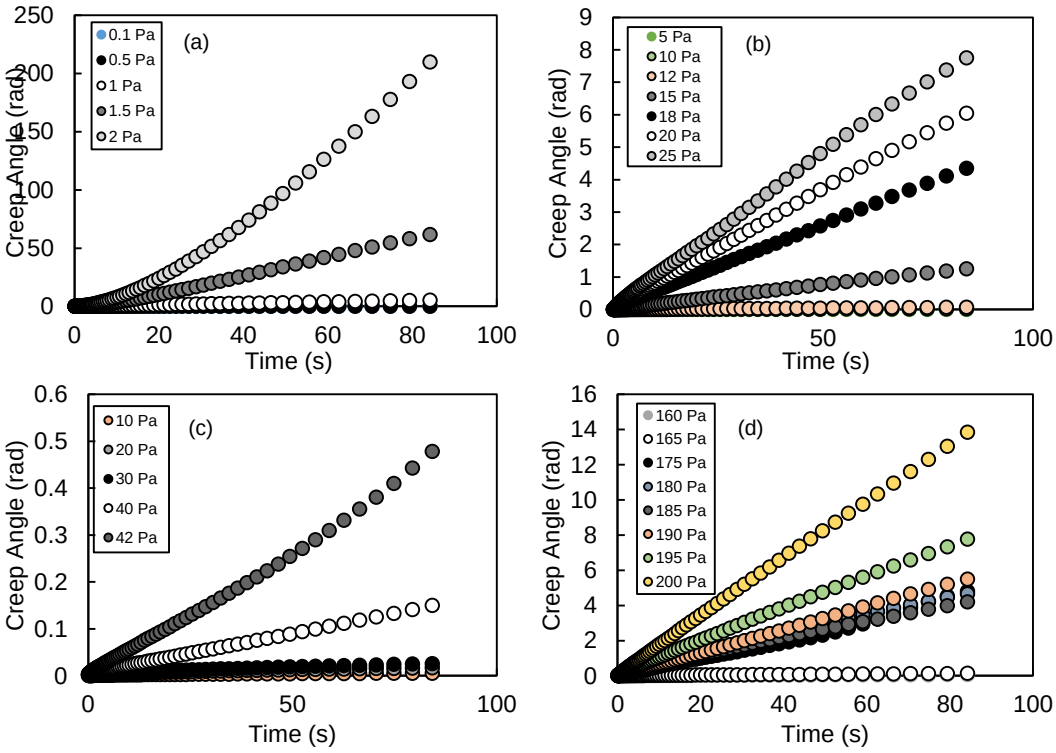

Figure 6.4-13 Creep data illustrating the creep angle as a function of time for CPM suspensions over varied applied stress. The data represents CPM in DI water dispersions at varying particle concentrations of (a) 20 vol%, (b) 30 vol%, (c) 40 vol% and (d) 50 vol%.

Figures 6.4-13 to 6.4-15 illustrate the approximation of the yield stress for each particulate system, at varying particle volume fractions.

For CPM dispersions, the creep data in Figure 6.4-13 illustrates that at low stress, <1 Pa for 20 vol%, <15 Pa for 30 vol%, <40 Pa for 40 vol% and <175 Pa for 50 vol%, indicate a slight creep in the particulate systems. At the applied stresses and below (extracted from the data in Figure 6.4-13), the systems are dominated by elastic properties and therefore behaving like an elastic solid. A slight increase in creep angle, followed by a plateau is indicative of this behaviour. At high applied stress (above the stresses extracted from Figure 6.4-13, w.r.t each varying particulate concentration), the creep angle increases proportionally with time, at a constant rate. As the creep angle proportionally increases with time this indicates the system is dominated by viscous properties, thus the onset of flow and thus yield stress properties. The yield stress of each particulate system can be approximated from Figure 6.4-13, for 20 vol% σ_y *= 1.5 -2 Pa*, for *30 vol%* σ_y *= 15-18 Pa*, for *40 vol%* σ_y *= 40-42 Pa* and for *50 vol%* σ_y *= 175-195 Pa.*

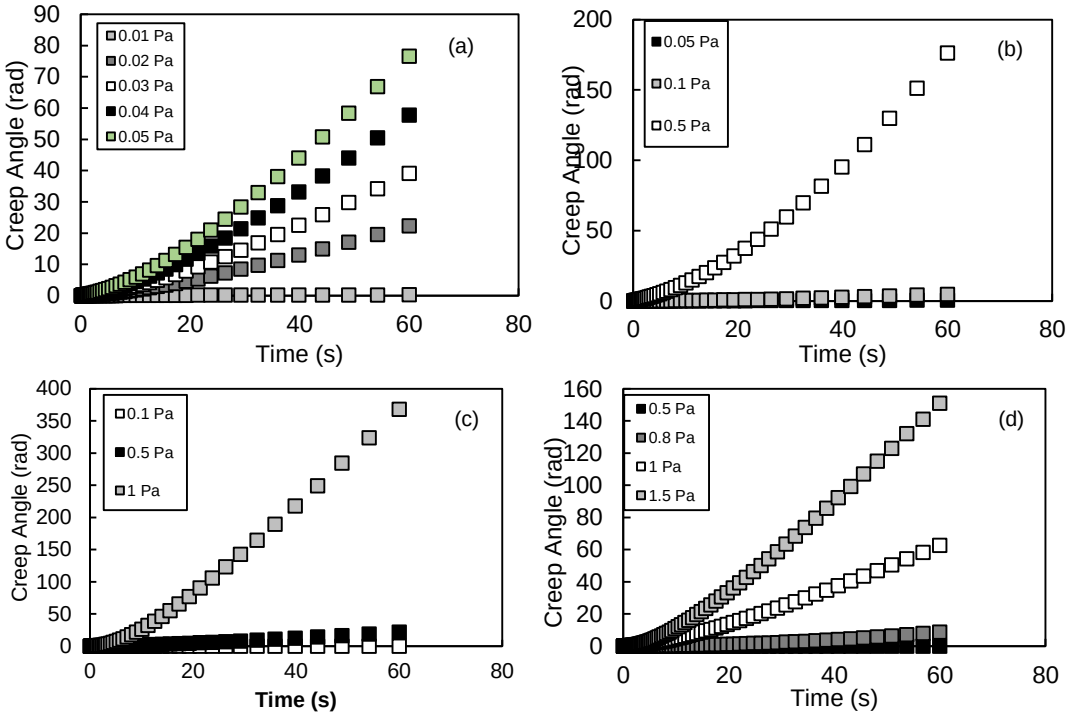

Figure 6.4-14 Creep data illustrating the creep angle as a function of time for ZM suspensions over varied applied stress. The data represents ZM in DI water dispersions at varying particle concentrations of (a) 20 vol%, (b) 30 vol%, (c) 40 vol% and (d) 50 vol%.

For ZM dispersions, the creep data is illustrated in Figure 6.4-14. At low stress application, <0.02 Pa for 20 vol%, <0.5 Pa for 30 vol%, <1 Pa for 40 vol% and 50 vol%, indicate dominance of elastic properties. Above the stated stress values, the creep angle illustrates a steady increase with time, which indicates that when t = ∞ the creep angle will indefinitely increase, implying the onset of a full flowing suspension. The yield stress of each particulate system can be approximated from Figure 6.4-14, 20 vol% (σ_y = *0.02-0.05 Pa*), *30 vol%* (σ_y = *0.1-0.5 Pa*), *40 vol%* (σ_y = *0.5-1 Pa*) and *50 vol%* (σ_y = *0.8-1.5 Pa*)

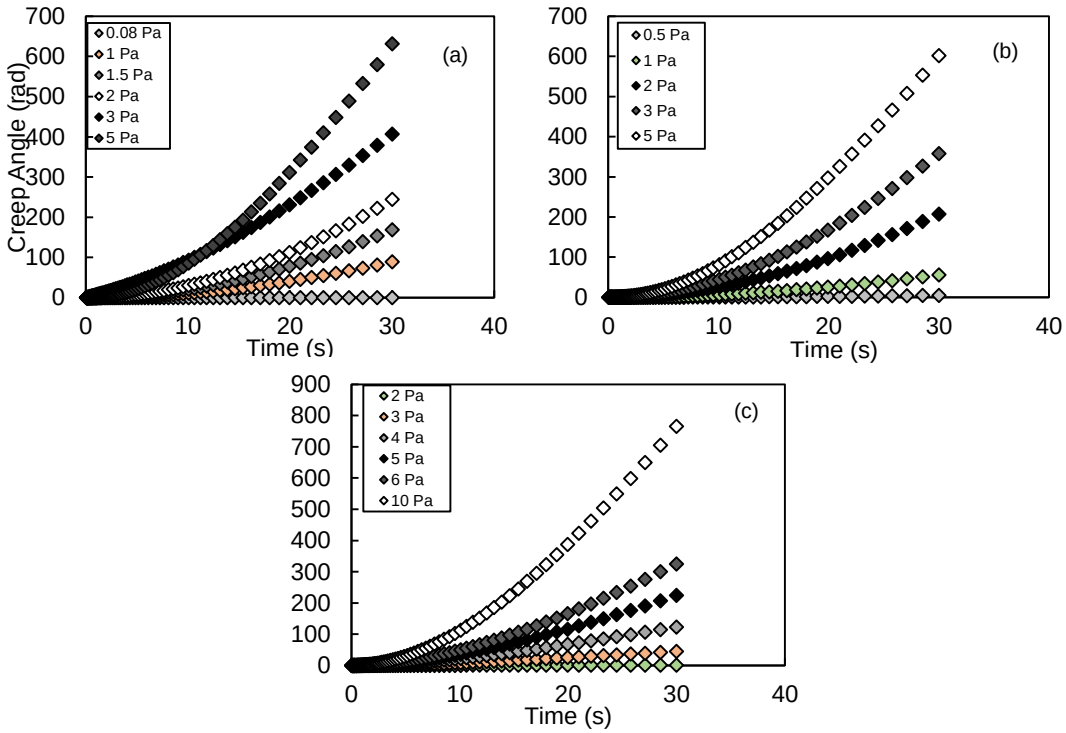

Figure 6.4-15 Creep data illustrating the creep angle as a function of time for ZMCA suspensions over varied applied stress. The data represents CPM in DI water dispersions at varying particle concentrations of (a) 20 vol%, (b) 30 vol% and (c) 40 vol%.

For ZMCA dispersions, the creep data is illustrated in Figure 6.4-15. At low stress application, <1 Pa for 20 vol%, <2 Pa for 30 vol% and for <4 Pa for 40 vol%, indicate elastic properties are dominant. The yield stress of each particulate system can be approximated from Figure 6.4-15, 20 vol% (σ_y = *1-5 Pa*), *30 vol%* (σ_y = *2-5 Pa*), *40 vol%* (σ_y = *4-10Pa*). All creep data can be supported by creep recovery method. Material response is recorded after the applied stress is removed, as a function of time.

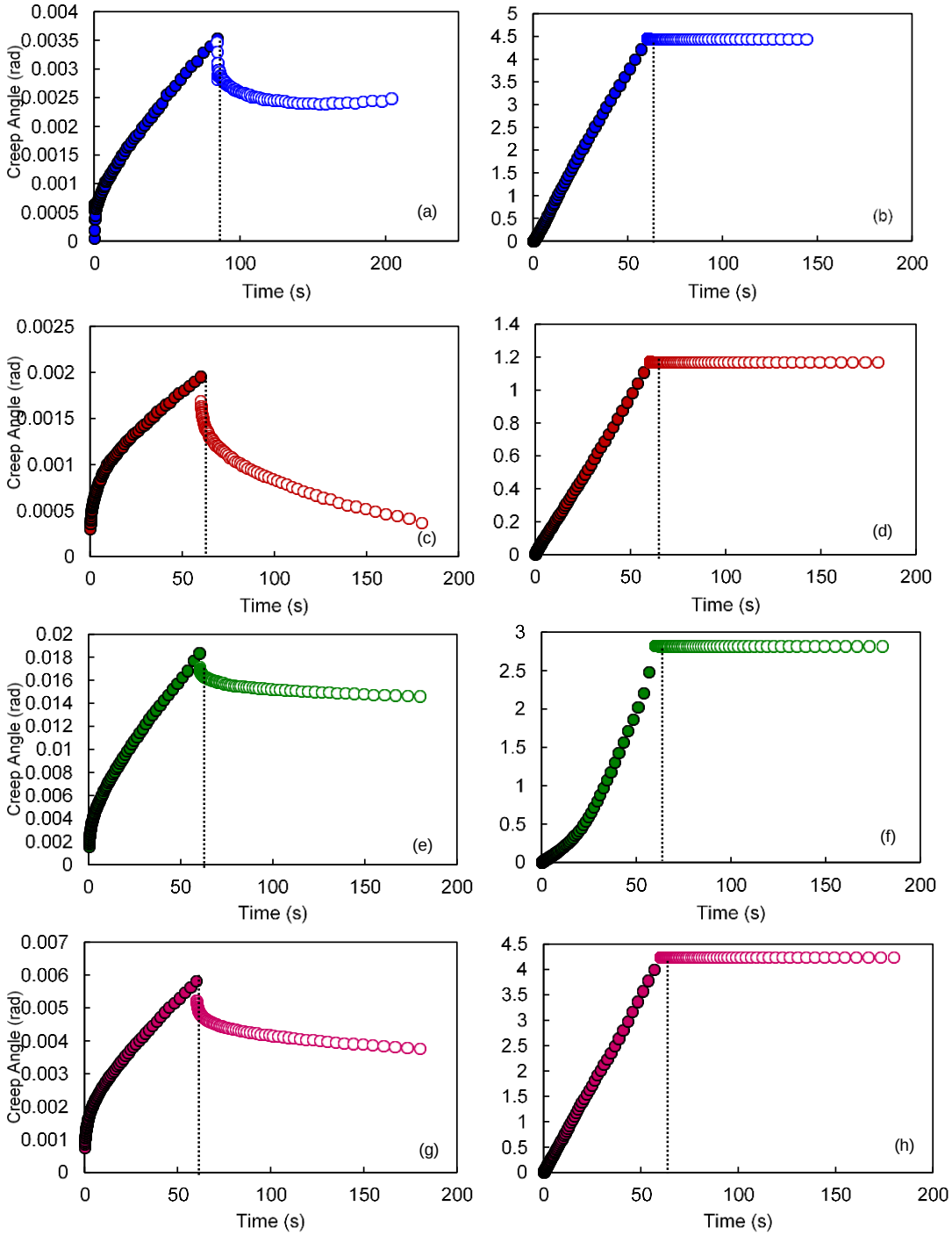

Figure 6.4-16 Creep recovery method applied to CPM particles dispersed in DI water at varying particle content. Suspensions of 20 vol% (blue filled and hollow circular data points) with applied stress of (a) 0.5 Pa and (b) 1 Pa; 30 vol% (red filled and hollow circular data points) with applied stress of (c) 15 Pa and (d) 18 Pa; 40 vol% (green filled and hollow circular data points) with applied stress of (e) 40Pa and (f) 42 Pa; 50 vol% (pink filled and hollow circular data points) with applied stress of (g) 165 Pa and (h) 175 Pa. The vertical dotted lines represents the time at which the applied stress was removed, after 60 s.

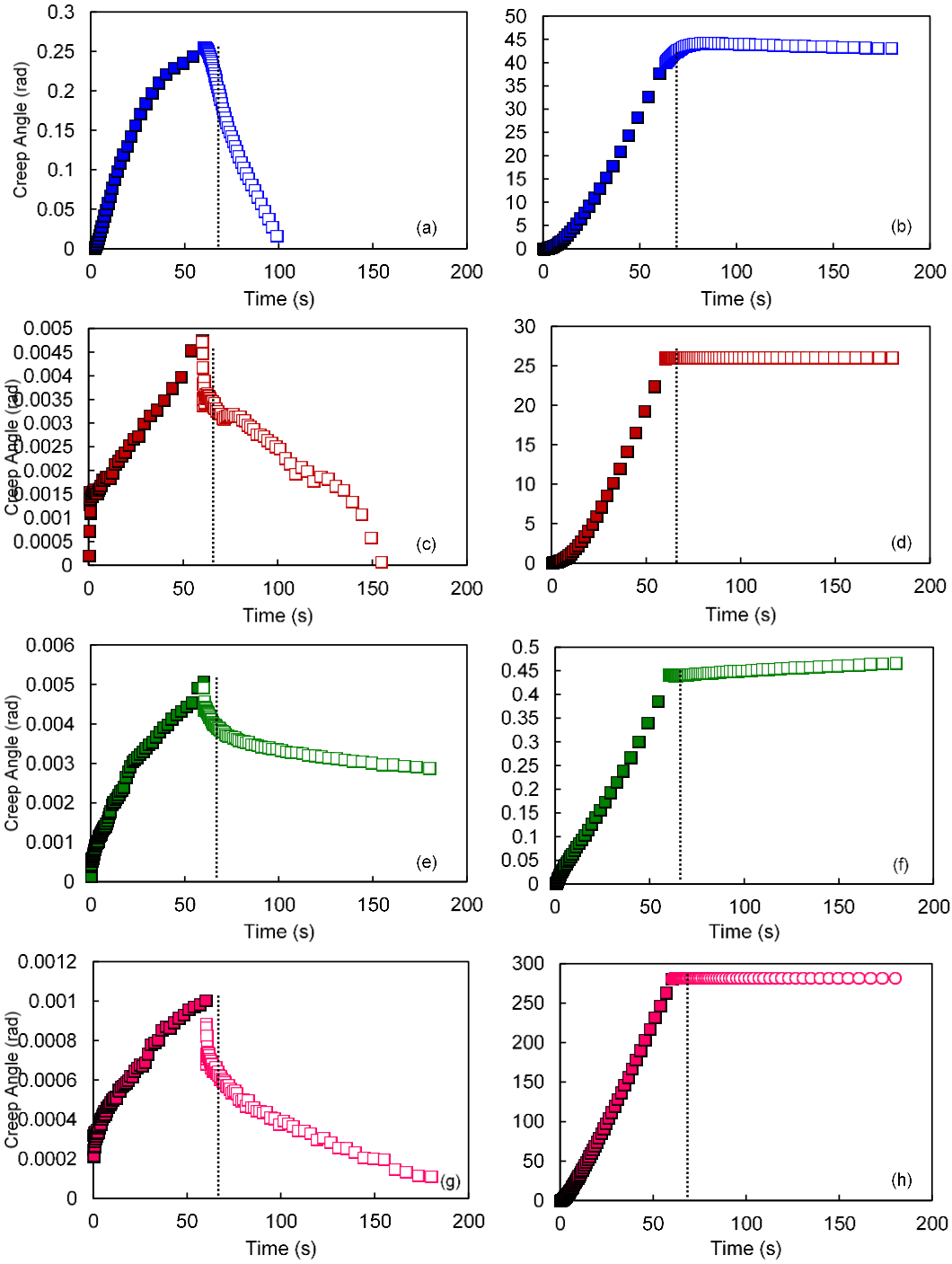

Figure 6.4-17 Creep recovery method applied to ZM particles dispersed in DI water at varying particle content. Suspensions of 20 vol% (blue filled and hollow circular data points) with applied stress of (a) 0.01 Pa and (b) 0.03 Pa; 30 vol% (red filled and hollow circular data points) with applied stress of (c) 0.05 Pa and (d) 0.1 Pa; 40 vol% (green filled and hollow circular data points) with applied stress of (e) 0.1 Pa and (f) 0.5 Pa; 50 vol% (pink filled and hollow circular data points) with applied stress of (g) 0.8 Pa and (h) 1 Pa. The vertical dotted lines represents the time at which the applied stress was removed, after 60 s.

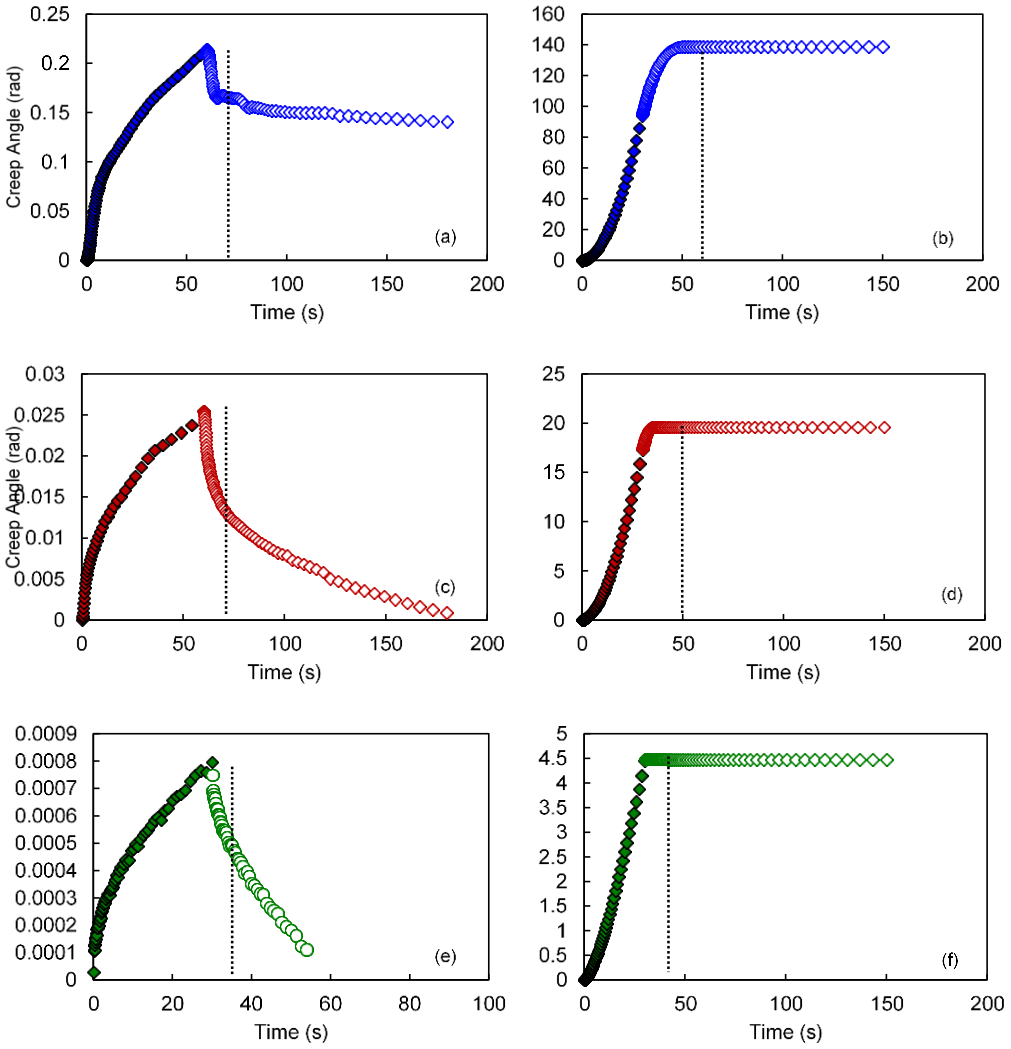

Figure 6.4-18 Creep recovery method applied to ZMCA particles dispersed in DI water at varying particle content. Suspensions of 20 vol% (blue filled and hollow circular data points) with applied stress of (a) 0.08 Pa and (b) 1 Pa; 30 vol% (red filled and hollow circular data points) with applied stress of (c) 1 Pa and (d) 2 Pa; 40 vol% (green filled and hollow circular data points) with applied stress of (e) 3 Pa and (f) 5 Pa. The vertical dotted lines represents the time at which the applied stress was removed, after 60 s.

Figures 6.4-16 to 6.4-18 illustrate the creep recovery response for CPM, ZM and ZMCA dispersions. The creep recovery method was employed to compare the behaviour of the suspension when different stresses were applied and further support the yield stress approximated using the creep flow curves.

Relating the response curves to the creep flow curves, consider 20 vol% dispersions for CPM, ZM and ZMCA. For CPM dispersions, Figure 6.4-13 (a) approximates the yield stress to be between 1-2 Pa. From Figure 6.4-16 (a) it can be implied that at 0.5 Pa shows viscoelastic properties and Figure 6.4-16 (b) shows pure viscous flow at 1 Pa. For ZM dispersions Figure 6.4-14 (a) approximates the yield stress to be between 0.02-0.05 Pa. Compare this to

creep recovery flow, figure 6.4-17 (a) illustrates elastic properties at 0.01 Pa and Figure 6.4-17 (b) indicates viscous flow at 0.03 Pa. For ZMCA dispersions, Figure 6.4-15 (a) approximates the yield stress to be between 1-5 Pa. Recovery data in Figure 6.4-18 (a) indicates viscoelastic properties at 0.08 Pa and Figure 6.4-18 (b) indicates viscous flow at 1 Pa. This analysis has been carried out for each particulate system at varying particle concentrations and plotted in Figure 6.4-19.

An interesting aspect of creep and recovery data is that it provides information about the structure of the suspension. Nuclear waste simulants show all three distinct behaviours upon removal of applied stress. For instance, Figures 6.4-14 (a & c) for ZM dispersions and Figure 6.4-15 (e) for ZMCA dispersions are all indicative of pure elastic behaviour due to the almost instantaneous recovery. All other stress applied below the yield illustrates that when a small stress is applied the structure has changed but then it is slowly recovering, which shows elastic properties, due to the fact that the recovery does not happen instantaneously this shows viscoelastic properties. At higher stress (yield stress and above), no recovery is illustrated.

An interesting comparison is to consider the relaxation period of CPM and ZM dispersions at 50 vol%, Figures 6.4-16 and 6.4-17 (g). For CPM dispersions complex behaviour is exhibited, where difference between the viscoelastic and viscous flow is ~10 Pa. In contrast to ZM dispersions where the difference is ~0.2 Pa. Comparing the recovery behaviour, where CPM illustrates slight recovery far below the yield stress and ZM illustrates full recovery close to the yield stress, over time. This behaviour is indicative of CPM dispersions to have a short relaxation period and the elastic deformation rapidly relaxes into a new structure, thus resulting in little recovery overtime. Titanium dioxide dispersions also pose a similar behaviour to CPM dispersions, as observed by Uhlherr et al., (Uhlherr et al., 2005).

6.4.2.3 Influence of particle properties on yield stress

To further understand the influence of particle properties on yield stress behaviour, yield stress values have been obtained using the creep/recovery method and plotted as a function of particle volume fraction for highly active nuclear waste simulants and TiO_2 in DI water dispersions, illustrated in Figure 6.4-19.

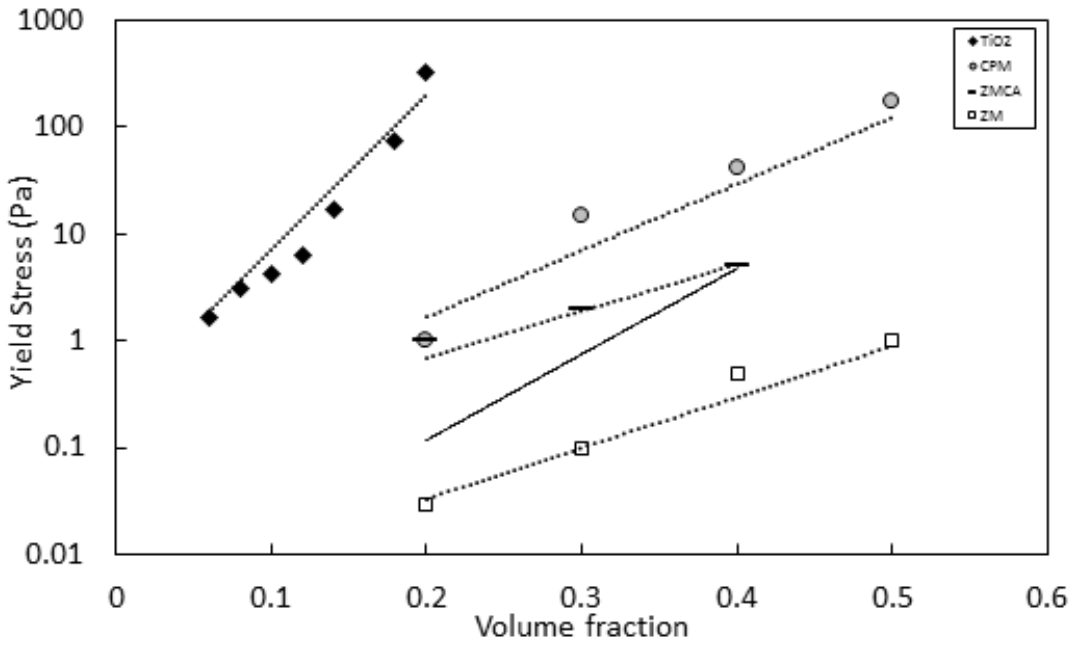

Figure 6.4-19 Yield stress data illustrating the influence of particle properties at varying particle concentrations of highly active nuclear waste simulants and TiO_2. All particulate systems are dispersed in DI water. The data represented are obtained using the Bohlin rheometer and V14 and C37 geometry.

To gain a clear understanding on the influence of particle properties on yield stress behaviour. The data in Figure 6.4-19 have been fitted to the Heymann et al (Heymann et al., 2002) their research discovers the dependency on volume fraction, where the yield stress increases with particle volume fraction. The relationship is described by Equation 6.4-7

$$\sigma_y = \sigma^* \left(\left(1 - \frac{\emptyset}{\emptyset_m} \right)^{-2} - 1 \right) \qquad 6.4\text{-}7$$

Where σ^* is a fitting parameter related to the yield stress at a given volume fraction and related to the size of the particles. Figure 6.4-19 represents experimental data fitted to equation 6.4-7, as proposed by Heymann et al (Heymann et al., 2002). The fitting parameter, σ^*, was treated as the only adjustable parameter and implemented $\emptyset_m$ values as stated in Table 26 (Section 6.4.1.2). Table 27 represents the key fitting parameter, related to the yield stress for TiO_2 and HAL dispersions.

Table 27 Model yield stress for suspensions of spheres and non-spherical particles using equation 6.4-7 as proposed by Heymann et al. (Heymann et al., 2002)

Particulate system	σ^* (Pa)	$\emptyset_m$	R^2
TiO_2	2.72	0.26	0.9551
CPM	1.50	0.55	0.9570
ZM	0.03	0.59	0.9808
ZMCA	0.033	0.37*	0.9985

*line of best-fit of equation 6.4-7 to the data with $\emptyset_m$ treated as a variable fitting parameter.

The fits obtained, presented in Table 27, delivers an excellent fit for spherical TiO_2 and CPM and for cubic ZM particles. Figure 6.4-19 illustrates two lines of best fit; (i) dotted line representing a maximum packing fraction of 37% and (ii) solid line representing a maximum packing fraction of 72%. Initial theoretical fits, where $\emptyset_m = 0.72$ (from compressive yield stress calculations, Section 6.5), indicates the Heymann et al equation excludes the effect of particle aspect ratio on overall dispersion yield stress. This relationship is confirmed by the deviated line of best fit (solid line) from the ZMCA experimental data, as illustrated in Figure 6.4-19.

Heymann et al. consider in their study that the equation shows dependence of yield stress on particle aspect ratio, this is accounted for by the relationship between the particle aspect ratio and the maximum packing fraction (i.e. as the particle aspect ratio increases the maximum packing fraction decreases). In the case of this research, results indicate ZMCA with properties $\emptyset_m = 0.72, Ar = 6$ and CPM $\emptyset_m = 0.55, Ar = 1$. All though the yield stress data, where suspensions containing particles with high aspect ratio exhibit a negligible yield stress over low and intermediate particle volume fractions and suspensions of spherical particles develop a yield stress at higher concentrations, supports conclusions made from Heymann et al. and Muller et al. studies it does not however support the relationship proposed by the Heymann yield stress equation. As indicated by the fits in Figure 6.4-19, there is no systematic dependence on the trend relating the yield stress fitting parameter σ* to the particle aspect ratio, albeit a reasonable relationship was illustrated for spherical particles.

At a low initial volume fraction ($\emptyset_o = 0.06$), ZMCA beds form to a maximum packing fraction of 0.72 using the Lumisizer, this is where the cuboidal ZMCA particles ZMCA particles tend to settle with the dominant particle-axis perpendicular to the direction of flow and thus forming a flat packed bed of cuboidal particles. However, for high initial volume fractions, the ZMCA form a disordered gel network that would have a much lower maximum packing fraction, as illustrated in Figure 5.4-21.

Considering Figure 5.4-21 and the Heymann et al. fit in Figure 6.4-19, it may be assumed that the dotted line for ZMCA data corresponds well to a maximum disordered gel packing fraction of 0.37.

An interesting comparison of the viscosity data, where spherical particles have lower viscosity values than cuboidal ZMCA particles, however at the same initial particle volume fractions the yield stress is significantly lower for

cuboidal ZMCA systems. It may be assumed at relatively low particle volume fractions, the elongated particle network is able to accommodate elastic stress to a greater extent than spherical particles at low volume fractions. Thus, the Heynmann yield stress equation does not substantiate the effect initial particle volume fraction but also the dependence of particle aspect ratio on yield stress.

The fitting parameter is related to the density of the interparticle interactions and particle friction within the sample matrix. Therefore, from the data illustrated in figure 6.4-19 it can be assumed that the yield stress is more dependent on the size of the particle rather than the aspect ratio. Heymann et al suggests for spherical suspensions that the there is an inverse relationship between particle size and σ^*, this indicates the higher yield stress for spherical particles, at a given volume fraction, is higher than for particles with varying aspect ratio. The relationship was supported by the experimental data, in particular spherical systems of TiO_2 and CPM illustrate significantly higher yield stress values, compared to the non-spherical cubic and cuboidal ZM and ZMCA systems, also supported by (Heymann et al., 2002, Mueller et al., 2009). The microstructural change of particulate systems considers the separation distance between neighbouring particles, this decreases with increasing volume fraction.

An approximation of the number of particles per unit volume has been calculated by using Equation 6.4-8

$$n = \frac{(6 \times M) \times 10^{12}}{\rho_p \times \pi \times d^3} \qquad \text{6.4-8}$$

Equation 6.4-8 expresses the number of particles per mL which considers the mass of the particles (*M*) in g, the particle density (ρ_p) in g/mL and the particle diameter (*d*) in µm. The number of particles for TiO_2 and HAL dispersions are presented in Figure 6.4-20 as a function of varying particle volume fraction.

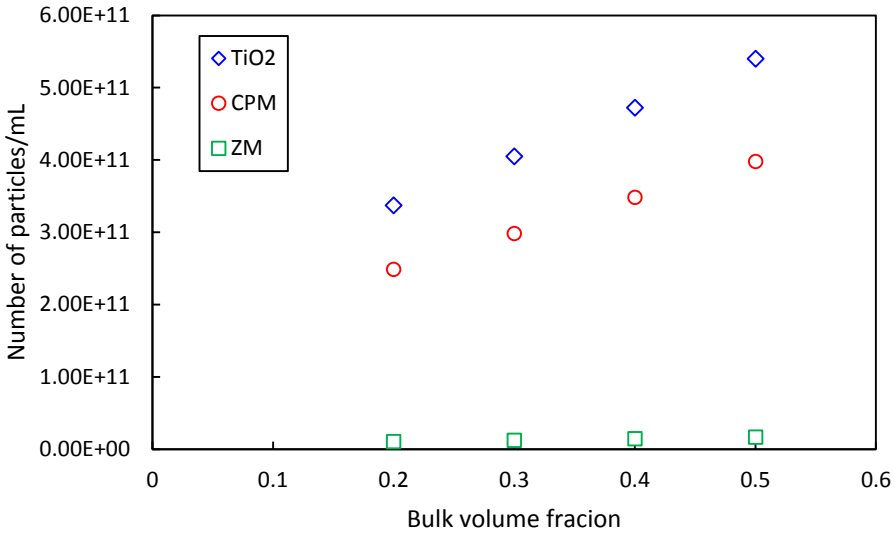

Figure 6.4-20 Illustrating data calculated number of particles per unit area and plotted as a function of particle volume fraction for HAL and TiO_2 dispersions.

Figure 6.4-20 supports the assumption that higher yield stress values are exhibited for smaller spherical TiO_2 and CPM due to the increased density of interparticle interactions per unit volume. The number of particles within a ZM dispersion is an order of magnitude lower than that of TiO_2 and CPM. Thus indicating the fewer cubic ZM and elongated ZMCA particles occupy a greater volume compared to CPM particles at any given volume fraction, hence fewer interparticle interactions, hence lower yield stress. From the experimental data and good agreement in theoretical fit, it can be suggested that there is no systematic dependence on particle aspect ratio on yield stress behaviour. Maybe due to the variation of interparticle friction for ZMCA dispersions.

An interesting observation made from Figure 6.4-19, is the large increase in yield of TiO_2 dispersions compared to CPM dispersions. At low volume fractions, 14-20 vol%, TiO_2 dispersions exhibit high yield stress values. In contrast, the yield stress value of CPM dispersions at 20 vol% is almost negligible. The high yield stress values are related to the dispersions being at $pH_{pzc.}$ Research conducted is in good agreement with the data illustrated in Figure 6.4-19. The effect of surface chemistry, including isoelectric point and stability on the yield stress of zirconia, silica and titania dispersions have exhibited similar behaviours (Leong et al., 1991, Leong et al., 1993, Johnson et al., 2002, Chen and Russel, 1991, Franks, 2002). As the TiO_2 particles are dispersed in DI water, the particle have no net charge, due to the depletion of the EDL, the particle network collapses and the particles aggregate. Thus leading to a sample matrix densely populated with

interparticle interactions, hence large yield stress values. This data is consistent with the zeta potential measurements (Figure 3.4-16), reduced settling velocities (Figure 5.4-7) and increased viscosity data (Section 6.5.1).

6.4.2.4 Effect of electrolyte concentration

The influence of electrolyte concentration on particle bonding, as a function of particle volume fraction has been investigated. This is of great relevance to the nuclear industry, where POCO requires the implementation of water to clean out the residual material. As the HAL solids are currently dispersed in 2M HNO_3, the electrolyte concentration will significantly decreased when the HASTs are diluted with H_2O.

The electrolyte concentration is varied from 0.5-2M HNO_3. All data have been analysed and extracted from the creep/recovery method, obtained using the Bohlin C-VOR. The data is illustrated in Figure 6.4-22 for CPM and ZM dispersions.

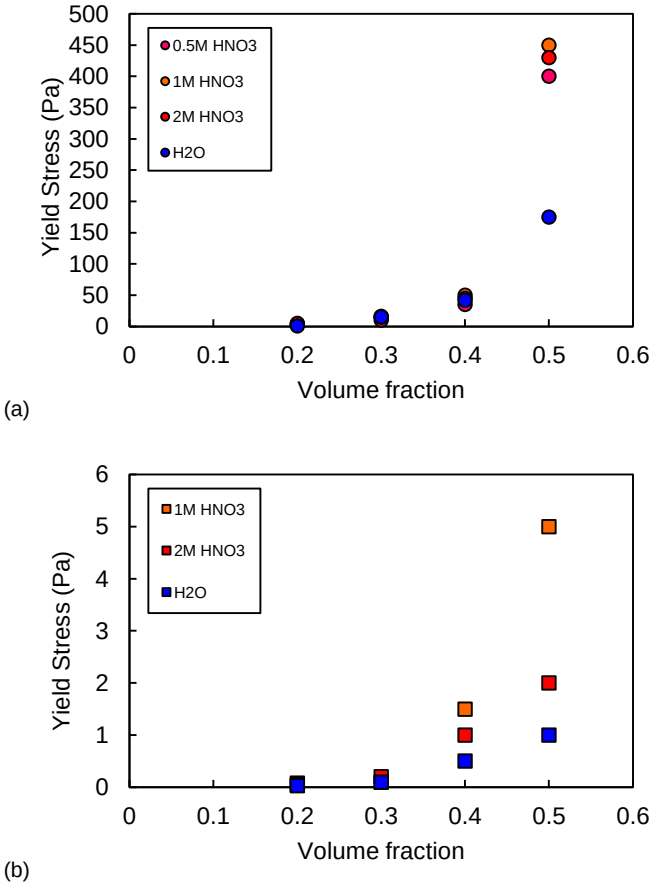

Figure 6.4-21 Yield stress data as a function of volume fraction for highly active nuclear waste simulants (a) CPM and (b) ZM. Data collected from Creep/creep recovery method using the Bohlin C-VOR.

Figure 6.4-21 illustrates the effect of salt concentration on CPM and ZM dispersions. The data illustrates an exponential increase with increasing

particle volume fractions, indicating the dependency on particle interactions. As the electrolyte concentration increases from 0-1M HNO_3 both illustrate a greater stress is required for full flow to occur at any given volume fraction, with increasing H^+ ions. The increase in H^+ concentration reduced the EDL which enhances the short range attractive forces causing particles to aggregate. The degree of aggregation increases with increasing H^+ ions, hence great yield stress values. Previous research carried out are in good agreement with the data presented in figure 6.4-20, where the relationship between the strength of particle bonding and shear yield stress was defined. The research indicates the greater the particle attraction the higher the yield stress required to initiate viscous flow properties (Scales et al., 1998, Nasser and James, 2006, Nasser and James, 2007).

Yield stress studies compares well to flow behaviour studies, Section 6.4.1, where CPM shows extreme yield stress change and a high degree of aggregation. ZM shows a small increase in YS, from limited increase in particle adhesion from electrolyte and then the same decrease at high concentration. A key difference between the flow behaviour and yield stress data above the gel-point and the settling studies below the gel-point the particles are already networked strongly together in a bed during yield stress measurements. Hence if the electrolyte concentration slightly increases the adhesion force is prominent in YS measurements than in suspension settling studies if aggregation is minor (in the case of ZM).

6.4.2.5 Influence of particle properties on yield stress of sediment bed

Further investigation on the bed structure is required, the rheological parameter, yield stress, can determine the stress required in order for full flow of the solids to occur upon consolidation. It is possible to determine the consolidation behaviour of the highly active nuclear waste simulants by determining the equilibrium height of the final sediment bed, from the sedimentation data. Yield stress data have been obtained for the sediment bed volume fraction for each particulate system. The initial volume fraction for the dispersions is 6 vol%.

Based on the values calculated in Figure 5.4-18, Section 5.4.24, dispersions of highly active nuclear waste simulants with respect to the volume fractions calculated under went yield stress analysis. The values indicate higher yield stress values for cubic ZMCA, compared to spherical CPM dispersions. This

hypothesis is tested and supported by yield stress measurements extracted from the creep/recovery method, illustrated in Figure 6.4-22.

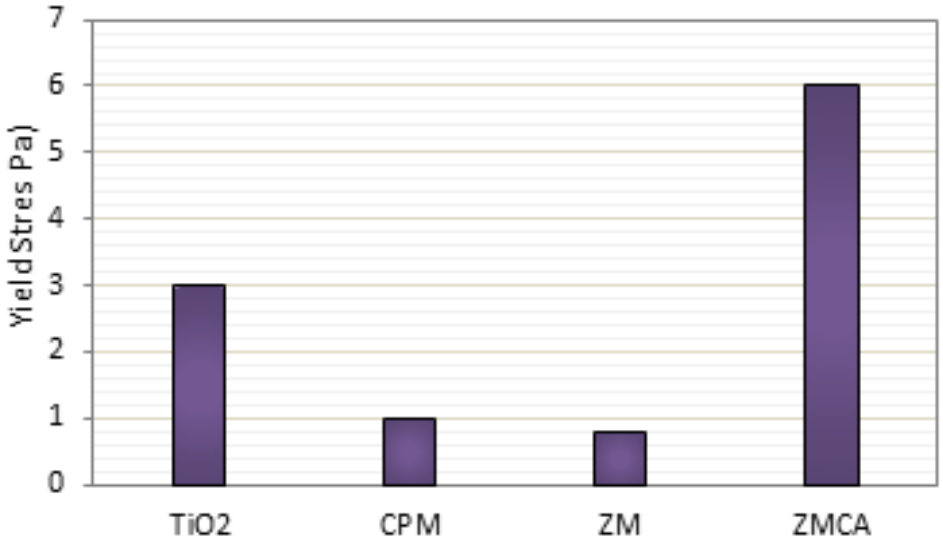

Figure 6.4-22 Yield stress data obtained using the creep/recovery method using the Bohlin C-VOR. Yield stress data of highly active nuclear waste simulants and TIO_2 dispersions, as a function of sediment bed volume fraction, initial volume fraction is 6 vol%.

Upon gravitational sedimentation, the particle volume fraction in the ZMCA sediment is much higher compared to CPM. From the yield stress data in Figure 6.4-22, this suggests that the energy required to re-suspend ZMCA solids will be 5 times higher than that of the CPM solids, with the same initial volume fraction. It can be assumed that the particles in the ZMCA settled bed have more contact points with other particles and create more inter-particle forces and thus more energy is required to break the structure of the bed. Based on the equilibrium height and volume fraction calculation, it can be assumed the ZMCA particles sediment into a flat packed bed, where face-to-face contact of the dominant particle axis. In the case of CPM the lower volume value suggests that the particles are further apart from each other, resulting in few inter-particle forces and therefore lower energy is required to re-suspend these solids.

Higher yield stress values for TiO_2 dispersions are related to the increased interparticle interactions due to aggregations, compared to CPM dispersions. It is expected for ZM dispersions to exhibit a higher sediment volume fraction and thus a higher yield stress than the values illustrated in Figure 5.4-18, Section 5.4.24 and Figure 6.4-22. The bulky cubic nature forms a stacked bed, compared to CPM and ZMCA dispersions, the number of interparticle forces are lower in a given unit volume. This results in reduced yield stress values. It is possible the underestimation of the yield stress and sediment volume fraction is due to the incomplete settling of the polydispersed

systems under gravitational conditions, thus neglecting the influence of the finer particles.

6.4.3 Compressive yield stress

Compressive yield stress measurements have been carried out using the Lumisizer. This enables analysis of the compressive behaviour of the sediment bed with an applied centrifugal force. Increasing centrifugal force is applied to the sediment bed, the change in sediment height as function of time is observed until no further collapse is possible. Compressive behaviour is illustrated in Figure 6.4-23 of the highly active nuclear waste simulants.

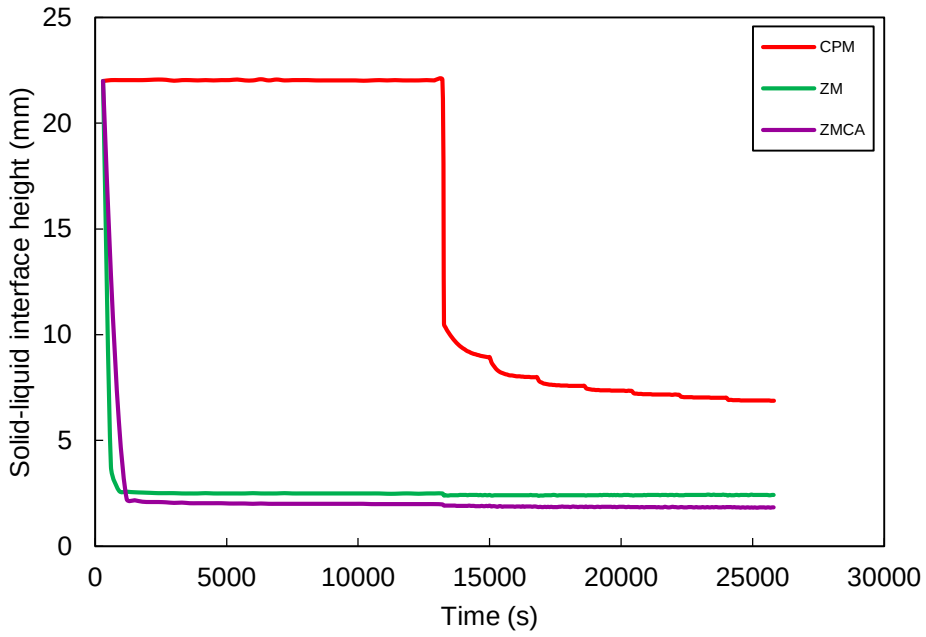

Figure 6.4-23 Effect of particle properties on the compression of sediment height of $\phi = 0.06$ highly active nuclear waste simulant dispersions (a) CPM, (b) ZM and (c) ZMCA. The vertical lines indicate the increase in centrifugal force as a function of time.

Figure 6.4-23 illustrates progressive compression with increasing applied centrifugal force of CPM dispersions. In contrast, both ZM and ZMCA systems are illustrated as incompressible. The aggregated CPM systems sediment into an open voluminous bed, once the progressive force is applied fluid is excluded from the aggregate voids. Compared to the ZM and ZMCA systems, which sediment into a densely packed bed due to their bulky nature. This is further supported by the calculation of the equilibrium height at increasing increments of centrifugal force, illustrated in Figure 6.4-24.

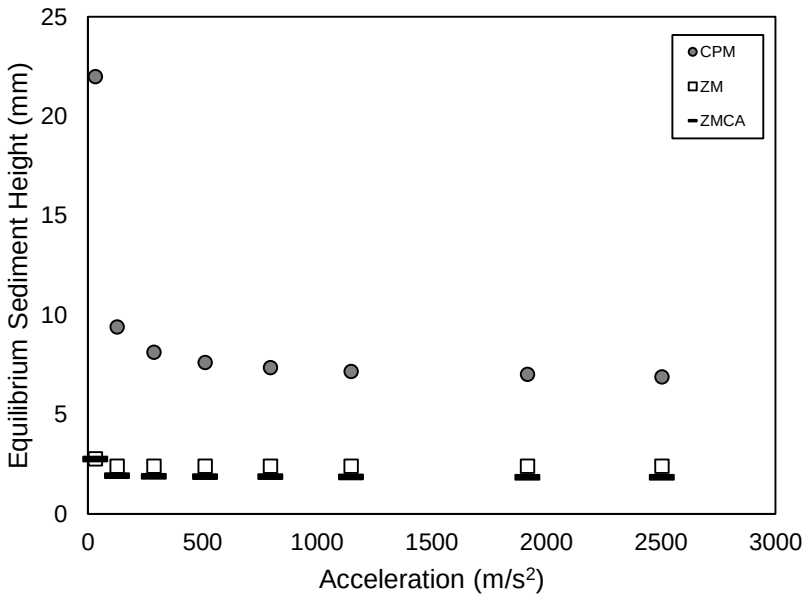

Figure 6.4-24 Equilibrium sediment height as a function of acceleration for 6 vol% highly active nuclear waste simulant dispersions.

Figure 6.4-24 illustrates the equilibrium height remains constant for ZM and ZMCA systems, irrespective of increased accelerations. This indicates the formation of a close packed bed of cubic and cuboidal particles, where the equilibrium height for ZM higher due to a more bulky morphology compared to ZMCA. In contrast to CPM where the equilibrium height rapidly decreases at low applied centrifugal force, until a plateau is achieved at high acceleration. Upon sedimentation aggregate structures of CPM create an open bed with larger irregular interparticle spacing, leading to a larger compressive behaviour compared to ZM and ZMCA.

Figure 6.4-24, also illustrates the significant decrease in height from the initial state to the final equilibrium height at the maximum acceleration for CPM Δh = 15 mm, ZM Δh = 19.5 mm and for ZMCA Δh = 21 mm. Due to the aggregated nature of CPM the distance of the travelled interface is lower.

The equilibrium volume fraction and the compressive yield stress at each increasing acceleration profile can be extracted and calculated using the Equations 6.3-18 and 6.3-19 mentioned in Section 6.3.4. Figure 6.4-25 illustrates the compression of the highly active nuclear waste simulant particle networks.

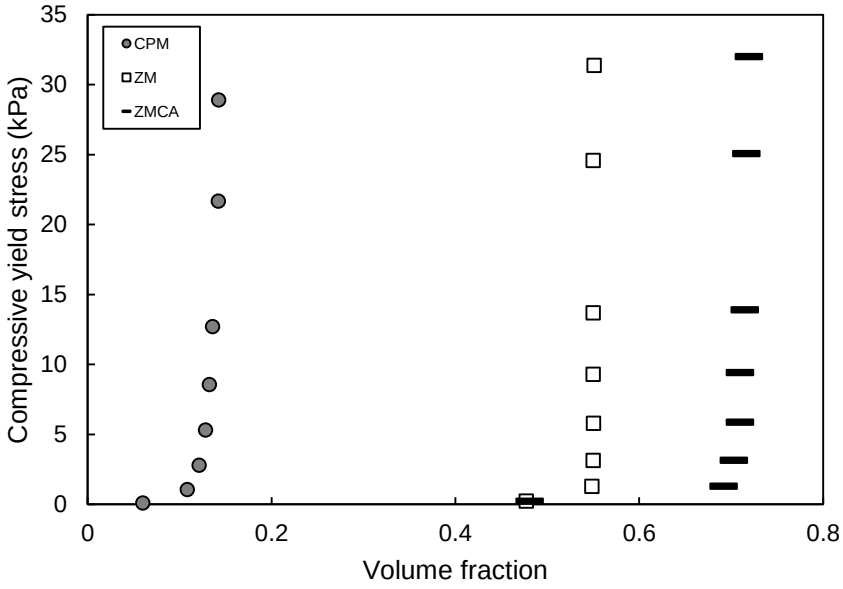

Figure 6.4-25 Compressive yield stress curves derived from volume fraction profiles for highly active nuclear waste simulants. The data represent the compressive yield stress $P_y(\phi_{eq})$ as a function of volume fraction of particle dispersion.

Figure 6.4-25 illustrates the compressive yield stress at equilibrium as a function of particle dispersion volume fraction. The data illustrates that CPM dispersions are more challenging to compress, compared to ZM and ZMCA. CPM dispersions require an increasing amount of compressive steps, where continuous reduction in sediment bed height is observed until equilibrium is attained. In contrast to ZM and ZMCA dispersions, this illustrates incompressibility.

Additionally, Figure 6.4-25 illustrates the compressive yield stress to be higher for ZMCA and ZM dispersions, indicating increase in compressive yield with increasing aspect ratio. CPM dispersions initially formed a low packed dense bed ($\emptyset_m = \sim 0.14$) at lower applied force, which leads to a lower overall compression at higher applied force. This is a result of the irregular interparticle spacing and a decrease in particle size, where fluid exclusion becomes complex. In contrast, ZM and ZMCA are non-aggregated systems (see Chapter 5) which tend to pack in ordered structure and to a highly dense bed, $\emptyset_m = \sim 0.55$ for ZM systems and $\emptyset_m = \sim 0.72$for ZMCA systems, upon a reduced application of a centrifugal force. Upon compression the particle network becomes stronger as sediment bed density and the stored elastic strain increases as a function of bulk volume fraction. It is suggested, therefore, that ZMCA, compromised of non aggregated particulate systems with an aspect ratio of ~6, has the ability to accommodate a higher elastic strain under lateral compressive stress, compared to CPM.

This study suggests that compressive stress is dependent on the microstructure of the particle suspension, where the bond strength and number is dependent on particle properties such as size, shape and volume fraction. Comparing the HAL suspension it maybe suggested the compressive yield stress behaviour is dominated by particle morphology. Buscal, Leong and Miller et al, however found, for alumina, zirconia and kaolin dispersions the increase in compressive yield stress is due to a decrease in particle size (Buscall and White, 1987, Miller et al., 1996).

Calculated packed bed volume fraction, under gravitational force, Chapter 3 show to be considerably lower than the volume fraction of sediment bed under applied centrifugal force, illustrated in Figure 6.4-25. This is to be expected, due to the application of accelerated force and in the case of ZM and ZMCA systems, the neglect of the submicron particles. Compressive yield stress measurements are 3-4 orders of magnitude higher than the shear yield values (Figure 6.4-22), suggesting the particle networks are weaker in shear than in compression and is supported by several studies (Buscall and White, 1987, Zhou et al., 1999, Nasser and James, 2008, Channell and Zukoski, 1997). Thus, the forces required to shear apart the consolidated bed is much less than to compress the HAL particulate bed.

6.5 Conclusions

The key findings of this chapter indicates the importance of rheological technique development to obtain reliable flow behaviour data. Once the technique was established the influence of solid-liquid properties were identified. Fundamental assumptions required for rheological analysis include, cylindrical flow around the vane blades, elimination of particle migration, appropriate viscometer gap (particle size << gap), selection of C37 and V14 geometry to eliminate wall slip effects for all dispersions at high volume fractions (i.e. above the gel-point). Implementation of the concepts enabled valid comparisons between each particulate systems to be made.

Key rheological data indicates that the suspension rheology of highly active nuclear waste simulants is a complex function of a number of physical properties

- Particle properties such as size and shape indicates flow behaviour is greatly influenced by non-spherical particles, the greater the deviation from a spherical particle the greater the influence. Direct effect of

shape on flow behaviour indicates the cuboidal ZMCA particles have a dominant influence of the viscosity of the suspension, compared to ZM particles.

- Particle volume fraction influences the behaviour of interactions. In dilute suspensions particle interactions are rare, semi-dilute regions hydrodynamic interactions are dominant and in concentrated regions particle-particle interactions become important.
- Continuous-phase electrolyte concentration alters the spatial arrangement of the particles in suspensions. Addition of background electrolyte reduces the particle-particle distance due to the depletion of the electrostatic potential barrier leading to aggregation of particles. Spherical dispersions with a particle size ≤ 1 µm, such as TiO_2 and CPM exhibited greater yield stress values than larger non-spherical ZM and ZMCA dispersions.
- Aggregating mechanism, this is influenced by the particle size and morphology. CPM aggregates form almost spherical aggregates, in contrast at high electrolyte concentration the ZMCA particles aggregates with respect to the dominant particle-axis producing sheets which align themselves in the direction of flow, reducing the viscosity.
- Bulk flow field is a function of particle morphology. The local flow around non-spherical ZMCA particles is complex compared to spherical CPM particles, thus a difference in contribution to the suspension viscosity. Change in orientation of ZMCA particles contributes to the increase in suspension viscosity. For any given volume fraction, ZMCA dispersions have a greater degree of inter-particle interactions than ZM and CPM particles, thus greater suspension viscosity.

Relating the data to process issues such as transportation and long-term storage of the waste, it is suggested that increase in particle aspect ratio, electrolyte concentration, particle volume fraction and a reduction in particle size enhance suspension viscosity.

The rheological data indicate a change in medium affects the flow behaviour of the particle suspension. Newtonian behaviour is exhibited when particles are dispersed in water and non-Newtonian behaviour is exhibited with particles are dispersed in nitric acid. Furthermore, rheological behaviour is affected by the agitation system employed and therefore during the

transportation and emptying of the tanks the agitation system employed must be tailored to the behaviour of the solids.

In terms of storage the HAL solids are kept in nitric acid where the jet ballasts will provide re-suspension and agitation, the particles will have endured stress, the rheological data suggests that the suspension will endure shear-thinning behaviour where agitation will reduce the viscosity of the waste within the storage tanks. The energy required to keep the particles in suspension is greatly influenced by particle properties. The application of rheological behaviours to the current storage, transportation and immobilisation of the highly active nuclear waste can be determined. The HAS tanks store the waste in controlled agitation conditions, airlifts and jetballasts. Taking into account the results of this study, the agitation systems will need to be tailored to the diverse flow profiles of the HAL particulate systems.

Manipulation of particle morphology by addition of an organic additive increases the aspect ratio of ZM systems, producing ZMCA particles. This has desirable effects for transportation through pipes, decreasing the chances of deposition to occur in pipes and thus eliminating corrosion of pipe lines through a decrease in blockages. However, the particles indicate under shearing conditions that they are more difficult to handle, compared to the cubic ZM dispersions.

Resuspension of the settled bed of HAL solids is greatly governed by the particle properties and the structure of particle network. The shear-yield stress is directly linked o the particle separation and electrophoretic mobility. As indicates by TiO_2 dispersions the maximum yield stress is exhibited when the dispersion naturally buffers at $pH_{pzc}=5.5$, where the short range van der Waals forces exceed the long range electrostatic forces. Additionally the yield stress is dominated by the increased number of interparticle forces per unit volume, as illustrated by CPM dispersions compared to ZM dispersions. Compressive yield stress analysis enables an understanding of how the bed compacts upon sedimentation. This indicates CPM particles would require less energy to re-suspend, compared to the cubic ZM particles, post consolidation. Ultimately, this research aims to convey that particle and dispersion characterisation, understanding the influences of the solid-liquid properties on sedimentation and rheology, are key parameters which link directly to the improvement of the nuclear waste treatment engineering process..

7 Conclusions & recommendations for future work

Summary

This chapter highlights key findings of the thesis. The influence of particle morphology on behaviours such as sedimentation and rheology, which link directly to HAL nuclear waste processing will be discussed. Further recommendations will also be discussed.

7.1 Conclusions

It is evident that particle properties do have an influence on behaviours such as sedimentation and rheology. The application of these behaviours to the current storage, transportation and immobilisation of the highly active nuclear waste can be determined. The HASTs store the waste in controlled agitation conditions, airlifts and jet ballasts. Taking into account the results of this study, the agitation systems will need to be tailored to the diverse sedimentation profiles of the particulate systems.

The reaction precipitation method, mentioned in Chapter 3, enabled the production of spheroidal CPM (Figure 3.4-1), cubic ZM (Figure 3.4-3) and cuboidal ZMCA (Figure 3.4-10) particles. The addition of an organic additive, citric acid, during ZM synthesis produces a citratomolybdate complex which is responsible for particle morphology modification. Morphological prediction using computational molecular modelling techniques revealed growth inhibition of the {2 0 0}, {-2 0 0}, {0 2 0} and {0 -2 0} faces, due to greater number of Zr sites for citratomolybdate complex affiliation, illustrated in Figure 4.5-32. The growth of the {0 0 4} and {0 0 -4} in the [0 0 1] and [0 0 -1] direction, along the c-axis continued and produced cuboidal ZMCA. Initial ZMCA synthesis, implementation of Method 1 (Section 3.4.5), produced poor yield ~ 30%. However, control of process parameters such as increasing the flow rate to 3.34 mL/min, modifying additive induction time ($t = 30\ mins$) and addition of a particle washing step, using AC, enabled the production of high yield of 70% for a reaction time of 5 days, Method 2 (Section 3.4.6).

Distinct particle properties were established for CPM, ZM and ZMCA and compared to a common oxide particle material titanium dioxide (TiO_2). Mean particle size of 0.69 µm, 1.13 µm, 2.31 µm, and 3.11 µm for CPM, TiO_2, ZM and ZMCA, respectively. As this technique assumes all particle systems are perfect spheres, the sizes are reported as volume equivalent sphere diameter, SEM image analysis technique was used to approximate the mean particle size (averaged over 100 particles) for ZM and ZMCA particulate systems. PSD results demonstrated the mean particle size between 3-4 µm for both systems, illustrated in Figure 3.4-15. A highlight of this research was the development of ZMCA particles, this enabled the direct effect of shape, where ZM and ZMCA particles exhibited similar PSD, density and chemical structure (Figure 3.4-18), to be explored on sedimentation and rheological behaviours.

Zeta potential measurements, Figure 3.4-16, highlight key effects caused by changes in pH; at low pH values the system is dominated by repulsive forces

resulting in large positive values, as the pH values increases the magnitude of surface charge is reduced and the zeta potential reaches pH_{pzc} (where the system is dominated by attractive forces) at pH 5 for TiO_2 and pH 4 for ZM systems, at higher pH values the charge reverses to negative values. A fundamental outcome of the zeta potential measurements demonstrated TiO_2-H_2O dispersions buffer at pH_{pzc}, thus the system is highly aggregated.

The microstructure of a particle network is governed by the particle properties such as the size, shape, density and surface charge and bulk liquid properties such as electrolyte concentration and pH. This research has focused on comparative studies between each particulate systems on physical behaviours, sedimentation and rheology, and thus provides microstructural explanations of the observations. It is the physical behaviours, dependant on solid-liquid properties, which contributes to the process engineering design of the nuclear waste treatment, as illustrated in Figure 7.1-1.

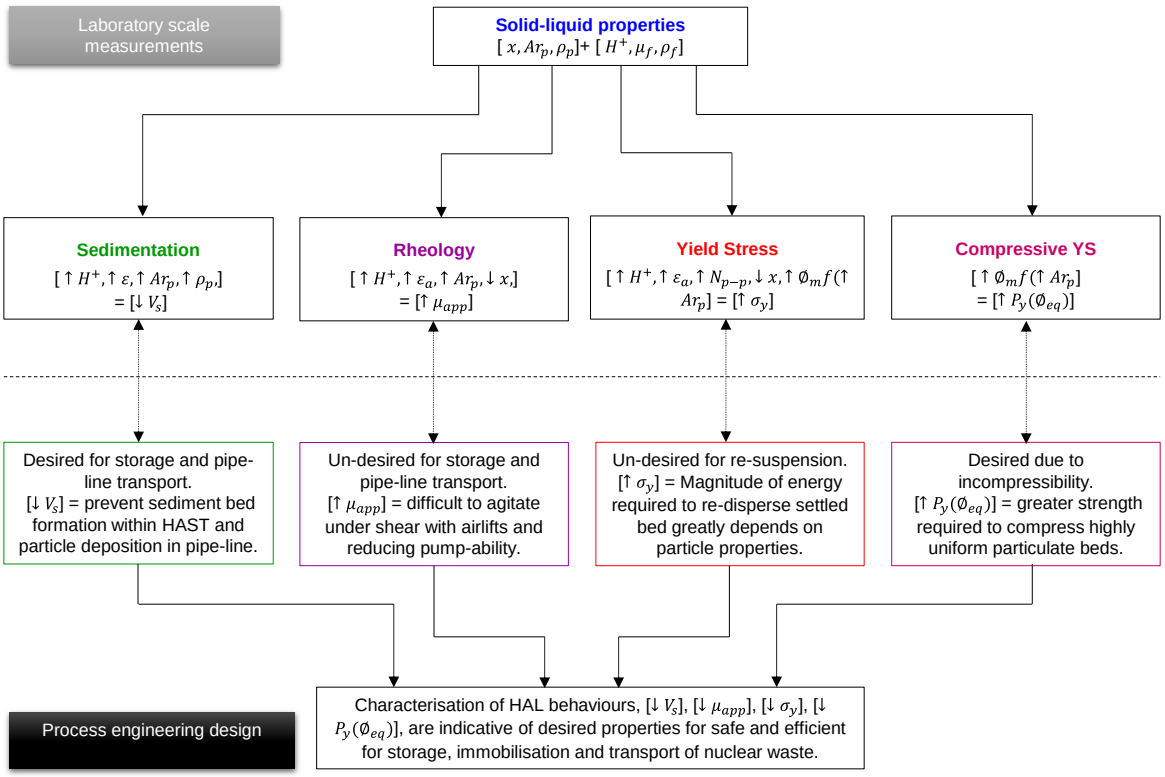

Figure 7.1-1 Flow diagram representing the studies carried out in this thesis and the possible consequences of the outcome on designing engineering facilities for nuclear waste management.

Sedimentation behaviour was characterised by a linearised R-Z model, proposed by Whitman and Maude, 1958. The fitting parameter, *n*, considers the particle size and shape on settling behaviours as a function of ϕ and thus yielded a relationship spheroidal > cubic > cuboidal, Figure 5.4-7. Where the large value of $n = 52$ for TiO_2-H_2O dispersions are due to the highly

aggregated nature of TiO_2 particles. In contrast, CPM ($n = 39$) particles indicated a less aggregated network and high density, which dominated the settling properties. Comparing ZM and ZMCA systems where $n = 10$ and $n = 14$, thus indicating the influence of increased aspect ratio of the ZMCA particles. ZMCA particles oscillate during sedimentation to achieve an equilibrium position, the rapid movement of the particles increase the drag flow acting on the particles and thus a reduction in settling properties. The addition of electrolyte (HNO_3) indicated increased V_s for TiO_2-HNO_3 and reduced V_s for CPM-HNO_3, reversed behaviour from H_2O dispersions, Figure 5.4-14. Thus indicating the aggregation network across the sample matrix reduces the extent to which fluid is excluded and results in reduced settling velocities.

This has desirable effects for transportation through pipes by decreasing the rate of particle deposition and thus reducing the onset of pipeline blockages and ultimately, corrosion.

Rheological flow behaviour data was fitted to a simplified Cross model yielding two parameters *K* (related to viscosity) and *n* (extent of shear-thinning). Larger values of K, ranging from 0.98 to 173 as a function of volume fraction (0.2-0.5), for CPM-H_2O dispersions suggested the reduced particle diameter creates particle network with increased interparticle interactions per unit volume, when compared to ZM-H_2O dispersions ($0.023 - 14.046$). Additionally, ZMCA expressed larger *K* values ranging from 0.63 to 75 as function of volume fraction (0.2-0.4), compared to ZM, thus indicating the influence of increased aspect ratio on flow behaviour. To further establish the influence of particle properties on viscosity, the dependency of viscosity on particle volume fraction was characterised using the Krieger-Dougherty model, yielding a relationship, cuboidal > sphere > cube. The fitting parameter [μ] (particle's contribution to suspension viscosity) indicated TiO_2 to have extremely large value of 23, related to the high degree of aggregation due to the dispersion located at pH_{pzc}, consistent with the reduced V_s in Chapter 5. For ZMCA systems exhibit $[\mu] = 19$, in contrast to ZM where $[\mu] = 8$. Particles of high aspect ratio rotate more rapidly as the tumble 'end over end' in shearing flow than spherical or cubic particles, therefore their approach velocity is much higher and hence leading to greater energy dissipated into the system and greater contribution to the suspension viscosity.

The effect of electrolyte concentration ranging from 0.5 M to 2 M HNO_3 was also investigated, Figure 6.5-9. The results indicated the presence of short range repulsive forces at ≥ 2 M HNO_3 for ZM dispersions. ZMCA particles aggregates with respect to the dominant particle-axis producing sheets which align themselves in the direction of flow, reducing the viscosity in contrast to ZMCA-H_2O dispersions.

The yield stress was characterised using an empirical model derived by Heymann et al (2002) yielding a fitting parameter σ^* (cognate to particle shape and size) and demonstrating a relationship, sphere > cuboidal > cubic. The data delivered a good fit to the experimental data for spheroidal TiO_2 and cubic ZM with σ^*giving a range 2.72-0.03 Pa. However, there was no evidence of a systematic dependence on particle aspect ratio, where the line of best by also considering the $\emptyset_m$ to be a fitting parameter and yielding a value of 0.37 for ZMCA systems. Thus concluding the value of σ^* is related to the number of interparticle interactions, Figure 6.5-20, which is governed by the size of the particle. The effect of increased electrolyte concentration also increase the yield stress of the dispersion.

The shear yield stress of a sediment created under gravitational force demonstrated the relationship cuboidal ($\emptyset_m = 0.42$) > sphere ($\emptyset_m = 0.11$) > cube ($\emptyset_m = 0.18$). Characterisation of compressive yield stress demonstrated the relationship, cuboidal ($\emptyset_m = 0.72$) > cubic ($\emptyset_m = 0.56$) > sphere ($\emptyset_m = 0.18$). Shear and compressive yield stress studies showed the maximum compressive stress to be orders of magnitude higher than shear yield stress. Thus indicating the strength required to compress the particle bed is greater than to shear the beds apart.

Resuspension of the settled bed of HAL solids is greatly governed by the particle properties. Sediment bed analysis enables an understanding of how the bed compacts upon sedimentation. This indicates CPM particles would require less energy to re-suspend, compared to the cubic ZM particles.

Ultimately, this research aims to convey that particle and dispersion characterisation, understanding the influences of the solid-liquid properties on sedimentation and rheology, are key parameters which link directly to the improvement of the nuclear waste treatment engineering process.

7.2 Recommendations for future work

The research presented in this thesis has provided fundamental understanding on the characterisation of two HAL solids, CPM and ZM.

Further interests resulted in morphological manipulation of ZM particles to ZMCA particles, which has the potential for advantageous nuclear waste processing. This research offers a reference point for expansion on future work to further understand HAL dispersions.

This research has focused on the synthesis of CPM, ZM and ZMCA where reaction steps have been proposed based on the stoichiometric chemistry. Further work could expand on understanding the crystallisation kinetics of HAL crystals. Methods include determining the nucleation kinetics and obtain the number of nuclei formed per unit volume, using the classical theory of nucleation (Horwitz et al., Volmer and Weber, 1926) determining the supersaturation ratio, this ultimately characterises the chemical driving force of the reaction using the equation devised by Sohnel et al., (Söhnel and Garside, 1992) measurement of crystal growth rate where is it possible to measure the average mass growth rate by considering the global mass increase of all crystals present (Boistelle and Astier, 1988). An alternative method for crystal growth rate measurement includes Quartz crystal microbalance (QCM) to measure the mass variation. The determination of key crystallisation kinetics will not only control particle size during synthesis but will be able to predict a possible scenario for bulk and surface crystallisation. This is fundamental to understand issues related to pipeline transport, where particle deposition creates a sediment layer and secondary nucleation initiates crystal growth, which in turn leads to blockages and pipeline corrosion and scale.

Morphological manipulation, with and organic additive, was considered in this thesis and led to the production of cuboidal particles. The HAL solids have been stored on tanks since the 1950's, it is unknown how, if at all, the particle morphology has changed over the years. Therefore, it is proposed to carry out further morphological manipulation studies to create an unusual particle shape. This can therefore contribute to developing model to describe the best and worst case scenario for the nuclear waste treatment process.

A challenge presented in this thesis was to develop a chemical model for quantitative analysis of hydrated ZM morphological prediction. Development from this work enables opportunities to predict the morphology for the ZMH structure. The locations of the water and hydroxyl groups need to be clearly defined for lattice energy optimisation and the morphological prediction using the surface and attachment energy models. A technique proposed, to locate and differentiate between the H_2O and –OH structures, is neutron scattering. This technique uses neutron sources to accurately locate the position of

hydrogen atoms, and differentiate between water the H_2O and –OH structures, where shorter bond lengths are indicative of the H_2O molecules. It is important to understand the possible mechanisms of radionuclei adsorption which can ultimately to lead morphological change. Change in morphology impacts process plant operations and therefore it is necessary to define the change in crystal chemistry for current processing and POCO of highly active nuclear waste.

Characterisation of individual HAL particulate dispersions were characterised in this research. There is clear indication that particle interactions determine the particle network which in turn influences the dispersion behaviour. The HASTs contain five precipitated solids, therefore it is suggested behavioural studies are continued for mixed systems. Additionally, simulated solutions containing other chemical components (i.e. ion concentration) should be used as the suspending fluid for mixed systems, as represented in this thesis surface charge is greatly influence by electrolyte concentration and pH. Therefore, further work implementing a range of salts, salts concentration and divalent salts should be considered to better understand the complex adsorption mechanisms onto CPM, ZM and ZMCA particles. Further to mixed system studies, temperature dependant studies should be considered and thus understand thermodynamic contribution to the behaviour of HAL. By considering mixed HAL solid systems, simulated suspending fluid containing a range of ions and temperature effects, this will lead to characterisation of HAL dispersions which ultimately represent the HAL waste stored in the HASTs.

There is a distinct link between surface charge characterisation and their resulting aggregation behaviour, which in turn affects the dispersion sedimentation and rheological behaviour. It would be of further interest to determine the contributing forces, in particular in the case of CPM particles where the zeta potential is zero at any given pH. A technique proposed for this is the Atomic force microscopy (AFM) (Binnig et al., 1986), this technique has the ability to measure the van der Waals and electrostatic forces and specific chemical bonding. This technique will also be able to confirm, if any, the presence of short range repulsive forces for ZM systems at 2 M HNO_3.

All experimental data represented in this thesis have been carried out on a laboratory scale. As the HASTs have a working capacity of ~140 m^3, it is of great interest to scale-up the measurements using HAL dispersions. Ultimately, the aim would be to consider scaling up the measurements to the

60 m^3 tank, located in Workington, UK. Initial measurements would consider individual HAL particulate systems, to compare with this study (on a laboratory scale), where further studies will include mixed systems. *In-situ* measurement techniques are required to characterise the behaviour. A proposed technique for sedimentation characterisation is the acoustic backscatter (ABS), mentioned in Chapter 5, Section 5.2.4. The basic principle of ABS requires a transducer to propagate short pulses of acoustic energy through a system, in the case a dispersion of barium sulphate in water. The acoustic energy is able to scatter once the material is detected; this is recorded by the receiver located in the transducer. Key parameters are required for the characterisation of the suspended material such as, the speed of sound in water, scattering properties of the suspended material and the sound propagation characteristics. The backscattered data therefore enables analysis of solids concentration and sediment bed depths.

Reference

AL-NAAFA, M. A. & SELIM, M. S. 1992. Sedimentation of monodisperse and bidisperse hard-sphere colloidal suspensions. *AIChE Journal,* 38**,** 1618-1630.

ALCOCK, N. W., DUDEK, M., GRYBOS, R., HODOROWICZ, E., KANAS, A. & SAMOTUS, A. 1990. Complexation between molybdenum(VI) and citrate: structural characterisation of a tetrameric complex, K4[(MoO2)4O3(cit)2][middle dot]6H2O. *Journal of the Chemical Society, Dalton Transactions***,** 707-711.

ALLAIN, C., CLOITRE, M. & WAFRA, M. 1995. Aggregation and Sedimentation in Colloidal Suspensions. *Physical Review Letters,* 74**,** 1478-1481.

ALLEN, S. & EVANS, J. 2003. Negative thermal expansion and oxygen disorder in cubic ZrMo 2 O 8. *Physical Review B,* 68**,** 134101.

AMBLER, C. 1961. Theory of Centrifugation. *Industrial & Engineering Chemistry,* 53**,** 430-433.

ANNABLE, T., BUSCALL, R., ETTELAIE, R. & WHITTLESTONE, D. 1993. The rheology of solutions of associating polymers: Comparison of experimental behavior with transient network theory. *Journal of Rheology (1978),* 37**,** 695-726.

AURAY, M. Q., M.; TARTE, P. 1986. New structure of high-temperature zirconium molybdate. *Acta Crystallogr., Sect. C: Cryst. Struct. Commun.,* 42**,** 257-259.

BADAWY, A. M. E., LUXTON, T. P., SILVA, R. G., SCHECKEL, K. G., SUIDAN, M. T. & TOLAYMAT, T. M. 2010. Impact of Environmental Conditions (pH, Ionic Strength, and Electrolyte Type) on the Surface Charge and Aggregation of Silver Nanoparticles Suspensions. *Environmental Science & Technology,* 44**,** 1260-1266.

BAGLEY, E. B. 1957. End Corrections in the Capillary Flow of Polyethylene. *Journal of Applied Physics,* 28**,** 624-627.

BANDYOPADHYAY, R. & GRANT, D. J. 2000. Influence of crystal habit on the surface free energy and interparticulate bonding of L-lysine monohydrochloride dihydrate. *Pharmaceutical development and technology,* 5**,** 27-37.

BARNES, H. & WALTERS, K. 1985. The yield stress myth? *Rheologica Acta,* 24**,** 323-326.

BARNES, H. A. 1995. A review of the slip (wall depletion) of polymer solutions, emulsions and particle suspensions in viscometers: its cause, character, and cure. *Journal of Non-Newtonian Fluid Mechanics,* 56**,** 221-251.

BARNES, H. A. 1997. Thixotropy—a review. *Journal of Non-Newtonian Fluid Mechanics,* 70**,** 1-33.

BARNES, H. A. 2000. *A Handbook of Elementary Rheology*, University of Wales, Institute of Non-Newtonian Fluid Mechanics.

BARNES, H. A. & CARNALI, J. O. 1990. The vane-in-cup as a novel rheometer geometry for shear thinning and thixotropic materials. *Journal of Rheology (1978),* 34**,** 841-866.

BARNES, H. A., HUTTON, J. F. & WALTERS, K. 1989. *An Introduction to Rheology*, Elsevier.

BARNES, H. A. & NGUYEN, Q. D. 2001. Rotating vane rheometry—a review. *Journal of Non-Newtonian Fluid Mechanics,* 98**,** 1-14.

BARTLETT, P., TEECE, L. J. & FAERS, M. A. Sudden collapse of a colloidal gel. *Physical Review E,* 85**,** 021404.

BATCHELOR, G. 1972. Sedimentation in a dilute dispersion of spheres. *Journal of fluid mechanics,* 52**,** 245-268.

BATCHELOR, G. 1977. The effect of Brownian motion on the bulk stress in a suspension of spherical particles. *Journal of Fluid Mechanics,* 83**,** 97-117.

BATCHELOR, G. K. & WEN, C. S. 1982. Sedimentation in a dilute polydisperse system of interacting spheres. Part 2. Numerical results. *Journal of Fluid Mechanics,* 124**,** 495-528.

BECKER, H. A. 1959. The effects of shape and reynolds number on drag in the motion of a freely oriented body in an infinite fluid. *The Canadian Journal of Chemical Engineering,* 37**,** 85-91.

BEEN, K. & SILLS, G. 1981. Self-weight consolidation of soft soils: an experimental and theoretical study. *Geotechnique,* 31**,** 519-535.

BENNA, M., KBIR-ARIGUIB, N., MAGNIN, A. & BERGAYA, F. 1999. Effect of pH on rheological properties of purified sodium bentonite suspensions. *Journal of Colloid and Interface Science,* 218**,** 442-455.

BERNHARDT, C. 1994. *Particle Size Analysis: Classification and Sedimentation Techniques*, Chapman & Hall.

BEYCHOK, M. R. *Aqueous Wastes: From Petroleum and Petrochemical Plants*, Books on Demand.

BINDING, D. M. 1988. An approximate analysis for contraction and converging flows. *Journal of Non-Newtonian Fluid Mechanics,* 27**,** 173-189.

BINGHAM, E. C. 2007. *Fluidity and Plasticity*.

BINNIG, G., QUATE, C. F. & GERBER, C. 1986. Atomic force microscope. *Physical review letters,* 56**,** 930.

BLACHIER, C., JACQUET, A., MOSQUET, M., MICHOT, L. & BARAVIAN, C. 2014. Impact of clay mineral particle morphology on the rheological properties of dispersions: A combined X-ray scattering, transmission electronic microscopy and flow rheology study. *Applied Clay Science,* 87**,** 87-96.

BLAIR, G. W. S. 1958. The importance of the sigma phenomenon in the study of the flow of blood. *Rheologica Acta,* 1**,** 123-126.

BOHLIN, L., CARLSON, T.-G. & BÄCKSTRÖM, G. 1980. Cone-plate instrument for stress relaxation measurements. *Journal of Colloid and Interface Science,* 73**,** 61-65.

BOISTELLE, R. & ASTIER, J. 1988. Crystallization mechanisms in solution. *Journal of Crystal Growth,* 90**,** 14-30.

BOUYER, E., MEKHLOUFI, G., HUANG, N., ROSILIO, V. & AGNELY, F. 2013. β-Lactoglobulin, gum arabic, and xanthan gum for emulsifying sweet almond oil: formulation and stabilization mechanisms of pharmaceutical emulsions. *Colloids and Surfaces A: Physicochemical and Engineering Aspects,* 433**,** 77-87.

BRAGG, W. H. 1934. *The Crystalline State*, MacMillan Company, New York, USA.

BRAGG, W. H. & BRAGG, W. L. 1957. *The Crystalline State: The determination of crystal structures, by H. Lipson and W. Cochran*, G. Bell and Sons Limited.

BRAVAIS, A. 1866. *Etudes Cristallographiques (Paris: Gauthier Villars)*.

BRISCOE, B. J., KHAN, A. U. & LUCKHAM, P. F. 1998. Stabilising zirconia aqueous suspensions using commercial polyvalent electrolyte solutions. *Journal of the European Ceramic Society,* 18**,** 2169-2173.

BROWN, L. & ZUKOSKI, C. 2003. Experimental tests of two-phase fluid model of drying consolidation. *AIChE journal,* 49**,** 362-372.

BROWN, P. J. & FORSYTH, J. B. 1973. *The crystal structure of solids*, Edward Arnold.

BUCKINGHAM, A. 1956. The polarizability of a pair of interacting atoms. *Trans. Faraday Soc.,* 52**,** 1035-1041.

BURATTO, B., USHER, S. P., PARRIS, D. & SCALES, P.J. 2014. Wall effects during settling in cylinders. *Journal of Colloids and Surfaces A: Physicochemical and Engineering Aspects*, 449, 157-169.

BÜRGER, R. & TORY, E. M. 2000. On upper rarefaction waves in batch settling. *Powder technology,* 108**,** 74-87.

BUSCALL, R. 1982. The elastic properties of structured dispersions: a simple centrifuge method of examination. *Colloids and Surfaces,* 5**,** 269-283.

BUSCALL, R., MCGOWAN, J. I. & MORTON-JONES, A. J. 1993. The rheology of concentrated dispersions of weakly attracting colloidal particles with and without wall slip. *Journal of Rheology,* 37**,** 621-641.

BUSCALL, R. & WHITE, L. R. 1987. The consolidation of concentrated suspensions. Part 1.—The theory of sedimentation. *Journal of the Chemical Society, Faraday Transactions 1: Physical Chemistry in Condensed Phases,* 83**,** 873-891.

BUX, J., HUNTER, T. N., PAUL, N., DODDS, J. M., PEAKALL, J. & BIGGS, S. R. Characterising Nuclear Simulant Suspensions In Situ With an Acoustic Backscatter System. ASME 2013 15th International Conference on Environmental Remediation and Radioactive Waste Management, 2013. American Society of Mechanical Engineers, V002T03A018-V002T03A018.

CAHN, R. W. 1954. Twinned crystals. *Advances in Physics,* 3**,** 363-445.

CAMPBELL, J. A., STROMATT, R. W., SMITH, M. R., BEAN, R. M., JONES, T. E. & STRACHAN, D. M. 1994. Organic Analysis at the Hanford Nuclear Site. *Analytical Chemistry,* 66**,** 1208A-1215A.

CARASCO, C., PEROT, B., MARIANI, A., EL KANAWATI, W., VALKOVIC, V., SUDAC, D. & OBHODAS, J. Material characterization in cemented radioactive waste with the associated particle technique. *Nuclear Instruments and Methods in Physics*

Research Section A: Accelerators, Spectrometers, Detectors and Associated Equipment, 619**,** 432-435.
CARLSON, S. & ANDERSEN, A. M. K. 2000. High-pressure transitions of trigonal α-ZrMo 2 O 8. *Physical Review B,* 61**,** 11209.
CARLSON, S. & KROGH ANDERSEN, A. M. 2001. High-pressure properties of TiP2O7, ZrP2O7 and ZrV2O7. *Journal of applied crystallography,* 34**,** 7-12.
CASSON, N. 1959. Rheology of disperse systems *Rheologica Acta***,** 84-104.
CHADWICK, M. D., GOODWIN, J. W., VINCENT, B., LAWSON, E. J. & MILLS, P. D. A. 2002. Rheological behaviour of titanium dioxide (uncoated anatase) in ethylene glycol. *Colloids and Surfaces A: Physicochemical and Engineering Aspects,* 196**,** 235-245.
CHAN, D. & POWELL, R. L. 1984. Rheology of suspensions of spherical particles in a newtonian and a non-newtonian fluid. *Journal of Non-Newtonian Fluid Mechanics,* 15**,** 165-179.
CHANDLER, H. 2010. Flow mechanisms and rheology of dense aqueous suspensions of titanium (IV) oxide. *Rheologica acta,* 49**,** 349-357.
CHANG, C. & POWELL, R. L. 1994. Effect of particle size distributions on the rheology of concentrated bimodal suspensions. *Journal of Rheology,* 38**,** 85-98.
CHANG, C. & SMITH, P. A. 1996a. Flow-induced structure in a system of nuclear waste simulant slurries. *Rheologica Acta,* 35**,** 382-389.
CHANG, C. & SMITH, P. A. 1996b. Rheological characterization of nuclear waste slurries. *Particulate science and technology,* 14**,** 165-180.
CHANNELL, G. M., MILLER, K. T. & ZUKOSKI, C. F. 2000. Effects of microstructure on the compressive yield stress. *AIChE journal,* 46**,** 72-78.
CHANNELL, G. M. & ZUKOSKI, C. F. 1997. Shear and compressive rheology of aggregated alumina suspensions. *AIChE Journal,* 43**,** 1700-1708.
CHEN, M. & RUSSEL, W. 1991. Characteristics of flocculated silica dispersions. *Journal of colloid and interface science,* 141**,** 564-577.
CHENG, D. C. H. 1984. Further observations on the rheological behaviour of dense suspensions. *Powder Technology,* 37**,** 255-273.
CHENG, D. C. H. & RICHMOND, R. A. 1978. Some observations on the rheological behaviour of dense suspensions. *Rheologica Acta,* 17**,** 446-453.
CHENG, X., MCCOY, J. H., ISRAELACHVILI, J. N. & COHEN, I. 2011. Imaging the microscopic structure of shear thinning and thickening colloidal suspensions. *Science,* 333**,** 1276-1279.
CHEUNG, M. K., POWELL, R. L. & MCCARTHY, M. J. 1996. Sedimentation of noncolloidal bidisperse suspensions. *AIChE journal,* 42**,** 271-276.
CHOI, G. & KRIEGER, I. 1986. Rheological studies on sterically stabilized model dispersions of uniform colloidal spheres: II. Steady-shear viscosity. *Journal of Colloid and Interface Science,* 113**,** 101-113.
CHUN, J., OH, T., LUNA, M. & SCHWEIGER, M. 2011. Effect of particle size distribution on slurry rheology: Nuclear waste simulant slurries. *Colloids and Surfaces A: Physicochemical and Engineering Aspects,* 384**,** 304-310.
CLARKE, B. 1967. Rheology of coarse settling suspensions. *Trans. Inst. Chem. Eng,* 45**,** 251-256.
CLEARFIELD, A. & BLESSING, R. H. 1972. The preparation and crystal structure of a basic zirconium molybdate and its relationship to ion exchange gels. *Journal of Inorganic and Nuclear Chemistry,* 34**,** 2643-2663.
COGSWELL, F. 1972a. Converging flow of polymer melts in extrusion dies. *Polymer Engineering & Science,* 12**,** 64-73.
COGSWELL, F. N. 1972b. Measuring the Extensional Rheology of Polymer Melts. *Transactions of The Society of Rheology (1957-1977),* 16**,** 383-403.
CÖLFEN, H. 2001. Double-Hydrophilic Block Copolymers: Synthesis and Application as Novel Surfactants and Crystal Growth Modifiers. *Macromolecular Rapid Communications,* 22**,** 219-252.
COMISSION, E. 2008. Attitudes towards radioactive waste *Special Euroborometer: TNS Opinion & Social*.
COUETTE, M. 1890. *Ann. Chim. Phys.,* 21**,** 433-510.
COUSSOT, P. 2007. Rheophysics of pastes: a review of microscopic modelling approaches. *Soft Matter,* 3**,** 528-540.

COZAR, O., MAGDAS, D. A. & ARDELEAN, I. 2008. EPR study of molybdenum-lead-phosphate glasses. *Journal of Non-Crystalline Solids,* 354**,** 1032-1035.

CRAWLEY, R. L. & GRAESSLEY, W. W. 1977. Geometry Effects on Stress Transient Data Obtained by Cone and Plate Flow. *Transactions of The Society of Rheology (1957-1977),* 21**,** 19-49.

CROSS, M. M. 1965. Rheology of non-Newtonian fluids: A new flow equation for pseudoplastic systems. *Journal of Colloid Science,* 20**,** 417-437.

CRUYWAGEN, J. J., ROHWER, E. A. & WESSELS, G. F. S. 1995. Molybdenum(VI) complex formation—8. Equilibria and thermodynamic quantities for the reactions with citrate. *Polyhedron,* 14**,** 3481-3493.

DANIEL, R. C., POLOSKI, A. P. & SAEZ, A. E. 2008. Vane rheology of cohesionless glass beads. *Powder Technology,* 181**,** 237-248.

DARBY, R. 1985. Couette viscometer data reduction for materials with a yield stress. *Journal of Rheology,* 24**,** 369-378.

DAVIES, L., DOLLIMORE, D. & SHARP, J. 1975. Sedimentation of supsensions: implications of theories of hindered settling. *Powder Technology,* 13**,** 123-132.

DAVIS, J. R. 2000. *Corrosion: Understanding the Basics*, A S M International.

DAVIS, R. & BIRDSELL, K. 1988. Hindered settling of semidilute monodisperse and polydisperse suspensions. *AIChE Journal,* 34**,** 123-129.

DAVIS, R. H. & ACRIVOS, A. 1985. Sedimentation of noncolloidal particles at low Reynolds numbers. *Annual Review of Fluid Mechanics,* 17**,** 91-118.

DAVIS, R. H. & GECOL, H. 1994. Hindered settling function with no empirical parameters for polydisperse suspensions. *AIChE Journal,* 40**,** 570-575.

DE BRUIJN, H. 1942. The viscosity of suspensions of spherical particles.(The fundamental η-c and φ relations). *Recueil des travaux chimiques des Pays-Bas,* 61**,** 863-874.

DECC 2013. DECC Electricity Generation Costs. *In:* CHANGE, D. O. E. C. (ed.).

DECC 2014. Increasing the use of low-carbon technologies. *In:* CHANGE, D. O. E. C. (ed.). UK.

DERJAGUIN, B. & LANDAU, L. 1941. The theory of stability of highly charged lyophobic sols and coalescence of highly charged particles in electrolyte solutions. *Acta Physicochim. URSS,* 14**,** 633-52.

DERJAGUIN, B. V., CHURAEV, N. V. & MULLER, V. M. 1987. The Derjaguin—Landau—Verwey—Overbeek (DLVO) Theory of Stability of Lyophobic Colloids. *Surface Forces.* Springer US.

DI FELICE, R. 1999. The sedimentation velocity of dilute suspensions of nearly monosized spheres. *International journal of multiphase flow,* 25**,** 559-574.

DJALILI-MOGHADDAM, M. & TOLL, S. 2006. Fibre suspension rheology: effect of concentration, aspect ratio and fibre size. *Rheologica acta,* 45**,** 315-320.

DOBSON, G. R. 1975. Interconversion of grease flow curves between rheometers. *Tribology International,* 8**,** 186-190.

DONNAY, J. D. H. A. H., D 1937. A New Law of Crystal Morphology Extending the Law of Bravais. *Am. Mineral.,* 22**,** 463.

DONSELAAR, L. N. & PHILIPSE, A. P. 1999. Interactions between silica colloids with magnetite cores: diffusion, sedimentation and light scattering. *Journal of colloid and interface science,* 212**,** 14-23.

DOUCET, F. J., GODDARD, D. T., TAYLOR, C. M., DENNISS, I. S., HUTCHISON, S. M. & BRYAN, N. D. 2002. The formation of hydrated zirconium molybdate in simulated spent nuclear fuel reprocessing solutions. *Physical Chemistry Chemical Physics,* 4**,** 3491-3499.

DUCKER, W. A., SENDEN, T. J. & PASHLEY, R. M. 1991. Direct measurement of colloidal forces using an atomic force microscope. *nature,* 353**,** 239-241.

DUNPHY GUZMAN, K. A., FINNEGAN, M. P. & BANFIELD, J. F. 2006. Influence of Surface Potential on Aggregation and Transport of Titania Nanoparticles. *Environmental Science & Technology,* 40**,** 7688-7693.

DZUY, N. Q. & BOGER, D. V. 1983. Yield Stress Measurement for Concentrated Suspensions. *Journal of Rheology,* 27**,** 321-349.

DZUY, N. Q. & BOGER, D. V. 1985. Direct Yield Stress Measurement with the Vane Method. *Journal of Rheology,* 29**,** 335-347.

EDWARDS, S. F. & DOI, M. 1986. The theory of polymer dynamics. *Clarendon, Oxford*.

EIDEN, S. & MARET, G. 2002. Preparation and Characterization of Hollow Spheres of Rutile. *Journal of Colloid and Interface Science,* 250**,** 281-284.

EINSTEIN, A. 1905. On the movement of small particles suspended in stationary liquids required by the molecular-kinetic theory of heat. *Annals of Physics,* 17**,** 549-560.

EINSTEIN, A. 1956. *Investigations on the theory of the Brownian movement.* Ph.D.

EVANS, J., HANSON, J. & SLEIGHT, A. 1998. Room-temperature superstructure of ZrV2O7. *Acta Crystallographica Section B: Structural Science,* 54**,** 705-713.

EVANS, J., MARY, T., VOGT, T., SUBRAMANIAN, M. & SLEIGHT, A. 1996. Negative thermal expansion in ZrW2O8 and HfW2O8. *Chemistry of materials,* 8**,** 2809-2823.

EVANS, J. S., DAVID, W. & SLEIGHT, A. 1999. Structural investigation of the negative-thermal-expansion material ZrW2O8. *Acta Crystallographica Section B: Structural Science,* 55**,** 333-340.

EVANS, J. S., HU, Z., JORGENSEN, J., ARGYRIOU, D., SHORT, S. & SLEIGHT, A. 1997. Compressibility, phase transitions, and oxygen migration in zirconium tungstate, ZrW2O8. *Science,* 275**,** 61-65.

FAN, L., MAO, Z.-S. & YANG, C. 2004. Experiment on Settling of Slender Particles with Large Aspect Ratio and Correlation of the Drag Coefficient. *Industrial & Engineering Chemistry Research,* 43**,** 7664-7670.

FENG, P., HAO, L., HUO, C., WANG, Z., LIN, W. & SONG, W. 2014. Rheological behavior of coal bio-oil slurries. *Energy,* 66**,** 744-749.

FIGLIUZZI, B., JEULIN, D., LEMAÎTRE, A., FRICOUT, G., PIEZANOWSKI, J.-J. & MANNEVILLE, P. 2012. Rheology of thin films from flow observations. *Experiments in fluids,* 53**,** 1289-1299.

FISCHER, W. H., BAUER, W. H. & WIBERLEY, S. E. 1961. Yield Stresses and Flow Properties of Carboxypolymethylene-Water Systems. *Transactions of The Society of Rheology (1957-1977),* 5**,** 221-235.

FLEMING, S. & ROHL, A. 2005. GDIS: a visualization program for molecular and periodic systems. *Zeitschrift für Kristallographie,* 220**,** 580-584.

FLURY, M., MATHISON, J. B. & HARSH, J. B. 2002. In Situ Mobilization of Colloids and Transport of Cesium in Hanford Sediments. *Environmental Science & Technology,* 36**,** 5335-5341.

FOURDRIN, C., ESNOUF, S., DAUVOIS, V., RENAULT, J. P., VENAULT, L., TABARANT, M., DURAND, D., CHENIÈRE, A., LAMOUROUX-LUCAS, C. & COCHIN, F. 2012. Irradiation effects in hydrated zirconium molybdate. *Journal of Nuclear Materials,* 426**,** 38-44.

FRANKS, G. V. 2002. Zeta potentials and yield stresses of silica suspensions in concentrated monovalent electrolytes: isoelectric point shift and additional attraction. *Journal of colloid and interface science,* 249**,** 44-51.

FRANKS, G. V. 2008. Colloids and fine particles. *Introduction to particle technology.* Second ed.: John Wiley & Sons, Ltd.

FRENCH, R. A., JACOBSON, A. R., KIM, B., ISLEY, S. L., PENN, R. L. & BAVEYE, P. C. 2009. Influence of ionic strength, pH, and cation valence on aggregation kinetics of titanium dioxide nanoparticles. *Environmental science & technology,* 43**,** 1354-1359.

FRIEDEL, G. 1907. Studies on the Law of Bravias. *Bull. Soc. Franc. Mineral.,* 30**,** 326.

GABITTO, J. & TSOURIS, C. 2008. Drag coefficient and settling velocity for particles of cylindrical shape. *Powder Technology,* 183**,** 314-322.

GALE, J. D. 1996. Empirical potential derivation for ionic materials. *Philosophical Magazine B,* 73**,** 3-19.

GALE, J. D. 2005. GULP: Capabilities and prospects. *Zeitschrift für Kristallographie,* 220**,** 552-554.

GALE, J. D. & ROHL, A. L. 2003. The general utility lattice program (GULP). *Molecular Simulation,* 29**,** 291-341.

GARRIDO, P., CONCHA, F. & BÜRGER, R. 2003. Settling velocities of particulate systems: 14. Unified model of sedimentation, centrifugation and filtration of flocculated suspensions. *International Journal of Mineral Processing,* 72**,** 57-74.

GARSIDE, J. & AL-DIBOUNI, M. R. 1977. Velocity-Voidage Relationships for Fluidization and Sedimentation in Solid-Liquid Systems. *Industrial & Engineering Chemistry Process Design and Development,* 16**,** 206-214.

GEICULESCU, O., HALLAC, B. B., RAJAGOPAL, R. V., CREAGER, S., DESMARTEAU, D. D., BORODIN, O. & SMITH, G. D. 2014. The Effect of Low-Molecular-Weight Polyethylene Glycol (PEG) Plasticizers on the Transport Properties of Lithium Fluorosulfonimide Ionic Melt Electrolytes. *The Journal of Physical Chemistry B*.

GODINEZ, I. G. & DARNAULT, C. J. G. 2011. Aggregation and transport of nano-TiO2 in saturated porous media: Effects of pH, surfactants and flow velocity. *Water Research,* 45**,** 839-851.

GOLDSMITH, H. & MASON, S. 1962. Particle motions in sheared suspensions XIII. The spin and rotation of disks. *Journal of Fluid Mechanics,* 12**,** 88-96.

GONÇALVES, E. V. & LANNES, S. C. D. S. 2010. Chocolate rheology. *Food Science and Technology (Campinas),* 30**,** 845-851.

GONZALEZ-ROMERO, E. M. 2011. Impact of partitioning and transmutation on the high level waste management. *Nuclear Engineering and Design,* 241**,** 3436-3444.

GOODWIN, J. W., HUGHES, R. W. & CHEMISTRY, R. S. O. 2000. *Rheology for Chemists: An Introduction*, Royal Society of Chemistry.

GOZANI, T. 2004. The role of neutron based inspection techniques in the post 9/11/01 era. *Nuclear Instruments and Methods in Physics Research Section B: Beam Interactions with Materials and Atoms,* 213**,** 460-463.

GREEN, M. D. 1997. Characterisation of suspensions in settling and compression.

GREEN, M. D. & BOGER, D. V. 1997. Yielding of suspensions in compression. *Industrial & engineering chemistry research,* 36**,** 4984-4992.

GREEN, M. D., LANDMAN, K. A., DE KRETSER, R. G. & BOGER, D. V. 1998. Pressure filtration technique for complete characterization of consolidating suspensions. *Industrial & engineering chemistry research,* 37**,** 4152-4156.

GROTE, D., PARK, S. & ZHOU, M. 2001. Dynamic behavior of concrete at high strain rates and pressures: I. experimental characterization. *International Journal of Impact Engineering,* 25**,** 869-886.

GUNES, D. Z., SCIROCCO, R., MEWIS, J. & VERMANT, J. 2008. Flow-induced orientation of non-spherical particles: Effect of aspect ratio and medium rheology. *Journal of Non-Newtonian Fluid Mechanics,* 155**,** 39-50.

H. M. LAUN, R. B., S. HESS, W. LOOSE, O. HESS 1992. Rheological and small angle neutron scattering investigation of shear-induced particle structures of cncentrated polymer dispersions submitted to plane Poiseuille and Couette flow. *Journal of Rheology,* 36**,** 45.

HALL, S., HAHN, T., SHMUELI, U., MCMAHON, B., WILSON, A. J. C. & CRYSTALLOGRAPHY, I. U. O. 2005. *International Tables for Crystallography, Definition and Exchange of Crystallographic Data*, Wiley.

HAMLEY, I. W. 2000. Introduction into soft matter: Polymers, Colloids, Amphiphiles and Liquid Crystals. John Wiley & Sons.

HAMM, B. A., WEST, W. L. & TATTERSON, G. B. 1989. Sludge suspension in waste storage tanks. *AIChE Journal,* 35**,** 1391-1394.

HANSEN, P. J. & WILLIAMS, M. C. 1987. Yield stress and flow measurements in ABA block copolymer melts. *Polymer Engineering & Science,* 27**,** 586-597.

HARTNETT, J. P. & HU, R. Y. 1989. Technical note: the yield stress—an engineering reality. *Journal of Rheology (1978-present),* 33**,** 671-679.

HASSEN, M. A. & DAVIS, R. H. 1989. Effects of particle interactions on the determination of size distributions by sedimentation. *Powder Technology,* 58**,** 285-289.

HAZZAB, A., TERFOUS, A. & GHENAIM, A. 2008. Measurement and modeling of the settling velocity of isometric particles. *Powder Technology,* 184**,** 105-113.

HE, Y., JIN, Y., CHEN, H., DING, Y., CANG, D. & LU, H. 2007. Heat transfer and flow behaviour of aqueous suspensions of TiO< sub> 2</sub> nanoparticles (nanofluids) flowing upward through a vertical pipe. *International Journal of Heat and Mass Transfer,* 50**,** 2272-2281.

HEATH, D. & TADROS, T. F. 1983. Influence of pH, electrolyte, and poly (vinyl alcohol) addition on the rheological characteristics of aqueous dispersions of sodium montmorillonite. *Journal of Colloid and Interface Science,* 93**,** 307-319.

HEYMANN, L., PEUKERT, S. & AKSEL, N. 2002. On the solid-liquid transition of concentrated suspensions in transient shear flow. *Rheologica acta,* 41**,** 307-315.

HIGHGATE, D. J. & WHORLOW, R. W. 1969. End effects and particle migration effects in concentric cylinder rheometry. *Rheologica Acta,* 8**,** 142-151.

HOBBIE, E., WANG, H., KIM, H., LIN-GIBSON, S. & GRULKE, E. 2003. Orientation of carbon nanotubes in a sheared polymer melt. *Physics of Fluids,* 15**,** 1196-1202.

HODGSON, P. E. 1999. *Nuclear Power, Energy and the Environment*, Imperial College Press.

HOLDICH, R. G. 2002. *Fundamentals of Particle Technology*, Midland Information Technology and Publishing.

HONE, J. H. E., HOWE, A. M. & WHITESIDES, T. H. 2000. Rheology of polystyrene latexes with adsorbed and free gelatin. *Colloids and Surfaces A: Physicochemical and Engineering Aspects,* 161**,** 283-306.

HORWITZ, E. P., DIETZ, M. L., CHIARIZIA, R., DIAMOND, H., MAXWELL III, S. L. & NELSON, M. R. 1995. Separation and preconcentration of actinides by extraction chromatography using a supported liquid anion exchanger: application to the characterization of high-level nuclear waste solutions. *Analytica Chimica Acta,* 310**,** 63-78.

HU, J., CHEN, M., FANG, X. & WU, L. 2011. Fabrication and application of inorganic hollow spheres. *Chemical Society Reviews,* 40**,** 5472-5491.

HUANG, X. & GARCIA, M. H. 1998. A Herschel–Bulkley model for mud flow down a slope. *Journal of fluid mechanics,* 374**,** 305-333.

HUNTER, R. J., MIDMORE, B. R. & ZHANG, H. 2001. Zeta Potential of Highly Charged Thin Double-Layer Systems. *Journal of Colloid and Interface Science,* 237**,** 147-149.

HUNTER, T. N., PEAKALL, J. & BIGGS, S. 2012. An acoustic backscatter system for in situ concentration profiling of settling flocculated dispersions. *Minerals Engineering,* 27–28**,** 20-27.

HUNTER, T. N., PEAKALL, J., UNSWORTH, T. J., ACUN, M. H., KEEVIL, G., RICE, H. & BIGGS, S. 2013. The influence of system scale on impinging jet sediment erosion: Observed using novel and standard measurement techniques. *Chemical Engineering Research and Design,* 91**,** 722-734.

HUR, S. C., CHOI, S.-E., KWON, S. & DI CARLO, D. 2011. Inertial focusing of non-spherical microparticles. *Applied Physics Letters,* 99**,** 044101.

ILIC, V. & VINCENT, J. 1994. Sedimentation of complex-shaped particles in a square tank at low Reynolds numbers. *International Journal of Multiphase Flow,* 20**,** 445-452.

ISO, Y., KOCH, D. L. & COHEN, C. 1996. Orientation in simple shear flow of semi-dilute fiber suspensions 1. Weakly elastic fluids. *Journal of non-newtonian fluid mechanics,* 62**,** 115-134.

ISRAELACHVILI, J. N. 1992. Adhesion forces between surfaces in liquids and condensable vapours. *Surface Science Reports,* 14**,** 109-159.

J. KETTLER, Y. B., E. MAUERHOFER, R. NABBI AND R, ODOJ 2007. Modelling of a prompt gamma neutron activation system for non-destructive determination of toxic elements in radioactive waste packages. *Safety Research for Nuclear Waste Disposal, Safety Research and Reactor Technology.*

J. L. PETTIER, D. E. A. R. T. High energy X-ray imaging on large dense objects: definition and performance studies of devices by simulation. 3rd International conference on Emerging Technologies in NDT; Greece, 2003.

JAMES, A., WILLIAMS, D. & WILLIAMS, P. 1987. Direct measurement of static yield properties of cohesive suspensions. *Rheologica Acta,* 26**,** 437-446.

JAMES P. M. SYVITSKI, K. W. G. L., ASPREY, K. W., SYVITSKI, J. P. M., K. WILLIAM G. LEBLANC, & ASPREY., K. W. 1991. *Interlaboratory, interinstrument calibration experimentPrinciples, methods, and application of particle size analysis*, Cambridge University Press.

JASTRZEBSKI, Z. D. 1967. Entrance Effects and Wall Effects in an Extrusion Rheometer during Flow of Concentrated Suspensions. *Industrial & Engineering Chemistry Fundamentals,* 6**,** 445-454.

JASWON, M. A. & DOVE, D. B. 1956. Twinning properties of lattice planes. *Acta Crystallographica,* 9**,** 621-626.

JEFFERY, G. B. 1922. The motion of ellipsoidal particles immersed in a viscous fluid. *Proceedings of the Royal Society of London. Series A, Containing papers of a mathematical and physical character***,** 161-179.

JIANG, J., MAY, I., SARSFIELD, M., OGDEN, M., FOX, D., JONES, C. & MAYHEW, P. 2005. A Spectroscopic Study of the Dissolution of Cesium Phosphomolybdate and Zirconium Molybdate by Ammonium Carbamate. *Journal of Solution Chemistry,* 34**,** 443-468.

JIANZHONG, L., XING, S. & ZHENJIANG, Y. 2003. Effects of the aspect ratio on the sedimentation of a fiber in Newtonian fluids. *Journal of Aerosol Science,* 34**,** 909-921.

JOBLING, A. & ROBERTS, J. 1959. Flow testing of viscoelastic materials. Design and calibration of the Roberts-Weissenberg Model R8 rheogoniometer. *Journal of Polymer Science,* 36**,** 421-431.

JOHNSON, S. B., DUNSTAN, D. E. & FRANKS, G. V. 2002. Rheology of Cross-Linked Chitosan–Alumina Suspensions Used for a New Gelcasting Process. *Journal of the American Ceramic Society,* 85**,** 1699-1705.

JOHNSON, S. B., FRANKS, G. V., SCALES, P. J., BOGER, D. V. & HEALY, T. W. 2000. Surface chemistry–rheology relationships in concentrated mineral suspensions. *International Journal of Mineral Processing,* 58**,** 267-304.

KAWATRA, S. K. 2012. Coal–Water Slurries. *Particle Technology and Applications***,** 111.

KAY, E. D., CALLOWAY, T. B., KOOPMAN, D. C., BRIGMON, R. L. & EIBLING, R. E. Rheology modifiers for radioactive waste slurries. ASME/JSME 2003 4th Joint Fluids Summer Engineering Conference, 2003. American Society of Mechanical Engineers, 855-863.

KELESSIDIS, V. C., TSAMANTAKI, C. & DALAMARINIS, P. 2007. Effect of pH and electrolyte on the rheology of aqueous Wyoming bentonite dispersions. *Applied Clay Science,* 38**,** 86-96.

KHALILI GARAKANI, A. H., MOSTOUFI, N., SADEGHI, F., HOSSEINZADEH, M., GT, FATOURECHI, H., SARRAFZADEH, M. H. & MEHRNIA, M. R. 2011. COMPARISON BETWEEN DIFFERENT MODELS FOR RHEOLOGICAL CHARACTERIZATION OF ACTIVATED SLUDGE. *Iranian Journal of Environmental Health Science & Engineering,* 8**,** 255-264.

KHAN, A. U., HAQ, A. U., MAHMOOD, N. & ALI, Z. 2012. Rheological studies of aqueous stabilised nano-zirconia particle suspensions. *Materials Research,* 15**,** 21-26.

KHAN, A. W. 2011. *Modelling the structure, properties and phase transformations of Caesium Phosphomolybdate.* Ph.D., The University of Leeds, UK.

KLEVTSOVA, R. F., GLINSKAYA, L. A., ZOLOTOVA, E. S. & KLEVTSOV, P. V. 1989. *Dokl. Akad. Nauk. SSSR,* 305**,** 91-95.

KOMAR, P. D. & REIMERS, C. E. 1978. Grain Shape Effects on Settling Rates. *The Journal of Geology,* 86**,** 193-209.

KONERT, M. & VANDENBERGHE, J. E. F. 1997. Comparison of laser grain size analysis with pipette and sieve analysis: a solution for the underestimation of the clay fraction. *Sedimentology,* 44**,** 523-535.

KORTHUIS, V., KHOSROVANI, N., SLEIGHT, A., ROBERTS, N., DUPREE, R. & WARREN, W. J. 1995. Negative thermal expansion and phase transitions in the ZrV2-xPxO7 series. *Chemistry of materials,* 7**,** 412-417.

KRIEGER, I. M. 1972. Rheology of monodisperse latices. *Advances in Colloid and Interface Science,* 3**,** 111-136.

KRIEGER, I. M. & DOUGHERTY, T. J. 1959. A mechanism for non-Newtonian flow in suspensions of rigid spheres. *Transactions of The Society of Rheology (1957-1977),* 3**,** 137-152.

KROGH ANDERSEN, A. M. & CARLSON, S. 2001. High-pressure structures of-and-ZrMo2O8. *Acta Crystallographica Section B: Structural Science,* 57**,** 20-26.

KRULIS, M. & ROHM, H. 2004. Adaption of a vane tool for the viscosity determination of flavoured yoghurt. *European Food Research and Technology,* 218**,** 598-601.

KUMAR, S., PIROG, T. W. & RAMKRISHNA, D. 2000. A new method for estimating hindered creaming/settling velocity of particles in Polydisperse Systems. *Chemical Engineering Science,* 55**,** 1893-1904.

KUMAR, S., SIVAIAH, M., VENKATESAN, K., KRISHNA, R., MURTHY, G. & SASIDHAR, P. 2003. Removal of cesium and strontium from acid solution using a composite of zirconium molybdate and zirconium tungstate. *Journal of Radioanalytical and Nuclear Chemistry,* 258**,** 321-327.

LAIGLE, D. & COUSSOT, P. 1997. Numerical modeling of mudflows. *Journal of Hydraulic Engineering,* 123**,** 617-623.

LARSON, R. G. 1999. *The Structure and Rheology of Complex Fluids*, OUP USA.

LAU, R., HASSAN, M. S., WONG, W. & CHEN, T. Revisit of the Wall Effect on the Settling of Cylindrical Particles in the Inertial Regime. *Industrial & Engineering Chemistry Research,* 49**,** 8870-8876.

LAUN, H. M. 1984. Rheological properties of aqueous polymer dispersions. *Die Angewandte Makromolekulare Chemie,* 123**,** 335-359.

LEACH, A. R. 2001. *Molecular modelling: principles and applications*, Pearson Education.

LENNARD-JONES, J. & STRACHAN, C. 1935. The Interaction of Atoms and Molecules with Solid Surfaces. I. The Activation of Adsorbed Atoms to Higher Vibrational States. *Proceedings of the Royal Society of London. Series A-Mathematical and Physical Sciences,* 150**,** 442-455.

LEONG, Y.-K., BOGER, D. V., SCALES, P. J., HEALY, T. W. & BUSCALL, R. 1993. Control of the rheology of concentrated aqueous colloidal systems by steric and hydrophobic forces. *J. Chem. Soc., Chem. Commun.*, 639-641.

LEONG, Y. K. 1997. Effects of steric and hydrophobic forces on the rheological properties of ZrO2 suspensions. *Colloid and Polymer Science,* 275**,** 869-875.

LEONG, Y. K., BOGER, D. V. & PARRIS, D. 1991. Surface chemistry and rheological properties of zirconia suspensions. *Journal of Rheology,* 35**,** 149-165.

LEONG, Y. K., BOGER, D. V., SCALES, P. J. & HEALY, T. W. 1996. Interparticle Forces Arising from Adsorbed Surfactants in Colloidal Suspensions: An Additional Attractive Force. *Journal of Colloid and Interface Science,* 181**,** 605-612.

LEONG, Y. K. & ONG, B. C. 2003. Critical zeta potential and the Hamaker constant of oxides in water. *Powder Technology,* 134**,** 249-254.

LEONG, Y. K., SCALES, P. J., HEALY, T. W. & BOGER, D. V. 1995. Effect of particle size on colloidal zirconia rheology at the isoelectric point. *Journal of the American Ceramic Society,* 78**,** 2209-2212.

LEWIS, G. & CATLOW, C. 1985. Potential models for ionic oxides. *Journal of Physics C: Solid State Physics,* 18**,** 1149.

LIDDEL, P. V. & BOGER, D. V. 1996. Yield stress measurements with the vane. *Journal of non-newtonian fluid mechanics,* 63**,** 235-261.

LIDDELL, P. V. & BOGER, D. V. 1994. Influence of processing on the rheology of titanium dioxide pigment suspensions. *Industrial & engineering chemistry research,* 33**,** 2437-2442.

LIND, C. 2012. Two Decades of Negative Thermal Expansion Research: Where Do We Stand? *Materials,* 5**,** 1125-1154.

LIND, C., VANDERVEER, D. G., WILKINSON, A. P., CHEN, J., VAUGHAN, M. T. & WEIDNER, D. J. 2001. New High-Pressure Form of the Negative Thermal Expansion Materials Zirconium Molybdate and Hafnium Molybdate. *Chemistry of Materials,* 13**,** 487-490.

LITCHFIELD, D. W. & BAIRD, D. G. 2006. The rheology of high aspect ratio nano-particle filled liquids.

LIU, W., SUN, W., BORTHWICK, A. G. L. & NI, J. 2013. Comparison on aggregation and sedimentation of titanium dioxide, titanate nanotubes and titanate nanotubes-TiO2: Influence of pH, ionic strength and natural organic matter. *Colloids and Surfaces A: Physicochemical and Engineering Aspects,* 434**,** 319-328.

LIU, X., CHEN, G. & SU, C. 2011. Effects of material properties on sedimentation and aggregation of titanium dioxide nanoparticles of anatase and rutile in the aqueous phase. *Journal of colloid and interface science,* 363**,** 84-91.

LIU, Y. J. & JOSEPH, D. D. 1993. Sedimentation of particles in polymer solutions. *Journal of Fluid Mechanics,* 255**,** 565-595.

M. DUNLAP, J. E. A. 1997. Introduction to the Scanning Electron Microscope. *Theory, Practise & Procedures* Faculity for advanced instrumentation.

MACMILLAN, R. H. 2010. *Mechanics of Fluid-Particle Systems with Special Reference to Agriculture: Theory and Worked Examples, a Book for Engineers and Engineering Students*, University of Melbourne Custom Book Centre.

MACOSKO, C. W. 1994. *Rheology: principles, measurements, and applications*, VCH.

MAGNALDO, A., MASSON, M. & CHAMPION, R. 2007. Nucleation and crystal growth of zirconium molybdate hydrate in nitric acid. *Chemical Engineering Science,* 62**,** 766-774.

MAGNIN, A. & PIAU, J. M. 1987. Shear rheometry of fluids with a yield stress. *Journal of Non-Newtonian Fluid Mechanics,* 23**,** 91-106.

MAGNIN, A. & PIAU, J. M. 1990. Cone-and-plate rheometry of yield stress fluids. Study of an aqueous gel. *Journal of Non-Newtonian Fluid Mechanics,* 36**,** 85-108.

MALVERN 1997. Introduction manual to Mastersizer 2000. Cole Parmer Instruments Company Limited, UK.

MALVERN 2004. Zetasizer Nano Series User Manual. Cole Palmer Instruments Company Limited.

MANGESANA, N., CHIKUKU, R., MAINZA, A., GOVENDER, I., VAN DER WESTHUIZEN, A. & NARASHIMA, M. 2008. The effect of particle sizes and solids concentration on the rheology of silica sand based suspensions. *JOURNAL-SOUTH AFRICAN INSTITUTE OF MINING AND METALLURGY,* 108**,** 237.

MARY, T., EVANS, J., VOGT, T. & SLEIGHT, A. 1996. Negative thermal expansion from 0.3 to 1050 Kelvin in ZrW2O8. *Science,* 272**,** 90-92.

MASHEDER, B. 2011. *Zirconium molybdate crystal growth and morphological control.* Ph.D., University of Bristol, UK.

MASLIYAH, J. H. 1979. HINDERED SETTLING IN A MULTI-SPECIES PARTICLE SYSTEM. *Chemical Engineering Science,* 34**,** 1166-1168.

MASON, L. J., BIGGS, S., TINSLEY, TP., MCKENDRICK, D. 2005. The influence of yield stress on the re-suspension properties of nuclear waste simulants. *7th World Congress in Chemical Enginering.* Glasgow.

MAUDE, A. & WHITMORE, R. 1958. A generalized theory of sedimentation. *British Journal of Applied Physics,* 9**,** 477.

MCARTHER, G. A. H., TINSLEY, T.P., MCKENDRICK, D. Development of a liquid jet sludge re-suspension model (used on pulse jets or jet ballasts). AIChE Annual Meeting, Conference Proceedings, 2005 Cincinnati, OH, USA,.

MCCLORY, C., MCNALLY, T., BAXENDALE, M., PÃ¶TSCHKE, P., BLAU, W. & RUETHER, M. Electrical and rheological percolation of PMMA/MWCNT nanocomposites as a function of CNT geometry and functionality. *European Polymer Journal,* 46**,** 854-868.

MCFARLANE, A. J., ADDAI-MENSAH, J. & BREMMELL, K. 2005. Rheology of flocculated kaolinite dispersions. *Korea-Australia Rheology Journal,* 17**,** 181-190.

MCKINLEY, G. H., BYARS, J. A., BROWN, R. A. & ARMSTRONG, R. C. 1991. Observations on the elastic instability in cone-and-plate and parallel-plate flows of a polyisobutylene Boger fluid. *Journal of Non-Newtonian Fluid Mechanics,* 40**,** 201-229.

MEGAW, H. D. 1973. *Crystal structures: a working approach*, Saunders.

METZNER, A. 1985. Rheology of suspensions in polymeric liquids. *Journal of Rheology (1978-present),* 29**,** 739-775.

MIE, G. 1908. Contributions to the optics of cloudy media, particularly of colloidal metal solutions. *Annals of physics,* 330**,** 337-445.

MIKULÁŠEK, P., WAKEMAN, R. & MARCHANT, J. 1997. The influence of pH and temperature on the rheology and stability of aqueous titanium dioxide dispersions. *Chemical Engineering Journal,* 67**,** 97-102.

MILLER, K. T., MELANT, R. M. & ZUKOSKI, C. F. 1996. Comparison of the compressive yield response of aggregated suspensions: Pressure filtration, centrifugation, and osmotic consolidation. *Journal of the American Ceramic Society,* 79**,** 2545-2556.

MILLS, P. & SNABRE, P. 1994. Settling of a suspension of hard spheres. *EPL (Europhysics Letters),* 25**,** 651.

MIRZA, S. & RICHARDSON, J. F. 1979. Sedimentation of suspensions of particles of two or more sizes. *Chemical Engineering Science,* 34**,** 447-454.

MITTAL, R. & CHAPLOT, S. 1999. Lattice dynamical calculation of isotropic negative thermal expansion in ZrW 2 O 8 over 0–1050 K. *Physical Review B,* 60**,** 7234.

MONROY-GUZMÁN, F., DíAZ-ARCHUNDIA, L. V. & CONTRERAS RAMíREZ, A. 2003. Effect of Zr:Mo ratio on 99mTc generator performance based on zirconium molybdate gels. *Applied Radiation and Isotopes,* 59**,** 27-34.

MONROY-GUZMAN, F., DÍAZ-ARCHUNDIA, L. V. & HERNÁNDEZ-CORTÉS, S. 2008. 99Mo/99mTc generators performances prepared from zirconium molybate gels. *Journal of the Brazilian Chemical Society,* 19**,** 380-388.

MONROY-GUZMAN, F., RIVERO GUTIÉRREZ, T., LÓPEZ MALPICA, I. Z., HERNÁNDEZ CORTES, S., ROJAS NAVA, P., VAZQUEZ MALDONADO, J. C. & VAZQUEZ, A. 2012. Production optimization of 99Mo/99mTc zirconium molybate gel generators at semi-automatic device: DISIGEG. *Applied Radiation and Isotopes,* 70**,** 103-111.

MOONEY, M. & EWART, R. H. 1934. The Conicylindrical Viscometer. *Journal of Applied Physics,* 5**,** 350-354.

MUELLER, S., LLEWELLIN, E. W. & MADER, H. M. 2009. The rheology of suspensions of solid particles. *Proceedings of the Royal Society A: Mathematical, Physical and Engineering Science*.

NASSER, M. & JAMES, A. 2006. The effect of polyacrylamide charge density and molecular weight on the flocculation and sedimentation behaviour of kaolinite suspensions. *Separation and purification technology,* 52**,** 241-252.

NASSER, M. & JAMES, A. 2007. Effect of polyacrylamide polymers on floc size and rheological behaviour of kaolinite suspensions. *Colloids and Surfaces A: Physicochemical and Engineering Aspects,* 301**,** 311-322.

NASSER, M. S. & JAMES, A. E. 2008. Compressive and shear properties of flocculated kaolinite–polyacrylamide suspensions. *Colloids and Surfaces A: Physicochemical and Engineering Aspects,* 317**,** 211-221.

NECHYPORCHUK, O., BELGACEM, M. N. & PIGNON, F. 2014. Rheological properties of micro-/nanofibrillated cellulose suspensions: Wall-slip and shear banding phenomena. *Carbohydrate polymers,* 112**,** 432-439.

NEHDI, M. & RAHMAN, M.-A. 2004. Estimating rheological properties of cement pastes using various rheological models for different test geometry, gap and surface friction. *Cement and concrete research,* 34**,** 1993-2007.

NGUYEN, Q. D., AKROYD, T., DE KEE, D. C. & ZHU, L. 2006. Yield stress measurements in suspensions: an inter-laboratory study. *Korea-Australia Rheology Journal,* 18**,** 15-24.

NGUYEN, Q. D. & BOGER, D. V. 1992. Measuring the Flow Properties of Yield Stress Fluids. *Annual Review of Fluid Mechanics,* 24**,** 47-88.

NINDO, C. I., TANG, J., POWERS, J. R. & TAKHAR, P. S. 2007. Rheological properties of blueberry puree for processing applications. *LWT - Food Science and Technology,* 40**,** 292-299.

NNL 2008a. Introduction to HA liquor chemistry and the HA Liquor Evaporation and Storage (HALES) plant. *Module 4: HALES process issues.*: National Nuclear Laboratory.

NNL 2008b. Introduction to HA liquor chemistry and the HA Liquor Evaporation and Storage (HALES) plant. *Module 3: Evaporator process chemistry.* National Nuclear Laoratory.

NNL 2008c. Introduction to HA liquor chemistry and the HA Liquor Evaporation and Storage (HALES) plant. *Module 2: Description of HALES plant.*: National Nuclear Laboratory.

NNL 2012. Modelling association of activity with zirconium molybdate solids. National Nuclear Laboratory: National Nuclear Laboratory; Sellafield Ltd; Nuclear Decommissioning Authority.

NOWACKI, W. 1972. Bemerkungen zur Geschichte der Raumgruppen-Symbole von FEDOROW, SCHOENFLIES und HERMANN-MAUGUIN. *Zeitschrift für Kristallographie-Crystalline Materials,* 135**,** 145-158.

ONR 2000. The storage of liquid high level waste at BFNL Sellafield. UK.

ORLEY, M. J. 2009. *Crystallisation of Barium Nitrate in the presence of divalent metal cations in relation to high level nuclear waste reprocessing.* Ph.D., The University of Leeds, UK.

OVARLEZ, G., MAHAUT, F., BERTRAND, F. & CHATEAU, X. 2011. Flows and heterogeneities with a vane tool: Magnetic resonance imaging measurements. *Journal of Rheology (1978-present),* 55**,** 197-223.

PABST, W., GREGOROVÃ¡, E. & BERTHOLD, C. 2006. Particle shape and suspension rheology of short-fiber systems. *Journal of the European Ceramic Society,* 26**,** 149-160.

PADMANABHAN, V., DAILLANT, J., BELLONI, L., MORA, S., ALBA, M. & KONOVALOV, O. 2007. Specific ion adsorption and short-range interactions at the air aqueous solution interface. *Physical review letters,* 99**,** 086105.

PARKS, G. A. 1965. The Isoelectric Points of Solid Oxides, Solid Hydroxides, and Aqueous Hydroxo Complex Systems. *Chemical Reviews,* 65**,** 177-198.

PASHLEY, R. 1981. Hydration forces between mica surfaces in aqueous electrolyte solutions. *Journal of colloid and interface science,* 80**,** 153-162.

PATWARDHAN, V. S. & TIEN, C. 1985. SEDIMENTATION AND LIQUID FLUIDIZATION OF SOLID PARTICLES OF DIFFERENT SIZES AND DENSITIES. *Chemical Engineering Science,* 40**,** 1051-1060.

PENKAVOVA, V., TIHON, J. & WEIN, O. 2011. Stability and rheology of dilute TiO2-water nanofluids. *Nanoscale research letters,* 6**,** 1-7.

PERRIN, J. 1914. *Atoms*, Constable & Company Ltd, UK.

POVOLO, F., SCHWARTZ, G. & HERMIDA, É. B. 1996a. Stress relaxation of PVC below the yield point. *Journal of Polymer Science Part B Polymer Physics,* 34**,** 1257-1267.

POVOLO, F., SCHWARTZ, G. & HERMIDA, É. B. 1996b. Temperature and strain rate dependence of the tensile yield stress of PVC. *Journal of applied polymer science,* 61**,** 109-117.

POWELL, R. L. 1991. Rheology of suspensions of rodlike particles. *Journal of statistical physics,* 62**,** 1073-1094.

PRINCEN, H. M. 1986. A Novel Design to Eliminate End Effects in a Concentric Cylinder Viscometer. *Journal of Rheology (1978-present),* 30**,** 271-283.

PRINETTO, F., CERRATO, G., GHIOTTI, G., CHIORINO, A., CAMPA, M. C., GAZZOLI, D. & INDOVINA, V. 1995. Formation of the MoVI Surface Phase on MoOx/ZrO2 Catalysts. *The Journal of Physical Chemistry,* 99**,** 5556-5567.

PRYDE, A. K., HAMMONDS, K. D., DOVE, M. T., HEINE, V., GALE, J. D. & WARREN, M. C. 1996. Origin of the negative thermal expansion. *Journal of Physics: Condensed Matter,* 8**,** 10973.

PRYDE, A. K., HAMMONDS, K. D., DOVE, M. T., HEINE, V., GALE, J. D. & WARREN, M. C. 1997. Rigid unit modes and the negative thermal expansion in ZrW2O8. *Phase Transitions,* 61**,** 141-153.

Q.D. NGUYEN, T. A., C.D. KEE, L. ZHU 2006. Yield stress measurements in suspensions: an inter-laboratory study. *Journal of Rheology* 18**,** 15-24.

QI, G., NATHAN, G. J. & KELSO, R. M. 2014. The influence of aspect ratio on distributions of settling velocities and orientations of long fibres. *Powder Technology,* 257**,** 192-197.

RAHMAN, I. A. & PADAVETTAN, V. 2012. Synthesis of silica nanoparticles by sol-gel: size-dependent properties, surface modification, and applications in silica-polymer nanocomposites — a review. *J. Nanomaterials,* 2012**,** 8-8.

RAHNAMA, M., KOCH, D. L. & SHAQFEH, E. S. 1995. The effect of hydrodynamic interactions on the orientation distribution in a fiber suspension subject to simple shear flow. *Physics of Fluids,* 7**,** 487-506.

RAO, B. S. M., GANTNER, E., REINHARDT, J., STEINERT, D. & ACHE, H. J. 1990. Characterization of the solids formed from simulated nuclear fuel reprocessing solutions. *Journal of Nuclear Materials,* 170**,** 39-49.

REINER, M. 1926. *Kolloid Z,* 39**,** 80-87.

RICHARDSON, J. F. & ZAKI, W. N. 1954. The sedimentation of a suspension of uniform spheres under conditions of viscous flow. *Chemical Engineering Science,* 3**,** 65-73.

RUSSEL, W. B., SAVILLE, D. A. & SCHOWALTER, W. R. 1989. *Colloidal Dispersions*, Cambridge University Press.

RYCHLEWSKI, J. 1984. On Hooke's law. *Journal of Applied Mathematics and Mechanics,* 48**,** 303-314.

S. O. EVANS, J. 1999. Negative thermal expansion materials [dagger]. *Journal of the Chemical Society, Dalton Transactions***,** 3317-3326.

SAHOO, P. P., SUMITHRA, S., MADRAS, G. & ROW, T. G. 2009. Synthesis, structure and photocatalytic properties of β-ZrMo2O8. *Bulletin of Materials Science,* 32**,** 337-342.

SALMELA, J., MARTINEZ, D. M. & KATAJA, M. 2007. Settling of dilute and semidilute fiber suspensions at finite Re. *AIChE Journal,* 53**,** 1916-1923.

SAMOTUS, A., KANAS, A., DUDEK, M., GRYBOŚ, R. & HODOROWICZ, E. 1991. 1:1 Molybdenum(VI) citric acid complexes. *Transition Metal Chemistry,* 16**,** 495-499.

SANDERS, M., LESLIE, M. & CATLOW, C. 1984. Interatomic potentials for SiO2. *J. Chem. Soc., Chem. Commun.***,** 1271-1273.

SASAKI, T., KOHYAMA, K., YASUI, T. & SATAKE, T. 2004. Rheological properties of white salted noodles with different amylose content at small and large deformation. *Cereal chemistry,* 81**,** 226-231.

SASSI, C. 1996. Cyclone separator. Google Patents.

SCALES, P. J., JOHNSON, S. B., HEALY, T. W. & KAPUR, P. C. 1998. Shear yield stress of partially flocculated colloidal suspensions. *AIChE Journal,* 44**,** 538-544.

SCOTTO DI SANTOLO, A., PELLEGRINO, A. M. & EVANGELISTA, A. 2010. Experimental study on the rheological behaviour of debris flow. *Nat. Hazards Earth Syst. Sci.,* 10**,** 2507-2514.

SELIM, M. S., KOTHARI, A. C. & TURIAN, R. M. 1983. Sedimentation of multisized particles in concentrated suspensions. *AIChE Journal,* 29**,** 1029-1038.

SENAPATI, P. K., PANDA, D. & PARIDA, A. 2009. Predicting viscosity of limestone–water slurry. *Journal of Minerals and Materials Characterization and Engineering,* 8**,** 203.

SESHADRI, V. & SUTERA, S. P. 1968. Concentration changes of suspensions of rigid spheres flowing through tubes. *Journal of Colloid and Interface Science,* 27**,** 101-110.

SHERWOOD, J. & MEETEN, G. 1997. The filtration properties of compressible mud filtercakes. *Journal of Petroleum Science and Engineering,* 18**,** 73-81.

SHIN, M., KOCH, D. L. & SUBRAMANIAN, G. 2009. Structure and dynamics of dilute suspensions of finite-Reynolds-number settling fibers. *Physics of Fluids,* 21**,** -.

SKARJA, G. A., KINLOUGH-RATHBONE, R. L., PERRY, D. W., RUBENS, F. D. & BRASH, J. L. 1997. A cone-and-plate device for the investigation of platelet biomaterial interactions. *Journal of Biomedical Materials Research,* 34**,** 427-438.

SMITH, P. A., RECTOR, D. R. & SHEKARRIZ, A. 2000. Microstructural and Rheological Characterization of Colloidal Aggregates of Nuclear Waste Slurries. *Mineral Processing and Extractive Metallurgy Review,* 20**,** 311-324.

SMYTH, H. D. 1945. *Atomic energy for military purposes*, Princeton University Press Princeton, NJ.

SÖHNEL, O. & GARSIDE, J. 1992. *Precipitation: basic principles and industrial applications*, Butterworth-Heinemann Oxford.

STICKEL, J., KNUTSEN, J., LIBERATORE, M., LUU, W., BOUSFIELD, D., KLINGENBERG, D., SCOTT, C. T., ROOT, T., EHRHARDT, M. & MONZ, T. 2009. Rheology measurements of a biomass slurry: an inter-laboratory study. *Rheologica Acta,* 48**,** 1005-1015.

STICKEL, J. J. & POWELL, R. L. 2005. Fluid mechanics and rheology of dense suspensions. *Annu. Rev. Fluid Mech.,* 37**,** 129-149.

STOKES, G. G. 1851. On the effect of the internal friction of fluids on the motion of pendulums. *Transactions of the Philosophical Cambridge Society* 9**,** 51-52.

STOKES, J. & TELFORD, J. 2004. Measuring the yield behaviour of structured fluids. *Journal of Non-Newtonian Fluid Mechanics,* 124**,** 137-146.

STOVER, C. A., KOCH, D. L. & COHEN, C. 1992. Observations of fibre orientation in simple shear flow of semi-dilute suspensions. *Journal of Fluid Mechanics,* 238**,** 277-296.

T. YURUGI, S. I., Y. NUMATA, K. SYKES 2001. SEM/EDX Integrated Analysis System. *SEMEDX Series.* Readout: Horiba Technical Reports.

TABUTEAU, H., COUSSOT, P. & DE BRUYN, J. R. 2007. Drag force on a sphere in steady motion through a yield-stress fluid. *Journal of Rheology (1978-present),* 51**,** 125-137.

TADROS, T. 2011. Interparticle interactions in concentrated suspensions and their bulk (Rheological) properties. *Advances in colloid and interface science,* 168**,** 263-277.

TEH, E. J., LEONG, Y. K., LIU, Y., FOURIE, A. B. & FAHEY, M. 2009. Differences in the rheology and surface chemistry of kaolin clay slurries: The source of the variations. *Chemical Engineering Science,* 64**,** 3817-3825.

THORNE, P. D. & HANES, D. M. 2002. A review of acoustic measurement of small-scale sediment processes. *Continental Shelf Research,* 22**,** 603-632.

TILLER, F. M. & SHIRATO, M. The role of porosity in Filtration: VI. New definition of filtration resistance. *Journal of American Institute of Chemical Engineers,* 10, 61-67.

TIU, C. & BOGER, D. V. 1974. COMPLETE RHEOLOGICAL CHARACTERIZATION OF TIME-DEPENDENT FOOD PRODUCTS. *Journal of Texture Studies,* 5**,** 329-338.

TORRES, M., GADALA-MARIA, F. & WILSON, D. 2013. Comparison of the rheology of bubbly liquids prepared by whisking air into a viscous liquid (honey) and a shear-thinning liquid (guar gum solutions). *Journal of Food Engineering,* 118**,** 213-228.

TRACEY, E., SMITH, P. & MORREY, E. 1996. Rheology of concentrated, heterogeneous slurries containing> 1M electrolyte—a case study in nuclear waste suspensions. *Journal of nuclear materials,* 230**,** 19-35.

TREVELYAN, B. & MASON, S. 1951. Particle motions in sheared suspensions. I. Rotations. *Journal of Colloid Science,* 6**,** 354-367.

TUCKER, M. G., GOODWIN, A. L., DOVE, M. T., KEEN, D. A., WELLS, S. A. & EVANS, J. S. 2005. Negative thermal expansion in ZrW 2 O 8: Mechanisms, rigid unit modes, and neutron total scattering. *Physical review letters,* 95**,** 255501.

TURIAN, R. M., MA, T. W., HSU, F. L. G. & SUNG, D. J. 1997. Characterization, settling, and rheology of concentrated fine particulate mineral slurries. *Powder Technology,* 93**,** 219-233.

TURNEY, M. A., CHEUNG, M. K., POWELL, R. L. & MCCARTHY, M. J. 1995. Hindered settling of rod-like particles measured with magnetic resonance imaging. *AIChE Journal,* 41**,** 251-257.

UHLHERR, P., GUO, J., TIU, C., ZHANG, X.-M., ZHOU, J.-Q. & FANG, T.-N. 2005. The shear-induced solid–liquid transition in yield stress materials with chemically different structures. *Journal of Non-Newtonian Fluid Mechanics,* 125**,** 101-119.

VAN DER ZWAAN, B. 2008. Prospects for nuclear energy in Europe. *International Journal of Global Energy Issues,* 30**,** 102-121.

VAN WAZER, J. R. 1963. *Viscosity and Flow Measurement: A Laboratory Handbook of Rheology*, John Wiley and Sons.

VELAMAKANNI, B. V., CHANG, J. C., LANGE, F. F. & PEARSON, D. S. 1990. New method for efficient colloidal particle packing via modulation of repulsive lubricating hydration forces. *Langmuir,* 6**,** 1323-1325.

VELAMAKANNI, B. V. & LANGE, F. F. 1991. EFFECT OF INTERPARTICLE POTENTIALS AND SEDIMENTATION ON PARTICLE PACKING DENSITY OF BIMODAL PARTICLE DISTRIBUTIONS DURING PRESSURE FILTRATION. *Journal of the American Ceramic Society,* 74**,** 166-172.

VERWEY, E. J. W., OVERBEEK, J. T. G. & VAN NES, K. 1948. *Theory of the stability of lyophobic colloids: the interaction of sol particles having an electric double layer*, Elsevier New York.

VESARATCHANON, J. S., NIKOLOV, A. & WASAN, D. T. 2008. Sedimentation of concentrated monodisperse colloidal suspensions: Role of collective particle interaction forces. *Journal of Colloid and Interface Science,* 322**,** 180-189.

VICKERS, D., ARCHER, L. A. & FLOYD-SMITH, T. 2009. Synthesis and characterization of cubic cobalt oxide nanocomposite fluids. *Colloids and Surfaces A: Physicochemical and Engineering Aspects,* 348**,** 39-44.

VINCENZI, D. 2013. Orientation of non-spherical particles in an axisymmetric random flow. *Journal of Fluid Mechanics,* 719**,** 465-487.

VINOGRADOV, G. V., ISAYEV, A. I., MUSTAFAEV, D. A. & PODOLSKY, Y. Y. 1978. Polarization-optical investigation of polymers in fluid and high-elastic states under oscillatory deformation. *Journal of Applied Polymer Science,* 22**,** 665-677.

VOLMER, M. & WEBER, A. 1926. Nucleus formation in supersaturated systems. *Z. Phys. Chem,* 119.

VUKASOVICH, M. S. & FARR, J. P. G. 1986. Molybdate in corrosion inhibition—A review. *Polyhedron,* 5**,** 551-559.

WANG, B. G., SHI, E. W. & ZHONG, W. Z. 1998. Twinning Morphologies and Mechanisms of ZnO Crystallites under Hydrothermal Conditions. *Crystal Research and Technology,* 33**,** 937-941.

WEC 2013. World energy resource 2013 survey summary London, UK: World Energy Council for Sustainable Energy.

WHEATLEY, P. J. 1981. *The Determination of Molecular Structure*, Dover.

WHORLOW, R. W. 1980. *Rheological Techniques*, E. Horwood.

WILSON, L. L., SPEERS, R. A. & TUNG, M. A. 1993. YIELD STRESSES IN MOLTEN CHOCOLATES. *Journal of Texture Studies,* 24**,** 269-286.

WILSON, P. D. 1996. *The Nuclear Fuel Cycle: From Ore to Wastes*, Oxford University Press.

WINTER, M. 1993. *Web Elements: the periodic table* [Online]. 1993].

XUEGANG, L., JIN, C., YANCHAO, Z. & JIANCHEN, W. 2012. Precipitation of Zirconium and Molybdenum in Simulated High-level Liquid Waste Concentration and Denitration Process. *Procedia Chemistry,* 7**,** 575-580.

XUEWU, Z., XIN, L., DEXIANG, G., WEI, Z., TONG, X. & YONGHONG, M. 1996. Rheological models for xanthan gum. *Journal of Food Engineering,* 27**,** 203-209.

YANG, H.-G., LI, C.-Z., GU, H.-C. & FANG, T.-N. 2001. Rheological Behavior of Titanium Dioxide Suspensions. *Journal of Colloid and Interface Science,* 236**,** 96-103.

YANG, H. G. & ZENG, H. C. 2004. Preparation of Hollow Anatase TiO2 Nanospheres via Ostwald Ripening. *The Journal of Physical Chemistry B,* 108**,** 3492-3495.

YILMAZ, H., SATO, K. & WATARI, K. 2007. AFM interaction study of alumina particle and c-sapphire surfaces at high-ionic-strength electrolyte solutions. *Journal of colloid and interface science,* 307**,** 116-123.

YOO, B. & RAO, M. A. 1994. EFFECT OF UNIMODAL PARTICLE SIZE AND PULP CONTENT ON RHEOLOGICAL PROPERTIES OF TOMATO PUREE. *Journal of Texture Studies,* 25**,** 421-436.

YOW, H. N. & BIGGS, S. 2013. Probing the stability of sterically stabilized polystyrene particles by centrifugal sedimentation. *Soft Matter,* 9**,** 10031-10041.

YU, J. G., GUO, H., DAVIS, S. A. & MANN, S. 2006. Fabrication of Hollow Inorganic Microspheres by Chemically Induced Self-Transformation. *Advanced Functional Materials,* 16**,** 2035-2041.

ZHANG, F., DAHLKILD, A. A. & LUNDELL, F. 2013. Nonlinear disturbance growth during sedimentation in dilute fibre suspensions. *Journal of Fluid Mechanics,* 719**,** 268-294.

ZHANG, X., GILES, D., BAROCAS, V., YASUNAGA, K. & MACOSKO, C. 1998. Measurement of foam modulus via a vane rheometer. *Journal of Rheology (1978-present),* 42**,** 871-889.

ZHAO, H., MULLER, I. S. & PEGG, I. L. Effects of aging and temperature on the rheological properties of simulated melter feed slurries for nuclear waste vitrification. Environmental Issues and Waste Management Technologies in the Ceramic and Nuclear Industries XI: Proceedings of the 107th Annual Meeting of The American Ceramic Society, Baltimore, Maryland, USA 2005, Ceramic Transactions, 2012. John Wiley & Sons, 223.

ZHENG, R., TANNER, R. I. & FAN, X.-J. 2011. Flow-Induced Alignment in Short-Fiber Reinforced Polymers. *Injection Molding.* Springer.

ZHOU, Z.-H., WAN, H.-L. & TSAI, K.-R. 1997. Molybdenum(VI) complex with citric acid: synthesis and structural characterization of 1:1 ratio citrato molybdate K2Na4[(MoO2)2(cit)2]·5H2O. *Polyhedron,* 16**,** 75-79.

ZHOU, Z., SCALES, P. J. & BOGER, D. V. 2001. Chemical and physical control of the rheology of concentrated metal oxide suspensions. *Chemical Engineering Science,* 56**,** 2901-2920.

ZHOU, Z., SOLOMON, M. J., SCALES, P. J. & BOGER, D. V. 1999. The yield stress of concentrated flocculated suspensions of size distributed particles. *Journal of Rheology,* 43**,** 651-671.

ZIRNSAK, M. A. & BOGER, D. V. 1998. Axisymmetric entry flow of semi-dilute xanthan gum solutions: prediction and experiment. *Journal of Non-Newtonian Fluid Mechanics,* 79**,** 105-136.

Appendix

Peer-reviewed Journal and Conference Contributions

Scientific Journal Contributions

PAUL, N., BIGGS, S., EDMONDSON, M., HUNTER, T. N. & HAMMOND, R. B. 2013. Characterising highly active nuclear waste simulants. *Chemical Engineering Research and Design,* 91**,** 742-751.

PAUL, N., BIGGS, S., EDMONDSON, M., HUNTER, T. N. & HAMMOND, R. B., MAXWEL, L. 2015. Synthesis of nuclear waste simulants by reaction precipitation: Formation of caesium phosphomolybdate, zirconium molybdate and morphology modification with citratomolybdate complex. Polyhedron, 89, 129-141.

Conference Contributions

PAUL, N., BIGGS, S., EDMONDSON, M., HUNTER, T. N. & HAMMOND, R. B. 2011. Characterising highly active nuclear waste simulants. IChemE Nuclear Fuel Cycle Conference, Manchester, 2012

PAUL, N., BIGGS, S., EDMONDSON, M., HUNTER, T. N. & HAMMOND, R. B. 2014. Characterisation of highly active nuclear waste simulants. IChemE Sustainable nuclear energy conference, Manchester 2014

*BUX, J., HUNTER, T. N., PAUL, N., DODDS, J. M., PEAKALL, J. & BIGGS, S. R. Characterising Nuclear Simulant Suspensions In Situ With an Acoustic Backscatter System. ASME 2013 15th International Conference on Environmental Remediation and Radioactive Waste Management, 2013. American Society of Mechanical Engineers, V002T03A018-V002T03A018

**un-related to this PhD thesis.*

Oral Presentations

IChemE Nuclear Fuel Cycle Conference, Manchester, UK, 2012

XVIth International Congress on Rheology, Lisbon, Portugal, 2012

IChemE Sustainable nuclear energy conference, Manchester, UK 2014